STOCHASTIC MODELLING OF TURBULENCE

WITH
APPLICATIONS
TO
WIND ENERGY

PHD THESIS
BY
EMIL HEDEVANG

AARHUS UNIVERSITY SEPTEMBER 2012

Stochastic modelling of turbulence
With applications to wind energy

PhD thesis by Emil Hedevang
Department of Mathematics, Aarhus University,
Ny Munkegade 118, 8000 Aarhus C, Denmark

Supervised by Jürgen Schmiegel

Industrial PhD project with Siemens Wind Power
With Martin Greiner as company supervisor

Submitted September 28, 2012

ABRIDGED CONTENTS

DETAILED CONTENTS

A · A Lévy based approach to isotropic random vector fields: With applications to turbulence 39
A.1 · Introduction 40
A.2 · Background and preliminaries 41
  A.2.1 · Normal inverse Gaussian distributions 41
  A.2.2 · Convolutions and Fourier transforms 42
  A.2.3 · Integration with respect to Lévy bases 43
A.3 · Constructing random vector fields 46
A.4 · Isotropic, incompressible vector fields 48
A.5 · Von Kármán, Matérn, and Shkarofsky correlations 50
A.6 · Application to atmospheric boundary layer flow 52
  A.6.1 · Description of the data 53
  A.6.2 · The three-dimensional model 54
  A.6.3 · The one-dimensional model 56
A.7 · Conclusion and outlook 59
A.A · Aspects of simulation 61
  A.A.1 · Approximating skeletons 62
  A.A.2 · Smooth partitions of unity 65
  A.A.3 · Partitions of kernels 66
  A.A.4 · Extension to higher dimensions 68
A.B · Integral transforms and spherical symmetries 68
Bibliography 71

B · A parsimonious and universal description of the turbulent energy dissipation 75
B.1 · Introduction 76
B.2 · Background on the data 77
B.3 · A Lévy based continuous multiplicative cascade model 79
  B.3.1 · Two-point correlators 80
  B.3.2 · Ambit sets and scaling of correlators 82
  B.3.3 · Three Lévy bases 82
B.4 · Data analysis 84
  B.4.1 · Distribution of the surrogate energy dissipation 84
  B.4.2 · Scaling and self-scaling of correlators 85
B.5 · Conclusion and outlook 89
B.A · The normal inverse Gaussian distribution 90
B.B · Integration with respect to Lévy bases 92
Bibliography 93

C · Wind turbine power curves incorporating turbulence intensity 97
C.1 · Introduction 98
C.2 · Background 99
  C.2.1 · Upstream, virtual, and driving wind 99
  C.2.2 · The static model 100
  C.2.3 · The quasi static model 101
  C.2.4 · The corrected, quasi static model 103
  C.2.5 · The dynamic model 103
C.3 · Measurements 104
C.4 · Model and method 106
  C.4.1 · The quasi static model revisited 107
  C.4.2 · The upstream, virtual, and driving wind revisited 110
  C.4.3 · The dynamic model revisited 111
  C.4.4 · The new method 113
C.5 · Results and discussion 115
  C.5.1 · The estimated zero-turbulence power curves and derived conventional power curves 116
  C.5.2 · Filling in the blanks: Prediction of performance under unmeasured turbulence intensities 120
  C.5.3 · Bridging the gap: When some wind speeds are not observed 121
  C.5.4 · Connecting the dots: A power curve from few data points 121
C.6 · Further applications and future work 123
C.7 · Conclusion 124
C.A · Implementation of the new method 124
C.B · Quadratic variation of power 127
Bibliography 128

D · High-frequency parametrization of engineering wind-farm wake models 131
D.1 · Introduction 132
D.2 · Data, wake models, and fitting objective 133
  D.2.1 · The data 133
  D.2.2 · Wake models 134
  D.2.3 · Parametrization of the free wind 135
  D.2.4 · Temporal reference frame 136
  D.2.5 · Fit objective 136
D.3 · Results 137
  D.3.1 · Quality of fits 137
  D.3.2 · Model parameter distributions 139
  D.3.3 · Heterogeneous free wind 142
  D.3.4 · Co-moving temporal frame of reference 142
D.4 · Conclusion 145
Bibliography 146

PREFACE

The work behind this thesis was financed as an industrial PhD project between Siemens Wind Power and Aarhus University. From the university side, the work was supervised by Jürgen Schmiegel, and from the company side, the work was supervised by Martin Greiner. This thesis consists of four papers.

Paper A
E. Hedevang and J. Schmiegel. A Lévy based approach to isotropic random vector fields: With applications to turbulence. *Bernoulli*, 2012. Submitted.

Paper B
E. Hedevang and J. Schmiegel. A parsimonious and universal description of the turbulent energy dissipation. *Eur. Phys. J. B*, 2012. Submitted.

Paper C
E. Hedevang. Wind turbine power curves incorporating turbulence intensity. *Wind Energy*, 2012. To appear.

Paper D
U. V. Poulsen, J. Scholz, E. Hedevang, J. Cleve, and M. Greiner. High-frequency parametrization of engineering wind-farm wake models. *Wind Energy*, 2012. Submitted, under revision.

Paper A concerns the construction of a stochastic spatial model for the turbulent velocity vector field. Paper B discusses a stochastic model for the turbulent energy dissipation. Paper C introduces a new method to estimate wind turbine performance from low-resolution statistics. Paper D compares simple engineering wake models and discusses their applicability to describe wind farm flows. The papers, parts of them, or related work have been presented at the following conferences, workshops, seminars, and visits.

- Euromech Colloquium 508 on wind turbine wakes, Madrid, Spain, October 2009
- iTi Conference on Turbulence, Bertinoro, Italy, September 2010
- Workshop in honour of Ole E. Barndorff-Nielsen's 75th birthday, Aarhus, Denmark, October 2010
- AWEA WINDPOWER 2011, Los Angeles, California, May 2011
- Workshop on Ambit Stochastics, Sandbjerg, Denmark, September 2011
- ISI 2011 58th World Statistics Congress, Dublin, Ireland, August 2011
- Oberwolfach Seminar on Statistics for SDEs, Oberwolfach, Germany, October 2011
- Visit to Julie Lundquist at University of Colorado, Boulder, Colorado, February to April 2012
- Visit to Björn Birnir at University of California, Santa Barbara, California, April 2012
- AWEA WINDPOWER 2012, Atlanta, Georgia, June 2012

ENGLISH SUMMARY

This thesis addresses stochastic modelling of turbulence with applications to wind energy in mind. The primary tool is *ambit processes*, a recently developed class of computationally tractable stochastic processes based on integration with respect to Lévy bases. The subject of ambit processes is still undergoing rapid development. Turbulence and wind energy are vast and complicated subjects. Turbulence has structures across a wide range of length and time scales, structures which cannot be captured by a Gaussian process that relies on only second order properties. Concerning wind energy, a wind turbine operates in the turbulent atmospheric boundary layer. In this respect, three regimes are of particular interest: modelling the turbulent wind before it interacts with the wind turbine (e.g. to be used in load simulations), modelling of the interaction of the wind with the wind turbine (e.g. to extract information about a wind turbine's production of power), and modelling the wake generated by the wind turbine so that its influence on other wind turbines further downstream in turn can be modelled (e.g. to be used in load simulations). The thesis makes the contributions listed below.

A spatial stochastic turbulence model based on ambit processes is proposed. It is shown how a prescribed isotropic covariance structure can be reproduced. Non-Gaussian turbulence models are obtained through non-Gaussian Lévy bases or through volatility modulation of Lévy bases. As opposed to spectral models operating in the frequency domain, the ambit process is formulated directly in the spatial domain. Anisotropy (e.g. in the atmospheric boundary layer flow) and inhomogeneity (e.g. the wake generated by a wind turbine) can therefore be modelled explicitly.

At the smallest scales the kinetic energy of the turbulent flow is dissipated into heat due to the internal friction caused by viscosity. An existing stochastic model, also expressed in terms of ambit processes, is extended and shown to give a universal and parsimonious description of the turbulent energy dissipation. The volatility modulation, referred to above, has previously been shown to be closely connected to the energy dissipation. The incorporation of the small scale dynamics into the spatial model opens the door to a fully fledged stochastic model of turbulence.

Concerning the interaction of wind and wind turbine, a new method is proposed to extract wind turbine power curves from low-frequency data. The method improves over the current IEC 61400-12-1 industry standard by being capable of incorporating the turbulence intensity into the estimation procedure.

Finally, three existing simple wake models for the average flow inside a wind farm are evaluated against measured wind power data at time scales from 15 s to 10 min. The wake models are shown to be incapable of capturing the dynamics of wakes.

DANSK SAMMENFATNING

Denne afhandling behandler stokastisk modellering af turbulens med henblik på anvendelser inden for vindenergi. Hovedredskabet er *ambitprocesser*, en nyligt udviklet klasse af beregningsmæssigt håndterbare stokastiske processer baseret på integration med hensyn til Lévy-baser. Emnet ambitprocesser er til stadighed under rivende udvikling. Turbulens og vindenergi er begge omfattende og komplicerede emner. Turbulens har strukturer på tværs af mange længde- og tidsskalaer, strukturer som ikke kan gengives af en gaussisk proces, der kun afhænger af andenordensegenskaber. Vedrørende vindenergi arbejder en vindmølle i det turbulente atmosfæriske grænselag. I den forbindelse er tre områder særligt interessante: modellering af den turbulente vind inden den vekselvirker med vindmøllen (f.eks. til brug inden for lastsimulationer), modellering af vekselvirkningen mellem vind og vindmølle (f.eks. for at uddrage information om vindmøllens produktion af elektricitet) og endelig modellering af slipstrømmen bag en vindmølle så dens indflydelse på andre møller kan modelleres (f.eks. til brug inden for lastsimulationer). Afhandlingen yder følgende bidrag til disse områder.

En stokastisk model baseret på ambitprocesser foreslås til modellering af rumlig turbulens. Det vises, hvorledes en på forhånd given isotropisk kovariansstruktur kan gengives. Ikke-gaussiske turbulensmodeller opnås gennem brugen af ikke-gaussiske Lévy-baser eller gennem brugen af volatilitetsmodulerede Lévy-baser. I modsætning til spektrale modeller, der er formuleret i frekvensdomænet, er ambitprocesserne formuleret direkte i det rumlige domæne. Anisotropi (som f.eks. i det atmosfæriske grænselag) og inhomogenitet (som f.eks. i slipstrømmen bag en vindmølle) kan derfor modelleres eksplicit.

På de mindste skalaer omdannes den kinetiske energi i en turbulent strøm til varme som følge af den interne friktion forårsaget af viskositeten. En eksisterende stokastisk model, også baseret på ambitprocesser, udvides og viser sig at give anledning til en universel og kortfattet beskrivelse af energidissipationen. Volatilitetsmodulationen, der blev henvist til ovenfor, er tidligere blevet vist at være nært forbundet med energidissipationen. Således åbnes døren for en stokastisk turbulensmodel, der kan gengive strukturen på både de små og de store skalaer.

Vedrørende vekselvirkningen mellem vind og vindmølle beskrives en ny metode til at estimere en vindmølles effektkurve ud fra lavfrekvente data. Metoden er en forbedring af den eksisterende industristandard (IEC-61400-12-1), idet metoden inddrager turbulensintensiteten i estimationen.

Til slut sammenlignes tre simple eksisterende slipstrømsmodeller for den gennemsnitlige luftstrøm gennem en vindmøllepark med produktionsdata på tidsskalaer fra 15 s til 10 min. Modellerne viser sig at være utilstrækkelige til at beskrive dynamikken af slipstrømmene.

ACKNOWLEDGEMENTS

Once upon a time, a young man grew fond of applied mathematics. And he thought that he ought to pursue this fondness, and so he went back to the university from which he had graduated in the early years of the third millennium. There he found Ole E. Barndorff-Nielsen and Jürgen Schmiegel who were scrutinizing big whirls that had little whirls that fed on their velocity, and the little whirls had lesser whirls and so on to viscosity. Ole and Jürgen agreed to let the young man enter their circle of study, and so he was sent out to find a pot of gold, for few can study rooflessly, and fewer still without food or drink.

In the middle of a large peninsula lay a company called Siemens Wind Power, and to this day it lies there still, and that company made and still makes enormous contraptions that harvest the wind for its energy. The young man saw that Martin Greiner worked there and that he too was scrutinizing the wirls, big and little. And the young man asked Martin if the company had a pot of gold so that he could ponder over the whirls. Indeed it had, and so it came to be that the young man should work on an industrial PhD project with Siemens Wind Power and Aarhus University with Martin Greiner and Jürgen Schmiegel as supervisors.

As time went by, the young man met many people who all helped, guided, and supported him. In particular, he met Jochen Cleve and Ioannis Antoniou at Siemens Wind Power and with them he studied wakes and power curves. At the university the young man met Uffe Poulsen, Jan Pedersen, and Kristjana Jónsdóttir and they all helped him with the wakes, the wirls, and the wonders of stochastics. In the new world, across the large sea, the young man found friendly and helpful people, and they were Julie Lundquist, Andrew Clifton, Arni Steingrimsson, Kristian Dixon, and Björn Birnir, just to name a few.

And the young man was lucky, indeed very lucky, for while the whirls and wakes wound about, the young man found a young girl, Stina is her name, and with her the young man now lives, and was it not for her, he probably would not have finished his project.

The young man is less young now, but he remains gratefull for all the patience, support, and help that he has received from all the good people, Siemens Wind Power, and Aarhus University. The fruits hang lower for the one who is standing on the shoulders of Ole, Jürgen, and Martin.

Emil Hedevang
September 2012

ONE

INTRODUCTION

Turbulence is a truly vast subject about which the published books and papers are legion. A few pages of introduction cannot possibly do justice to such a subject. Instead, the reader is referred to one of the many fine books, for example the recent and excellent book by Tsinober (2009).

1.1 STYLISED FEATURES

Stochastic modelling of turbulence concerns the description of the turbulent velocity vector field as a stochastic process. It should be contrasted with the deterministic Navier-Stokes equations governing the motion of a fluid. Stochastic modelling of turbulence is therefore not based on physical laws, but rather attempts to construct stochastic processes that reproduce a certain set of stylised features of turbulence. These stylised feastures may in turn be derived from physical laws, from direct numerical simulations of the Navier-Stokes equations, or from measurements of fluid flows.

Most well known stylised features of turbulence include the following. The simplest, non-trivial structure of the turbulent velocity vector field is the second order structure. Atmospheric boundary layer flow is, for example, anisotropic and the spectral tensor of Mann (1998) captures some of this anisotropy. Moving to intermediate length scales, where the flow informally feels neither the influence of the large scales nor the smallest scales, we have the Kolmogorov 2/3-law of the second order structure function (second moment of velocity increments as a function of separation), equivalent to the Kolmogorov 5/3-law of the spectrum (Kolmogorov, 1941a; Oboukhov, 1941a,b). At the smallest scales, where the kinetic energy of the fluid dissipates into heat due to the internal friction imposed by viscosity, we have approximately exponential decay of the energy spectrum (Sirovich et al., 1994). Concerning higher order structures, we have the Kolmogorov 4/5-law of the third order structure function (Kolmogorov, 1941b). This is the only exact result derived directly from the Navier-Stokes equations (Frisch, 1995). Another stylised feature concerns the distribution of the velocity increments themselves. The distribution is known to be highly non-Gaussian across a wide range of separations with a distinctive shape well described by the normal inverse Gaussian distributions (Barndorff-Nielsen et al., 2004). The fact that normal inverse Gaussian distributions fit the distribution of velocity increments well is not a coincidence. Birnir (2012) shows, from a stochastic version of the Navier-Stokes equations, that the law of the velocity increments is approximately generalised hyperbolic. Regarding the velocity derivatives, we have, for example, the invariants of the velocity gradient tensor (Rosales and Meneveau, 2006) and the intermittent behaviour of the energy dissipation which, since Kolmogorov (1962) and Oboukhov (1962), has recieved much attention,

see Cleve et al. (2004), Schmiegel et al. (2004), Cleve et al. (2005), Schmiegel (2005), Cleve et al. (2008), and the references therein. Recently, it has been shown by multipower variation ratios that the turbulent velocity is a non-semimartingale (Barndorff-Nielsen and Schmiegel, 2012).

The stochastic modelling of turbulence may either be implicity or explicitly. In the implicit case, the velocity field is sought as a solution to some stochastic (differential or integral) equation. In the explicit case, the velocity field is given explicitely, say, as an *ambit process*,

$$v(x,t) = \int_{A(x,t)} f(x,t;y,s)\Lambda(dy\,ds),$$

where f, A, and Λ remain unspecified for the moment. The explicit modelling has the advantage that no equations need to be solved in order to obtain a realisation of the velocity field. In Paper A and Paper B, we give examples of such processes employed to model the turbulent velocity field and the turbulent energy dissipation, respectively.

1.2 A MOTIVATION FROM WIND ENERGY

Stochastic modelling of turbulence has many potential applications to wind energy. If wind energy is to gain widespread adoption, beyond what it has already obtained, it must be reliable, efficient, and inexpensive. In order to achieve these goals, wind turbines must be designed and verified accordingly. The design and verification phases necessarily involve simulation of the wind turbine's response to the wind conditions imposed on it. It is too expensive and too time-consuming to build and test every design proposal. In principle, the simulation problem is trivial: Just solve the Navier-Stokes equations governing the motion of the air subject to the boundary conditions imposed by the geometry of the environment and the wind turbine itself. In practice, this is impossible: The Navier-Stokes equations are notorious for their difficulty. The truly vast subject of computational fluid dynamics seeks to overcome these problems in various ways, trying to find suitable compromises between fidelity and computational burden. Yet, accurate simulation of the behaviour of a whole wind turbine operating in the atmospheric boundary layer requires tremendous computational resources. If one such simulation is to be performed for, say, every iteration of an optimisation procedure seeking to find the optimal wind turbine within a given design space, the problem immediately becomes intractable. To complicate matters, the flow of air in the atmospheric boundary layer is *turbulent*, exhibiting intricate structures across a wide range of length scales and time scales, from kilometres and hours to millimetres and milliseconds. There is a priori no reason to believe why some length and time scales should not exert influence on a wind turbine.

Despite the deterministic nature of the Navier-Stokes equations, the turbulent motion of air appears *stochastic*. The turbulent motion may therefore be described as a stochastic process. Synthetic realisations of turbulent wind fields can then be generated and applied to interaction models which describe the behaviour of wind turbines operating in a given wind field. If the stochastic description of the turbulent wind field and the interaction model are suffi-

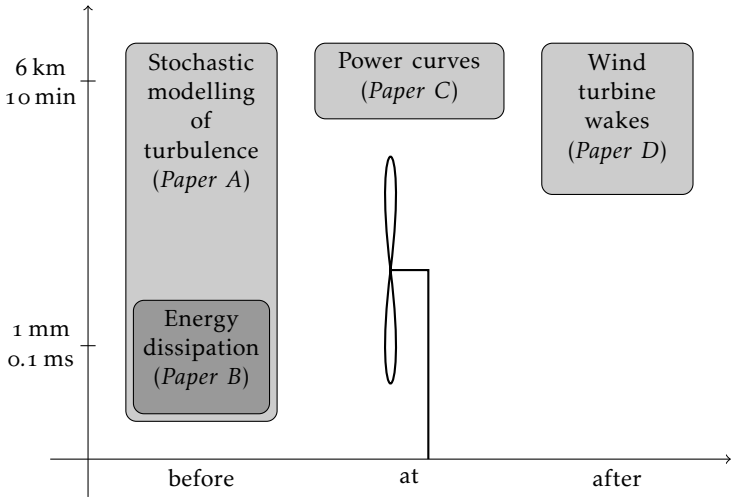

FIGURE 1.1. The scope of the thesis and its relation to wind energy. The wind blows from left to right.

ciently realistic, and if they are sufficiently computationally inexpensive, then we have obtained a useful tool for the design and verification of wind turbines. The majority of the attention of this thesis is on the stochastic models of turbulence, not on the interaction models.

The Gaussian stochastic processes are among the simplest to use. Gaussian processes have the appealing property of being determined completely by their first and second order structure, that is, their means and covariances. In addition, it is fairly straightforward to simulate from Gaussian processes (Kelley and Jonkman, 2012; Mann, 1998). Consequently, Gaussian stochastic models of turbulence are widely applied in the wind energy industry. But turbulence is not Gaussian. In fact, turbulence is highly non-Gaussian with intermittent bursts of strong activity. Gaussian processes are not able to accurately model turbulence. It is therefore important to investigate whether the non-Gaussian nature of turbulence is important to wind turbines or whether the Gaussian approximation is sufficient. It has been indicated that wind turbines indeed are sensitive to the inermittency of turbulence (Hedevang et al., 2010; Mücke et al., 2011; Wächter et al., 2012). However, Gaussian processes may be adequate, especially in combination with sufficiently large safety margins in the design of the wind turbine. But the question still stands: Would it be possible to design more reliable, more efficient, and less expensive wind turbines, if more realistic stochastic turbulence models were employed in the design and verification of wind turbines? This thesis does not answer that question but rather addresses the more humble subject of providing a stepping stone towards a fully fledged stochastic model of the turbulent motion of a fluid, for example, the air in the atmospheric boundary layer. The main tool is the framework of *ambit stochastics*.

The relation of the four papers of this thesis to wind energy is sketched in fig. 1.1. Along the vertical axis we have the length and time scales of turbulence, from kilometres and hours to millimetres and milliseconds. Along the horizontal axis we have three different regimes of interest: modelling of

the wind before it interacts with the wind turbine, modelling of the response of the wind turbine, and modelling of the wind after it has interacted with the wind turbine, to describe its effect on other wind turbines further downstream of the flow. Each paper is represented by a shaded region which marks what the paper addresses in terms of length and time scales of turbulence and in terms of the regime of interest with respect to a wind turbine.

Firstly, Paper A discusses the spatial modelling of turbulence as an *ambit process*. The focus is on the second order structure, but higher order structures such as intermittency can be included in a natural way through volatility modulation. Futhermore, it is shown how the highly idealised case of isotropic turbulence can be extended to more general scenarios, like, for example, atmospheric boundary layer flow.

Secondly, Paper B discusses the use of ambit processes to model the energy dissipation in a turbulent flow. The energy dissipation is an important object for modelling, especially since it is intimately related to the volatility modulation that allows ambit processes to reproduce the intermittent characteristics of turbulence. It is shown how the ambit process formulation gives rise to a parsimonious and universial description of the energy dissipation. It is parsimonious in the sense that two-point statistics are determined from one-point statistics, and universal in the sense that the description is apparently independent of the Reynolds number.

Thirdly, in Paper C we consider modelling of the response of the wind turbine in terms of power production. The goal is to infer the so-called power curve from measured data of very low resolution, specifically, ten-minute averages and standard deviations of wind speed and produced power which are standard in the wind energy industry. The presented method improves over the current industry standard by being able to account for some of the influence that turbulence has on wind power production.

Finally, in Paper D simple engineering wake models are applied to power production data of a wind farm. The purpose is to investigate how well these models and simple generalisations of them are able to describe the behavior of intra farm wakes, in particular the influence of wakes on the production of power. The need for more accurate models is demonstrated.

TWO

AMBIT STOCHASTICS

The term *ambit* means *scope*, *extent*, or *bounds* of something. Informally, an ambit process is a stochastic process where the scope of influence of random events is explicitly defined. More formally, we say that a process $X = (X(\xi))_{\xi\in\Xi}$ on a set Ξ is an ambit process, if X is of the form

$$X(\xi) = \int_{A(\xi)} f(\xi,\zeta)\sigma(\zeta)\,\Lambda(d\zeta), \tag{2.1}$$

where Λ is a Lévy basis (infinitely divisible, independently scattered random measure) on a set Z, $A(\xi) \subseteq Z$ is the ambit set, f is a deterministic function on $\Xi \times Z$, and σ is a process on Z which is independent of Λ and which provides the volatility modulation of the Lévy basis. In sec. 2.1, we give a more rigorous definition of the integral in (2.1). For now we also leave f, σ, and Λ unspecified and require only that the product $f\sigma\Lambda$ is meaningful. For example, f, σ, and Λ could all be real-valued, or they could be matrix-valued, real-valued, and vector-valued, respectively. The ambit set $A(\xi)$, which may be all of Z, determines the extent of the volatility modulated Lévy basis that is allowed to contribute to the integral, hence the name. More general definitions exist, where, for example, the Lévy basis is subordinated (Barndorff-Nielsen and Pedersen, 2012), and where the process σ is not independent of the Lévy basis (Basse-O'Connor et al., 2012).

Ambit processes are natural building blocks for the construction of causal processes, for example processes modelling the development of some quantity over time. Brownian semistationary processes (Barndorff-Nielsen and Schmiegel, 2009) are an important example. A Brownian semistationary process $X = (X(t))_{t\in\mathbb{R}}$ is of the form

$$X(t) = \mu + \int_{-\infty}^{t} g(t-s)\sigma(s)\,dB(s) + \int_{-\infty}^{t} q(t-s)a(s)\,ds,$$

where $\mu \in \mathbb{R}$, $g, q\colon \mathbb{R} \to \mathbb{R}$ are deterministic, non-negative functions, σ and a are càdlàg processes, and B is Brownian motion. In this case, the ambit set is $A(t) = (-\infty, t]$ and prevents events from the future ($s > t$) to influence the present. When σ and a are stationary, then so is X, hence the name *semistationary*. Brownian semistationary processes have been shown to reproduce many stylised features of turbulence (Barndorff-Nielsen and Schmiegel, 2007a,b, 2008; Hedevang, 2011). The volatility process σ can, under mild assumptions, be determined from a suitably normalised version of the quadratic variation of the process X (Barndorff-Nielsen et al., 2011b).

Ambit processes are also applied to construct spatio-temporal processes (Barndorff-Nielsen and Schmiegel, 2004; Schmiegel, 2007; Schmiegel et al.,

2004)

$$X(x,t) = \int_{A(x,t)} f(x,t;y,s)\sigma(y,s)\Lambda(dy\,ds).$$

where $(x,t) \in \mathbb{R}^3 \times \mathbb{R}$ and $A(x,t) \subseteq \mathbb{R}^3 \times (-\infty, t]$. Again, the definition of the ambit set ensures causality. The case $A(x,t) = \mathbb{R}^3 \times (-\infty, t]$ corresponds to a causal model with infinite speed of propagation of innovation (e.g. incompressible fluid flow). If we choose the ambit set to be a cone with its apex at (x,t), we obtain a model with finite speed of propagation of innovation (e.g., compressible fluid flow). In Schmiegel et al. (2004), Schmiegel (2005), and Paper B, other examples of causal, spatio-temporal ambit processes are given. In Paper A, a purely spatial ambit process is constructed.

Other applications of ambit processes include tumour growth (Jónsdóttir et al., 2008; Schmiegel, 2006) and finance (Barndorff-Nielsen et al., 2011a, 2012). Consult the Ambit Stochastics webpage for further references.

After integration with respect to Lévy bases has been recalled in sec. 2.1, we proceed to a spatial model for the turbulent velocity field in sec. 2.2, and finally to the modelling of the surrogate energy dissipation in sec. 2.3.

2.1 INTEGRATION WITH RESPECT TO LÉVY BASES

We denote by $M_{m,d}$ the vector space of $m \times d$ matrices with real entries, by $M_d = M_{d,d}$ the vector space of square matrices, and by M_d^+ the cone of symmetric and non-negative definite square matrices. Let $\langle -, - \rangle$ denote the Euclidean inner product on $\mathbb{R}^d$ and $\|-\|$ denote the derived norm and operator norm. Let $D = \{x \in \mathbb{R}^d \mid \|x\| \leq 1\}$ denote the closed unit ball in $\mathbb{R}^d$. $\mathcal{B}(S)$ denotes the σ-algebra of Borel subsets of a given metric space S, and $\mathcal{B}_b(S)$ denotes the set of bounded Borel subsets. All random variables and processes are assumed to be defined on a common probability space.

For any infinitely divisible $\mathbb{R}^n$-valued random variable X, we let $C(- \ddagger X)$ denote the cumulant function. By the Lévy-Khinchine representation (Sato, 1999, Thm. 8.1),

$$C(z \ddagger X) = i\langle a, z\rangle - \frac{1}{2}\langle z, bz\rangle + \int_{\mathbb{R}^d} (e^{i\langle z,x\rangle} - 1 - i\langle z, x\rangle 1_D(x))\, c(dx)$$

where $a \in \mathbb{R}^d$, $b \in M_d^+$, and c is a Lévy measure on $\mathbb{R}^d$. The triplet (a, b, c) is called the characteristic triplet and determines uniquely the distribution of X.

In the following, Lévy bases and integration with respect to Lévy bases are discussed and the results needed are stated. We refer to Rajput and Rosinski (1989), Barndorff-Nielsen and Stelzer (2011), Pedersen (2003), and Schmiegel (2007) for proofs and further details.

DEFINITION 2.1. Let $S \in \mathcal{B}(\mathbb{R}^n)$ be non-empty. An $\mathcal{B}_b(S)$-indexed family $\Lambda = \{\Lambda(A) \mid A \in \mathcal{B}_b(S)\}$ of $\mathbb{R}^d$-valued random variables is called a Lévy basis on S, if Λ is an infinitely divisible and independently scattered random measure, i.e., if the following three properties hold.

- For every $A \in \mathcal{B}_b(S)$, $\Lambda(A)$ is infinitely divisible.

- For any disjoint $A_1, \dots, A_N \in \mathcal{B}_b(S)$, $\Lambda(A_1), \dots, \Lambda(A_N)$ are independent.
- For every sequence $(A_j)_{j=1}^{\infty}$ of disjoint elements in $\mathcal{B}_b(S)$ with $\bigcup_{j=1}^{\infty} A_j \in \mathcal{B}_b(S)$, we get that $\sum_{j=1}^{\infty} \Lambda(A_j) = \Lambda(\bigcup_{j=1}^{\infty} A_j)$ holds a.s.

A Lévy basis Λ in S induces three set functions $a\colon \mathcal{B}_b(S) \to \mathbb{R}^d$, $b\colon \mathcal{B}_b(S) \to M_d^+$, $c\colon \mathcal{B}_b(S) \times \mathcal{B}(\mathbb{R}^d) \to \mathbb{R}$ by letting $(a(A), b(A), c(A,-))$ be the characteristic triplet of $\Lambda(A)$. It can be shown that a_j is a signed measure, $b_{j,k}$ is a measure for $j = k$ and a signed measure for $j \neq k$, $c(-,B)$ is a measure for every $B \in \mathcal{B}(\mathbb{R}^d)$, and $c(A,-)$ is a Lévy measure for every $A \in \mathcal{B}_b(S)$. Given set functions a, b, and c having the above properties, there exists an $\mathbb{R}^d$-valued Lévy basis Λ on S such that $(a(A), b(A), c(A,-))$ is the characteristic triplet of $\Lambda(A)$. Therefore, (a, b, c) will be called the characteristic triplet of the Lévy basis. Furthermore, the set function $\lambda\colon \mathcal{B}_b(S) \to [0, \infty]$ defined by

$$\lambda(A) = |a|(A) + \operatorname{tr}(b(A)) + \int_{\mathbb{R}^d} 1 \wedge \|x\|^2 \, c(A, dx)$$

has a unique extension to a σ-finite measure on $\mathcal{B}(S)$ which is called the control measure and also denoted by λ. See also Pedersen (2003).

Let (a, b, c) denote the characteristic triplet of a Lévy basis Λ on S with control measure λ. Let $a' = da/d\lambda$ and $b' = db/d\lambda$ denote the Radon-Nikodym derivatives. As in Rajput and Rosinski (1989, Lemma 2.3), the function c may be extended to a σ-finite measure on $\mathcal{B}(S) \otimes \mathcal{B}(\mathbb{R}^d)$, and there exists a function $c'\colon S \times \mathcal{B}(\mathbb{R}^d) \to [0, \infty]$ such that $c'(s,-)$ is a Lévy measure on $\mathcal{B}(\mathbb{R}^d)$ for every $s \in S$, $c'(-,B)$ is measurable for every $B \in \mathcal{B}(\mathbb{R}^d)$, and

$$\int_{S \times \mathbb{R}^d} h(s,x)\, c(ds \times dx) = \int_S \int_{\mathbb{R}^d} h(s,x)\, c'(s, dx)\, \lambda(ds)$$

for every measurable function $h\colon S \times \mathbb{R}^d \to [0, \infty]$. Therefore, we may informally think of c' as $dc/d\lambda$. Thus, for every $s \in S$, $(a'(s), b'(s), c'(s,-))$ is the characteristic triplet of an $\mathbb{R}^d$-valued random variable $\Lambda'(s)$ which will be called the spot variable at s. The spot variable and control measure determine the distribution of the Lévy basis in the sense that

$$C(z \ddagger \Lambda(A)) = \int_A C(z \ddagger \Lambda'(s))\, \lambda(ds)$$

for every $A \in \mathcal{B}_b(S)$.

The definition of the integral over a set $A \in \mathcal{B}(S)$ of a deterministic measurable function $f\colon S \to M_{m,d}$ with respect to an $\mathbb{R}^d$-valued Lévy basis on S is

$$\int_A f \, d\Lambda = \operatorname*{plim}_{j \to \infty} \int_A f_j \, d\Lambda.$$

where $(f_j)_{j=1}^{\infty}$ is a sequence of simple functions such that $f_j \to f$ λ-a.s., and such that the sequence $(\int_A f_j \, d\Lambda)_{j=1}^{\infty}$ converges in probability for every $A \in \mathcal{B}(S)$. The Λ-integral is by construction infinitely divisible.

The following proposition expresses the distribution of the integral $\int_S f \, d\Lambda$ in terms of the function f, the spot variable Λ' and the control measure λ. It is a straightforward generalisation of Rajput and Rosinski (1989, Prop. 2.6) and also stated in Barndorff-Nielsen and Stelzer (2011). For necessary and suffi-

cient conditions for Λ-integrability, see Barndorff-Nielsen and Stelzer (2011, Prop. 2.3) and Rajput and Rosinski (1989, Thm. 2.7).

PROPOSITION 2.2. *Let Λ denote a Lévy basis on $S \in \mathcal{B}(\mathbb{R}^n)$, and let Λ' and λ denote the corresponding spot and control measure. If a measurable function $f : S \to M_{m,d}$ is Λ-integrable, then $\int_S |C(f(s)^T z \ddagger \Lambda'(s))|\, \lambda(ds) < \infty$ for all $z \in \mathbb{R}^m$, and*

$$C\Big(z \ddagger \int_S f\, d\Lambda\Big) = \int_S C(f(s)^T z \ddagger \Lambda'(s))\, \lambda(ds)$$

for all $z \in \mathbb{R}^m$.

On the one hand, the control measure and spot variables corresponding to a Lévy basis are derived from the characteristic triplet of the Lévy basis. On the other hand, when building stochastic processes using Lévy bases, it it desirable to specify the Lévy basis in terms of random variables and an accompanying measure. The following definition and lemma exemplify how this may be accomplished. The proof of the lemma is straightforward.

DEFINITION 2.3. Let $S \in \mathcal{B}(\mathbb{R}^n)$ denote a Borel subset and let $\Lambda^* = \{\Lambda^*(s) \mid s \in S\}$ denote an S-indexed family of $\mathbb{R}^d$-valued independent infinitely divisible random variables, and let λ^* denote a σ-finite measure on $\mathcal{B}(S)$. Then Λ^* is called a seed variable on S, λ^* is called a seed measure on S, and the pair (Λ^*, λ^*) is called a Lévy seed on S.

DEFINITION 2.4. A Lévy seed (Λ^*, λ^*) on $S \in \mathcal{B}(\mathbb{R}^n)$ is called homogeneous, if the distribution of $\Lambda^*(s)$ does not depend on $s \in S$ and if λ^* is the Lebesgue measure on S.

LEMMA 2.5. *Let (Λ^*, λ^*) denote a Lévy seed on $S \in \mathcal{B}(\mathbb{R}^n)$ and let $(a^*(s), b^*(s), c^*(s,-))$ denote the characteristic triplet of $\Lambda^*(s)$. Assume that the following holds,*

- *$a^* : S \to \mathbb{R}^d$ is measurable with $\int_A \|a^*(s)\|\, \lambda^*(ds) < \infty$ for all $A \in \mathcal{B}_b(S)$,*
- *$b^* : S \to M_d^+$ is measurable with $\int_A \|b^*(s)\|\, \lambda(ds) < \infty$ for all $A \in \mathcal{B}_b(S)$,*
- *$c^*(-, B) : S \to [0, \infty]$ is measurable for each $B \in \mathcal{B}(\mathbb{R}^d)$, and there exists a measurable function $K : S \to \mathbb{R}_+$ such that $\int_A K(s)\, \lambda^*(ds) < \infty$ for all $A \in \mathcal{B}_b(S)$ and such that $\int_{\mathbb{R}^d} 1 \wedge \|x\|^2\, c^*(s, dx) < K(s)$ for all $s \in S$.*

Then $a(A) = \int_A a^*(s)\, \lambda^*(ds)$ defines a set function such that a_j is a signed measure on $\mathcal{B}_b(S)$; $b(A) = \int_A b^*(s)\, \lambda^*(ds)$ defines a set function such that $b_{j,k}$ is a measure on $\mathcal{B}_b(S)$ for $j = k$ and a signed measure for $j \neq k$; and $c(A, B) = \int_A c^*(s, B)\, \lambda^*(ds)$ defines a set function such that $c(A, -)$ is a Lévy measure on $\mathbb{R}^d$ for all $A \in \mathcal{B}_b(S)$ and such that $c(-, B)$ is a measure on $\mathcal{B}_b(S)$ for all $B \in \mathcal{B}(\mathbb{R}^d)$.

COROLLARY 2.6. *Suppose the Lévy seed (Λ^*, λ^*) on $S \in \mathcal{B}(\mathbb{R}^n)$ satisfies the assumptions in lemma 2.5. Then there exists an $\mathbb{R}^d$-valued Lévy basis Λ on S with (a, b, c) as characteristic triplet. Furthermore, the seed (Λ^*, λ^*) is related to the spot variable and control measure through the following relations,*

$$\begin{aligned} a^*(s)\lambda^*(ds) &= a'(s)\lambda(ds), \\ b^*(s)\lambda^*(ds) &= b'(s)\lambda(ds), \\ c^*(s, dx)\lambda^*(ds) &= c'(s, dx)\lambda(ds). \end{aligned}$$

Note that a homogeneous Lévy seed always satisfies the assumptions of lemma 2.5. Furthermore, for a homogeneous Lévy seed, the corresponding control measure is proportional to the Lebesgue measure, since in this case we have

$$\lambda(A) = \left(\|a^*\|_1 + \operatorname{tr}(b^*) + \int_{\mathbb{R}^d} 1 \wedge \|x\|_2^2 \, c^*(dx) \right) \operatorname{Leb}(A).$$

It follows that a', b', and c' are proportional to a^*, b^*, and c^*, respectively. In Paper A and Paper B, the Lévy bases are given in terms of homogeneous Lévy seeds.

COROLLARY 2.7. *Let (Λ^*, λ^*) be a Lévy seed such that the conditions of lemma 2.5 are satisfied, and let Λ denote the Lévy basis corresponding to the seed. Let $f : S \to M_{m,d}$ denote an Λ-integrable function. Then*

$$C\left(z \ddagger \int_S f \, d\Lambda \right) = \int_S C(f(s)^T z \ddagger \Lambda^*(s)) \, \lambda^*(ds)$$

for all $z \in \mathbb{R}^m$.

For a process σ on S that is independent of the Lévy basis Λ, the integral $\int_S f \sigma \, d\Lambda$ is defined conditional on σ, provided $s \mapsto f(s)\sigma(s)$ is almost surely Λ-integrable. In this case, the cumulant function is given by

$$C\left(z \ddagger \int_S f \sigma \, d\Lambda \right) = \log E\left[\exp\left(\int_S C\left((f(s)\sigma(s))^T z \ddagger \Lambda^*(s) \right) \lambda^*(ds) \right) \right].$$

Progress is being made in the case where the process σ is not necessarily independent of the Lévy basis (Basse-O'Connor et al., 2012).

2.2 SPATIAL TURBULENCE

In Mann (1998), the atmospheric turbulent velocity vector field is modelled at a fixed instant in time as a homogeneous Gaussian process. This model is widely applied in the wind energy industry. However, turbulence is not Gaussian, exhibiting velocity increments whose distributions have tails much heavier than the Gaussian distribution (Barndorff-Nielsen et al., 2004). In Mücke et al. (2011), Wächter et al. (2012), and Hedevang et al. (2010), it is shown that the intermittent, non-Gaussian character of the atmospheric boundary layer turbulence influences wind turbines in terms of loads and production of electricity. A model based on a random time change of a nested Gaussian drift-diffusion process is proposed in Mücke et al. (2011) and Wächter et al. (2012) to model the turbulent velocity field as a non-Gaussian process. Somewhat related, Rosales and Meneveau (2006) and Biss (2009) propose to simulate non-Gaussian turbulent vector fields by modifying an existing Gaussian realisation.

As a stepping stone towards a fully fledged spatio-temporal model for the turbulent velocity vector field, we seek in Paper A to provide a purely spatial non-Gaussian model describing the field at a fixed instant in time. While the volatility modulation in (2.1) is of central importance (Barndorff-Nielsen and Schmiegel, 2007b, 2008, 2009), it remains unspecified in Paper A and the focus is mostly on the second order structure, i.e., the correlation structure.

For functions $f, g\colon \mathbb{R}_+ \to \mathbb{R}$, we define the g-transform of f by $g[f](z) = \int_0^\infty f(r)g(rz)\,dr$, provided the integrals exist. For a vector $x \in \mathbb{R}^3$ we define

$$\mathrm{sk}(x) = \begin{bmatrix} 0 & x_3 & -x_2 \\ -x_3 & 0 & x_1 \\ x_2 & -x_1 & 0 \end{bmatrix}$$

as the skew-symmetric matrix generated by x. Furthermore, we let $\hat{x} = x/\|x\|$ when $x \neq 0$, and $\hat{x} = 0$ when $x = 0$. We let $\operatorname{sinc} x = (\sin x)/x$ for $x \neq 0$ and $\operatorname{sinc} 0 = 1$. Then sinc is bounded and smooth and likewise are the derivatives sinc′ and sinc″.

2.2.1 A LÉVY BASED MODEL FOR SPATIAL TURBULENCE

Let $(\Lambda^*, \mathrm{Leb})$ denote an $\mathbb{R}^3$-valued homogeneous Lévy seed on $\mathbb{R}^3$ whose corresponding Lévy basis is denoted by Λ. Let σ denote an $\mathbb{R}$-valued homogeneous process on $\mathbb{R}^3$. Assume that σ and Λ are independent. Let $f\colon \mathbb{R}^3 \to M_3$ denote a matrix-valued deterministic function such that for all $x \in \mathbb{R}^3$ we have that $y \mapsto f(x-y)\sigma(y)$ is almost surely Λ-integrable. We define the $\mathbb{R}^3$-valued process X on $\mathbb{R}^3$ by

$$X(x) = \int_{\mathbb{R}^3} f(x-y)\sigma(y)\,\Lambda(dy). \tag{2.2}$$

The function f is called the kernel. For the sake of simplicity we also assume that $E[\Lambda^*] = 0$ and $E[\sigma^2] = 1$. Then it can be shown that the covariance tensor R of the process X is given by

$$R = (h_{\mathrm{even}} C) * (h_{\mathrm{even}} C)^T - (h_{\mathrm{odd}} C) * (h_{\mathrm{odd}} C)^T, \tag{2.3}$$

where $f = f_{\mathrm{even}} + f_{\mathrm{odd}}$ is the decomposition of the kernel into its even and odd part, and C is a matrix square root of $\mathrm{cov}(\Lambda^*)$ in the sense that $CC^T = \mathrm{cov}(\Lambda^*)$. From (2.3) we see that if we want to find a kernel f that reproduces a given covariance tensor R, then we may assume that $\mathrm{cov}(\Lambda^*) = I$ and that f is either even or odd. Under these assumptions, (2.3) may be solved by Fourier methods since a matrix-version of the convolution theorem yields the following proposition.

PROPOSITION 2.8. *Let $R\colon \mathbb{R}^n \to M_n$ denote a covariance tensor.*

If Q_{even} is an even root of the spectral tensor $F_n[R]$, i.e. $F_n[R] = Q_{even}Q_{even}^T$, and if Q_{even} is integrable, then $f_{even} = (2\pi)^{-n/2} F_n^{-1}[Q_{even}]$ defines a real, even, and matrix-valued function that satisfies

$$R = f_{even} * f_{even}^T, \qquad F_n[R] = (2\pi)^n F_n[f_{even}] F_n[f_{even}]^T.$$

If Q_{odd} is an odd root of the spectral tensor $F_n[R]$, i.e. $F_n[R] = Q_{odd}Q_{odd}^T$, and if Q_{odd} is integrable, then $f_{odd} = -i(2\pi)^{-n/2} F_n^{-1}[Q_{odd}]$ defines a real, odd, and matrix-valued function that satisfies

$$R = -f_{odd} * f_{odd}^T, \qquad F_n[R] = -(2\pi)^n F_n[f_{odd}] F_n[f_{odd}]^T.$$

In general, the Fourier transforms may be cumbersome to evaluate, but under the assumption of isotropy and incompressibility it follows (Batchelor,

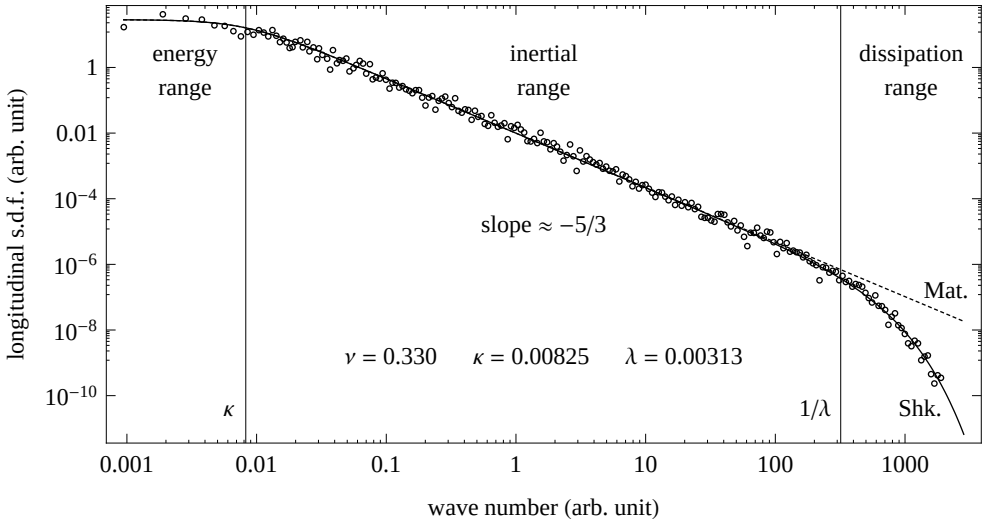

FIGURE 2.1. The longitudinal one-dimensional spectral density measured in the atmospheric boundary layer. Circles denote the estimated spectral density using Welsh's overlapping segment averages with a Hanning taper, a segment length of 4 million, and a segment overlap of 50%. The black solid and dashed curves denote the fitted Shkarofsky and Matérn spectral densities, respectively. The vertical lines mark the estimated values of κ and $1/\lambda$ for the Shkarofsky spectral density.

1959; Robertson, 1940) that the spectral tensor can conveniently be expressed in terms of a single function, the energy spectrum $E\colon \mathbb{R} \to \mathbb{R}$, specifically

$$F_3[R](y) = \frac{E(\|y\|)}{4\pi\|y\|^2}(-\hat{y}\hat{y}^T + I),$$

where the energy spectrum in turn is related to the longitudinal correlation function ρ_1 through

$$E(z) = \sigma^2 z^3 \frac{d}{dz}\left(\frac{1}{z}\frac{d}{dz}F_1[\rho_1](z)\right). \tag{2.4}$$

By exploiting the much simpler form of the isotropic, incompressible spectral tensor we obtain, as shown in Paper A, expressions for even and odd kernels in terms of fairly simple integral transforms involving the energy spectrum.

PROPOSITION 2.9. *Let E denote the energy spectrum of an isotropic and incompressible stochastic vector field on $\mathbb{R}^3$. Assume that $r \mapsto E(r)^{1/2}r$ is integrable. Then*

$$\begin{aligned} f_{even}(x) = \frac{1}{2^{3/2}\pi}\Big((\operatorname{sinc} + 3\operatorname{sinc}'')[E(r)^{1/2}r](\|x\|)\hat{x}\hat{x}^T \\ + (\operatorname{sinc} - \operatorname{sinc}'')[E(r)^{1/2}r](\|x\|)I\Big), \\ f_{odd}(x) = \frac{-1}{2^{1/2}\pi}\operatorname{sinc}'[E(r)^{1/2}r](\|x\|)\operatorname{sk}(\hat{x}) \end{aligned}$$

satisfiey $R = f_{even} * f_{even}^T = -f_{odd} * f_{odd}^T$.

2.2.2 AN EXAMPLE FROM ATMOSPHERIC BOUNDARY LAYER FLOW

For illustration, we consider a data set consisting of 20 million one-point measurements of the longitudinal component of the wind velocity in the atmospheric boundary layer (Dhruva, 2000, data set no. 3). The Taylor frozen flow

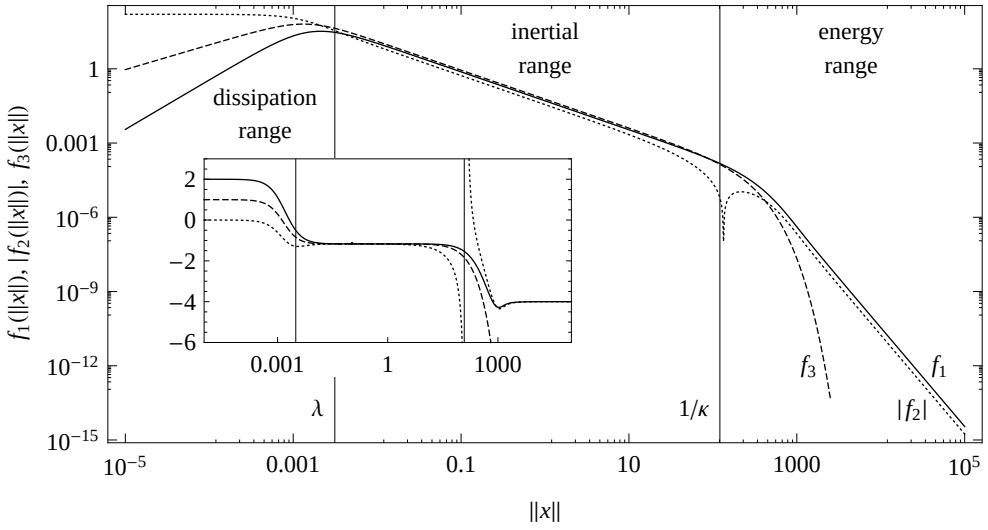

FIGURE 2.2. The scalar functions f_1 (solid), f_2 (dotted), and f_3 (dashed) determining the even and odd kernels $f_{\text{even}}(x) = f_1(\|x\|)\hat{x}\hat{x}^T + f_2(\|x\|)I$ and $f_{\text{odd}}(x) = f_3(\|x\|)\,\text{sk}(\hat{x})$ of the isotropic and incompressible three-dimensional model. The kernels will reproduce a correlation structure whose longitudinal correlation is the Shkarofsky correlation fitted to the atmospheric boundary layer data set. The functions f_1 and f_3 are non-negative whereas $f_2(r)$ is non-negative for $r < r_0$ and negative for $r > r_0$ where r_0 is slightly larger than $1/\kappa$. The inset shows the local slope of the scalar functions $f_1, |f_2|, f_3$ in the double logarithmic representation.

hypothesis (Taylor, 1938) is invoked to interpret the time series as longitudinal spatial measurements. In Paper A, we apply (2.4) to relate the energy spectrum to the longitudinal one-dimensional spectral density $F_1[\rho_1]$ from the data set, see fig 2.1. It must be emphasized that atmospheric boundary layer turbulence is not homogeneous and isotropic. Our example is therefore more of an idealised character. We shall later see ways to introduce inhomogeneity and anisotropy into the ambit stochastics framework.

We see that the Shkarofsky correlation (Shkarofsky, 1968),

$$\rho_{\text{Shkarofsky}}(x) = \frac{(\kappa\sqrt{\|x\|^2+\lambda^2})^\nu K_\nu(\kappa\sqrt{\|x\|^2+\lambda^2})}{(\kappa\lambda)^\nu K_\nu(\kappa\lambda)},$$

$$F_1[\rho_{\text{Shkarofsky}}](z) = \frac{\lambda}{\sqrt{2\pi}}\frac{(\kappa\lambda)^\nu}{K_\nu(\kappa\lambda)}\Big(\lambda\sqrt{\kappa^2+z^2}\Big)^{-\nu-1/2}K_{-\nu-1/2}\Big(\lambda\sqrt{\kappa^2+z^2}\Big),$$

fit the data very well. The Shkarofsky correlation is a generalisation of the Matérn correlation (Guttorp and Gneiting, 2006) which in turn is a generalisation of the von Kármán correlation (von Kármán, 1948). The parameters $\kappa > 0$ and $\lambda > 0$ are scale parameters that, in the case of turbulence, determine the extent of the inertial range, and the parameter $\nu > 0$ is a shape parameter determining the decay of the spectral density in the inertial range. The value $\nu = 1/3$ yields the 5/3-law of Kolmogorov.

Under the assumptions of isotropy and incompressibility, the even kernel f_{even} and odd kernel f_{odd} are given by proposition 2.9. While the kernels are matrix-valued, they are given in terms of three scalar-valued functions $f_1, f_2, f_3 \colon \mathbb{R}_+ \to \mathbb{R}$, specifically

$$f_{\text{even}}(x) = f_1(\|x\|)\hat{x}\hat{x}^T + f_2(\|x\|)I, \qquad f_{\text{odd}}(x) = f_3(\|x\|)\,\text{sk}(\hat{x}).$$

Figure 2.2 shows the functions f_1, f_2, f_3 calculated numerically from the Shkarofsky energy spectrum (2.4) with the parameters estimated from the atmospheric boundary layer data set, see fig. 2.1. Within the dissipation range and the inertial range, the even and odd kernels display similar behaviour, but in the energy range (large length scales) the odd kernel decays rapidly whereas the even kernel decays only algebraically.

2.2.3 SIMULATION

Simulating from the three-dimensional model is challenging if the structures are to be reproduced across all length scales from approximately 10^{-3} to 10^{4}, i.e., across seven orders of magnitude. As detailed in appendix A of Paper A, the kernels may through the use of a partition of unity be decomposed into "smaller" kernels each of which yields a computationally tractable simulation problem.

2.2.4 VOLATILITY MODULATION

The kernel f has been derived from the covariance tensor R under the assumption that $E[\Lambda^*] = 0$ and $E[\sigma^2] = 1$. These assumptions conveniently ensured that the covariance tensor does not depend on the volatility modulation provided by σ. The volatility modulation is necessary if the ambit process (2.2) is to reproduce any turbulent structure beyond the correlation structure. Indeed, it is shown in Paper A that the behaviour of distributions of velocity increments at all lags and the two-point correlator of the surrogate energy dissipation cannot be reproduced without volatility-modulation. However, using a normal inverse Gaussian Lévy basis, it is shown that it is possible to reproduce the distribution of the velocity increments at a single lag, but not all lags simultaneously. Note that the use of a normal inverse Gaussian Lévy basis yields discontinuous samples paths of the velocity which is physically unrealistic.

The crucial observation that the volatility σ in the case of Brownian semistationary processes can be estimated from a suitably normalised version of the quadratic variation links σ to the physical notion of energy dissipation. For a velocity field (of a fluid) denoted by v, the energy disspation ϵ is defined by

$$\epsilon = 2\nu \sum_{i,j=1}^{3} \left(\frac{\partial v_i}{\partial x_j} + \frac{\partial v_j}{\partial x_i} \right)^2,$$

where ν is the viscosity of the fluid. Under the assumption of isotropy, the surrogate energy dissipation $\epsilon = 15\nu(\partial v_1/\partial x_1)^2$ is a proxy for the energy dissipation. Thus, if we approximate the surrogate energy dissipation with squared velocity increments, we have essentially the volatility process σ (up to appropriate normalisation). Schmiegel et al. (2004), Schmiegel (2005), and Paper B demonstrate how the energy dissipation may be modelled as the exponential of an ambit processs. It remains to be investigated how the energy dissipation relates, under the three-dimensional model, to the volatility modulation of

the Lévy basis.

2.2.5 BREAKING ISOTROPY AND HOMOGENEITY

From the point of view of the wind energy industry, the isotropic three-dimensional model is far too idealised, as the atmospheric boundary layer turbulence is anisotropic since, in general, we have $R(0)_{11} > R(0)_{22} > R(0)_{33}$ (Panofsky and Dutton, 1984). Proposition 2.8 can be applied to the "sheared" spectral tensor of Mann (1998) to produce a kernel yielding the desired anisotropy. However, the presented Lévy based framework allows for anisotropy to be introduced in other ways. If we consider the process $X = f_{\text{even}} * \sigma \, d\Lambda$ where $f_{\text{even}}(x) = f_1(\|x\|)\hat{x}\hat{x}^T + f_2(\|x\|)I$ is the even kernel from earlier, then the covariance tensor R is given by $R(x) = \int_{\mathbb{R}^3} f_{\text{even}}(x-y)\operatorname{cov}(\Lambda^*)f_{\text{even}}(y)\,dy$. We get that

$$R(0) = a\operatorname{cov}(\Lambda^*) + b\operatorname{tr}(\operatorname{cov}(\Lambda^*))I \tag{2.5}$$

where

$$a = 4\pi \int_0^\infty \left(\tfrac{2}{15}f_1(r)^2 + \tfrac{2}{3}f_1(r)f_2(r) + f_2(r)^2\right)r^2\,dr,$$
$$b = 4\pi \int_0^\infty \tfrac{1}{15}f_2(r)^2 r^2\,dr.$$

Therefore, by specifying $\operatorname{cov}(\Lambda^*)$ appropriately according to (2.5), any covariance matrix $R(0)$ can be achieved. Some anisotropy can therefore be modelled through the Lévy basis.

Since the derived kernels contain most of their mass near zero, see fig. 2.2, the outcome of the Lévy basis near a given point contributes most to the value of the process $X = f * \sigma \, d\Lambda$ at that given point. Therefore, inhomogeneity and anisotropy of the process may be encoded in the Lévy basis. This has some potential applications to wind energy. Firstly, the passage of a wind front, where the variance of the wind speed increases, say, can conveniently be modelled by letting the variance of the Lévy basis increase in the direction of the motion of the wind front (Nielsen et al., 2007). Secondly, properties like wind shear and veer (the dependency of magnitude and direction on height above ground) may likewise be encoded in the Lévy basis. Finally, the wake behind a wind turbine causes the wind field, experienced by a downstream wind turbine, to be greatly inhomogeneous. An appropriately constructed Lévy basis could ensure that the model reproduces the dynamics of the wake as well as the lower mean wind speed and higher turbulence intensity[1] inside the wake. In turn, this can be applied to load and performance calculations of wind turbines within wind farms.

2.3 ENERGY DISSIPATION

Given the close connection between the energy disspation and the volatility modulation, an accurate model of the former serves a double purpose: to model an important physical phenomenon and to provide an important in-

1 · The turbulence intensity is defined as the ratio of the standard deviation of the wind speed to the mean wind speed.

gredient in the model for the velocity. In this section we will consider the modelling of the energy dissipation from Paper B.

Since the pioneering work of Kolmogorov (1962) and Oboukhov (1962), the small-scale intermittency of the energy dissipation in turbulence has received much attention (Frisch, 1995; Sreenivasan and Antonia, 1997). The small scale intermittency is primarily expressed in terms of multifractal and universal scaling of inertial range statistics, such as structure functions, extended self-similarity (Benzi et al., 1993), scaling and self-scaling of correlators (Schmiegel, 2005), and breakdown coefficients (Cleve et al., 2008).

Discrete and continuous random cascade processes have proved useful in describing phenomenologically the small-scale behaviour of the turbulent energy dissipation (Benzi et al., 1984; Cleve and Greiner, 2000; Frisch et al., 1978; Jouault et al., 1999, 2000; Mandelbrot, 1974; Meneveau and Sreenivasan, 1991; Schertzer and Lovejoy, 1987). In Cleve et al. (2005), the surrogate energy dissipation is modelled as a discrete random multiplicative cascade process. Choosing the law of the cascade generators to be log-normal yields the Kolmogorov-Oboukhov model. A continuous analogue to the discrete multiplicative cascade processes is formulated in terms of integrals with respect to Lévy bases and has been shown (Barndorff-Nielsen and Schmiegel, 2004; Schmiegel, 2005; Schmiegel et al., 2004) to be computationally tractable and to accurately describe the two- and three-point statistics of the energy dissipation.

In the cited works, focus is on the modelling of n-point statistics of the energy dissipation, not on the distribution of the energy dissipation itself. Indeed, Schmiegel (2005) concludes with a remark that the law of the Lévy basis driving the cascade model should be inferred and its dependency on the Reynolds number should be investigated.

Both discrete and continuous multiplicative cascade processes suggest that the law of the logarithm of the energy dissipation should be infinitely divisible. Among the infinitely divisible distributions are the normal, stable, and normal inverse Gaussian distributions. The three classes of distributions each have their own tail behaviour.

The use of stable Lévy bases for modelling of the energy dissipation has been investigated in Cleve et al. (2008) and it is concluded, by analysing the breakdown coefficients, that "except for the log-normal limit, this leaves no room for the log-stable modelling of the turbulent energy cascade." Paper B investigates the alternative of using a normal inverse Gaussian Lévy basis to model the energy dissipation and, in particular, addresses the one-point distributions and two-point statistics.

The use of normal inverse Gaussian distributions in turbulence modelling is not new. In Cleve et al. (2005), the parameters of the normal inverse Gaussian cascade generator are estimated from scaling exponents and cumulants, both of which are moment estimates which are notorious for their sensitivity to outliers. Indeed, estimation of the normal inverse Gaussian parameters (and those of other distributions) may not be feasible from sample moments. In Paper B, we apply maximum likelihood methods instead, as these methods suffer no such deficiencies.

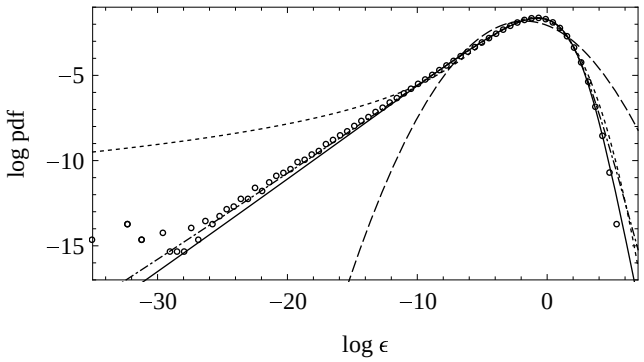

FIGURE 2.3. Distribution of the logarithm of the surrogate energy dissipation represented through the logarithm of the probability density function from a helium jet experiment: data (circles), normal fit (long dashes), stable fit (short dashes), normal inverse Gaussian fit (dots and dashes), and normal inverse Gaussian fit constrained to possess finite exponential moments of order four (black curve).

In Schmiegel (2005), the surrogate energy dissipation ϵ is modelled as a $(1+1)$-dimensional stochastic process (one dimension in space and one in time) given as the exponential of an integral with respect to a Lévy basis Z on $\mathbb{R}^2$,

$$\epsilon(x,t) = \exp\Big(\int_{A(x,t)} Z(dx'\,dt')\Big), \tag{2.6}$$

where $A(x,t) \subseteq \mathbb{R}^2$ is the ambit set. We assume that the Lévy basis Z is given in terms of a homogeneous Lévy seed (Z^*, Leb), and that the ambit sets are defined by $A(x,t) = A + (x,t)$ for some bounded Borel set $A \subseteq \mathbb{R}^2$. Thus, we ensure that ϵ is stationary in space x and time t. The model (2.6) is an example of a random multiplicative cascade process in continuous space and time.

The distribution of $\log\epsilon$ is given by

$$K(s \ddagger \log\epsilon(t)) = K(s \ddagger Z^*)|A|, \tag{2.7}$$

where $K(s \ddagger X) = \log E[\exp(sX)]$. By (2.7), the distribution of the surrogate energy dissipation is, under the model (2.6), determined by the distribution of the Lévy seed Z^*. In Paper B, it is shown (see fig. 2.3) that the empirical distribution of the logarithm of the surrogate energy dissipation is well described by the normal inverse Gaussian distribution. For comparison, normal and stable fits are provided as well. In Paper B, it is also shown that the shape of the distributions is *universal*, i.e. the shape parameters are apparently independent on the Reynolds number, at least for the thirteen data sets considered in the paper. The normal inverse Gaussian distribution is superior to the normal distribution and the stable distribution in terms of describing the distribution of the energy dissipation, and the normal inverse Gaussian distribution is superior to the normal distribution and competitive with the stable distribution in terms of reproducing the scaling and self-scaling exponents of the two-point correlators (see below).

An observable that embodies the intermittency of the energy dissipation is the two-point correlator. The two-point correlator $c_{p,q}$ of order (p,q) is defined

by

$$c_{p,q}(t_1,t_2) = E[\epsilon(t_1)^p \epsilon(t_2)^q]/(E[\epsilon(t_1)^p]E[\epsilon(t_2)^q]).$$

The sum $p+q$ is the *total order* of the correlator $c_{p,q}$. Data analysis (Cleve et al., 2004; Schmiegel et al., 2004) reveals that, at least for $p+q \leq 3$, the two-point correlators exhibit *scaling*,

$$c_{p,q}(\Delta t) := c_{p,q}(t, t+\Delta t) \propto \Delta t^{-\tau(p,q)},$$

in a range of Δt comparable to the inertial range of the velocity structure functions. For $(p,q) = (1,1)$, the exponent $\tau(1,1)$ is known as the *intermittency exponent*. It can be shown that, under the model (2.6),

$$c_{p,q}(t_1,t_2) = \exp(K(p,q)|A(0,t_1) \cap A(0,t_2)|) \tag{2.8}$$

where

$$K(p,q) = K(p+q \ddagger Z') - K(p \ddagger Z') - K(q \ddagger Z'). \tag{2.9}$$

The exponent in (2.8) is expressed as a product where the first factor depends only on the Lévy basis and the order of the correlator, and the second factor depends only on the overlap of the ambit sets. This provides a way of modelling a wide range of correlators, since the shape of the ambit set, under suitable assumptions, can be determined from the correlator. In Paper B, a flexible class of parameterized ambit sets is used to fit the estimated correlators.

In Schmiegel (2005), it is shown that the two-point correlators also have the property of *self-scaling*,

$$c_{p_2,q_2}(\Delta t) = c_{p_1,q_1}(\Delta t)^{\tau(p_1,q_1;p_2,q_2)},$$

for an even wider range of Δt, much like the scaling range of extended self-similarity (Benzi et al., 1993) of the structure functions is wider than the scaling range of the pure structure functions. Here the exponent $\tau(p_1,q_1;p_2,q_2) = \tau(p_2,q_2)/\tau(p_1,q_1)$ is the self-scaling exponent. By (2.8) we immediately obtain self-scaling of the correlators under the model (2.6),

$$c_{p_2,q_2}(\Delta t) = c_{p_1,q_1}(\Delta t)^{K(p_1,q_1;p_2,q_2)},$$

where

$$K(p_1,q_1;p_2,q_2) = K(p_2,q_2)/K(p_1,q_1)$$

is the self-scaling exponent. The self-scaling property is independent of the shape of the ambit set and thus scaling of the correlators is not necessary for self-scaling of the correlators. The Lévy seed Z^* determines though (2.7) the distribution of the surrogate energy dissipation and through (2.9) the self-scaling exponents. In Paper B, it is shown that the self-scaling exponents estimated from data are, to good approximation, predicted by the shape parameters of the one-point distribution of the energy dissipation. The model is therefore *parsimonious*, since the structure of a more complicated object (the two-point correlator) is predicted by the structure of a simpler object (the one-point distribution). Furthermore, since the correlators are moment estimates, they are sensitive to outliers. The parameters of the one-point distributions of

the energy dissipation can be estimated using maximum likelihood methods which are less sensitive to outliers.

THREE

WIND TURBINE POWER CURVES

We now change perspective and consider turbulence from the point of view of a wind turbine. More precisely, how turbulence affects the power production of a wind turbine. In contrast to Paper A and Paper B, where the structure of turbulence across all length and time scales was discussed, Paper C only considers the so-called ten-minute statistics. In particular, this implies that the inertial and dissipation ranges are not resolved.

The subject of power curves addresses the problem of describing, verifying, and predicting the performance of a wind turbine under given wind conditions. Informally, the power curve expresses the produced power as a function of wind speed. Since the wind turbine extracts power from a large region of space, the power must be a function of the entire wind field surrounding the wind turbine. Furthermore, the power must be a function of the current state of the wind turbine (the pitch angle of the blades, the amount of soil accumulated on the blades, just to name a few). The current state is in turn a function of the history of the wind turbine, which includes the wind field at past times. Ignoring air density for the moment, we therefore assume that the power $p(t)$ at time t is a function f of the wind field $v(x,s)$ for all $s \leq t$ and x in a suitable region R of space around the wind turbine,

$$p(t) = f\Big((v(x,s))_{s\leq t, x\in R}\Big). \tag{3.1}$$

The function f in turn depends in particular on the complicated aerodynamics governing the flow through the wind turbine rotor. We call it the *power curve*. Empirical determination of the power curve in (3.1) is impossible since the entire wind field surrounding the wind turbine cannot be measured. A much coarser approach is therefore taken. The power curve is in the IEC 61400-12-1 standard defined as the mean power P as a function of the mean hub height wind speed U measured 2–4 rotor diametres upstream of the wind turbine,

$$P = f(U). \tag{3.2}$$

The mean wind speed U must not be measured near the wind turbine, since the wind turbine disturbes the flow. It is recognised that the mean power depends on the air density as well, but this dependency can be incorporated through a suitable correction of the mean wind speed. In addition to the air density, it is realised in numerous papers and reports that the mean power depends on many more parameters, in particular the wind speed profile (shear), inflow angle, wind direction (veer), turbulence intensity, turbulent kinetic energy, and the dynamic response of the wind turbine to the wind, see Christensen and Dragt (1986), Elliott and Cadogan (1990), Sheinman and Rosen (1992), Rosen and Sheinman (1994, 1996), Frandsen et al. (2000), Kaiser et al. (2003), Langreder et al. (2004), Pedersen (2004), Rauh and Peinke (2004), van

FIGURE 3.1. An informal sketch of the concepts of upstream wind u, virtual wind v, and driving wind w. The upstream wind is not disturbed by the wind turbine. The virtual wind is the fictive wind field at the location of the wind turbine if the wind turbine was not there to disturb the wind field. The driving wind is the fictive wind field that is strictly homogeneous across the rotor and causes the same power production as the virtual wind field.

Radecke (2004), Eecen et al. (2006), Gottschall et al. (2006), Sumner and Masson (2006), Albers et al. (2007), Kaiser et al. (2007), Gottschall and Peinke (2007, 2008), Anahua et al. (2008), Tindal et al. (2008), Albers (2009), Wagner et al. (2009, 2011), Wächter et al. (2011), and Wharton and Lundquist (2012a,b) and references therein. While appealing due to its simplicity, the model (3.2) is therefore far too unrealistic. In Paper C, it is demonstated how a simple model allows the turbulence intensity to be incorporated into the estimation of wind turbine power curves.

3.1 UPSTREAM, VIRTUAL, AND DRIVING WIND

Since the wind turbine disturbs the flow, any wind speed measured at the location of the turbine cannot be used as a reference wind in a power curve measurement. To acknowledge this, Christensen and Dragt (1986) introduce three useful wind fields: the upstream wind u, the virtual wind v, and the driving wind w. See fig. 3.1 for an informal sketch. The *virtual wind* v is defined to be the fictive wind field at the location of the wind turbine as it would be if the wind turbine was not there to disturb the flow. The virtual wind therefore defines the wind energy resource at the location of the wind turbine.

Suitably far upstream of the wind turbine (assuming that it is not in the wake of another wind turbine) the influence of the wind turbine is negligible. The wind field here is called the *upstream wind* u. In the setting of Paper C, only ten minute means and standard deviations of the upstream wind are measured by cup anemometers at hub height and at the lowest tip height. It will therefore be assumed that the mean and standard deviation of the virtual wind speed at a given height are equal to those of the upstream wind speed at the same height.

The virtual wind is not homogeneous over the rotor. It is therefore useful to introduce the *driving wind* w as the fictive wind field that is strictly homogeneous across the rotor and causes the same power production as the virtual wind. While the driving wind is often not mentioned explicitly, it is used implicitly whenever the wind turbine power is considered as a function of a

single wind speed. In the IEC 61400-12-1 standard, the mean driving wind is implicitly taken to be the hub height upstream mean wind speed.

For any time-dependent quantity $x(t)$, we denote by X the timewise average $X = \frac{1}{T}\int_0^T x(s)\,ds$ where T is a given time interval. Thus, U, V, W denote the mean upstream, virtual, and driving wind speeds; σ_u, σ_v, σ_w denote the corresponding standard deviations; and $I_u = \sigma_u/U$, $I_v = \sigma_v/V$, $I_w = \sigma_w/W$ denote the corresponding turbulence intensities. Similarly, p, P, σ_p are the instantaneous power, the mean power, and the standard deviation of power. The upstream wind will henceforth refer to the measured wind speed at hub height at the meteorology mast, and not to the upstream wind field.

3.2 A QUASI STATIC MODEL

Under the quasi static model (Rosen and Sheinman, 1994), the instantaneous power $p(t)$ is assumed to be a function of the instantaneous driving wind speed $w(t)$,

$$p(t) = f(w(t)). \tag{3.3}$$

As in Paper C, the mean power P over a given time interval T is then

$$P = \frac{1}{T}\int_0^T p(t)\,dt = \frac{1}{T}\int_0^T f(w(t))\,dt = \int_0^\infty \phi(x) f(x)\,dx \tag{3.4}$$

where ϕ denotes the probability density function of the driving wind speed during the time interval under consideration. The function f may be interpreted as the *zero-turbulence power curve*. Given a data set $\{(\phi_i, P_i, \sigma_{p,i}) \mid i = 1,\dots,N\}$ of distributions of driving wind speeds and corresponding means and standard deviations of power, the problem to solve is

$$\text{find } f \text{ such that } \int_0^\infty f(x)\phi_i(x)\,dx = P_i \text{ for all } i = 1,\dots,N. \tag{3.5}$$

This problem is *ill-posed*: a solution may not exist, if a solution exists it may not be unique, and small changes to the input data may cause large changes in the solution. This is especially important since the $P_1,\dots,P_N$ are measurements to which some error will always be connected, and since the distribution of the fictive driving wind speeds must be modeled in terms of other measurements, and since the quasi static model is a very simplified model of the wind turbine. Therefore, some kind of robustness to errors and misspecifications is introduced by observing that the problem (3.5) informally has the structure of a Fredholm equation of the first kind, though the variable i is discrete instead of continuous. Tikhonov regularization (Tikhonov, 1963a,b) is then applied in Paper C to solve (3.5).

3.3 MODELLING THE DRIVING WIND

The power in (3.3) and (3.4) is expressed in terms of the driving wind, so the driving wind must be expressed in terms of the upstream wind, since only the upstream wind can be measured. Here we describe the simple model employed in Paper C that represents the driving wind, on the level of statistical quantities, in terms of the upstream wind. It must be emphasized that the

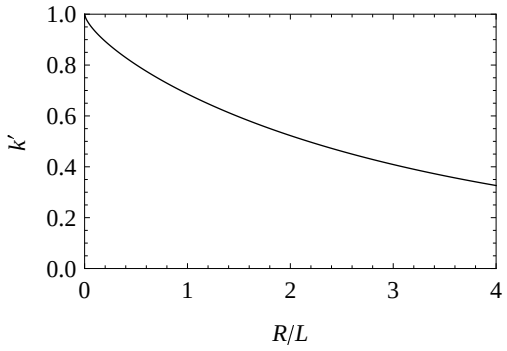

FIGURE 3.2. The factor k' in (3.6) as a function of the ratio R/L of the rotor radius R and the integral length L.

simple model does not provide an exact representation.

We assume that only the longitudinal velocity component is relevant and we let u and v denote the longitudinal component of the upstream and virtual wind fields, respectively. Basic for the following are the assumptions that the statistics of the virtual wind field are the same as those of the upstream wind field, that the upstream wind field is stationary and isotropic, and that its correlation structure is that of von Kármán with longitudinal integral length L. Inspired by Elliott and Cadogan (1990), we also assume that the driving wind w is the spatial average of the virtual wind over the rotor disk. It can then be shown that the mean driving wind speed W is equal to the mean upstream wind speed U, and that the standard deviation σ_w of the driving wind is given by

$$\sigma_w = k'\sigma_u \quad \text{where} \quad k' = \sqrt{\frac{16}{\pi}\int_0^1 \kappa(s)\rho_{\text{trans}}(2Rs)\,ds}, \tag{3.6}$$

where $\kappa(s) = s\arccos(s) - s^2\sqrt{1-s^2}$. The factor k' in (3.6) depends, under the simple model, only on the ratio R/L of the rotor radius R and the integral length L.

Figure 3.2 (a) shows the factor k' as a function of the ratio R/L. When the size of the rotor is comparable to the integral length, which is the case for modern wind turbines, the factor k' is significantly smaller than 1. This implies that a one-point measurement of the standard deviation of the upstream wind speed must be appropriately scaled to represent the standard deviation of the driving wind speed. The scaling factor k' in (3.6) is derived under the highly idealized model considered in this subsection. Nevertheless, as shown in Paper C, the model does indicate the necessity of transforming the measured upstream wind speed, if the standard deviation (or the turbulence intensity) of the upstream wind is to be incorporated into the power curve estimation.

3.4 A DYNAMIC MODEL

The quasi static model allow us to derive a simple expression of the mean power of a wind turbine subject to a given distribution of wind speeds. Unfor-

tunately, the quasi static model ignores the dynamic behavior of the wind turbine. To overcome this drawback, a more sophisticated dynamic model based on a stochastic differential equation is employed,

$$dp_{\text{dyn}}(t) = -\beta_1(p_{\text{dyn}}(t) - f(w(t)))\,dt + \beta_2\,dB(t). \tag{3.7}$$

Here $1/\beta_1$ (the characteristic response time) and β_2 (the noise strength) are constants, f (the zero-turbulence power curve) is a deterministic function, w is the driving wind, and B is a standard Brownian motion independent of the driving wind. In the limit $\beta_1 \to \infty$, the quasi static model is obtained. The dynamic model (3.7) is a simplified version of a dynamic model presented in Gottschall et al. (2006), Gottschall and Peinke (2007, 2008), Anahua et al. (2008), and Wächter et al. (2011). After eliminating the initial condition from the solution to (3.7), we can express the dynamic power as an ambit process,

$$p_{\text{dyn}}(t) = \int_{-\infty}^{t} \beta_1 e^{-\beta_1(t-s)} f(w(s))\,ds + \frac{\beta_2}{\beta_1}\int_{-\infty}^{t} \beta_1 e^{-\beta_1(t-s)}\,dB(s). \tag{3.8}$$

In case the driving wind is stationary, it follows immediately from (3.8) that the mean power, under the dynamic model, is equal to the mean power under the quasi static model. From the point of view of mean values, no large error is committed in using the quasi static model. However, for the quasi static model to match the predicted standard deviation of power with that of the dynamic model, the standard deviation of the driving wind must be scaled further, in addition to the scaling in (3.6), see Paper C for details.

3.5 THE NEW METHOD

We conclude from the above considerations that, in order to account for the size of the rotor, the fluctuations (in terms of the standard deviation) of the driving wind must be scaled down compared to those of the upstream wind; and, in order to account for the lack of dynamic response in the quasi static model, these fluctuations must be further scaled down. We summarize these conclusions by

$$\sigma_w = k\sigma_u$$

for some parameter k which must be estimated from data in addition to the zero-turbulence power curve f. We will assume that the mean driving wind W can be represented by the mean upstream wind U. This is justifiable when the mean wind speeds do not vary too much with height (low vertical shear). In the presense of shear, the equivalent wind (Wagner et al., 2009, 2011) may be used to provide a better representation of the mean driving wind speed.

The new method for power curve estimation, as described in Paper C, assumes that the probability density function ϕ_w of the driving wind speed is normal and determined by the mean and standard deviation. This is an idealising assumption, but there are few alternatives when the turbulence is not resolved below the scale of ten minutes. It follows that the predicted mean

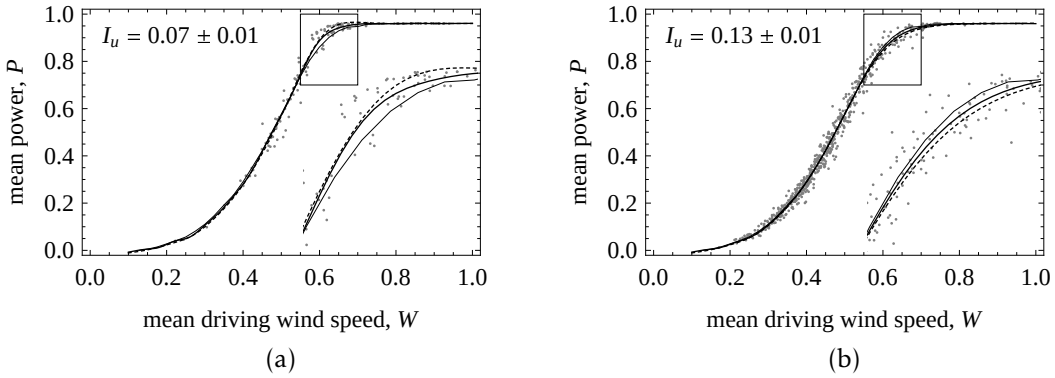

FIGURE 3.3. Two examples of conventional power curves derived from the estimated zero-turbulence power curve f when k is chosen optimally (solid) and when k is held fixed at 1 (dashed) for turbulence intensities $I_u = 0.07$ (a) and $I_u = 0.13$ (b). The thin curve denotes the IEC 61400-12-1 power curve calculated from the whole main data set. The gray dots denote a subset of the data set with turbulence intensities as indicated in each subfigure. A magnified version of the rectangle is shown in the lower right corner.

power is given as

$$P = \int_0^\infty f(x)\phi(x; U, k\sigma_u)\,dx, \tag{3.9}$$

where $\phi(-; \mu, \sigma)$ denotes the probaility density function of a normal distribution with mean μ and standard deviation σ. Paper C describes in detail how f and k can be estimated from data.

The relation (3.9) allows us to incorporate the turbulence intensity into the power curve estimation. Indeed, suppose that f and k have been estimated. Then the mean power at mean upstream wind speed U and turbulence intensity I_u is given by

$$P(U, I_u) = \int_0^\infty f(x)\phi(x; U, kI_uU)\,dx.$$

For fixed turbulence intensity I_u, $P(-, I_u)$ is also called the conventional power curve.

Figure 3.3 shows that the new method is able to account for some of the influence of turbulence intensity on the mean power. If the size of the rotor and the response of the wind turbine is ignored by letting $k = 1$, then the impact of turbulence intensity is exaggerated.

As a further application of the method, it is shown in Paper C how the performance of a wind turbine can be predicted for turbulence intensities that are not measured. Furthermore, the power curve can still be estimated even though the data set might contain missing data for certain wind speeds. These applications are important as they allow for fast power curve measurements.

3.6 TOWARDS HIGH-FREQUENCY DATA

In Paper C, only data of very low temporal resolution (ten minutes) are used to estimate the wind turbine power curve. In general, we may ask about estimating a power curve from high-frequency data. Gottschall et al. (2006), Gottschall and Peinke (2007, 2008), and Anahua et al. (2008) discuss this

problem. In this section, we indicate another approach. Part of this work is in collaboration with Jan Pedersen from Aarhus University.

Again, the driving wind will be used to address the fact that the wind speed and produced power are not measured in the same location. Consider the dynamic model (3.7)

$$dp(t) = -\beta_1(p(t) - f(w(t)))\,dt + \beta_2\,dW(t) \tag{3.10}$$

for $0 \le t \le T$ and where β_1 and β_2 are constants. From the quadratic variation of the power we may estimate β_2 as demonstrated in appendix B of Paper C. We will assume β_1 to be known in advance. The stochastic differential equation (3.10) represents the stochastic integral equation

$$(p(t)) \overset{\mathbb{P}}{=} \left(p(0) + \beta_1 \int_0^t f(w(s))\,ds + \int_0^t p(s)\,d(-\beta_1 s) + \beta_2 W(t)\right), \tag{3.11}$$

where $\mathbb{P}$ is some probability measure and W is a $\mathbb{P}$-Wiener process. Suppose p is a solution to (3.11) for $0 \le t \le T$. For any $\sigma(w)$-adapted process ψ we may ask if there exists a probability measure $\mathbb{P}^\psi$ and a $\mathbb{P}^\psi$-Wiener process W^ψ such that p is also a solution to

$$(p(t)) \overset{\mathbb{P}^\psi}{=} \left(p(0) + \beta_1 \int_0^t \psi(s)\,ds + \int_0^t p(s)\,d(-\beta_1 s) + \beta_2 W^\psi(t)\right). \tag{3.12}$$

Relation (3.12) is true for $(\psi(t)) = (f(w(t)))$. Assume that (3.12) holds for a given ψ. Given any $\sigma(w)$-adapted process ϕ we rewrite (3.12) as

$$\begin{aligned}(p(t)) \overset{\mathbb{P}^\psi}{=} \Bigg(p(0) + \beta_1 \int_0^t \phi(s)\,ds + \int_0^t p(s)\,d(-\beta_1 s) \\ + \beta_2\left(W^\psi(t) - \frac{\beta_1}{\beta_2}\int_0^t (\phi(s) - \psi(s))\,ds\right)\Bigg).\end{aligned}$$

We define the process $N^{\psi,\phi}$ by

$$(N^{\psi,\phi}(t)) = \left(\frac{\beta_1}{\beta_2}\int_0^t (\phi(s) - \psi(s))\,ds\right),$$

and the probability measure $\mathbb{P}^\phi$ by

$$\mathbb{P}^\phi(A) = \int_A \mathcal{E}(N^{\psi,\phi})(T)\,d\mathbb{P}^\psi,$$

where $\mathcal{E}$ denotes the Doléans-Dade exponential. Then, $\mathbb{P}^\phi$ and $\mathbb{P}^\psi$ are locally equivalent, and by Girsanov's and Lévy's theorems we have that $W^\phi := W^\psi - [N^{\psi,\phi}, W^\psi]$ defines a $\mathbb{P}^\phi$-Wiener process. A short calculation shows that

$$W^\phi \overset{\mathbb{P}^\phi}{=} \left(W^\psi(t) - \frac{\beta_1}{\beta_2}\int_0^t (\phi(s) - \psi(s))\,ds\right),$$

and therefore p is also a solution to

$$(p(t)) \overset{\mathbb{P}^\phi}{=} \left(p(0) + \beta_1 \int_0^t \phi(s)\,ds + \int_0^t p(s)\,d(-\beta_1 s) + \beta_2 W^\phi(t)\right),$$

for $0 \le t \le T$. Since p was assumed to be a solution to (3.11), it follows that P^ψ and W^ψ, for any $\sigma(w)$-adapted ψ, can be constructed such that (3.12) also

holds. By (3.12) we may express W^ϕ in terms of p and ψ, and get

$$\mathcal{E}(N^{\psi,\phi})(t) = \exp\Big(\frac{\beta_1^2}{\beta_2^2}\Big(\frac{1}{\beta_1}\int_0^t (\phi(s)-\psi(s))\,dp(s) + \int_0^t (\phi(s)-\psi(s))(p(s)-\psi(s))\,ds - \frac{1}{2}\int_0^t (\phi(s)-\psi(s))^2\,ds\Big)\Big).$$

Since we are only interested in the period $0 \le t \le T$, the Radon-Nikodym derivative $d\mathbb{P}^\phi/d\mathbb{P}^\psi$ is given by $d\mathbb{P}^\phi/d\mathbb{P}^\psi = \mathcal{E}(N^{\psi,\phi})(T)$. In particular, we have

$$\frac{d\mathbb{P}^{f(w)}}{d\mathbb{P}^0} = \exp\Big(\frac{\beta_1^2}{\beta_2^2}\Big(\frac{1}{\beta_1}\int_0^T f(w(s))\,dp(s) + \int_0^T f(w(s))(p(s)-\tfrac{1}{2}f(w(s)))\,ds\Big)\Big) =: r(f,w,p).$$

Given a realisation $\tilde{p}$ of p, and given a model for the driving wind as a stochastic process, we then obtain a likelihood functional for the zero-turbulence power curve f,

$$L(f;\tilde{p}) = \int_{\text{driv}} r(f,w,\tilde{p})\,\mathbb{P}_{\text{driv}}(dw) \tag{3.13}$$

where the integral is with respect to the probability measure $\mathbb{P}_{\text{driv}}$ of the driving wind speed process. Hence, a maximum likelihood estimate of the zero-turbulence power curve can be calculated, provided a model for the driving wind is at hand that allows efficient evaluation of $L(f;\tilde{p})$, for example by Monte Carlo simulations.

A model for the driving wind (Gaussian or not) requires at least the autocovariance function to be specified. In Paper C, it is shown that the variance of the driving wind is smaller than the variance of the upstream wind. If we adopt the simple model that the driving wind speed is the spatial average over the rotor disk of the longitudinal component of the (assumed isotropic) virtual wind, then it can be shown that the autocovariance function cov_w of the driving wind is given by

$$\text{cov}_w(x) = \sigma_v^2\,\frac{16}{\pi}\int_0^1 \kappa(s)h(x,2Rs)\,ds,$$

where $\kappa(s) = s\arccos s - s^2(1-s^2)^{1/2}$ and $h(x,y) = \rho_1(z) + \frac{1}{2}\rho_1'(z)y^2/z$ with $z^2 = x^2+y^2$. Here σ_v^2 is the variance of the virtual wind, ρ_1 is the longitudinal autocorrelation function of the virtual wind, and R is the radius of the rotor. Let $S_2(x) = E[(w(x)-w(0))^2]$ denote the second order structure function of the driving wind. Then it follows, after some approximations, that for $x \ll R$ we have

$$\frac{d\log S_2(x)}{d\log x} \approx 2 = \frac{6}{3}. \tag{3.14}$$

Note that for a modern wind turbine, the radius of the rotor is comparable to the integral length. Hence, x lies within the inertial range when $x \ll R$. Curiously, the result in (3.14) follows from purely geometric reasoning and therefore holds independent of the longitudinal autocorrelation function ρ_1. We therefore tentatively conclude that, from the point of view of a wind turbine, the Kolmogorov 2/3-law should be replaced by a 6/3-law. This should be taken into consideration when modelling the driving wind in (3.13).

FOUR

WIND TURBINE WAKES

We now change perspective once more and consider the wind after it has interacted with a wind turbine and is to potentially interact with another wind turbine further downstream. A wake behind a wind turbine is generated because the wind turbine extracts kinetic energy from the flow and reduces its velocity. The wake rotates in the opposite direction of the wind turbine rotor. The structure of the wake is complicated due to the shedding of tip vortices from the blades and turbulence generated by the mechanical structure of the wind turbine. The turbulence intensity is greater inside the wake than in the surrounding flow. See Burton et al. (2001) and the references given in the introduction of Paper D for further details. Understanding wakes in wind farms is essential since most wind turbines in a modern wind farm will often operate in the wake of one or more upstream wind turbines.

The simplest wake models concern average quantities, for example, the average wind speed at some distance downstream of the wind turbine generating the wake. By construction, they ignore any dynamic structure below the length T of the averaging period. Probably the simplest wake model is the Jensen model (Jensen, 1983) where the wake radius $R_{\text{wake}}(x)$ is assumed to expand linearly as a function of the downstream position x,

$$R_{\text{wake}}(x) = R + kx.$$

Here R is the rotor radius and k is a parameter that determines the rate of expansion of the wake. Two versions of the Frandsen model (Frandsen et al., 2006) are also discussed in Paper D. A calculation based on balance of momentum shows that the wind speed $u(x)$ experienced by a downstream wind turbine in a full or partial wake is given by

$$u(x) = v_0\left(1 - \left(1 - \sqrt{1 - C_T(v_0)}\right)\left(\frac{R}{R_{\text{wake}}(x)}\right)^2 \frac{A_{\text{overlap}}}{A_{\text{rotor}}}\right),$$

where v_0 denotes the undisturbed upstream wind speed, C_T is the thrust coefficient, and $A_{\text{overlap}}/A_{\text{rotor}}$ is the fraction of the rotor disc that is covered by the wake. This ratio is determined by the wind direction θ. The wind direction is assumed to be the same across the wind farm. If a wind turbine is exposed to several wakes, the wakes are combined by adding the squared velocity deficits, $(1 - u(x)/v_0)^2$ (Katic et al., 1987). Thus, the mean wind speed experienced by a wind turbine in the wind farm (and hence the power P^{model}) is determined by three parameters: the upstream wind speed v_0, the wake expansion parameter k, and the common wind direction θ.

Given a data set $\{(P_1, y_1), \ldots, (P_n, y_n)\}$ consisting of the measured average power P_i and average yaw angle y_i for each wind turbine in the wind farm, the upstream wind speed v_0 is determined by inversion of power curves as detailed in Paper D. Two cases are considered: homogeneous upstream wind speed, where v_0 is assumed to be the same for all wind turbines, and hetero-

geneous upstream wind speed, where v_0 is allowed to vary across the wind farm. For each data set, the wake expansion parameter k and direction θ are determined by minimising the fit error

$$\epsilon = \frac{\sum_{i=1}^{n} |P_i - P_i^{\text{model}}(k, \theta)|}{\sum_{i=1}^{n} P_i}.$$

Rather discouragingly, the typical fit is around 10 % to 20 % with significant tails in the range 30 % to 50 %. As the averaging time T increases from 15 s to 10 min the fit error decreases and appears to attain its limit when $T = 10$ min. This is interpreted as an intrinsic limitation of the wake model as 10 min seems to be enough to average out all fluctuations caused by dynamic effects like wake meandering. A homogeneous upstream wind speed yields a larger fit error than the use of a heterogeneous upstream wind speed.

Due to the size of a modern wind farm, it easily takes the wind 10 min to propagate through the wind farm. Naively, the speed of propagation should be less than the upstream wind speed, since the wind farm extracts kinetic energy from the wind. However, a simple model that attempts to take this propagation time into account suggests that the propagation speed is actually greater than the upstream wind speed. Whether this is due to entrainment of fast winds from above the wind farm (Calaf et al., 2010) is a subject for further investigation. The correction for the propagation time causes a significant decrease in fit error only in situations where the upstream wind speed suddenly changes.

Is is also shown in Paper D that the wake expansion parameter k depends on the spacing of the wind turbines with larger values of k corresponding to shorter spacing. This, of course, implies that the assumption of linear expansion is erroneous. (To a somewhat lesser extent, a similar behaviour is observed for the Frandsen model). One can motivate that the wake expansion should be sub-linear. Note that the wake in the Jensen model is the average wake of the time period under consideration. The instantaneous wake is more tubular with a radius slightly larger than the rotor radius. This tubular wake is pertubed randomly as it moves downstream. A simple model for the position of the centre of the wake is Brownian motion. The width of the average wake at a distance x downstream of the wind turbine is then approximately proportional to the standard deviation of the Brownian motion at x, i.e. proportional to $\sqrt{x}$. This yields essentially the Frandsen model.

Paper D demonstrates that the simple engineering wake models are insufficient for an adequate description of the behaviour of wakes inside wind farms. For applications, such as wind farm layout and controller optimisation, more sophisticated models are needed to capture the entrainment of air from the surroundings and the dynamic meandering of the wakes.

Application of ambit processes to the modelling of wakes is still in its infancy. We may, as suggested in subsec. 2.2.5, construct an inhomogeneous Lévy basis from which a turbulent velocity field describing the wake can be generated.

FIVE

CONCLUSION

In Paper A, integrals of deterministic functions with respect to volatility modulated Lévy bases were proposed to model spatial turbulence. It was shown how the second order structure is determined by the so-called kernel and how the kernel may be derived from a prescribed covariance tensor. In the case of isotropic incompressible turbulence, the kernel was represented in terms of simple integral transforms of the energy spectrum. An example was given where the kernel was derived from the Shkarofsky energy spectrum whose parameters were estimated from atmospheric boundary layer flow measurements. The volatility modulation remained unspecified, yet it is necessary for the model to reproduce other stylised features of turbulence.

In Paper B, an existing model for the turbulent energy dissipation, given as the exponential of an ambit process, was used to study the relationship between the one-point distribution and the two-point correlators of the energy dissipation. The normal inverse Gaussian distribution was found capable of describing the distribution of (the logarithm of) the energy dissipation to very good approximation. The shape of the distribution was shown to be universal, that is, independent of the Reynolds number. Furthermore, the self-scaling exponents of the two-point correlators were determined completely from the shape of the distribution of the energy dissipation. Hence the model is parimonious.

In Paper C, the focus is on modelling of the power output of a wind turbine as it operates in the turbulent wind field. A simple quasi static model was employed to express the measured ten-minute means and standard deviations of power in terms of the so-called zero-turbulence power curve, statistics of the measured upstream wind speed, and an auxiliary parameter which attempts to account for the size of the rotor and the dynamic response of the wind turbine. From these quantities, the conventional power curve at any desirable turbulence intensity can be obtained. A method was derived to estimate the zero-turbulence power curve from ten-minute statistics, and the method was shown to improve over the existing industry standard for power curve estimation.

In Paper D, three existing simple engineering wake models for the average flow within a wind farm were evaluated against measured power data at time scales from 15 s to 10 min. The models and generalisations of them were shown capable of capturing some of the average wake behaviour, but a considerable residual fit error remained present at all time scales. More sophisticated wakes models are therefore necessary to accurately capture the dynamics of wakes in wind farms and possibly entrainment of air from above.

Looking forward, consider fig. 5.1 which has been augmented compared to fig. 1.1 to indicate areas of future research. As ambit processes have demonstrated their capability to model many aspects of turbulence, the first goal

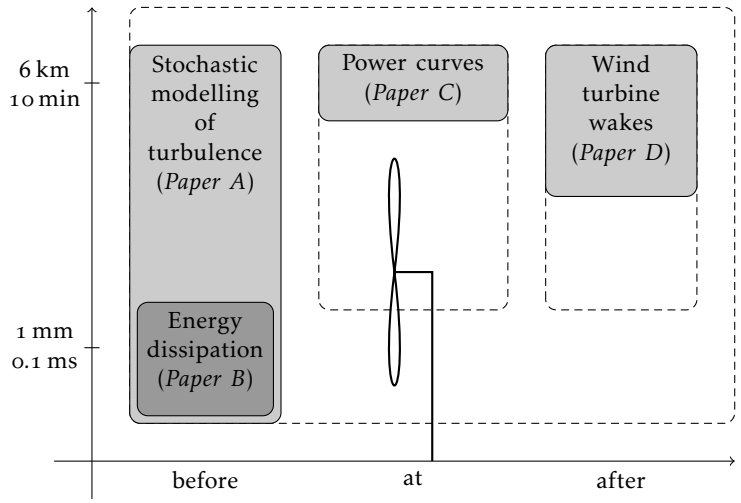

FIGURE 5.1. Where to go from here. The solid boxes represent the work accomplished in the four papers. The dashed curves extend the boxes to indicate areas of future research: estimation of power curves from high-frequency data, modelling of wakes dynamics in wind farms, and application of ambit stochastics to both subjects.

will be to properly specify a volatility modulation of the Lévy basis beneath the spatial turbulence model such that the derived energy dissipation accurately reproduces known stylised features. The application to wind turbine load calculations is immediate. Ultimately, this endeavour should produce a fully fledged spatio-temporal model of turbulence, capable of reproducing the structures of turbulence across all relevant length and time scales, including the anisotropy and inhomogeneity of atmospheric boundary layer flow.

Concerning power curves, it was indicated in sec. 3.6 how the analysis of stochastic differential equations might be applied to estimate wind turbine power curves from high-frequency data. This requires the modelling of the small scales of the driving wind. Regarding wakes, it was suggested in subsec. 2.2.5 that a suitable choice of an inhomogeneous Lévy basis has the potential to model the presence of wakes in wind farms. In this way, we may expand the regime of wake modelling towards smaller scales of turbulence.

BIBLIOGRAPHY

The Ambit Stochastics Project webpage. URL http://thiele.au.dk/research/project-groups/ambit/.

Wind turbines – Part 12-1: Power performance measurements of electricity producing wind turbines (IEC 61400-12-1). International Electrotechnical Commission, 2005.

A. Albers. Turbulence normalisation of wind turbine power curve measurements. Technical report, Deutsche WindGuard Consulting GmbH, 2009.

A. Albers, T. Jakobi, R. Rohden, and J. Stoltenjohannes. Influence of meteorological variables on measured wind turbine power curves. In *Proceedings of EWEC*, Milan, 2007.

E. Anahua, S. Barth, and J. Peinke. Markovian power curves for wind turbines. *Wind Energy*, 11(3):219–232, 2008.

O. E. Barndorff-Nielsen and J. Pedersen. Meta-times and extended subordination. *Theory Probab. Appl.*, 56(2):319–327, 2012.

O. E. Barndorff-Nielsen and J. Schmiegel. Lévy-based spatial-temporal modelling, with applications to turbulence. *Russian Math. Surveys*, 59(1):65–90, 2004.

O. E. Barndorff-Nielsen and J. Schmiegel. Ambit processes: with applications to turbulence and tumour growth. In F. Benth, G. Di Nunno, T. Lindstrom, B. Øksendal, and T. Zhang, editors, *Stochastic analysis and applications*, volume 2 of *Abel Symp.*, pages 93–124. Springer, Berlin, 2007a.

O. E. Barndorff-Nielsen and J. Schmiegel. A stochastic differential equation framework for the turbulent velocity field. *Theory Probab. Appl.*, 52:372–388, 2007b.

O. E. Barndorff-Nielsen and J. Schmiegel. Time change, volatility, and turbulence. In A. Sarychev, A. Shiryaev, M. Guerra, and M. Grossinho, editors, *Mathematical control theory and finance*, pages 29–53. Springer, Berlin, 2008.

O. E. Barndorff-Nielsen and J. Schmiegel. Brownian semistationary processes and volatility/intermittency. In H. Albrecher, W. Runggaldier, and W. Schachermayer, editors, *Advanced financial modelling*, volume 8 of *Radon Ser. Comput. Appl. Math.*, pages 1–25. Walter de Gruyter, Berlin, 2009.

O. E. Barndorff-Nielsen and J. Schmiegel. Variation ratios in turbulence. Forthcoming, 2012.

O. E. Barndorff-Nielsen and R. Stelzer. Multivariate supOU processes. *Ann. Appl. Probab.*, 21(1):140–182, 2011.

O. E. Barndorff-Nielsen, P. Blæsild, and J. Schmiegel. A parsimonious and universal description of turbulent velocity increments. *Eur. Phys. J. B*, 41: 345–363, 2004.

O. E. Barndorff-Nielsen, F. Benth, and A. Veraart. Modelling electricity forward markets by ambit fields. Available at http://dx.doi.org/10.2139/ssrn.1938704, 2011a.

O. E. Barndorff-Nielsen, J. M. Corcuera, and M. Podolskij. Multipower variation for Brownian semistationary processes. *Bernoulli*, 17(4):1159–1194, 2011b.

O. E. Barndorff-Nielsen, F. E. Benth, and A. Veraart. Modelling energy spot prices by volatility modulated Lévy-driven Volterra processes. *Bernoulli*, 2012. To appear.

A. Basse-O'Connor, S. E. Graversen, and J. Pedersen. A unified approach to stochastic integration on the real line. *Theory Probab. Appl.*, 2012. To appear.

G. K. Batchelor. *The theory of homogeneous turbulence*. Cambridge University Press, 1959.

R. Benzi, G. Paladin, G. Parisi, and A. Vulpiani. On the multifractal nature of fully developed turbulence and chaotic systems. *J. Phys. A*, 17(18):3521, 1984.

R. Benzi, S. Ciliberto, C. Baudet, G. Chavarria, and R. Tripiccione. Extended self-similarity in the dissipation range of fully developed turbulence. *Europhys. Lett.*, 24(4):275–279, 1993.

B. Birnir. The Kolmogorov-Obukhov Statistical Theory of Turbulence. In preparation, 2012.

K. H. Biss. Windfeldmodellierung mit multifraktaler Turbulenz. Master's thesis, Institut für Theoretische Physik, Justus-Liebig-Universität, Gießen, 2009.

T. Burton, D. Sharpe, N. Jenkins, and E. Bossanyi. *Wind Energy Handbook*. Wiley, 2001.

M. Calaf, C. Meneveau, and J. Meyers. Large eddy simulation study of fully developed wind-turbine array boundary layers. *Phys. Fluids*, 22(1):015110, 2010.

C. J. Christensen and J. B. Dragt. Accuracy of power curve measurements (M-2632). Technical report, Risø National Laboratory, 1986.

J. Cleve and M. Greiner. The Markovian metamorphosis of a simple turbulent cascade model. *Phys. Lett. A*, 273:104–108, 2000.

J. Cleve, M. Greiner, B. R. Pearson, and K. R. Sreenivasan. Intermittency exponent of the turbulent energy cascade. *Phys. Rev. E*, 69(6):066316, 2004.

J. Cleve, T. Dziekan, J. Schmiegel, O. E. Barndorff-Nielsen, B. R. Pearson, K. R. Sreenivasan, and M. Greiner. Finite-size scaling of two-point statistics and the turbulent energy cascade generators. *Phys. Rev. E*, 71(2):026309, 2005.

J. Cleve, J. Schmiegel, and M. Greiner. Apparent scale correlations in a random multifractal process. *Eur. Phys. J. B*, 63(1):109–116, 2008.

B. R. Dhruva. *An experimental study of high Reynolds number turbulence in the atmosphere.* PhD thesis, Yale University, 2000.

P. Eecen, F. Mouzakis, and A. Cuerva. Accuwind. Technical report, Energy Research Centre of the Netherlands, 2006.

D. Elliott and J. Cadogan. Effects of wind shear and turbulence on wind turbine power curves. In *European Community Wind Energy Conference and Exhibition*, Madrid, 1990.

S. Frandsen, I. Antoniou, J. Hansen, L. Kristensen, H. Madsen, B. Chaviaropoulos, D. Douvikas, J. Dahlberg, A. Derrick, and P. Dunbabin. Redefinition power curve for more accurate performance assessment of wind farms. *Wind Energy*, 3(2):81–111, 2000.

S. Frandsen, R. Barthelmie, S. Pryor, O. Rathmann, S. Larsen, J. Højstrup, and M. Thøgersen. Analytical modelling of wind speed deficit in large offshore wind farms. *Wind Energy*, 9(1-2):39–53, 2006.

U. Frisch. *Turbulence*. Cambridge Univ. Press, 1995.

U. Frisch, P. L. Sulem, and M. Nelkin. A simple dynamical model of intermittent fully developed turbulence. *J. Fluid Mech.*, 87(04):719–736, 1978.

J. Gottschall and J. Peinke. Stochastic modelling of a wind turbine's power output with special respect to turbulent dynamics. *J. Phys. Conf. Ser.*, 75: 012045, 2007.

J. Gottschall and J. Peinke. How to improve the estimation of power curves for wind turbines. *Environ. Res. Lett.*, 3:015005, 2008.

J. Gottschall, E. Anahua, S. Barth, and J. Peinke. Stochastic modelling of wind speed power production correlations. *Proc. Appl. Math. Mech.*, 6:665–666, 2006.

P. Guttorp and T. Gneiting. Studies in the history of probability and statistics. XLIX. On the Matérn correlation family. *Biometrika*, 93(4):989–995, 2006.

E. Hedevang. Stochastic modelling of turbulence. Progress Report. Unpublished. Available upon request, 2011.

E. Hedevang. Wind turbine power curves incorporating turbulence intensity. *Wind Energy*, 2012. To appear.

E. Hedevang and J. Schmiegel. A Lévy based approach to isotropic random vector fields: With applications to turbulence. *Bernoulli*, 2012a. Submitted.

E. Hedevang and J. Schmiegel. A parsimonious and universal description of the turbulent energy dissipation. *Eur. Phys. J. B*, 2012b. Submitted.

E. Hedevang, K. H. Biss, J. Cleve, and M. Greiner. Intermittent Fingerprints in Wind-Turbine Interactions. Poster presented at iTi 2010, Bertinoro, Italy, 2010.

N. O. Jensen. A note on wind turbine interaction (m-2411). Technical report, Risø National Laboratory, Roskilde, Denmark, 1983.

K. Ý. Jónsdóttir, J. Schmiegel, and E. B. V. Jensen. Lévy-based growth models. *Bernoulli*, 14(1):62–90, 2008.

B. Jouault, P. Lipa, and M. Greiner. Multiplier phenomenology in random multiplicative cascade processes. *Phys. Rev. E*, 59:2451–2454, 1999.

B. Jouault, M. Greiner, and P. Lipa. Fix-point multiplier distributions in discrete turbulent cascade models. *Physica D*, 136:125–144, 2000.

K. Kaiser, H. Hohlen, and W. Langreder. Turbulence correction for power curves. In *EWEC*, Madrid, 2003.

K. Kaiser, W. Langreder, H. Hohlen, and J. Højstrup. Turbulence correction for power curves. In J. Peinke, P. Schaumann, and S. Barth, editors, *Wind Energy, Proceedings of the Euromech Colloquium*, pages 159–162. Springer, 2007.

I. Katic, J. Højstrup, and N. Jensen. A simple model for cluster efficiency. In *European Wind Energy Association Conference and Exhibition, Rome, 1986*, volume 1, page 407, Rome, 1987.

N. Kelley and B. Jonkman. NWTC Computer-Aided Engineering Tools (TurbSim). URL http://wind.nrel.gov/designcodes/preprocessors/turbsim/, 2012.

A. N. Kolmogorov. The local structure of turbulence in incompressible viscous fluid for very large Reynolds numbers. *Dokl. Akad. Nauk. SSSR*, 30:299–303, 1941a.

A. N. Kolmogorov. Dissipation of energy in locally isotropic turbulence. *Dokl. Akad. Nauk. SSSR*, 32:15–17, 1941b.

A. N. Kolmogorov. A refinement of previous hypotheses concerning the local structure of turbulence in a viscous incompressible fluid at high Reynolds number. *J. Fluid Mech.*, 13(1):82–85, 1962.

W. Langreder, K. Kaiser, H. Hohlen, and J. Højstrup. Turbulence correction for power curves. In *EWEC*, London, 2004.

B. B. Mandelbrot. Intermittent turbulence in self-similar cascades: divergence of high moments and dimension of the carrier. *J. Fluid Mech.*, 62(02):331–358, 1974.

J. Mann. Wind field simulation. *Prob. Engng. Mech.*, 13(4):269–282, 1998.

C. Meneveau and K. R. Sreenivasan. The multifractal nature of turbulent energy dissipation. *J. Fluid Mech.*, 224:429–484, 1991.

T. Mücke, D. Kleinhans, and J. Peinke. Atmospheric turbulence and its influence on the alternating loads on wind turbines. *Wind Energy*, 14(2):301–316, 2011.

M. Nielsen, G. C. Larsen, and K. S. Hansen. Simulation of inhomogeneous, non-stationary and non-gaussian turbulent winds. *J. Phys. Conf. Ser.*, 75(1): 012060, 2007.

A. M. Oboukhov. On the distribution of energy in the spectrum of turbulent flow. *Dokl. Akad. Nauk. SSSR*, 32(1):22–24, 1941a.

A. M. Oboukhov. Spectral energy distribution in a turbulent flow. *Izv. Akad. Nauk. SSSR Ser. Geogr. Geofiz.*, 5(4–5):453–466, 1941b.

A. M. Oboukhov. Some specific features of atmospheric tubulence. *J. Fluid Mech.*, 13(01):77–81, 1962.

H. Panofsky and J. Dutton. *Atmospheric turbulence: models and methods for engineering applications*. Wiley, 1984.

J. Pedersen. The Lévy-Ito decomposition of an independently scattered random measure. MaPhySto Research Report. Available at www.maphysto.dk, 2003.

T. F. Pedersen. On wind turbine power performance measurements at inclined airflow. *Wind Energy*, 7(3):163–176, 2004.

U. V. Poulsen, J. Scholz, E. Hedevang, J. Cleve, and M. Greiner. High-frequency parametrization of engineering wind-farm wake models. *Wind Energy*, 2012. Submitted.

B. S. Rajput and J. Rosinski. Spectral representations of infinitely divisible processes. *Probab. Th. Rel. Fields*, 82(3):451–487, 1989.

A. Rauh and J. Peinke. A phenomenological model for the dynamic response of wind turbines to turbulent wind. *J. Wind Eng. Ind. Aerod.*, 92(2):159–183, 2004.

H. P. Robertson. The invariant theory of isotropic turbulence. *Proc. Cambridge Philos. Soc.*, 36:209–223, 1940.

C. Rosales and C. Meneveau. A minimal multiscale Lagrangian map approach to synthesize non-Gaussian turbulent vector fields. *Phys. Fluids*, 18:075104, 2006.

A. Rosen and Y. Sheinman. The average output power of a wind turbine in a turbulent wind. *J. Wind Eng. Ind. Aerod.*, 51(3):287–302, 1994.

A. Rosen and Y. Sheinman. The power fluctuations of a wind turbine. *J. Wind Eng. Ind. Aerod.*, 59(1):51–68, 1996.

K.-i. Sato. *Lévy processes and infinitely divisible distributions*. Cambridge University Press, 1999.

D. Schertzer and S. Lovejoy. Physical modeling and analysis of rain and clouds by anisotropic scaling multiplicative processes. *J. Geophys. Res*, 92(D8): 9693–9714, 1987.

J. Schmiegel. Self-scaling of turbulent energy dissipation correlators. *Phys. Lett. A*, 337:342–353, 2005.

J. Schmiegel. Self-scaling tumor growth. *Phys. A*, 367:509–524, 2006.

J. Schmiegel. Spatio-temporal modelling. Unpublished notes, 2007.

J. Schmiegel, J. Cleve, H. C. Eggers, B. R. Pearson, and M. Greiner. Stochastic energy-cascade model for $(1 + 1)$-dimensional fully developed turbulence. *Phys. Lett. A*, 320(4):247–253, 2004.

Y. Sheinman and A. Rosen. A dynamic model of the influence of turbulence on the power output of a wind turbine. *J. Wind Eng. Ind. Aerod.*, 39:329–341, 1992.

I. Shkarofsky. Generalized turbulence space-correlation and wave-number spectrum-function pairs. *Can. J. Phys.*, 46(19):2133–2153, 1968.

L. Sirovich, L. Smith, and V. Yakhot. Energy spectrum of homogeneous and isotropic turbulence in far dissipation range. *Phys. Rev. Lett.*, 72(3):344–347, 1994.

K. R. Sreenivasan and R. Antonia. The phenomenology of small-scale turbulence. *Annu. Rev. Fluid Mech.*, 29:435–472, 1997.

J. Sumner and C. Masson. Influence of atmospheric stability on wind turbine power performance curves. *J. Sol. Energ. Eng.*, 128(4):531–538, 2006.

G. I. Taylor. The spectrum of turbulence. *Proc. R. Soc. Lond. A*, 164(919): 476–490, 1938.

A. N. Tikhonov. Solution of incorrectly formulated problems and the regularization method. *Soviet Math. Dokl.*, 5:1035–1038, 1963a.

A. N. Tikhonov. Regularization of incorrectly posed problems. *Soviet Math. Dokl.*, 4:1624–1627, 1963b.

A. Tindal, C. Johnson, M. LeBlanc, K. Harman, E. Rareshide, and A. Graves. Site-specific adjustments to wind turbine power curves. In *AWEA WINDPOWER*, Houston, 2008.

A. Tsinober. *An Informal Conceptual Introduction to Turbulence*. Springer, 2009.

H. van Radecke. Turbulence correction of power curves. In *DEWEK*, Wilhelmshaven, 2004.

T. von Kármán. Progress in the statistical theory of turbulence. *Proc. Nat. Acad. Sci.*, 34:530–539, 1948.

M. Wächter, P. Milan, T. Mücke, and J. Peinke. Power performance of wind energy converters characterized as stochastic process: applications of the Langevin power curve. *Wind Energy*, 14(6):711–717, 2011.

M. Wächter, H. Heißelmann, M. Hölling, A. Morales, P. Milan, T. Mücke, J. Peinke, N. Reinke, and P. Rinn. The turbulent nature of the atmospheric boundary layer and its impact on the wind energy conversion process. *J. Turbul.*, 13(26):1–21, 2012.

R. Wagner, I. Antoniou, S. M. Pedersen, M. S. Courtney, and H. E. Jørgensen. The influence of the wind speed profile on wind turbine performance measurements. *Wind Energy*, 12(4):348–362, 2009.

R. Wagner, M. Courtney, J. Gottschall, and P. Lindelöw-Marsden. Accounting for the speed shear in wind turbine power performance measurement. *Wind Energy*, 14:993–1004, 2011.

S. Wharton and J. K. Lundquist. Assessing atmospheric stability and its impacts on rotor-disk wind characteristics at an onshore wind farm. *Wind Energy*, 15:525–546, 2012a.

S. Wharton and J. K. Lundquist. Atmospheric stability affects wind turbine power collection. *Environ. Res. Lett.*, 7:014005, 2012b.

PAPER A

A LÉVY BASED APPROACH TO ISOTROPIC VECTOR FIELDS: WITH APPLICATIONS TO TURBULENCE

E. Hedevang[1,2] and J. Schmiegel[3]

1 · Department of Mathematics, Aarhus University, Denmark
2 · Siemens Wind Power, Borupvej 16, 7330 Brande, Denmark
3 · Department of Engineering, Aarhus University, Denmark

ABSTRACT

Using integration of deterministic, matrix-valued functions with respect to vector-valued, volatility modulated Lévy bases, we construct random vector fields on $\mathbb{R}^n$. In the statistically homogeneous case, the vector field is given as a convolution of a deterministic kernel with respect to a homogeneous, volatility modulated Lévy basis. With applications to turbulence in mind, the kernel is, in the isotropic and incompressible case, expressed in terms of the energy spectrum. The theory is applied to atmospheric boundary layer turbulence where, in particular, the Shkarofsky correlation family (a generalisation of the Matérn correlation family) is shown to fit the data well. Since turbulence possesses structure across a wide range of length scales, simulation is non-trivial. Using a smooth partition of unity, a simple algorithm is derived to decompose the simulation problem into computationally tractable subproblems. Applications within the wind energy industry are suggested.

A.1 INTRODUCTION

Ambit processes constitute a flexible framework for constructing spatio-temporal stochastic processes. An ambit process $X = \{X(\xi) \mid \xi \in \Xi\}$ on a set Ξ is defined as

$$X(\xi) = \int_{A(\xi)} f(\xi, \zeta)\sigma(\zeta)\Lambda(d\zeta), \tag{A.1}$$

where Λ is a Lévy basis on a set Z, $A(\xi) \subseteq Z$ is the ambit set, f is a deterministic function on $\Xi \times Z$, and σ is a process on Z which is independent of Λ and which provides the volatility modulation of the Lévy basis. More general definitions exist, where, for example, the Lévy basis is subordinated (Barndorff-Nielsen and Pedersen, 2012), and where the process σ is not indendent of the Lévy basis (Basse-O'Connor et al., 2012). Ambit processes have been applied in different contexts, including turbulence (Barndorff-Nielsen and Schmiegel, 2004, 2009), tumour growth (Jónsdóttir et al., 2008; Schmiegel, 2006), and finance (Barndorff-Nielsen et al., 2011, 2012). In particular, they have been shown to be able to accurately model the intermittency of the turbulent energy dissipation (Hedevang and Schmiegel, 2012; Schmiegel, 2005; Schmiegel et al., 2004), and the temporal behaviour of the one-point measurements of the velocity in the atmospheric boundary layer (Hedevang, 2011).

In Mann (1998), the atmospheric turbulent velocity vector field is modelled at a fixed instant in time as a homogeneous Gaussian process. This model is widely applied in the wind energy industry. However, turbulence is not Gaussian, exhibiting velocity increments whose distributions have tails much heavier than the Gaussian distribution (Barndorff-Nielsen et al., 2004). In Mücke et al. (2011) and Wächter et al. (2012), it is shown that the intermittent, non-Gaussian character of the atmospheric boundary layer turbulence influences wind turbines in terms of loads and production of electricity. A model based on a random time change of a nested Gaussian drift-diffusion process is proposed to model the turbulent velocity field as a non-Gaussian process. Somewhat related, Rosales and Meneveau (2006) and Biss (2009) propose to simulate non-Gaussian turbulent vector fields by modifying an existing Gaussian realisation.

As a stepping stone towards a fully fledged spatio-temporal model for the turbulent velocity vector field, we seek in this paper to provide a purely spatial, inherent non-Gaussian model of the type (2.1) describing the field at a fixed instant in time. The model will be specified to account for turbulent dynamics. However, it is important to stress that the presented methods are not restricted to turbulence and have potential application for a wide range of spatial dynamics. While the volatility modulation in (2.1) is of central importance (Barndorff-Nielsen and Schmiegel, 2008, 2009), in the present paper it will remain unspecified and focus will mostly be on the second order structure, i.e. the correlation structure.

The paper is organised as follows. Section A.2 provides some background on integration of deterministic functions with respect to Lévy bases, in addition to notation and some conventions. Section A.3 constructs random vector fields using convolutions of deterministic matrix-valued functions (the ker-

nels) with respect to vector-valued Lévy bases and demonstrates how the kernel, under some mild assumptions, is determined from the covariance tensor of the process. Section A.4 recalls the consequences of isotropy on the form of the covariance tensor and spectral tensor of a random vector field and shows how the additional assumption of incompressibility provides one further simplification. The kernel of an isotropic and incompressible process is then expressed in terms of the energy spectrum. Section A.5 discusses the spatial correlation structures of von Kármán, Matérn, and Shkarofsky and provides the results necessary to express the kernel in terms of the Shkarofsky correlation structure. Section A.6 applies the theory to a data set consisting of measurements of the turbulent velocities in the atmospheric boundary layer. Kernels that reproduce the isotropic and incompressible Shkarofsky covariance tensor are derived. Furthermore, to illuminate the importance of volatility modulation of the Lévy basis, a one-dimensional model is used for simulations. Section A.7 concludes the paper and provides an outlook on future work and applications within the wind energy industry. The two appendices elaborate on aspects of simulation and contain some technical lemmas used in the derivation of the kernels, respectively.

A.2 BACKGROUND AND PRELIMINARIES

Let $M_{m,d}$ denote the vector space of $m \times d$ matrices with real entries, let $M_d = M_{d,d}$ denote the vector space of square matrices, and let M_d^+ denote the cone of symmetric and non-negative definite square matrices. Let $\langle -, - \rangle$ denote the Euclidean inner product on $\mathbb{R}^d$ and $\|-\|$ the derived norm and operator norm. Let $D = \{x \in \mathbb{R}^d \mid \|x\| \leq 1\}$ denote the closed unit ball in $\mathbb{R}^d$. $\mathcal{B}(S)$ denotes the σ-algebra of Borel subsets of a given metric space S, and $\mathcal{B}_b(S)$ denotes the set of bounded Borel subsets. For functions $f, g \colon \mathbb{R}_+ \to \mathbb{R}$, we define the g-transform of f by $g[f](z) = \int_0^\infty f(r) g(rz)\, dr$, provided the integrals exist. For a vector $x \in \mathbb{R}^3$ we define

$$\operatorname{sk}(x) = \begin{bmatrix} 0 & x_3 & -x_2 \\ -x_3 & 0 & x_1 \\ x_2 & -x_1 & 0 \end{bmatrix}$$

as the skew-symmetric matrix generated by x. Furthermore, we let $\hat{x} = x/\|x\|$ when $x \neq 0$, and $\hat{x} = 0$ when $x = 0$. Throughout this paper, all random variables and processes are assumed to be defined on a common probability space $(\Omega, \mathcal{F}, P)$.

A.2.1 NORMAL INVERSE GAUSSIAN DISTRIBUTIONS

For later reference, we briefly discuss the normal inverse Gaussian distribution $\mathrm{NIG}(\alpha, \beta, \mu, \delta)$, whose probability density function is given by

$$\mathrm{pdf}_{\mathrm{NIG}}(x) = \frac{\delta \alpha e^{\delta\gamma}}{\pi} e^{\beta(x-\mu)} \frac{K_1(\alpha\sqrt{\delta^2 + (x-\mu)^2})}{\sqrt{\delta^2 + (x-\mu)^2}},$$

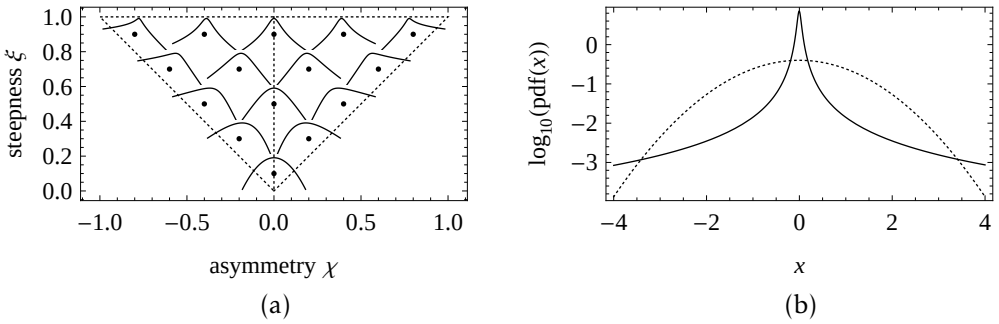

FIGURE A.1. (a) The normal inverse Gaussian shape triangle. The black dots mark positions (χ, ξ) in the shape triangle, and the graphs nearby show the logarithm of the probability density function of the normal inverse Gaussian distribution with the corresponding asymmetry χ, steepness ξ, zero mean, and unit variance, plotted on the interval $[-3, 3]$. (b) The logarithm of the probability density function of a $\mathrm{NIG}^{\nabla}(0.999, 0.09, 0, 1)$-distribution (solid) and a Gaussian distribution (dashed). Both distributions have zero mean and unit variance.

where $\gamma = (\alpha^2 - \beta^2)^{1/2}$. The alternative parametrisation $\mathrm{NIG}^{\nabla}(\xi, \chi, m, v)$ will be used when convenient. Here ξ, χ, m, and v denote the steepness, asymmetry, mean, and variance, respectively. The two parameterizations are related by

$$\xi = (1 + \delta\gamma)^{-1/2}, \qquad \chi = \beta\xi/\alpha, \qquad m = \mu + \delta\beta/\gamma, \qquad v = \delta\alpha^2/\gamma^3.$$

In the second parametrisation, the domain of the parameters is

$$0 < \xi < 1, \qquad -\xi < \chi < \xi, \qquad v > 0, \qquad m \in \mathbb{R}.$$

The shape parameters (χ, ξ) therefore lie in the so-called normal inverse Gaussian shape triangle, see fig. A.1 (a) for examples of possible shapes. The normal distribution is obtained in the limit $\xi \downarrow 0$. Figure A.1 (b) shows another example of a normal inverse Gaussian distribution compared to a normal distribution. These two distributions will be used in simulations in subsec. A.6.3. The normal inverse Gaussian distributions form a subclass of the generalised hyperbolic distributions, see Barndorff-Nielsen (1978) and Blæsild (1981) and the references therein. The generalised hyperbolic distributions have found wide applications, in particular in finance (McNeil et al., 2005; Prause, 1999). Also see Barndorff-Nielsen et al. (2004) for applications of the normal inverse Gaussian distributions to turbulence.

A.2.2 CONVOLUTIONS AND FOURIER TRANSFORMS

For matrix valued functions $g\colon \mathbb{R}^n \to M_{d_1,d_2}$ and $h\colon \mathbb{R}^n \to M_{d_2,d_3}$ the convolution $g * h\colon \mathbb{R}^n \to M_{d_1,d_3}$ is defined by

$$(g * h)(x) = \int_{\mathbb{R}^n} g(x - y)h(y)\,dy$$

where the integral is calculated entry-wise. It follows that $(g * h)^T = h^T * g^T$. Likewise, the matrix-valued Fourier transform $F_n[g]$ is also defined entry-wise,

$$F_n[g](y) = \frac{1}{(2\pi)^n} \int_{\mathbb{R}^n} g(x)e^{-i\langle x,y\rangle}\,dx,$$

and the corresponding inverse Fourier transform is given by

$$F_n^{-1}[g](x) = \int_{\mathbb{R}^n} g(y) e^{i\langle x,y\rangle}\, dy.$$

It follows that $F_n[g^T] = F_n[g]^T$ and $F_n[g * h] = (2\pi)^n F_n[g] F_n[h]$.

A.2.3 INTEGRATION WITH RESPECT TO LÉVY BASES

For any infinitely divisible $\mathbb{R}^n$-valued random variable X, we let $C(- \ddagger X)$ denote the cumulant function. By the Lévy-Khinchine representation (Sato, 1999, Thm. 8.1),

$$C(z \ddagger X) = i\langle a, z\rangle - \frac{1}{2}\langle z, bz\rangle + \int_{\mathbb{R}^d} (e^{i\langle z,x\rangle} - 1 - i\langle z, x\rangle 1_D(x))\, c(dx)$$

where $a \in \mathbb{R}^d$, $b \in M_d^+$, and c is a Lévy measure on $\mathbb{R}^d$. The triplet (a, b, c) is called the characteristic triplet and determines uniquely the distribution of X.

In the following, Lévy bases and integration with respect to Lévy bases are discussed and the results needed for the rest of the paper are stated. We refer to Rajput and Rosinski (1989), Barndorff-Nielsen and Stelzer (2011), Pedersen (2003), and Schmiegel (2007) for proofs and further details.

DEFINITION A.1. Let $S \in \mathcal{B}(\mathbb{R}^n)$ be non-empty. An $\mathcal{B}_b(S)$-indexed family $\Lambda = \{\Lambda(A) \mid A \in \mathcal{B}_b(S)\}$ of $\mathbb{R}^d$-valued random variables is called a Lévy basis on S, if Λ is an infinitely divisible and independently scattered random measure, i.e., if the following three properties hold.

- For every $A \in \mathcal{B}_b(S)$, $\Lambda(A)$ is infinitely divisible.
- For any disjoint $A_1, \ldots, A_N \in \mathcal{B}_b(S)$, $\Lambda(A_1), \ldots, \Lambda(A_N)$ are independent.
- For every sequence $(A_j)_{j=1}^\infty$ of disjoint elements in $\mathcal{B}_b(S)$ with $\bigcup_{j=1}^\infty A_j \in \mathcal{B}_b(S)$, we get that $\sum_{j=1}^\infty \Lambda(A_j) = \Lambda(\bigcup_{j=1}^\infty A_j)$ holds a.s.

A Lévy basis Λ in S induces three set functions $a\colon \mathcal{B}_b(S) \to \mathbb{R}^d$, $b\colon \mathcal{B}_b(S) \to M_d^+$ and $c\colon \mathcal{B}_b(S) \times \mathcal{B}(\mathbb{R}^d) \to \mathbb{R}$ by letting $(a(A), b(A), c(A, -))$ be the characteristic triplet of $\Lambda(A)$. It can be shown that a_j is a signed measure, $b_{j,k}$ is a measure for $j = k$ and a signed measure for $j \neq k$, $c(-, B)$ is a measure for every $B \in \mathcal{B}(\mathbb{R}^d)$, and $c(A, -)$ is a Lévy measure for every $A \in \mathcal{B}_b(S)$. Given set functions a, b, and c having the above properties, there exists an $\mathbb{R}^d$-valued Lévy basis Λ on S such that $(a(A), b(A), c(A, -))$ is the characteristic triplet of $\Lambda(A)$. Therefore, (a, b, c) will be called the characteristic triplet of the Lévy basis. Furthermore, the set function $\lambda\colon \mathcal{B}_b(S) \to [0, \infty]$ defined by

$$\lambda(A) = |a|(A) + \operatorname{tr}(b(A)) + \int_{\mathbb{R}^d} 1 \wedge \|x\|^2\, c(A, dx)$$

has a unique extension to a σ-finite measure on $\mathcal{B}(S)$ which is called the control measure and is also denoted by λ. See also Pedersen (2003).

Let (a, b, c) denote the characteristic triplet of a Lévy basis Λ on S with control measure λ. Let $a' = da/d\lambda$ and $b' = db/d\lambda$ denote the Radon-Nikodym derivatives. As in Rajput and Rosinski (1989, Lemma 2.3) the function c may

be extended to a σ-finite measure on $\mathcal{B}(S)\otimes\mathcal{B}(\mathbb{R}^d)$, and there exists a function $c'\colon S\times\mathcal{B}(\mathbb{R}^d)\to[0,\infty]$ such that $c'(s,-)$ is a Lévy measure on $\mathcal{B}(\mathbb{R}^d)$ for every $s\in S$, $c'(-,B)$ is measurable for every $B\in\mathcal{B}(\mathbb{R}^d)$, and

$$\int_{S\times\mathbb{R}^d} h(s,x)\,c(ds\times dx)=\int_S\int_{\mathbb{R}^d} h(s,x)\,c'(s,dx)\,\lambda(ds)$$

for every measurable function $h\colon S\times\mathbb{R}^d\to[0,\infty]$. Therefore, we may informally think of c' as $dc/d\lambda$. Thus, for every $s\in S$, $(a'(s),b'(s),c'(s,-))$ is the characteristic triplet of an $\mathbb{R}^d$-valued random variable $\Lambda'(s)$ which will be called the spot variable at s. The spot variable and control measure determine the distribution of the Lévy basis in the sense that

$$C(z\ddagger\Lambda(A))=\int_A C(z\ddagger\Lambda'(s))\,\lambda(ds)$$

for every $A\in\mathcal{B}_b(S)$.

The integral over a set $A\in\mathcal{B}(S)$ of a deterministic measurable function $f\colon S\to M_{m,d}$ with respect to an $\mathbb{R}^d$-valued Lévy basis on S is defined as

$$\int_A f\,d\Lambda=\operatorname*{plim}_{j\to\infty}\int_A f_j\,d\Lambda.$$

where $(f_j)_{j=1}^\infty$ is a sequence of simple functions such that $f_j\to f$ λ-a.s., and such that the sequence $(\int_A f_j\,d\Lambda)_{j=1}^\infty$ converges in probability for every $A\in\mathcal{B}(S)$. The Λ-integral is by construction infinitely divisible.

The following proposition expresses the distribution of the integral $\int_S f\,d\Lambda$ in terms of the function f, the spot variable Λ' and the control measure λ. It is a straightforward generalisation of Rajput and Rosinski (1989, Prop. 2.6) and also stated in Barndorff-Nielsen and Stelzer (2011). For necessary and sufficient conditions for Λ-integrability, see Barndorff-Nielsen and Stelzer (2011, Prop. 2.3) and Rajput and Rosinski (1989, Thm. 2.7).

PROPOSITION A.2. *Let Λ denote a Lévy basis on $S\in\mathcal{B}(\mathbb{R}^n)$, and let Λ' and λ denote the corresponding spot and control measure. If the measurable function $f\colon S\to M_{m,d}$ is Λ-integrable, then $\int_S|C(f(s)^Tz\ddagger\Lambda'(s))|\,\lambda(ds)<\infty$ for all $z\in\mathbb{R}^m$, and*

$$C\Big(z\ddagger\int_S f\,d\Lambda\Big)=\int_S C(f(s)^Tz\ddagger\Lambda'(s))\,\lambda(ds)$$

for all $z\in\mathbb{R}^m$.

On the one hand, the control measure and spot variables corresponding to a Lévy basis are derived from the characteristic triplet of the Lévy basis. On the other hand, when building stochastic processes using Lévy bases, it is desirable to specify the Lévy basis in terms of random variables and an accompanying measure. The following definition and lemma exemplify how this may be accomplished. The proof of the lemma is straightforward.

DEFINITION A.3. Let $S\in\mathcal{B}(\mathbb{R}^n)$ denote a Borel subset and let $\Lambda^*=\{\Lambda^*(s)\mid s\in S\}$ denote an S-indexed family of $\mathbb{R}^d$-valued independent infinitely divisible random variables, and let λ^* denote a σ-finite measure on $\mathcal{B}(S)$. Then Λ^* is called a seed variable on S, λ^* is called a seed measure on S, and the pair (Λ^*,λ^*) is called a Lévy seed on S.

DEFINITION A.4. A Lévy seed (Λ^*, λ^*) on $S \in \mathcal{B}(\mathbb{R}^n)$ is called homogeneous, if the distribution of $\Lambda^*(s)$ does not depend on $s \in S$ and if λ^* is the Lebesgue measure on S.

LEMMA A.5. *Let (Λ^*, λ^*) denote a Lévy seed on $S \in \mathcal{B}(\mathbb{R}^n)$ and let the characteristic triplet of $\Lambda^*(s)$ be denoted by $(a^*(s), b^*(s), c^*(s,-))$. Assume that*

- *$a^* \colon S \to \mathbb{R}^d$ is measurable with $\int_A \|a^*(s)\| \, \lambda^*(ds) < \infty$ for all $A \in \mathcal{B}_b(S)$,*
- *$b^* \colon S \to M_d^+$ is measurable with $\int_A \|b^*(s)\| \, \lambda(ds) < \infty$ for all $A \in \mathcal{B}_b(S)$,*
- *$c^*(-, B) \colon S \to [0, \infty]$ is measurable for each $B \in \mathcal{B}(\mathbb{R}^d)$, and there exists a measurable function $K \colon S \to \mathbb{R}_+$ with the properties that $\int_A K(s) \, \lambda^*(ds) < \infty$ for all $A \in \mathcal{B}_b(S)$ and $\int_{\mathbb{R}^d} 1 \wedge \|x\|^2 \, c^*(s, dx) < K(s)$ for all $s \in S$.*

Then

$$a(A) = \int_A a^*(s) \, \lambda^*(ds), \quad b(A) = \int_A b^*(s) \, \lambda^*(ds), \quad c(A, B) = \int_A c^*(s, B) \, \lambda^*(ds)$$

defines set functions such that a_j is a signed measure on $\mathcal{B}_b(S)$, $b_{j,k}$ is a measure on $\mathcal{B}_b(S)$ for $j = k$ and a signed measure for $j \neq k$, $c(A, -)$ is a Lévy measure on $\mathbb{R}^d$ for all $A \in \mathcal{B}_b(S)$, and $c(-, B)$ is a measure on $\mathcal{B}_b(S)$ for all $B \in \mathcal{B}(\mathbb{R}^d)$.

COROLLARY A.6. *Suppose the Lévy seed (Λ^*, λ^*) on $S \in \mathcal{B}(\mathbb{R}^n)$ satisfies the assumptions in lemma A.5. Then there exists an $\mathbb{R}^d$-valued Lévy basis Λ on S with (a, b, c) as characteristic triplet. Furthermore, the seed (Λ^*, λ^*) is related to the spot variable and control measure by*

$$\begin{aligned} a^*(s)\lambda^*(ds) &= a'(s)\lambda(ds), \\ b^*(s)\lambda^*(ds) &= b'(s)\lambda(ds), \\ c^*(s, dx)\lambda^*(ds) &= c'(s, dx)\lambda(ds). \end{aligned}$$

Note that a homogeneous Lévy seed always satisfies the assumptions of lemma A.5. Furthermore, for a homogeneous Lévy seed, the corresponding control measure is proportional to the Lebesgue measure, since in this case we have

$$\lambda(A) = \left(\|a^*\|_1 + \operatorname{tr}(b^*) + \int_{\mathbb{R}^d} 1 \wedge \|x\|_2^2 \, c^*(dx) \right) \operatorname{Leb}(A).$$

It follows that a', b', and c' are proportional to a^*, b^*, and c^*, respectively.

COROLLARY A.7. *Let (Λ^*, λ^*) denote a Lévy seed such that the conditions of lemma A.5 are satisfied, and let Λ denote the Lévy basis corresponding to the seed. Let $f \colon S \to M_{m,d}$ denote an Λ-integrable function. Then*

$$C\left(z \ddagger \int_S f \, d\Lambda \right) = \int_S C(f(s)^T z \ddagger \Lambda^*(s)) \, \lambda^*(ds)$$

for all $z \in \mathbb{R}^m$.

For a process σ on S that is independent of the Lévy basis Λ, the integral $\int_S f \sigma \, d\Lambda$ is defined conditional on σ, provided $s \mapsto f(s)\sigma(s)$ is almost surely Λ-integrable. In this case, the cumulant function is given by

$$C\left(z \ddagger \int_S f \sigma \, d\Lambda \right) = \log E\left[\exp\left(\int_S C\left((f(s)\sigma(s))^T z \ddagger \Lambda^*(s) \right) \lambda^*(ds) \right) \right].$$

Basse-O'Connor et al. (2012) discuss the case where the process σ is not independent of the Lévy basis.

A.3 CONSTRUCTING RANDOM VECTOR FIELDS

In this section we will discuss random vector field based on integrals of deterministic matrix-valued functions with respect to vector-valued Lévy bases. A homogeneous spatial model is constructed as a convolution of a deterministic kernel with respect to a volatility modulated Lévy basis, and the kernel is expressed in terms of the covariance tensor, or, equivalently, the spectral tensor.

Let Ξ be any non-empty set. We wish to define an $\mathbb{R}^m$-valued stochastic process $X = \{X(\xi) \mid \xi \in \Xi\}$ on Ξ with a prescribed covariance structure. To that end let $S \in \mathcal{B}(\mathbb{R}^n)$ be given and let Λ denote an $\mathbb{R}^d$-valued Lévy basis on S. We will assume that Λ is derived from a Lévy seed (Λ^*, λ^*) as explained in lemma A.5, but the results below may just as well be formulated in terms of the Lévy spot variable and control measure. Let σ be an $\mathbb{R}$-valued process on S that is independent of the Lévy basis, and let $f : \Xi \times S \to M_{m,d}$ denote a function such that $s \mapsto f(\xi, s)\sigma(s)$ is almost surely Λ-integrable for every $\xi \in \Xi$. We define the process X by

$$X(\xi) = \int_S f(\xi, s)\sigma(s)\Lambda(ds). \tag{A.2}$$

The finite dimensional marginal distributions of X are given by corollary A.7. Specifically, let $\xi_1, \ldots, \xi_N \in \Xi$ be given. Then, for $z = (z_1, \ldots, z_M)^T \in \mathbb{R}^{Nm}$, we have

$$\begin{aligned} &C(z \ddagger (X(\xi_1), \ldots, X(\xi_N))^T) \\ &\quad = \log E\Big[\exp\Big(\int_S C\Big(\sigma(s) \sum_{j=1}^N f(\xi_j, s)^T z_j \ddagger \Lambda^*(s)\Big)\lambda^*(ds)\Big)\Big]. \end{aligned} \tag{A.3}$$

The following lemma follows easily by differentiation and is central to the later applications.

LEMMA A.8. *Let the process X be defined as in (A.2), and suppose that X, Λ^*, and σ have finite second moments. Then*

$$\begin{aligned} E[X(\xi)] &= \int_S f(\xi, s) E[\Lambda^*(s)] E[\sigma(s)]\, \lambda^*(ds), \\ \operatorname{cov}(X(\xi), X(\xi')) &= \int_S f(\xi, s) \operatorname{cov}(\Lambda^*(s)) f(\xi', s)^T E[\sigma(s)^2]\, \lambda^*(ds) \\ &\quad + \int_S \int_S f(\xi, s) E[\Lambda^*(s)] (f(\xi', s') E[\Lambda^*(s')])^T \\ &\qquad \cdot \operatorname{cov}(\sigma(s), \sigma(s'))\, \lambda^*(ds)\, \lambda^*(ds'). \end{aligned}$$

With applications to turbulence in mind, some special cases are of particular interest. The case $m = 1$ corresponds to the modelling of a single velocity component, e.g., the stream-wise component or the magnitude (norm) of the velocity. The case $m = 3$ corresponds to the modelling of all three velocity components. The case $m = 2$ is not without interest, as it is perfectly conceiv-

able to have measurements of only two of the three velocity components. The set Ξ will be some subset of space-time, $\Xi \subseteq \mathbb{R}^3 \times \mathbb{R}$. The case $\Xi \subseteq \{x_0\} \times \mathbb{R}$ corresponds to a purely temporal model where the velocity is modelled as a function of time at a fixed point in space. Purely temporal models for turbulence are studied in e.g. Barndorff-Nielsen and Schmiegel (2009) and Ferrazzano and Klüppelberg (2012). The case $\Xi \subseteq \mathbb{R}^3 \times \{t_0\}$ corresponds, on the other hand, to a purely spatial model where the velocity is modelled at a fixed instant of time.

An $\mathbb{R}^m$-valued process on $\mathbb{R}^{d_{\text{space}}} \times \mathbb{R}^{d_{\text{time}}}$ will be called $(d_{\text{space}} + d_{\text{time}}, m)$-dimensional. By one- or three-dimensional processes, we will understand $(1 + 0, 1)$- or $(3 + 0, 3)$-dimensional processes, respectively.

Through a series of simplifying assumptions we will obtain a homogeneous, purely spatial model with a prescribed covariance tensor. Assume that $\Xi = S = \mathbb{R}^n$ and that (Λ^*, Leb) is a homogeneous $\mathbb{R}^d$-valued Lévy seed on $\mathbb{R}^n$, and let Λ denote the corresponding $\mathbb{R}^d$-valued Lévy basis. Let σ denote an $\mathbb{R}$-valued stationary process on $\mathbb{R}^n$ that is independent of Λ. Suppose that $f : \mathbb{R}^n \to M_{m,d}$ satisfies that $f\sigma$ is almost surely Λ-integrable. Then

$$X(\xi) = \int_{\mathbb{R}^n} f(\xi - s)\sigma(s)\,\Lambda(ds) \tag{A.4}$$

defines an $\mathbb{R}^m$-valued stochastic process on $\mathbb{R}^n$ which, by (A.3), is homogeneous. In short, we will occasionally write $X = f * \sigma\, d\Lambda$. In this setting, the function f in the Λ-integral is called the kernel function. The convolution-style formulation of (A.4) lays the foundation of efficient simulation methods, see appendix A.A. Since the mean value of a homogeneous process is constant, we may assume it to be zero. Assume therefore that Λ^* has zero mean and finite second moment, and that σ has finite second moment with $E[\sigma^2] = 1$. By lemma A.8, we have that $E[X] = 0$ and

$$R(\xi) = \operatorname{cov}(X(\xi), X(0)) = \int_{\mathbb{R}^n} f(\xi - s)\operatorname{cov}(\Lambda^*) f(-s)^T\, ds,$$

where R denotes the covariance tensor. Under these assumptions, the covariance tensor does not depend on the volatility modulation of the Lévy basis, and only on the kernel function and the covariance matrix of the seed.

Let C denote a matrix square root of $\operatorname{cov}(\Lambda^*)$ such that $CC^T = \operatorname{cov}(\Lambda^*)$. We decompose f as the sum $f = f_{\text{even}} + f_{\text{odd}}$ of its even part and odd part. Let $h = fC$. Then $h_{\text{even}} = f_{\text{even}}C$ and $h_{\text{odd}} = f_{\text{odd}}C$, and so

$$R = h_{\text{even}} * h_{\text{even}}^T - h_{\text{odd}} * h_{\text{odd}}^T + h_{\text{odd}} * h_{\text{even}}^T - h_{\text{even}} * h_{\text{odd}}^T.$$

Since R is symmetric, $R = R^T$, it follows that

$$h_{\text{odd}} * h_{\text{even}}^T = h_{\text{even}} * h_{\text{odd}}^T,$$

which implies that the covariance tensor is given by

$$\begin{aligned} R &= h_{\text{even}} * h_{\text{even}}^T - h_{\text{odd}} * h_{\text{odd}}^T \\ &= (f_{\text{even}}C) * (f_{\text{even}}C)^T - (f_{\text{odd}}C) * (f_{\text{odd}}C)^T, \end{aligned}$$

and that the spectral tensor $F_n[R]$ is given by

$$\begin{aligned} F_n[R] &= (2\pi)^n \Big(F_n[h_{\text{even}}] F_n[h_{\text{even}}]^T - F_n[h_{\text{odd}}] F_n[h_{\text{odd}}]^T \Big) \\ &= (2\pi)^n \Big(F_n[f_{\text{even}}] \operatorname{cov}(\Lambda^*) F_n[f_{\text{even}}]^T - F_n[f_{\text{odd}}] \operatorname{cov}(\Lambda^*) F_n[f_{\text{odd}}]^T \Big). \end{aligned}$$

In order to find a kernel f that reproduces a given covariance tensor R, the above shows that we may choose the Lévy seed such that $\operatorname{cov}(\Lambda^*) = I$ and $C = I$. The following proposition provides a way to determine a kernel function given a covariance tensor, or, equivalently, a spectral tensor. The proposition follows easily from the properties of convolutions and Fourier transforms.

PROPOSITION A.9. *Let $R\colon \mathbb{R}^n \to M_n$ denote a covariance tensor.*

If Q_{even} is an even root of the spectral tensor $F_n[R]$, i.e. $F_n[R] = Q_{even} Q_{even}^T$, and if Q_{even} is integrable, then $f_{even} = (2\pi)^{-n/2} F_n^{-1}[Q_{even}]$ defines a real, even, and matrix-valued function that satisfies

$$R = f_{even} * f_{even}^T, \qquad F_n[R] = (2\pi)^n F_n[f_{even}] F_n[f_{even}]^T.$$

If f_{even} is Λ-integrable, then the covariance tensor of the process $X = f_{even} * d\Lambda$ is R.

If Q_{odd} is an odd root of the spectral tensor $F_n[R]$, i.e. $F_n[R] = Q_{odd} Q_{odd}^T$, and if Q_{odd} is integrable, then $f_{odd} = -i(2\pi)^{-n/2} F_n^{-1}[Q_{odd}]$ defines a real, odd, and matrix-valued function that satisfies

$$R = -f_{odd} * f_{odd}^T, \qquad F_n[R] = -(2\pi)^n F_n[f_{odd}] F_n[f_{odd}]^T.$$

If f_{odd} is Λ-integrable, then the covariance tensor of the process $X = f_{odd} * d\Lambda$ is R.

Note that the even and odd kernels f_{even} and f_{odd} both yield the same covariance tensor R, and so will the linear combination $f = (1-\alpha)^{1/2} f_{\text{even}} + \alpha^{1/2} f_{\text{odd}}$ for any $\alpha \in [0,1]$.

A.4 ISOTROPIC, INCOMPRESSIBLE VECTOR FIELDS

In the following we recall the implications of isotropy and incompressibility and show how the kernel f in (A.4) under these assumptions can be expressed concisely in terms of the so-called energy spectrum.

Robertson (1940) argued that the general form of the covariance tensor R of a homogeneous and isotropic vector field X on $\mathbb{R}^3$ is $R(x) = A(\|x\|)\hat{x}\hat{x}^T + B(\|x\|)I$ where A and B are scalar functions. We may assume that $A(0) = 0$, so that $R(0) = B(0)I$. Likewise, isotropy implies that the spectral tensor is of the form $F_3[R](y) = C(\|y\|)\hat{y}\hat{y}^T + D(\|y\|)I$ where C and D are scalar functions.

It is convenient to express the covariance tensor in terms of the longitudinal and lateral correlation functions ρ_1 and ρ_2, see fig. A.2. Following Batchelor (1959), we have

$$\begin{aligned} \rho_1(r) &= \frac{R_{11}(|r|,0,0)}{R_{11}(0)} = \frac{A(|r|) + B(|r|)}{B(0)}, \\ \rho_2(r) &= \frac{R_{22}(|r|,0,0)}{R_{22}(0)} = \frac{B(|r|)}{B(0)}. \end{aligned}$$

By isotropy, the three components of X have the same variance which we de-

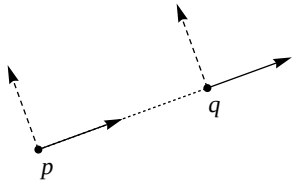

FIGURE A.2. Let r denote the distance between the points p and q. The longitudinal correlation $\rho_1(r)$ is the correlation of the velocity components at p and q along the line between p and q, as indicated by the solid arrows. Likewise, the transversal correlation $\rho_2(r)$ is the correlation of the velocity components at p and q perpendicular to the line between p and q as indicated by the dashed arrows.

note by σ^2. Then $B(0) = \sigma^2$, and

$$R(x) = \sigma^2\Big((\rho_1(\|x\|) - \rho_2(\|x\|))\hat{x}\hat{x}^T + \rho_2(\|x\|)I\Big).$$

In the context of turbulence, the velocity field is often assumed to be differentiable and furthermore incompressible when the mean velocity is small compared to the speed of sound in the fluid under consideration. The incompressibility of X can be expressed in terms of the continuity equation,

$$\frac{\partial X_1}{\partial x_1}(x) + \frac{\partial X_2}{\partial x_2}(x) + \frac{\partial X_3}{\partial x_3}(x) = 0, \tag{A.5}$$

which implies, see Batchelor (1959), that the lateral correlation function is given in terms of the longitudinal correlation function,

$$\rho_2(r) = \rho_1(r) + \tfrac{1}{2} r\rho_1'(r). \tag{A.6}$$

For the spectral tensor $F_3[R]$, the additional assumption of incompressibility implies that $C = -D$, in which case the spectral tensor is conveniently expressed in terms of the energy spectrum E,

$$F_3[R](y) = \frac{E(\|y\|)}{4\pi\|y\|^2}(-\hat{y}\hat{y}^T + I), \tag{A.7}$$

where the energy spectrum in turn is related to the longitudinal correlation function ρ_1 through

$$E(z) = \sigma^2 z^3 \frac{d}{dz}\left(\frac{1}{z}\frac{d}{dz}F_1[\rho_1](z)\right). \tag{A.8}$$

To apply proposition A.9 to calculate the kernel in (A.4), we need square roots of the spectral tensor. These are provided by the following lemma.

LEMMA A.10. *Let $F_3[R](y) = \frac{E(\|y\|)}{4\pi\|y\|^2}(-\hat{y}\hat{y}^T + I)$ denote an isotropic and incompressible spectral tensor with energy spectrum E. A real and even square root Q_{even} of $F_3[R]$ is given by*

$$Q_{even}(y) = \sqrt{\frac{E(\|y\|)}{4\pi\|y\|^2}}(-\hat{y}\hat{y}^T + I). \tag{A.9}$$

A real and odd square root Q_{odd} of $F_3[R]$ is given by

$$Q_{odd}(y) = \sqrt{\frac{E(\|y\|)}{4\pi\|y\|^2}}\,\mathrm{sk}(\hat{y}). \tag{A.10}$$

PROOF. The results follow easily from direct calculation. One may also observe that the matrix $I - \hat{y}\hat{y}^T$ is a projection onto the plane orthogonal to y. From this, (A.9) follows immediately. □

The odd root of the spectral tensor is also used in Mann (1998) to simulate a Gaussian three-dimensional process with a given energy spectrum. This model is not restricted to isotropic turbulence and can also reproduce the shear observed in atmospheric boundary layer turbulence. However, the model of Mann (1998) does not account for the non-Gaussian densities of velocity increments. The model (A.4) is, by definition, not restricted to Gaussian densities.

By combining lemma A.10 with proposition A.9 and using the technical lemmas of appendix A.B, we obtain the following result expressing the kernel in (A.4) in terms of the energy spectrum.

PROPOSITION A.12. *Let E denote the energy spectrum of an isotropic and incompressible stochastic vector field on $\mathbb{R}^3$. Assume that $r \mapsto E(r)^{1/2} r$ is integrable. The even square root (A.9) of the corresponding spectral tensor $F_3[R]$ is integrable, and*

$$f_{even}(x) = \frac{1}{2^{3/2}\pi}\Big((\operatorname{sinc} + 3\operatorname{sinc}'')[E(r)^{1/2}r](\|x\|)\hat{x}\hat{x}^T + (\operatorname{sinc} - \operatorname{sinc}'')[E(r)^{1/2}r](\|x\|)I\Big)$$

satisfies $R = f_{even} * f_{even}^T$. The odd square root (A.10) of the corresponding spectral tensor $F_3[R]$ is integrable, and

$$f_{odd}(x) = \frac{-1}{2^{1/2}\pi}\operatorname{sinc}'[E(r)^{1/2}r](\|x\|)\operatorname{sk}(\hat{x})$$

satisfies $R = -f_{odd} * f_{odd}^T$.

The sinc-, sinc'-, and sinc''-transforms may all be expressed in terms of sin-transforms. Furthermore, the two integral transforms that constitute the even kernel may, under some mild assumptions, be expressed in terms of a single integral transform. However, from the point of view of numerics, the authors found no advantage in doing either. In our applications, the numerical integration scheme of Levin (1996) can be applied to efficiently evaluate the integral transforms.

A.5 VON KÁRMÁN, MATÉRN, AND SHKAROFSKY CORRELATIONS

In von Kármán (1948), it is argued that the energy spectrum of homogeneous, isotropic turbulence at high Reynolds number should satisfy $E(z) \propto z^4$ for small values of z and $E(z) \propto z^{-5/3}$ when z is in the so-called inertial range. The behaviour $E(z) \propto z^{-5/3}$ corresponds to Kolmogorov's celebrated 5/3-law (Kolmogorov, 1941). Von Kármán (1948) suggests the interpolation $E(z) \propto z^4(\kappa^2+z^2)^{-17/6}$ which displays the two scaling behaviours for $z \ll \kappa$ and $z \gg \kappa$, respectively. Furthermore, von Kármán notes that the longitudinal correlation function

$$\rho_{\mathrm{vK}}(r) = \frac{2^{2/3}}{\Gamma(1/3)}(\kappa|r|)^{1/3}K_{1/3}(\kappa|r|) \tag{A.11}$$

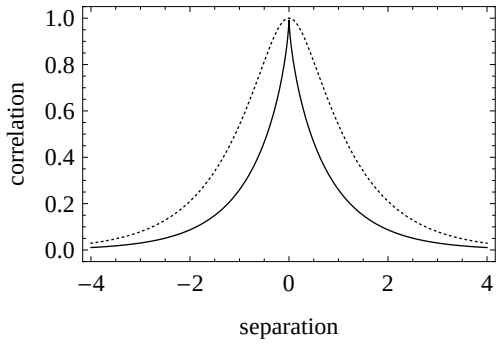

FIGURE A.3. The solid curve shows the Matérn correlation function with $\nu = 1/3$ (the von Kármán case) and $\kappa = 1$. The dashed curve shows the Shkarofsky correlation function with $\nu = 1/3$, $\kappa = 1$, and $\lambda = 1/2$. Note the cusp at zero for the Matérn correlation function.

yields the desired energy spectrum. The von Kármán correlation structure is a special case of the Matérn family of spatial correlation functions on $\mathbb{R}^n$,

$$\rho_{\text{Mat}}(x) = \frac{2^{1-\nu}}{\Gamma(\nu)}(\kappa\|x\|)^\nu K_\nu(\kappa\|x\|) \tag{A.12}$$

where $\nu > 0$ is a shape parameter and $\kappa > 0$ is a scale parameter. The von Kármán correlation function is obtained by setting $\nu = 1/3$. See Guttorp and Gneiting (2006) for an excellent background on the Matérn correlation family.

The sample paths of a stochastic process need not be differentiable. If the vector field is not differentiable, the concept of incompressibility in the sense of (A.5) is meaningless. However, the expressions in (A.6) and (A.7) are still well-defined, and we can avoid the problem of differentiability by requiring that isotropic, incompressible vector fields have a spectral tensor given by (A.7). A stationary stochastic process is differentiable in mean square if and only if its correlation function is twice differentiable. The longitudinal correlation function (A.11) does not yield a process which is differentiable in mean square. Indeed, the Mátern correlation function (A.12) is twice differentiable if and only if $\nu > 1$.

The von Kármán correlation structure gives an infinitely long inertial range which is not realistic in the case of finite Reynolds number. At the smallest scales, viscous forces become dominant and the kinetic energy of the flow is dissipated into heat. Shkarofsky (1968) argues that the longitudinal correlation function should not have a cusp at zero, but rather have zero first derivative and negative, but finite, second derivative. Accordingly, Shkarofsky proposes the correlation function

$$\rho_{\text{Shk}}(x) = \frac{(\kappa\sqrt{\|x\|^2 + \lambda^2})^\nu K_\nu(\kappa\sqrt{\|x\|^2 + \lambda^2})}{(\kappa\lambda)^\nu K_\nu(\kappa\lambda)}, \tag{A.13}$$

which has these properties, see fig. A.3. The parameter $\lambda > 0$ is a second scale parameter. In the limit $\lambda \to 0$ the Matérn correlation family is obtained.

PROPOSITION A.13. *Suppose that the longitudinal correlation function ρ_1 is either the Matérn correlation (A.12) or the Shkarofsky correlation (A.13). Then the corresponding longitudinal one-dimensional spectral density function $F_1[\rho_1]$ is given*

as follows,

$$F_1[\rho_{Mat}](z) = \frac{\Gamma(\nu+1/2)}{\sqrt{\pi}\Gamma(\nu)}\kappa^{2\nu}(\kappa^2+z^2)^{-\nu-1/2}, \tag{A.14}$$

$$F_1[\rho_{Shk}](z) = \frac{\lambda}{\sqrt{2\pi}}\frac{(\kappa\lambda)^\nu}{K_\nu(\kappa\lambda)}\Big(\lambda\sqrt{\kappa^2+z^2}\Big)^{-\nu-1/2}K_{-\nu-1/2}\Big(\lambda\sqrt{\kappa^2+z^2}\Big). \tag{A.15}$$

Furthermore, the energy spectrum (A.7) *of the corresponding isotropic and incompressible vector field is given by*

$$E_{Mat}(z) = \sigma^2\frac{4\Gamma(\nu+5/2)}{\sqrt{\pi}\Gamma(\nu)}\kappa^{2\nu}z^4(\kappa^2+z^2)^{-\nu-5/2},$$

$$E_{Shk}(z) = \sigma^2\frac{\lambda^5}{\sqrt{2\pi}}\frac{(\kappa\lambda)^\nu}{K_\nu(\kappa\lambda)}z^4\Big(\lambda\sqrt{\kappa^2+z^2}\Big)^{-\nu-5/2}K_{-\nu-5/2}\Big(\lambda\sqrt{\kappa^2+z^2}\Big). \tag{A.16}$$

PROOF. The first two identities follow from (Gradshteyn and Ryzhik, 2007, formulas 6.699.12 and 6.726.4). The last two identities follow from (A.8) by differentiation and use of the identity $\frac{d}{dz}z^\nu K_\nu(z) = -z^\nu K_{\nu-1}(z)$. □

The Shkarofsky energy spectrum satisfies $\int_0^\infty E_{\text{Shk}}(r)^{1/2}r\,dr < \infty$. Indeed, the energy spectrum is bounded, and from the asymptotic property of the Bessel functions, $K_\mu(z) \sim e^{-z}z^{-1/2}$ for large z, the integrability follows easily. Proposition A.12 may therefore be applied to calculate a kernel f which in (A.4) will yield the Shkarofsky energy spectrum. On the other hand, the Matérn energy spectrum satisfies the corresponding integrability condition if and only if $\nu > 1/2$. In the context of turbulence we have $\nu = 1/3$ (the von Kármán case) in order to obtain the Kolmogorov 5/3-law in the inertial range. Therefore, proposition A.12 cannot immediately be applied to the von Kármán case.

Note that the Shkarofsky spectral density (A.15) decreases exponentially fast to zero as $z \to \infty$ and does therefore not satisfy the Paley-Wiener condition,

$$\int_{-\infty}^{\infty}\frac{\log F_1[\rho_{\text{Shk}}](z)}{1+z^2}\,dz > -\infty. \tag{A.17}$$

Consequently (Doob, 1953, Thm. XII.5.3), a Brownian semistationary process (Barndorff-Nielsen and Schmiegel, 2009) cannot possess the Shkarofsky correlation structure.

A.6 APPLICATION TO ATMOSPHERIC BOUNDARY LAYER FLOW

To illustrate the presented methods, we will study a data set consisting of measurements of the longitudinal velocity component in atmospheric boundary layer flow. We first demonstrate that the Shkarofsky correlation fits the data very well. We then derive examples of kernels which will yield a three-dimensional isotropic and incompressible random vector field whose longitudinal correlation is that of Shkarofsky. Since atmospheric boundary layer turbulence possesses structures across a wide range of length scales, simulation under the three-dimensional model is non-trivial. We therefore consider also a one-dimensional model for which simulation is simpler to perform. Using a normal inverse Gaussian Lévy basis we are able to reproduce some of

the non-Gaussian behaviour of the velocity increments. However, the use of a non-Gaussian Lévy basis yields discontinuous, i.e. physically unrealistic sample paths.

A.6.1 DESCRIPTION OF THE DATA

The data consist of 20 million one-point measurements of the longitudinal component of the wind velocity in the atmospheric boundary layer, 35 m above ground. The measurements were performed using a hot-wire anemometer and sampled at 5 kHz. The time series can be assumed to be stationary, the mean is $U = 8.3\,\mathrm{m/s}$, and the standard deviation is $\sigma = 2.3\,\mathrm{m/s}$. We refer to Dhruva (2000) for further details on the data set (the data set is called no. 3 therein). The data are standardised to have zero mean and unit variance.

To interpret the data set in the spatial domain, we apply the Taylor frozen flow hypothesis (Taylor, 1938), which states that the turbulent flow may be considered as a frozen field which, in time, is convected with the mean flow without relevant distortion, provided the velocity fluctuations are small compared to the mean flow velocity. Thus, if u denotes the velocity component in the mean flow direction, i.e., the longitudinal component, and if x denotes the position along a line in the mean flow direction, then u as a function of space x and time t satisfies the relation

$$u(x,t) = u(x - U\tau, t + \tau),$$

where τ denotes some offset in time. The Taylor frozen flow hypothesis is assumed to be valid when $\sigma/U \ll 1$. This is not the case for the present data set, since $\sigma/U \approx 0.28$. In such cases various corrections exist to appropriately express spatial statistics in terms of the measured temporal statistics. In particular, the Lumley correction, see e.g. Champagne (1978), may be applied to the longitudinal one-dimensional spectral density $F_1[\rho_1]$. The Lumley correction is noticeable at the smallest length scales (the dissipation range). However, the Shkarofsky spectral density fit the corrected spectral density equally well, and the application of the correction has no influence on the conclusions of the present paper. We will therefore, for the sake of convenience and simplicity, apply only the Taylor frozen flow hypothesis and not any further corrections. The sampling frequency 5 kHz and $U = 8.3\,\mathrm{m/s}$ imply a spatial resolution of 1.66 mm. In what follows, all spatial length scales refer to the unit meter.

The longitudinal one-point spectral density $F_1[\rho_1]$ is estimated from data using Welsh's overlapping segment averages with a Hanning taper, a segment length of 4 million, and a segment overlap of 50%. See Percival and Walden (1993) for details on the method. The parameters of the Shkarofsky spectral density (A.15) are estimated using a least squares method in the double logarithmic representation of the spectral density. The fitted parameters and the corresponding spectral density are shown in fig A.4 together with the measured spectral density. The agreement between data and fit is excellent. We see that $\nu \approx 1/3$ which agrees with Kolmogorov's 5/3-law for the inertial range. For comparison, the Matérn spectral density (A.14) is also shown, with the

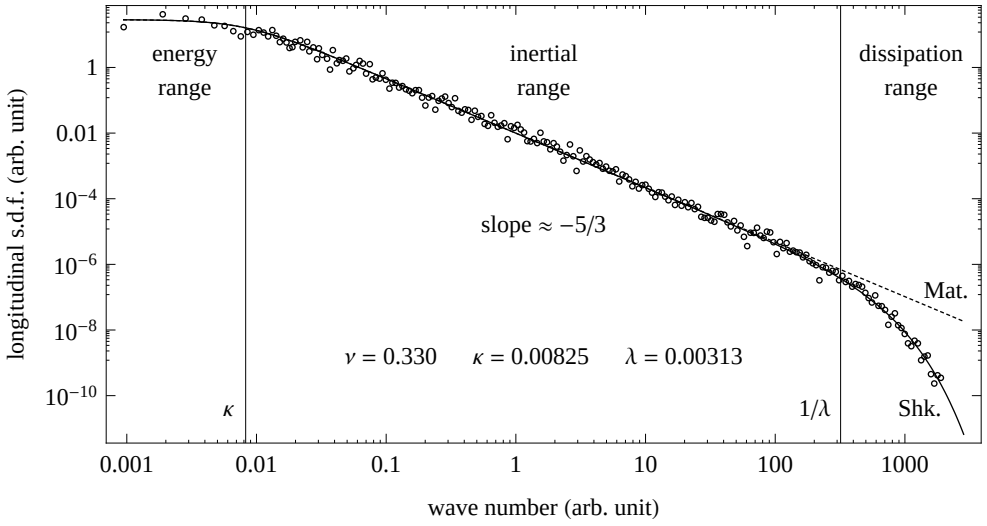

FIGURE A.4. The longitudinal one-dimensional spectral density measured in the atmospheric boundary layer. Circles denote the estimated spectral density using Welsh's overlapping segment averages with a Hanning taper, a segment length of 4 million, and a segment overlap of 50%. The black solid and dashed curves denote the fitted Shkarofsky and Matérn spectral densities, respectively. The vertical lines mark the estimated values of κ and $1/\lambda$ for the Shkarofsky spectral density.

same setting of the parameters ν and κ as for the Shkarofsky spectral density. It is evident from the figure that the Matérn spectral density cannot reproduce the behaviour of the data at high wave numbers (small length scales).

The Shkarofsky energy spectrum may seem like a convenient expression which happens to fit the data well due to its flexibility. However, it is close to a more rigorously derived result for the behaviour of the energy in the inertial and dissipation ranges of fully developed isotropic turbulence. Sirovich et al. (1994) show that

$$E(z) \propto \begin{cases} (\lambda z)^{7/6} K_{17/6}(\lambda z) + \frac{1}{5}(\lambda z)^{13/6} K_{23/6}(\lambda z) & z \gg \kappa, \\ \left((\lambda z)^{2/3} + \frac{9}{110}(\lambda z)^{5/3}\right) e^{-\lambda z} & z \to \infty. \end{cases} \tag{A.18}$$

The corresponding results for the Shkarofsky energy spectrum are

$$E_{\text{Shk}}(z) \propto \begin{cases} (\lambda z)^{7/6} K_{17/6}(\lambda z) & z \gg \kappa, \\ (\lambda z)^{2/3} e^{-\lambda z} & z \to \infty. \end{cases}$$

It is possible to modify the Shkarofsky energy spectrum such that (A.18) is obtained while the expressions for the spectrum and correlation function remain simple. This is outside of the scope of the present paper. Note that the spectrum (A.18) decays exponentially fast to zero as $z \to \infty$ and therefore does not satisfy the Paley-Wiener condition (A.17).

A.6.2 THE THREE-DIMENSIONAL MODEL

Under the assumptions of isotropy and incompressibility, the even kernel f_{even} and odd kernel f_{odd} are given by proposition A.12. The matrix-valued kernels can be expressed in terms of three scalar-valued functions $f_1, f_2, f_3 \colon \mathbb{R}_+ \to \mathbb{R}$,

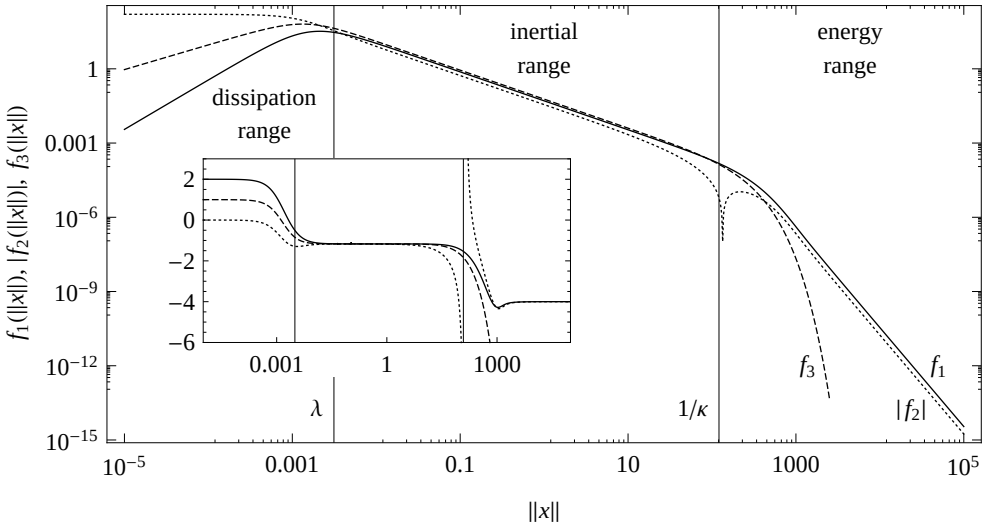

FIGURE A.5. The scalar functions f_1 (solid), f_2 (dotted), and f_3 (dashed) determining the even and odd kernels $f_{\text{even}}(x) = f_1(\|x\|)\hat{x}\hat{x}^T + f_2(\|x\|)I$ and $f_{\text{odd}}(x) = f_3(\|x\|)\,\text{sk}(\hat{x})$ of the isotropic and incompressible three-dimensional model. The kernels will reproduce a correlation structure whose longitudinal correlation is the Shkarofsky correlation fitted to the atmospheric boundary layer data set. The functions f_1 and f_3 are non-negative whereas $f_2(r)$ is non-negative for $r < r_0$ and negative for $r > r_0$ where r_0 is slightly larger than $1/\kappa$. The inset shows the local slope of the scalar functions $f_1, |f_2|, f_3$ in the double logarithmic representation.

specifically

$$f_{\text{even}}(x) = f_1(\|x\|)\hat{x}\hat{x}^T + f_2(\|x\|)I, \qquad f_{\text{odd}}(x) = f_3(\|x\|)\,\text{sk}(\hat{x}).$$

Figure A.5 shows the functions f_1, f_2, f_3 calculated numerically from the Shkarofsky energy spectrum (A.16) with the parameters estimated from the atmospheric boundary layer data set, see fig. A.4. Within the dissipation range and the inertial range, the even and odd kernels display similar behaviour, but in the energy range (large length scales) the odd kernel decays rapidly whereas the even kernel decays only algebraically.

It is not guaranteed that the derived kernels are integrable with respect to an arbitrary Lévy basis. However, since the derived kernels are bounded, and since we assume the homogeneous Lévy seed to have finite second moment, it can be shown that a sufficient condition for Λ-integrability is that the operator norm of the kernel is square integrable, if Λ^* is Gaussian with zero mean, and integrable and square integrable otherwise. Since the operator norms of $\hat{x}\hat{x}^T$, I, and $\text{sk}(\hat{x})$ are equal to 1, and since f_1, f_2, and f_3 are bounded and decay not slower than r^{-4} as $r \to \infty$, according to the inset of fig. A.5, integrability of both the even and odd kernel with respect to any Lévy basis derived from a homogeneous seed with finite second moment is guaranteed.

Simulating from the three-dimensional model is challenging if the structures are to be reproduced across all length scales from approximately 10^{-3} to 10^4, i.e., across seven orders of magnitude. As detailed in appendix A.A, the kernels may through the use of a partition of unity be decomposed into "smaller" kernels each of which yields a computationally tractable simulation problem. The details of the three-dimensional model will be studied through

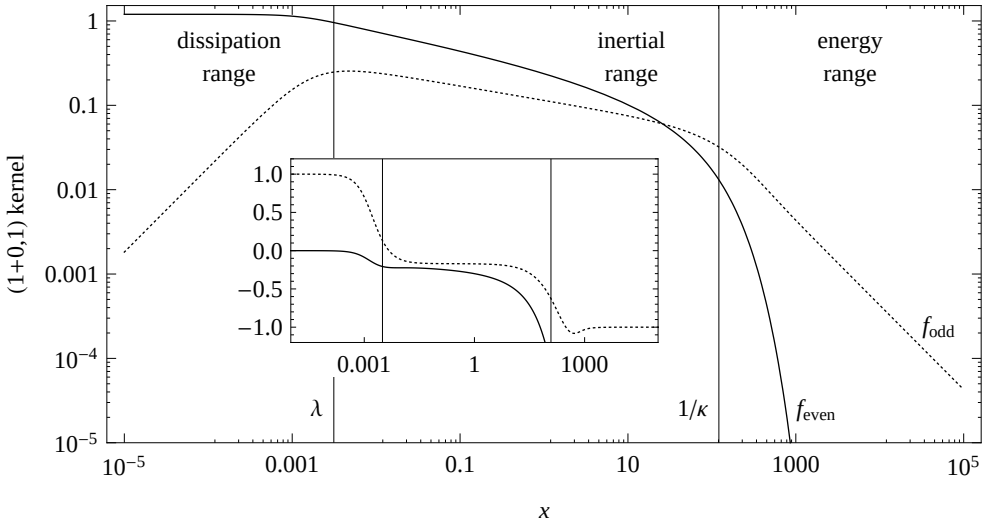

FIGURE A.6. Even kernel f_{even} (solid) and odd kernel f_{odd} (dashed) under the one-dimensional model. The kernels will reproduce a correlation structure whose longitudinal correlation is the Shkarofsky correlation fitted to the atmospheric boundary layer data set. The inset shows the local slope of the kernels in the double logarithmic representation.

simulations in a forthcoming paper.

A.6.3 THE ONE-DIMENSIONAL MODEL

Under the one-dimensional model we seek to model the longitudinal velocity component along a line in the direction of the mean flow. The one-dimensional model is considerably simpler than the three-dimensional model as the covariance tensor reduces to the auto-covariance function $R\colon \mathbb{R} \to \mathbb{R}$. So far we have focused on reproducing the correlation structure. In this subsection we will use the one-dimensional model to provide a few simulated examples to compare the model to the measured data set in terms of higher order statistics. The simulations show that the absense of volatility modulation implies that the model is capable of reproducing only part of the observed features of the measured data. The simulation procedure is described in appendix A.A.

The even and odd roots of the longitudinal one-dimensional spectral density $F_1[R]$ are given as

$$Q_{\text{even}}(y) = F_1[R](y)^{1/2}, \qquad Q_{\text{odd}}(y) = \operatorname{sign}(y) F_1[R](y)^{1/2}.$$

From proposition A.9 it follows that the corresponding kernels are

$$f_{\text{even}}(x) = \sqrt{2/\pi}\cos[F_1[R]^{1/2}](x), \qquad f_{\text{odd}}(x) = \sqrt{2/\pi}\sin[F_1[R]^{1/2}](x).$$

Figure A.6 shows the even and odd kernels calculated from the estimated Shkarofsky longitudinal one-dimensional spectral density function (A.15). Compared to the three-dimensional model, the behaviour of the even and odd kernels has been reversed: The even kernel decays rapidly whereas the odd kernel decays only as r^{-1} as $r \to \infty$ (see the inset of fig. A.6).

The conditions for Λ-integrability (with respect to a Lévy basis derived from a homogeneous seed with finite second moment) of the three-dimensio-

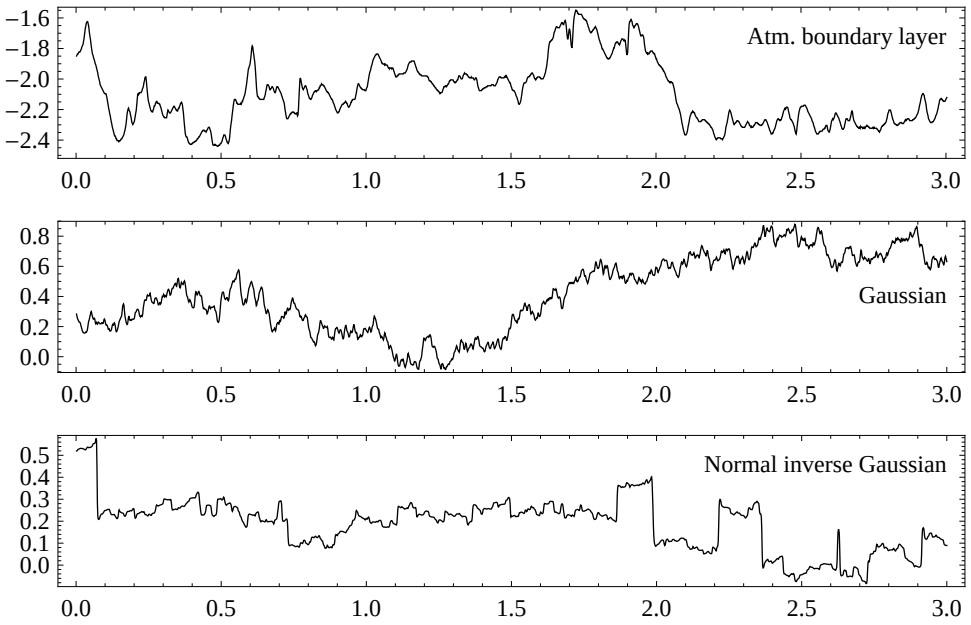

FIGURE A.7. An except of the measured data (top), a simulation using the odd kernel and a Gaussian homogeneous Lévy basis with $\Lambda^* \sim N(0,1)$ (middle), and a simulation using the odd kernel and a normal inverse Gaussian homogeneous Lévy basis with $\Lambda^* \sim \mathrm{NIG}^{\triangledown}(0.999, 0.09, 0, 1)$ (bottom). The normal inverse Gaussian simulation appears continuous since it is constructed as a linear interpolation of a simulated skeleton as described in appendix A.A.

nal kernels also apply for to one-dimensional kernels. Due to the rapid decay of the even kernel, Λ-integrability is guaranteed. However, due to the slow decay, the odd kernel is not integrable in general, only square integrable. It will therefore only be integrable with respect to a Gaussian Lévy basis with zero mean. In practice, the problem can easily be avoided by truncating the kernel.

The kernels have been derived entirely from the auto-covariance function and therefore determine only the second order structure of the process. Higher order properties, for example distribution of increments, are determined by the choice of the Lévy basis. Figure A.7 compares an excerpt of the measured data with two simulations using the odd kernel. One simulation uses a homogeneous seed with $\Lambda^* \sim N(0,1)$ and the second uses a homogeneous seed with $\Lambda^* \sim \mathrm{NIG}^{\triangledown}(0.999, 0.09, 0, 1)$. See fig. A.1 for a comparison of the distributions of the seeds. The nature of the two simulations differ from the measured data. Informally, the Gaussian simulation displays too many small increments and too few large ones compared to the measured data, whereas the normal inverse Gaussian simulation displays jumps of size comparable to the increments of the measured data set. The extreme steepness of the normal inverse Gaussian seed is needed in the absense of volatility modulation to ensure that the increments of the process at intermediate lags resemble those of the measured data, see below. The discontinuity of the normal inverse Gaussian simulation is a consequence of the use of a non-Gaussian Lévy basis. A suitably volatility modulated Gaussian Lévy basis will yield a process that has continuous sample paths and is capable of reproducing many stylised features of turbulence (Barndorff-Nielsen and Schmiegel, 2009; Hedevang, 2011).

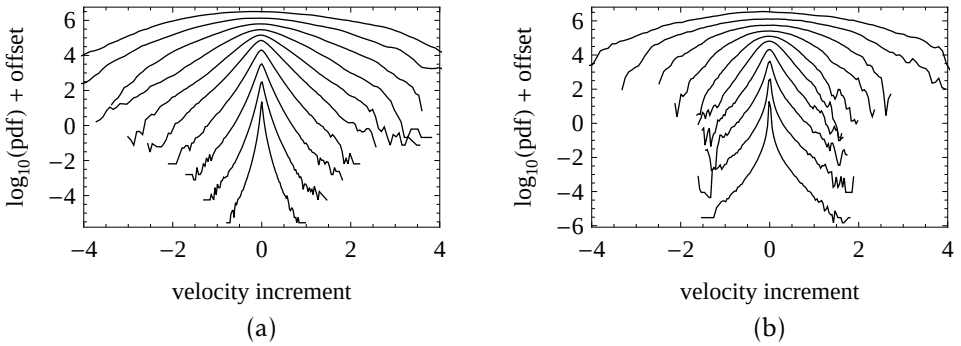

FIGURE A.8. Distribution ($\log_{10}$(pdf) offset vertically for clarity) of increments of (a) the measured data set and (b) a simulation using the odd kernel and a normal inverse Gaussian homogeneous Lévy basis with $\Lambda^* \sim \mathrm{NIG}^{\nabla}(0.999, 0.09, 0, 1)$. The increments are calculated over ten logarithmically spaced lags from 5 mm to 166 m, spanning approximately the entire inertial range. The lag increases from bottom to top.

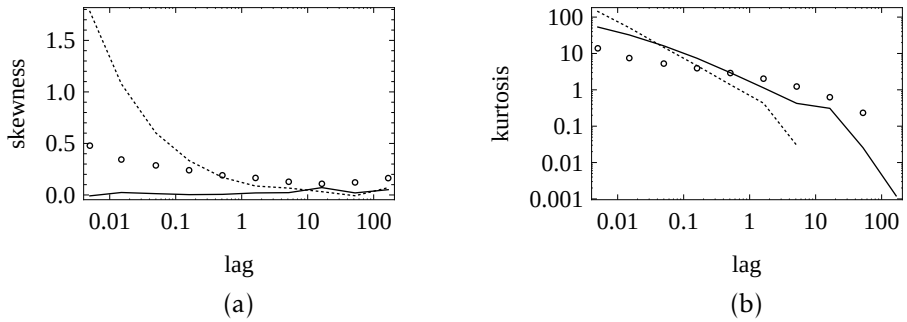

FIGURE A.9. The skewness (a) and kurtosis (b) of the increments over various lags for the measured data set (circles), a simulation using the odd kernel (dashed), and a simulation using the even kernel (solid). Both simulation used a normal inverse Gaussian homogeneous Lévy basis with $\Lambda^* \sim \mathrm{NIG}^{\nabla}(0.999, 0.09, 0, 1)$). The kurtosis is negative for a few of the largest lags and therefore not shown in the double logarithmic representation.

The distribution of the increments $\Delta_l v(x) = v(x) - v(x-l)$ over some lag l of the turbulent velocities is known to be highly non-Gaussian across a wide range of lags and well described by normal inverse Gaussian distributions (Barndorff-Nielsen et al., 2004). Figure A.8 compares the distributions of the measured increments $\Delta_l v(x)$ across various lags to the distributions of the increments of the normal inverse Gaussian simulation using the odd kernel. The increments of the normal inverse Gaussian simulation using the even kernel are similar and not shown. As the lag increases, the distributions become less steep and ultimately get close to normal. However, the transition towards normality appears to be faster for the simulation than for the measured data. This is confirmed by fig. A.9 (b) which shows that the kurtosis of the simulated increments decreases much faster as a function of the lag than the kurtosis of the measured increments. This emphasizes the necessity of volatility modulation. Figure A.9 (a) shows the skewness of the increments for the measured data set and for the normal inverse Gaussian simulation using both the even and the odd kernel. The skewness of the increments corresponding to the odd kernel decreases much faster than the measured skewness. Not surprisingly, the skewness is zero for the increments corresponding to the even kernel. The skewness of the velocity increments of the measured data manifests Kolmogorov's 4/5-law. The particular choice of the normal inverse Gaussian

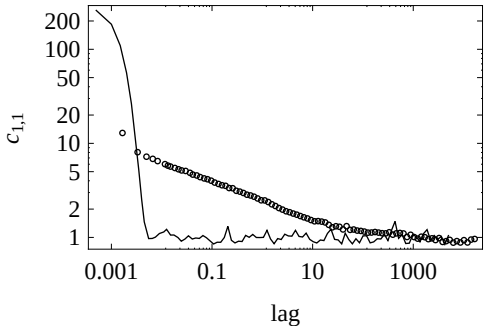

FIGURE A.10. The two-point correlator $c_{1,1}$ of order $(1,1)$ of the surrogate energy dissipation (approximated using squared increments over the smallest lag) of the measured data set (circles) and a normal inverse Gaussian simulation using the odd kernel (solid) as a function of lag in double logarithmic representation.

Lévy basis ensures that the skewness and kurtosis of the increments of the simulation using the odd kernel agree reasonably well with the those of the measured data when the lag is near 0.2 m (equally possible for any other lag). We conclude that a highly peaked, slightly asymmetric normal inverse Gaussian Lévy basis is able to reproduce some of the non-Gaussian behaviour of the turbulent velocity increments at a fixed lag, but not for all lags simultaneously.

In addition to the heavy-tailed distribution of the velocity increments, the large increments tend to occur in clusters, i.e., in rapid succession followed by relative calm periods. Some of this behaviour is captured in the two-point correlator of the surrogate energy dissipation (Cleve et al., 2004). The surrogate energy dissipation is given as $\epsilon = 15\nu(\partial v/\partial x)^2$, where ν denotes the viscosity. The two-point correlator (of order $(1,1)$) of the surrogate energy dissipation is then defined by $c_{1,1}(l) = E[\epsilon(l)\epsilon(0)]/(E[\epsilon(l)]E[\epsilon(0)])$. Figure A.10 shows the characteristic power law behaviour of $c_{1,1}$ observed in most turbulent data sets. Notice that this behaviour is not reproduced by the simulated data as the correlator quickly drops to approximately 1 when the lag is near 0.005, corresponding to essentially uncorrelatedness of the surrogate energy dissipation at greater lags. The observed behaviour is due to the lack of volatility-modulation of the Lévy basis.

A.7 CONCLUSION AND OUTLOOK

A random vector field was defined as the convolution of a deterministic matrix-valued function (the kernel) with respect to a vector-valued Lévy basis. Under some mild assumptions, any covariance structure can be reproduced, and the kernel can be expressed in terms of the covariance tensor to be modelled. In case the random vector field is isotropic and incompressible, the kernel can be expressed in terms of the energy spectrum.

With applications to turbulence in mind, a data set consisting of measurements of the longitudinal velocity component at a single point in space was analysed. The Shkarofsky correlation was shown to fit the data very well, from

the largest length scales in the energy range across the inertial range and to the smallest length scales in the dissipation range. Under the assumption of incompressibility the corresponding even and odd kernels were derived, each of them reproducing the Shkarofsky correlation.

Since turbulence possesses structure across a wide range of length scales, simulation is non-trivial if all scales are to be resolved. The straightforward approach is computationally intractable on an ordinary modern computer. The simulation problem can be solved by partitioning the kernel into smaller kernels using a smooth partition of unity.

While simulations from the three-dimensional model were not given, the one-dimensional model was used as a proxy to demonstrate that the use of a highly peaked and slightly skewed normal inverse Gaussian Lévy basis is able to reproduce the distribution of increments for a fixed lag. The model was not able to reproduce the intermittency of turbulence, the fingerprint of which appears in the scaling of the two-point correlator of squared velocity increments.

So far, a possible volatility modulation σ in (A.1) has not been used. Under the purely temporal model considered by Barndorff-Nielsen and Schmiegel (2009) the σ-process is, up to a normalisation constant, determined by the quadratic variation of the process. This in turn essentially allows us to identify the σ-process with the surrogate energy dissipation, $\epsilon = 15\nu(\partial v/\partial x)^2$. Cleve et al. (2008) and Hedevang and Schmiegel (2012) demonstrate how the surrogate energy dissipation may be modelled as the exponential of an ambit process, specifically

$$\epsilon(x,t) = \exp\Big(\int_{A(x,t)} d\Lambda\Big) = \exp(\Lambda(A(x,t)))$$

where the integrand is constant and equal to 1. For three-dimensional velocity measurements, no surrogate is needed, and the energy dissipation is given as

$$\epsilon = \sum_{i,j=1}^{3} \Big(\frac{\partial v_i}{\partial x_j} + \frac{\partial v_j}{\partial x_i}\Big)^2.$$

It remains to be investigated how this expression relates to a volatility modulation of the Lévy basis. In addition, the three-dimensional model should be investigated in more detail and compared to full three-dimensional data (see Rosales and Meneveau (2006) for a list of statistical features).

From the point of view of the wind energy industry, the isotropic three-dimensional model is far too idealised, as the atmospheric boundary layer turbulence is anisotropic since, in general, we have $R(0)_{11} > R(0)_{22} > R(0)_{33}$ (Panofsky and Dutton, 1984). Proposition A.9 can be applied to the "sheared" spectral tensor of Mann (1998) to produce a kernel yielding the desired anisotropy. However, the presented Lévy based framework allows for anisotropy to be introduced in other ways. If we consider the process $X = f_{\text{even}} * \sigma\, d\Lambda$ where $f_{\text{even}}(x) = f_1(\|x\|)\hat{x}\hat{x}^T + f_2(\|x\|)I$ is the even kernel from earlier, then the covariance tensor R is given by $R(x) = \int_{\mathbb{R}^3} f_{\text{even}}(x-y)\operatorname{cov}(\Lambda^*) f_{\text{even}}(y)\, dy$. Some calculations will then show that

$$R(0) = a\operatorname{cov}(\Lambda^*) + b\operatorname{tr}(\operatorname{cov}(\Lambda^*))I \tag{A.19}$$

where

$$a = 4\pi \int_0^\infty \left(\tfrac{2}{15} f_1(r)^2 + \tfrac{2}{3} f_1(r) f_2(r) + f_2(r)^2 \right) r^2 \, dr,$$
$$b = 4\pi \int_0^\infty \tfrac{1}{15} f_2(r)^2 r^2 \, dr.$$

Therefore, by specifying $\operatorname{cov}(\Lambda^*)$ appropriately according to (A.19), any covariance matrix $R(0)$ can be achieved. Thus, the anisotropy can be modelled through the Lévy basis.

Since the derived kernels contain most of their mass near zero, see fig. A.5, the outcome of the Lévy basis near a given point contributes most to the value of the process $X = f * \sigma \, d\Lambda$ at that given point. Therefore, a possible inhomogeneity and anisotropy of the process may be encoded in the Lévy basis. This has some potential applications to wind energy. Firstly, the passage of a wind front, where the variance of the wind speed increases, say, can conveniently be modelled by letting the variance of the Lévy basis increase in the direction of the motion of the wind front (Nielsen et al., 2007). Secondly, properties like wind shear and veer (the dependency of magnitude and direction on height above ground) may likewise be encoded in the Lévy basis. Finally, the wake behind a wind turbine causes the wind field, experienced by a downstream wind turbine, to be strongly inhomogeneous. An appropriately constructed Lévy basis could ensure that the model reproduces the rotation of the wake as well as the lower mean wind speed and higher turbulence intensity[1] inside the wake. In turn, this can be applied to load and performance calculations of wind turbines within wind farms.

A.A ASPECTS OF SIMULATION

Simulation of the processes considered in this paper is in principle trivial since efficient convolution algorithms can be applied. Unfortunately, since atmospherical boundary layer turbulence possesses structure across a wide range of scales, the straightforward approach obtained by discretising the kernel in (A.4) easily yields a discrete convolution problem that is too large to be computed on an ordinary modern computer, even in the one-dimensional case. The purpose of this appendix is to elaborate on the problem and demonstrate a way to solve it.

For the sake of simplicity of the exposition we will consider only scalar-valued processes defined on $\mathbb{R}$, i.e., the one-dimensional case, and we assume no volatility modulation, i.e., $\sigma \equiv 1$. At the expense of some additional bookkeeping, the results of this appendix extend to the $(n+0, n)$-dimensional case. Let X be defined as in (A.4),

$$X(x) = \int_{\mathbb{R}} f(x-y) \, \Lambda(dy),$$

where Λ is a Lévy basis given by a homogeneous seed $(\Lambda^*, \mathrm{Leb})$ and where $f : \mathbb{R} \to \mathbb{R}$ is Λ-integrable.

1 · The turbulence intensity is defined as the ratio of the standard deviation of the wind speed to the mean wind speed.

A.A.1 APPROXIMATING SKELETONS

Let $\delta > 0$. By the δ-skeleton X^δ of X we will understand the process on $\delta\mathbb{Z}$ obtained by evaluating X at integer multiples of δ,

$$X^\delta(\delta k) = X(\delta k).$$

The δ-skeleton will through interpolation be extended to a process on $\mathbb{R}$, also to be denoted by X^δ. In this language, a simulation from X will constitute a realisation of some δ-skeleton at some finite subset of the integers.

We have that

$$X^\delta(\delta k) = \sum_{j=-\infty}^{\infty} \int_{(\delta(j-1),\delta j]} f(\delta k - y)\,\Lambda(dy) \quad \text{a.s.} \tag{A.20}$$

The cumulant functions of the inner integrals are given by

$$C\Big(t \ddagger \int_{(\delta(j-1),\delta j]} f(\delta k - y)\,\Lambda(dy)\Big) = \int_{\delta(k-j)}^{\delta(k-j+1)} C(f(y)t \ddagger \Lambda^*)\,dy.$$

In the Gaussian case, where $\Lambda^* \sim N(\alpha^*, \beta^*)$, the distribution of the δ-skeleton is given by

$$X^\delta(\delta k) \sim \sum_{j=-\infty}^{\infty} (\alpha^*_{k-j} + (\beta^*_{k-j})^{1/2} N_j(0,1))$$

where

$$\alpha^*_j = \alpha^* \int_{\delta j}^{\delta(j+1)} f(y)\,dy, \qquad \beta^*_j = \beta^* \int_{\delta j}^{\delta(j+1)} f(y)^2\,dy,$$

and where the $N_j(0,1)$, $j \in \mathbb{Z}$, are independent. If the integrals in α^*_j and β^*_j can be evaluated efficiently and if all but finitely many are negligible, we obtain an efficient way of simulating any δ-skeleton. In the three-dimensional case, this would be equivalent to the Fourier space analogue employed in Mann (1998).

In the non-Gaussian case, for example, if the distribution of the seed Λ^* is normal inverse Gaussian, the decomposition (A.20) does not necessarily yield a sum of independent random variables whose distributions are normal inverse Gaussian. To proceed we will instead approximate the δ-skeleton by replacing the kernel function with a step function. Let $\delta > 0$ and $n > 0$ be given. By a (δ, n)-skeleton $X^{\delta,n}$ of X we will understand a process on $\delta\mathbb{Z}$ defined by

$$X^{\delta,n}(\delta k) = \int_{\mathbb{R}} f^{\delta,n}(\delta k - y)\,\Lambda(dy)$$

where

$$f^{\delta,n}(y) = \sum_{j=-n+1}^{n} 1_{(\delta(j-1),\delta j]}(y) f^{\delta,n}_j$$

and where $f^{\delta,n}_j = f(x_j)$ for some $x_j \in (\delta(j-1), \delta j]$. The function $f^{\delta,n}$ will also be called a (δ, n)-skeleton of f. A (δ, n)-skeleton of X may through interpolation be extended to a process on $\mathbb{R}$.

We must now address how well the distribution of the marginals of the

skeleton and the auto-covariance function of the skeleton approximate those of the original process. The cumulants of the lowest orders provide a simple measure of similarity of distributions. Let c_m denote the cumulant of m'th order. Then

$$c_m(X(t)) = c_m(\Lambda^*) \int_{\mathbb{R}} f(y)^m \, dy,$$
$$c_m(X^{\delta,n}(\delta k)) = c_m(\Lambda^*) \sum_{j=-n+1}^{n} (f_j^{\delta,n})^m \delta.$$

Hence, the cumulants of the marginals of the skeleton $X^{\delta,n}$ approximate those of the original process X well, if

$$\Big| \int_{\mathbb{R}} f(y)^m \, dy - \sum_{j=-n+1}^{n} (f_j^{\delta,n})^m \delta \Big| \tag{A.21}$$

is small. Since the finite sum in (A.21) is a Riemann sum approximation to the integral in (A.21), an approximation to any desired level of accuracy is always possible, provided f^m is Riemann-integrable.

The auto-covariance function R of X is given by

$$R(x) = \operatorname{cov}(X(x), X(0)) = \operatorname{var}(\Lambda^*) \int_{\mathbb{R}} f(|x| + y) f(y) \, dy.$$

Likewise, the auto-covariance function $R^{\delta,n}$ of the (δ, n)-skeleton $X^{\delta,n}$ is given by

$$R^{\delta,n}(\delta k) = \operatorname{var}(\Lambda^*) \sum_{j=-n+1}^{n-|k|} f_{|k|+j}^{\delta,n} f_j^{\delta,n} \delta.$$

Furthermore, if we extend the (δ, n)-skeleton through interpolation to a process on $\mathbb{R}$,

$$X^{\delta,n}(x) = \sum_{l=l_0}^{l_1} h_l(x) X^{\delta,n}(\delta(\lfloor |x|/\delta \rfloor + l))$$

such that the extension agrees with the skeleton on integer multiples of δ, then it follows that the auto-covariance function of the extended process is given in terms of the auto-covariance function of the skeleton in a similar way,

$$R^{\delta,n}(x) = \sum_{l=l_0}^{l_1} h_l(x) R^{\delta,n}(\delta(\lfloor |x|/\delta \rfloor + l)).$$

Zeroth order interpolation is obtained when $l_0 = 0$, $l_1 = 0$, and $h_0(x) = 1$. First order (linear) interpolation is obtained when $l_0 = 0$, $l_1 = 1$, $h_0(x) = 1 - x + \delta \lfloor x/\delta \rfloor$, and $h_1(x) = x - \delta \lfloor x/\delta \rfloor$.

We summarise the above discussion in the following proposition which provides some simple guidelines for how the (δ, n)-skeleton can be used to approximate the process X.

PROPOSITION A.15. *Let $X(x) = \int_{\mathbb{R}} f(x - y) \Lambda(dy)$ where Λ is given in terms of a homogeneous Lévy seed $(\Lambda^*, \mathrm{Leb})$. Let $\delta > 0$ and let n be a positive integer. Let $f^{\delta,n}$ be a (δ, n)-skeleton of f, and let $X^{\delta,n}(\delta k) = \int_{\mathbb{R}} f^{\delta,n}(\delta k - y) \Lambda(dy)$ denote the*

f	m	δ	n	$\left\lvert\int_{\mathbb{R}} f(y)^m\,dy - \sum_{j=-n+1}^{n}(f_j^{\delta,n})^m\delta\right\rvert$
f_{even}	1	0.0005	3×10^6	1.64×10^{-7}
—	2	—	—	1.52×10^{-8}
—	3	—	—	1.10×10^{-8}
—	4	—	—	1.14×10^{-8}
f_{odd}	2	0.0005	2×10^9	2.57×10^{-7}
—	4	—	—	1.17×10^{-10}

TABLE A.1. The absolute error (fifth column) relevant for the cumulants of orders $m = 1,2,3,4$ of the marginal distribution of the process $f * d\Lambda$ obtained when replacing the kernel f by a (δ,n)-skeleton $f^{\delta,n}$ with $f_j^{\delta,n} = f(\delta(j-1/2))$.

corresponding (δ,n)-skeleton of X. Provided the m'th cumulants of the marginals of X and $X^{\delta,n}$ exist, they satisfy

$$c_m(X(0)) - c_m(X^{\delta,n}(0)) = c_m(\Lambda^*)\Big(\int_{\mathbb{R}} f(y)^m\,dy - \sum_{j=-n+1}^{n}(f_j^{\delta,n})^m\delta\Big). \quad \text{(A.22)}$$

Furthermore, if the auto-covariance function R of X is approximated by an interpolation of the auto-covariance function $R^{\delta,n}$ of the skeleton, then the corresponding interpolation of the skeleton provides, on the level of covariances, an approximation of the process X.

Figure A.6 shows the even and odd kernels that each will yield the estimated Shkarofsky correlation structure, see fig. A.4, under the one-dimensional model. The kernels display structures across a wide range of scales, especially the odd kernel which decays only algebraically at small and large arguments. Table A.1 shows the absolute error of the approximating sum in (A.22) for cumulants of orders 1 to 4. For the odd kernel, the cumulants of odd order are all zero. The values of δ and n were chosen to ensure that the cumulants are approximated to six significant digits, that the auto-covariance function is well approximated by the skeleton, and that the spectral density function estimated from simulations from the skeleton agrees with the Shkarofsky spectral density function. The (δ,n)-skeleton $f^{\delta,n}$ was defined by $f_j^{\delta,n} = f(\delta(j-1/2))$. Since the resolution of the data set is $\delta_{\text{data}} = 0.0017$, we conclude that the resolution δ of the approximating skeleton should be 3 to 4 times smaller. Figure A.11 (a) shows excellent agreement between the estimated Shkarofsky correlation and the approximation obtained from the $(0.0005, 3\times10^6)$-skeleton of the even kernel.

Since the skeleton of the odd kernel requires $n = 2\times10^9$ to obtain an accurate approximation of the cumulants and of the auto-covariance function, merely storing the kernel in memory is close to the limit of an ordinary modern computer. The additional storage needed for the realisation of the Lévy basis and to perform the convolution is then beyond the limits of such a computer. This motivates a decomposition of the problem into parts as explained in the following subsections. Each part should be sufficiently small to be computationally tractable. Note, however, that the even kernel decays much faster at large scales and hence requires only $n = 3\times10^6$ which is trivially manageable.

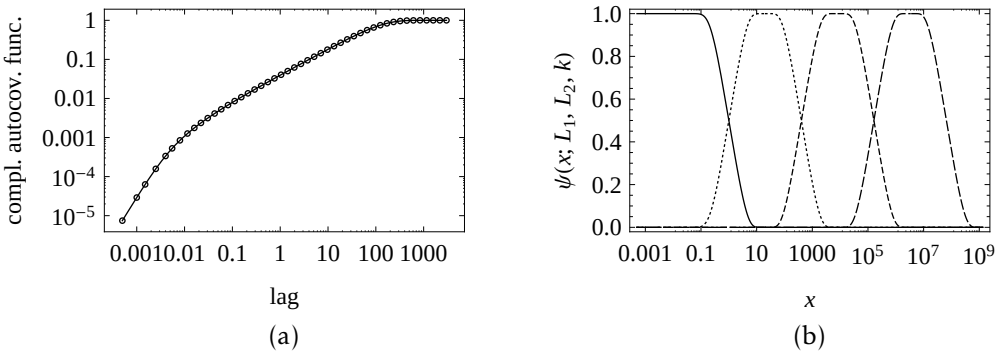

FIGURE A.11. (a) The complementary auto-covariance functions $1-R$ in double logarithmic representation. The solid curve denotes the estimated Shkarofsky correlation, and the circles denote the approximation obtained from the (δ, n)-skeleton of the even kernel with $\delta = 0.0005$ and $n = 3\times 10^6$. (b) The function $\psi(x; L_1, l_2, k)$ from the smooth partition of unity (A.23) plotted with $L_1 = 0.1$ and $L_2 = 6$ for $k = 0, 1, 2, 3$ (from left to right).

A.A.2 SMOOTH PARTITIONS OF UNITY

In this subsection we construct a smooth partition of unity. It is used to decompose the kernels into parts that each yield a computationally tractable process. Consider the function $\phi_1 : \mathbb{R} \to \mathbb{R}$ defined by

$$\phi_1(x) = \begin{cases} 0 & x \le 0, \\ e^{-1/x} & x > 0. \end{cases}$$

The function ϕ_1 can be used as the fundamental building block in the construction of smooth partitions of unity on the real line. Specifically, define ϕ_2 by

$$\phi_2(x) = \frac{\phi_1(x)}{\phi_1(x) + \phi_1(1-x)}.$$

Then ϕ_2 is smooth, $\phi_2(x) = 0$ for $x \le 0$, $\phi_2(x) = 1$ for $x \ge 1$, and strictly increasing on the interval $(0, 1)$. Define for $a < b < c < d$ the function ϕ_3 by

$$\phi_3(x; a, b, c, d) = \phi_2\Big(\frac{x-a}{b-a}\Big)\phi_2\Big(\frac{d-x}{d-c}\Big).$$

Then ϕ_3 is smooth, zero outside of the interval (a, d), and 1 on the interval $[b, c]$. Define for $L > 0$ and $0 \le r < 1$ the function ϕ_4 by

$$\phi_4(x; L, r) = \phi_3(x; -L, -rL, rL, L).$$

Then ϕ_4 is smooth, zero outside of the interval $(-L, L)$, and 1 on the interval $[-rL, rL]$. In the case $r = 0$, ϕ_4 has the simple expression,

$$\phi_4(x; L, 0) = \begin{cases} 1 & x = 0, \\ \Big(1 + \exp\Big((1 - (|x|/L))^{-1} - (|x|/L)^{-1}\Big)\Big)^{-1} & 0 < |x| < L, \\ 0 & |x| \ge L. \end{cases}$$

f	δ	n	$\max_m \left\lvert \int_{\mathbb{R}} f(y)^m \, dy - \sum_{j=-n+1}^{n} (f_j^{\delta,n})^m \delta \right\rvert$
$f_{\text{even},0}$	0.0005	40400	2.02×10^{-8}
$f_{\text{even},1}$	0.05	30000	5.86×10^{-7}
$f_{\text{even},2}$	5.	300	2.71×10^{-9}
$f_{\text{odd},0}$	0.0005	40400	2.94×10^{-11}
$f_{\text{odd},1}$	0.05	162800	4.11×10^{-10}
$f_{\text{odd},2}$	5.	200000	1.11×10^{-10}
$f_{\text{odd},3}$	500.	2000	6.55×10^{-13}

TABLE A.2. The maximal absolute error (fourth column) relevant to the approximation of the first four cumulants of the marginal distributions of the processes $f_{\text{even},k} * d\Lambda$ and $f_{\text{odd},k} * d\Lambda$ using a (δ, n)-skeleton of the partitioned kernels $f_{\text{even},k}$ and $f_{\text{odd},k}$, respectively.

Furthermore, $\lim_{r \to 1} \phi_4(x; L, r) = 1_{(-L,L)}(x)$. Define for $k = 0, 1, 2, \ldots$ the function ϕ_5 by

$$\begin{aligned} \phi_5(x; L, r, k) &= \phi_4(|x| - kL(1+r); L, r) \\ &= \begin{cases} \phi_4(x; L, r) & k = 0, \\ \phi_4(x - kL(1+r); L, r) + \phi_4(x + kL(1+r); L, r) & k \neq 0. \end{cases} \end{aligned}$$

Then $\{\phi_5(-; L, r, k) \mid k = 0, 1, 2, \ldots\}$ constitutes a smooth partition of unity on the real line.

Informally, the structure of the estimated kernels is more naturally separated into regions on a logarithmic scale than on a linear scale. Define therefore for $L_1 > 0$, $L_2 > 0$, and $k = 0, 1, 2, \ldots$ the function ψ by

$$\psi(x; L_1, L_2, k) = \phi_5(\operatorname{arcsinh}(x/L_1); L_2, 0, k). \tag{A.23}$$

Then $\{\psi(-; L_1, L_2, k) \mid k = 0, 1, 2, \ldots\}$ constitutes a smooth partition of unity on the real line. Figure A.11 (b) shows $\psi(-; L_1, L_2, k)$ with $L_1 = 0.1$ and $L_2 = 6$ for $k = 0, 1, 2, 3$.

A.A.3 PARTITIONS OF KERNELS

Let $f : \mathbb{R} \to \mathbb{R}$ denote a kernel and let $\{\psi_k \mid k = 0, 1, 2, \ldots\}$ denote a non-negative smooth partition of unity on $\mathbb{R}$. Define $f_k = f\psi_k$. Then $f * d\Lambda = \sum_{k=0}^{\infty} f_k * d\Lambda$. The idea is to choose the partition of unity such that each summand can be approximated sufficiently well using (δ_k, n_k)-skeletons with each n_k small enough to yield a computationally tractable discrete convolution. In practice, the infinite sum must be truncated at some K. The truncation limit can, for example, be chosen such that the cumulants of the marginals of $\sum_{k=0}^{K} f_k * d\Lambda$ are sufficiently close to those of the original process $f * d\Lambda$. It is important to note that the process $f * d\Lambda$ is decomposed into a sum of processes defined in terms of the same Lévy basis.

We now partition the estimated even and odd kernels as follows. Let the partition of unity be given by $\psi(-; 0.1, 6, k)$. We define the partitioned kernel functions by

$$\begin{aligned} f_{\text{even},k}(x) &= f_{\text{even}}(x)\psi(x; 0.1, 6, k), \quad k = 0, 1, 2; \\ f_{\text{odd},k}(x) &= f_{\text{odd}}(x)\psi(x; 0.1, 6, k), \quad k = 0, 1, 2, 3. \end{aligned}$$

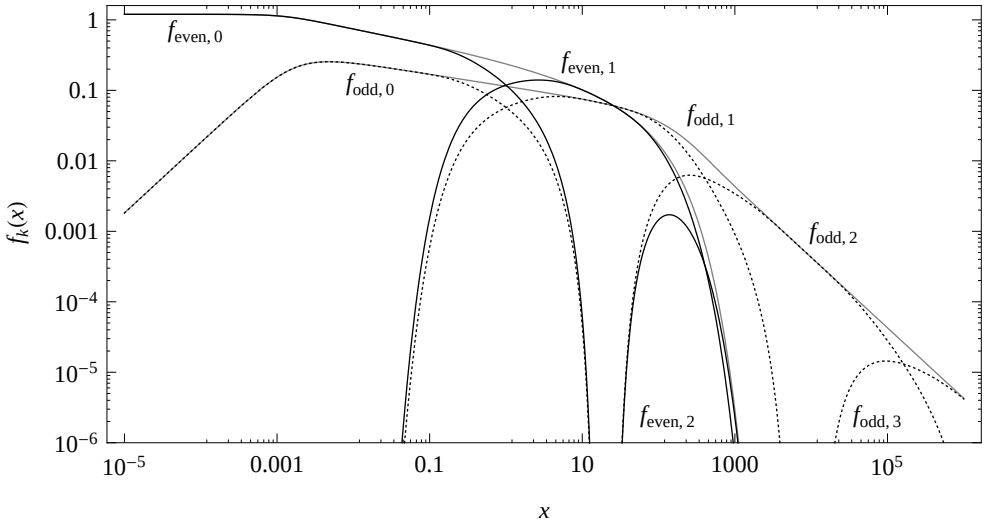

FIGURE A.12. Double logarithmic representation of the partitioned kernel functions $f_{\text{even},k}$ (solid) and $f_{\text{odd},k}$ (dashed) given by $f_{\text{even/odd},k}(x) = f_{\text{even/odd}}(x)\psi(x; 0.1, 6, k)$ for $k = 0, 1, 2$ (the even case) and $k = 0, 1, 2, 3$ (the odd case). The original kernel functions are shown in grey.

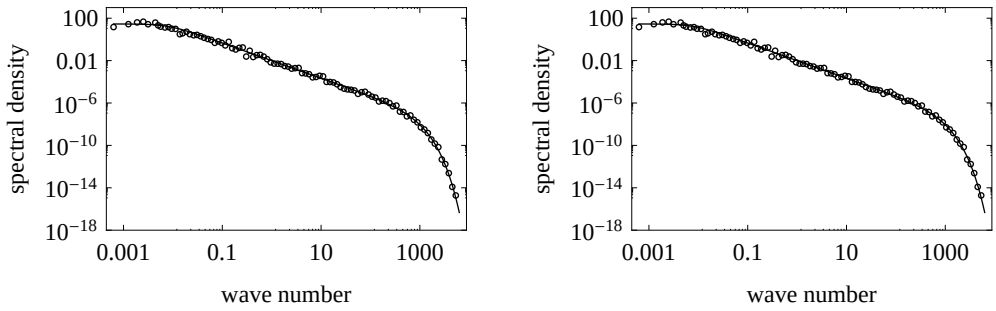

FIGURE A.13. The solid curve shows the longitudinal one-dimensional Shkarofsky spectral density function estimated from the atmospheric boundary layer data. The circles show the spectral density function estimated from a simulation of length 10^8 using the partitioned even kernel (a) and odd kernel (b), respectively, with resolutions and sizes of the skeletons as shown in tab. A.2. The spectral density function was estimated using Welsh's overlapping segment averages with a Hanning taper, a segment length of 20 million, and a segment overlap of 50%.

Figure A.12 shows the partitioned kernels. Truncation limits of $K = 2$ and $K = 3$ were deemed sufficient in the even and odd case, respectively. Table A.2 shows that, by partitioning the kernels using a suitable partition of unity, the resolution δ of the skeleton can in most cases be increased by several orders of magnitude when compared to the unpartitioned case (see tab. A.1). This implies in turn that the the size n of the skeleton can be decreased by several orders of magnitude.

The simulation of $f * d\Lambda$ using partitioned kernels can be described as follows. Assume that the (δ_k, n_k)-skeleton $f^{\delta_k, n_k} * d\Lambda$ has been simulated and refined to a δ_1-skeleton through interpolation. Then simulate the (δ_{k+1}, n_{k+1})-skeleton $f^{\delta_{k+1}, n_{k+1}} * d\Lambda$ by appropriately using the already simulated parts of the Lévy basis. Refine the simulated (δ_{k+1}, n_{k+1})-skeleton to a δ_1-skeleton through interpolation. Repeat until all $K + 1$ skeletons have been simulated

and refined to δ_1-skeletons. Finally, calculate the sum of the $K+1$ skeletons to obtain a δ_1-skeleton of $f * d\Lambda$.

Figure A.13 shows excellent agreement of the spectral density function from which the kernels were derived and the spectral density function estimated from a long simulation using the partitioned kernels. The simulation of a 0.0005-skeleton of $f_{\text{even}} * d\Lambda$ and of $f_{\text{odd}} * d\Lambda$ of size 10^8 using the approach of partitioned kernels took in both cases approximately a minute on an ordinary laptop.

A.A.4 EXTENSION TO HIGHER DIMENSIONS

Let $\{\psi_k : \mathbb{R} \to \mathbb{R} \mid k = 0, 1, 2, \ldots\}$ be a partition of unity on $\mathbb{R}$. Let S be a set. For any function $g : S \to \mathbb{R}$ we obtain a partition of unity $\{\psi_k^g\}$ on S by defining $\psi_k^g = \psi_k \circ g$. In particular a norm on $\mathbb{R}^n$ induces a natural partition of unity on $\mathbb{R}^n$. We may therefore easily extend the procedure of partitioning the kernel from the previous section to higher dimensions, though the bookkeeping will be more involved. Application of this approach to the three-dimensional model in sec. A.6.2 is beyond the scope of the present paper and will be studied in a forthcoming paper.

A.B INTEGRAL TRANSFORMS AND SPHERICAL SYMMETRIES

This appendix contains the results needed in proposition A.12 to express the kernel in the three-dimensional isotropic and incompressible model in terms of various integral transforms of the energy spectrum. All the results follow from integration in spherical coordinates.

Any unit vector $\hat{r} \in \mathbb{R}^3$ may be expressed in spherical coordinates,

$$\hat{r}(\alpha, \beta) = (\cos\alpha, \sin\alpha\cos\beta, \sin\alpha\sin\beta)^T,$$

where $\alpha \in [0, \pi]$ and $\beta \in [0, 2\pi)$. The matrix $Z(\alpha, \beta)$ defined by

$$\begin{aligned} Z(\alpha,\beta) &= \begin{bmatrix} \hat{r}(\alpha,\beta) & \hat{r}(\alpha+\frac{\pi}{2},\beta) & \hat{r}(\frac{\pi}{2},\beta+\frac{\pi}{2}) \end{bmatrix} \\ &= \begin{bmatrix} \cos\alpha & -\sin\alpha & 0 \\ \sin\alpha\cos\beta & \cos\alpha\cos\beta & -\sin\beta \\ \sin\alpha\sin\beta & \cos\alpha\sin\beta & \cos\beta \end{bmatrix} \end{aligned}$$

is then orthogonal and satisfies the relation

$$Z(\alpha,\beta)^T \hat{r}(\alpha,\beta) = (1,0,0)^T. \tag{A.24}$$

LEMMA A.16. *Let $f : \mathbb{R}^3 \to \mathbb{R}$ be integrable. Let $y \in \mathbb{R}^3$ with $y = \|y\|\hat{r}(\alpha,\beta)$. Then the Fourier transform of f at y is given by*

$$F_3[f](y) = \frac{1}{(2\pi)^3} \int_0^\infty \int_0^\pi \int_0^{2\pi} f(rZ(\alpha,\beta)\hat{r}(\theta,\phi)) e^{-ir\|y\|\cos\theta} r^2 \sin\theta \, d\phi \, d\theta \, dr.$$

If $y = 0$ we may choose $\alpha = \beta = 0$ so that $Z(\alpha,\beta) = I$. A similar identity holds for the inverse Fourier-transform.

PROOF. The identity follows from the transformation theorem using the orthogonality of $Z(\alpha,\beta)$, followed by application of (A.24), and then transfor-

mation to spherical coordinates. □

LEMMA A.18. *Let $A\colon \mathbb{R}_+ \to \mathbb{R}$ be a function such that $r \mapsto A(r)r^2$ is integrable. Then the Fourier transform of the function $\mathbb{R}^3 \to \mathbb{R}$ given by $x \mapsto A(\|x\|)$ exists, and*

$$F_3[A(\|x\|)](y) = \frac{1}{2\pi^2}\operatorname{sinc}[A(r)r^2](\|y\|).$$

PROOF. The existence of the Fourier transform is ensured by the assumption of integrability. Let $y \in \mathbb{R}^3$ be given and let $y = \|y\|\hat{r}(\alpha,\beta)$ be the spherical representation of y. By lemma A.16 we get

$$\begin{aligned} F_3[A(\|x\|)](y) &= \frac{1}{(2\pi)^3}\int_0^\infty\int_0^\pi\int_0^{2\pi} A(\|rZ(\alpha,\beta)\hat{r}(\theta,\phi)\|)e^{-ir\|y\|\cos\theta} \\ &\qquad\qquad \cdot r^2\sin\theta\,d\phi\,d\theta\,dr \\ &= \frac{1}{(2\pi)^2}\int_0^\infty A(r)r^2\int_0^\pi e^{-ir\|y\|\cos\theta}\sin\theta\,d\theta\,dr. \end{aligned}$$

The $d\theta$-integral is equal to $2\operatorname{sinc}(r\|y\|)$ as can be seen by a change of integration variable. It follows that

$$F_3[A(\|x\|)](y) = \frac{1}{2\pi^2}\int_0^\infty A(r)r^2\operatorname{sinc}(r\|y\|)\,dr = \frac{1}{2\pi^2}\operatorname{sinc}[A(r)r^2](\|y\|).$$

This completes the proof. □

LEMMA A.20. *Let $A\colon \mathbb{R}_+ \to \mathbb{R}$ be a function such that $r \mapsto A(r)r^2$ is integrable. Then the Fourier transform of the function $\mathbb{R}^3 \to M_3$ given by $x \mapsto A(\|x\|)\hat{x}\hat{x}^T$ exists, and*

$$\begin{aligned} F_3[A(\|x\|)\hat{x}\hat{x}^T](y) = \frac{1}{2\pi^2}\Big(&(-\tfrac{1}{2}\operatorname{sinc} - \tfrac{3}{2}\operatorname{sinc}'')[A(r)r^2](\|y\|)\hat{y}\hat{y}^T \\ &+ (\tfrac{1}{2}\operatorname{sinc} + \tfrac{1}{2}\operatorname{sinc}'')[A(r)r^2](\|y\|)I\Big). \end{aligned}$$

PROOF. The existence of the Fourier transform is ensured by the assumed integrability. Let $y \in \mathbb{R}^3$ be given and let $y = \|y\|\hat{r}(\alpha,\beta)$ be the spherical representation of y. Write $Z = Z(\alpha,\beta)$ for brevity. By lemma A.16 we get

$$\begin{aligned} &F_3[A(\|x\|)\hat{x}\hat{x}^T](y) \qquad\qquad (A.25)\\ &= \frac{1}{(2\pi)^3}\int_0^\infty\int_0^\pi\int_0^{2\pi} A(r)Z\hat{r}(\theta,\phi)\hat{r}(\theta,\phi)^T Z^T e^{-ir\|y\|\cos\theta} r^2\sin\theta\,d\phi\,d\theta\,dr \\ &= \frac{1}{(2\pi)^3} Z\int_0^\infty A(r)r^2\int_0^\pi e^{-ir\|y\|\cos\theta}\sin\theta\int_0^{2\pi}\hat{r}(\theta,\phi)\hat{r}(\theta,\phi)^T\,d\phi\,d\theta\,dr\,Z^T. \end{aligned}$$

The $d\phi$-integral is

$$\begin{aligned} &\int_0^{2\pi}\begin{bmatrix} \cos^2\theta & \cos\theta\cos\phi\sin\theta & \cos\theta\sin\theta\sin\phi \\ \cos\theta\cos\phi\sin\theta & \cos^2\phi\sin^2\theta & \cos\phi\sin^2\theta\sin\phi \\ \cos\theta\sin\theta\sin\phi & \cos\phi\sin^2\theta\sin\phi & \sin^2\theta\sin^2\phi \end{bmatrix} d\phi \\ &\quad = \begin{bmatrix} 2\pi\cos^2\theta & 0 & 0 \\ 0 & \pi\sin^2\theta & 0 \\ 0 & 0 & \pi\sin^2\theta \end{bmatrix}. \end{aligned}$$

The $d\theta$-integral in (A.25) is therefore also a diagonal matrix whose entries are determined by the following two integrals. The first integral follows by

differentiation and change of variables, whereas the second integral follows by change of variables and partial integration. For brevity we write $z = r\|y\|$. Then

$$\begin{aligned}2\pi\int_0^\pi e^{-iz\cos\theta}\sin\theta\cos^2\theta\,d\theta &= -2\pi\frac{d^2}{dz^2}\int_0^\pi e^{-iz\cos\theta}\sin\theta\,d\theta\\ &= 4\pi(-\operatorname{sinc}''(z)),\\ \pi\int_0^\pi e^{-iz\cos\theta}\sin\theta\sin^2\theta\,d\theta &= 4\pi\Big(\tfrac{1}{2}\operatorname{sinc}(z)+\tfrac{1}{2}\operatorname{sinc}''(z)\Big).\end{aligned}$$

Let $a_1 = -\operatorname{sinc}''[A(r)r^2](\|y\|)$ and $a_2 = (\frac{1}{2}\operatorname{sinc}+\frac{1}{2}\operatorname{sinc}'')[A(r)r^2](\|y\|)$. We then get

$$\begin{aligned}F_3[A(\|x\|)\hat{x}\hat{x}^T](y) &= \frac{1}{2\pi^2}Z\operatorname{diag}(a_1,a_2,a_2)Z^T = \frac{1}{2\pi^2}((a_1-a_2)\hat{y}\hat{y}^T + a_2 I)\\ &= \frac{1}{2\pi^2}\Big((-\tfrac{1}{2}\operatorname{sinc}-\tfrac{3}{2}\operatorname{sinc}'')[A(r)r^2](\|y\|)\hat{y}\hat{y}^T\\ &\qquad +(\tfrac{1}{2}\operatorname{sinc}+\tfrac{1}{2}\operatorname{sinc}'')[A(r)r^2](\|y\|)I\Big).\end{aligned}$$

It is easy to verify that the formula also holds in the case $y = 0$ with the convention that $\hat{0} = 0$. This completes the proof. □

COROLLARY A.22. *Let $A\colon \mathbb{R}_+ \to \mathbb{R}$ satisfy that $r \mapsto A(r)r^2$ is integrable. The Fourier transform of the function $\mathbb{R}^3 \to M_3$ given by $x \mapsto A(\|x\|)(-\hat{x}\hat{x}^T + I)$ then exists, and*

$$\begin{aligned}F_3[A(\|x\|)(-\hat{x}\hat{x}^T+I)](y) = \frac{1}{2\pi^2}\Big((\tfrac{1}{2}\operatorname{sinc}+\tfrac{3}{2}\operatorname{sinc}'')[A(r)r^2](\|y\|)\hat{y}\hat{y}^T\\ +(\tfrac{1}{2}\operatorname{sinc}-\tfrac{1}{2}\operatorname{sinc}'')[A(r)r^2](\|y\|)I\Big).\end{aligned}$$

LEMMA A.23. *Let $A\colon \mathbb{R}_+ \to \mathbb{R}$ satisfy that $r \mapsto A(r)r^2$ is integrable. Then the Fourier transform of the function $\mathbb{R}^3 \to M_3$ given by $x \mapsto A(\|x\|)\operatorname{sk}(\hat{x})$ exists, and*

$$F_3[A(\|x\|)\operatorname{sk}(\hat{x})](y) = i\frac{1}{2\pi^2}\operatorname{sinc}'[A(r)r^2](\|y\|)\operatorname{sk}(\hat{y})$$

with the convention that $\hat{y} = 0$ when $y = 0$.

PROOF. The existence of the Fourier transform is ensured by the assumed integrability. Let $y \in \mathbb{R}^3$, $y \neq 0$, be given and let $y = \|y\|\hat{r}(\alpha,\beta)$ be the spherical representation of y. By lemma A.16 we get

$$\begin{aligned}&F_3[A(\|x\|)\operatorname{sk}(\hat{x})](y)\\ &\quad= \frac{1}{(2\pi)^3}\int_0^\infty A(r)r^2\int_0^\pi e^{-ir\|y\|\cos\theta}\sin\theta\int_0^{2\pi}\operatorname{sk}(Z(\alpha,\beta)\hat{r}(\theta,\phi))\,d\phi\,d\theta\,dr.\end{aligned}$$

It is straightforward to verify that the $d\phi$-integral is equal to $2\pi\cos\theta\operatorname{sk}(\hat{y})$. Then, substitution with $u = \cos\theta$ followed by partial integration will shows that the $d\theta$-integral is equal to $2i\operatorname{sinc}'(r\|y\|)\operatorname{sk}(\hat{y})$. It follows that

$$\begin{aligned}F_3[A(\|x\|)\operatorname{sk}(\hat{x})](y) &= i\frac{1}{2\pi^2}\int_0^\infty A(r)r^2\operatorname{sinc}'(r\|y\|)\,dr\operatorname{sk}(\hat{y})\\ &= i\frac{1}{2\pi^2}\operatorname{sinc}'[A(r)r^2](\|y\|)\operatorname{sk}(\hat{y}).\end{aligned}$$

If $y = 0$, then $F_3[A(\|x\|)\operatorname{sk}(\hat{x})](y) = 0$ since $x \mapsto A(\|x\|)\operatorname{sk}(\hat{x})$ is odd. □

ACKNOWLEDGEMENTS

The authors thank K.R. Sreenivasan for granting permission to use the atmospheric boundary layer data set and wish to acknowledge fruitful discussions with Jan Pedersen, Uffe V. Poulsen (who suggested the even root of the isotropic, incompressible spectral tensor), and Kristjana Ý. Jónsdóttir. Part of this work was carried out while the first author visited Julie Lundquist at Colorado University, Boulder, and a draft was presented during a visit to the University of California, Santa Barbara.

BIBLIOGRAPHY

O. E. Barndorff-Nielsen. Hyperbolic distributions and distributions on hyperbolae. *Scand. J. Statist.*, 5:151–157, 1978.

O. E. Barndorff-Nielsen and J. Pedersen. Meta-times and extended subordination. *Theory Probab. Appl.*, 56(2):319–327, 2012.

O. E. Barndorff-Nielsen and J. Schmiegel. Lévy-based spatial-temporal modelling, with applications to turbulence. *Russian Math. Surveys*, 59(1):65–90, 2004.

O. E. Barndorff-Nielsen and J. Schmiegel. Time change, volatility, and turbulence. In A. Sarychev, A. Shiryaev, M. Guerra, and M. Grossinho, editors, *Mathematical control theory and finance*, pages 29–53. Springer, Berlin, 2008.

O. E. Barndorff-Nielsen and J. Schmiegel. Brownian semistationary processes and volatility/intermittency. In H. Albrecher, W. Runggaldier, and W. Schachermayer, editors, *Advanced financial modelling*, volume 8 of *Radon Ser. Comput. Appl. Math.*, pages 1–25. Walter de Gruyter, Berlin, 2009.

O. E. Barndorff-Nielsen and R. Stelzer. Multivariate supOU processes. *Ann. Appl. Probab.*, 21(1):140–182, 2011.

O. E. Barndorff-Nielsen, P. Blæsild, and J. Schmiegel. A parsimonious and universal description of turbulent velocity increments. *Eur. Phys. J. B*, 41: 345–363, 2004.

O. E. Barndorff-Nielsen, F. Benth, and A. Veraart. Modelling electricity forward markets by ambit fields. Available at http://dx.doi.org/10.2139/ssrn.1938704, 2011.

O. E. Barndorff-Nielsen, F. E. Benth, and A. Veraart. Modelling energy spot prices by volatility modulated Lévy-driven Volterra processes. *Bernoulli*, 2012. To appear.

A. Basse-O'Connor, S. E. Graversen, and J. Pedersen. A unified approach to stochastic integration on the real line. *Theory Probab. Appl.*, 2012. To appear.

G. K. Batchelor. *The theory of homogeneous turbulence*. Cambridge University Press, 1959.

K. H. Biss. Windfeldmodellierung mit multifraktaler Turbulenz. Master's thesis, Institut für Theoretische Physik, Justus-Liebig-Universität, Gießen, 2009.

P. Blæsild. The two-dimensional hyperbolic distribution and related distributions, with an application to Johannsen's bean data. *Biometrika*, 68(1): 251–263, 1981.

F. H. Champagne. The fine-scale structure of the turbulent velocity field. *J. Fluid Mech.*, 86(1):67–108, 1978.

J. Cleve, M. Greiner, B. R. Pearson, and K. R. Sreenivasan. Intermittency exponent of the turbulent energy cascade. *Phys. Rev. E*, 69(6):066316, 2004.

J. Cleve, J. Schmiegel, and M. Greiner. Apparent scale correlations in a random multifractal process. *Eur. Phys. J. B*, 63(1):109–116, 2008.

B. R. Dhruva. *An experimental study of high Reynolds number turbulence in the atmosphere.* PhD thesis, Yale University, 2000.

J. L. Doob. *Stochastic processes*. John Wiley & Sons Inc., 1953.

V. Ferrazzano and C. Klüppelberg. Turbulence modeling by time-series methods, 2012. Submitted.

I. S. Gradshteyn and I. M. Ryzhik. *Table of integrals, series, and products*. Elsevier/Academic Press, seventh edition, 2007.

P. Guttorp and T. Gneiting. Studies in the history of probability and statistics. XLIX. On the Matérn correlation family. *Biometrika*, 93(4):989–995, 2006.

E. Hedevang. Stochastic modelling of turbulence. Progress Report. Unpublished. Available upon request, 2011.

E. Hedevang and J. Schmiegel. A parsimonious and universal description of the turbulent energy dissipation. *Eur. Phys. J. B*, 2012. Submitted.

K. Ý. Jónsdóttir, J. Schmiegel, and E. B. V. Jensen. Lévy-based growth models. *Bernoulli*, 14(1):62–90, 2008.

A. N. Kolmogorov. The local structure of turbulence in incompressible viscous fluid for very large Reynolds numbers. *Dokl. Akad. Nauk. SSSR*, 30:299–303, 1941.

D. Levin. Fast integration of rapidly oscillatory functions. *J. Comput. Appl. Math.*, 67(1):95–101, 1996.

J. Mann. Wind field simulation. *Prob. Engng. Mech.*, 13(4):269–282, 1998.

A. J. McNeil, R. Frey, and P. Embrechts. *Quantitative risk management*. Princeton University Press, 2005.

T. Mücke, D. Kleinhans, and J. Peinke. Atmospheric turbulence and its influence on the alternating loads on wind turbines. *Wind Energy*, 14(2):301–316, 2011.

M. Nielsen, G. C. Larsen, and K. S. Hansen. Simulation of inhomogeneous, non-stationary and non-gaussian turbulent winds. *J. Phys. Conf. Ser.*, 75(1): 012060, 2007.

H. Panofsky and J. Dutton. *Atmospheric turbulence: models and methods for engineering applications*. Wiley, 1984.

J. Pedersen. The Lévy-Ito decomposition of an independently scattered random measure. MaPhySto Research Report. Available at www.maphysto.dk, 2003.

D. B. Percival and A. T. Walden. *Spectral Analysis for Physical Applications: Multitaper and Conventional Univariate Techniques*. Cambridge University Press, 1993.

K. Prause. *The Generalized Hyperbolic Model: Estimation, Financial Derivatives and Risk Measures*. PhD thesis, Albert-Ludwigs University, 1999.

B. S. Rajput and J. Rosinski. Spectral representations of infinitely divisible processes. *Probab. Th. Rel. Fields*, 82(3):451–487, 1989.

H. P. Robertson. The invariant theory of isotropic turbulence. *Proc. Cambridge Philos. Soc.*, 36:209–223, 1940.

C. Rosales and C. Meneveau. A minimal multiscale Lagrangian map approach to synthesize non-Gaussian turbulent vector fields. *Phys. Fluids*, 18:075104, 2006.

K.-i. Sato. *Lévy processes and infinitely divisible distributions*. Cambridge University Press, 1999.

J. Schmiegel. Self-scaling of turbulent energy dissipation correlators. *Phys. Lett. A*, 337:342–353, 2005.

J. Schmiegel. Self-scaling tumor growth. *Phys. A*, 367:509–524, 2006.

J. Schmiegel. Spatio-temporal modelling. Unpublished notes, 2007.

J. Schmiegel, J. Cleve, H. C. Eggers, B. R. Pearson, and M. Greiner. Stochastic energy-cascade model for $(1 + 1)$-dimensional fully developed turbulence. *Phys. Lett. A*, 320(4):247–253, 2004.

I. Shkarofsky. Generalized turbulence space-correlation and wave-number spectrum-function pairs. *Can. J. Phys.*, 46(19):2133–2153, 1968.

L. Sirovich, L. Smith, and V. Yakhot. Energy spectrum of homogeneous and isotropic turbulence in far dissipation range. *Phys. Rev. Lett.*, 72(3):344–347, 1994.

G. I. Taylor. The spectrum of turbulence. *Proc. R. Soc. Lond. A*, 164(919): 476–490, 1938.

T. von Kármán. Progress in the statistical theory of turbulence. *Proc. Nat. Acad. Sci.*, 34:530–539, 1948.

M. Wächter, H. Heißelmann, M. Hölling, A. Morales, P. Milan, T. Mücke, J. Peinke, N. Reinke, and P. Rinn. The turbulent nature of the atmospheric boundary layer and its impact on the wind energy conversion process. *J. Turbul.*, 13(26):1–21, 2012.

PAPER B

A PARSIMONIOUS AND UNIVERSAL DESCRIPTION OF THE TURBULENT ENERGY DISSIPATION

E. Hedevang[1,2] and J. Schmiegel[3]

1 · Department of Mathematics, Aarhus University, Denmark
2 · Siemens Wind Power, Borupvej 16, 7330 Brande, Denmark
3 · Department of Engineering, Aarhus University, Denmark

ABSTRACT

We discuss continuous cascade models and their potential for modelling the energy dissipation in a turbulent flow. Continuous cascade processes, expressed in terms of stochastic integrals with respect to Lévy bases, are examples of ambit processes. These models are known to reproduce the scaling and self-scaling of correlators, two experimentally observed properties of turbulence. We compare three models: a normal model, a normal inverse Gaussian model and a stable model. We show that the normal inverse Gaussian model is superior to both, the normal and the stable model, in terms of reproducing the distribution of the energy dissipation; and that the normal inverse Gaussian model is superior to the normal model and competitive with the stable model in terms of reproducing the self-scaling exponents of two-point correlators. Furthermore, we show that the presented analysis is parsimonious in the sense that the self-scaling exponents of the two-point correlators are predicted from the one-point distribution of the energy dissipation, and that the shape of these distributions is independent of the Reynolds number.

B.1 INTRODUCTION

Since the pioneering work of Kolmogorov (1962) and Oboukhov (1962), where the turbulent energy dissipation is assumed to be log-normally distributed, the small-scale intermittency of the energy dissipation in turbulence has received much attention (Frisch, 1995; Sreenivasan and Antonia, 1997). The small scale intermittency is primarily expressed in terms of multifractal and universal scaling of inertial range statistics, including extended self-similarity (Benzi et al., 1993), scaling and self-scaling of correlators (Schmiegel, 2005), and the statistics of breakdown coefficients (Cleve et al., 2008).

Discrete and continuous random cascade processes have proved useful in describing phenomenologically the small-scale behaviour of the turbulent energy dissipation (Benzi et al., 1984; Cleve and Greiner, 2000; Frisch et al., 1978; Jouault et al., 1999, 2000; Mandelbrot, 1974; Meneveau and Sreenivasan, 1991; Schertzer and Lovejoy, 1987). In Cleve et al. (2005), the surrogate energy dissipation is modelled as a discrete random multiplicative cascade process. Choosing the law of the cascade generators to be log-normal yields the Kolmogorov-Oboukhov model. A continuous analogue to the discrete multiplicative cascade processes is formulated in terms of integrals with respect to Lévy bases and has been shown (Barndorff-Nielsen and Schmiegel, 2004; Schmiegel, 2005; Schmiegel et al., 2004) to be computationally tractable and to accurately describe the two- and three-point statistics of the energy dissipation.

In the cited works, focus is on the modelling of n-point statistics of the energy dissipation, not the distribution of the energy dissipation itself. Indeed, Schmiegel (2005) concludes with a remark that the law of the Lévy basis driving the cascade model should be inferred and its dependency on the Reynolds number should be investigated.

Both, discrete and continuous multiplicative cascade processes, suggest that the law of the logarithm of the energy dissipation should be infinitely divisible. Among the infinitely divisible distributions are the normal, stable, and normal inverse Gaussian distributions. These three classes of distributions each have their own tail behaviour.

The use of stable Lévy bases for modelling of the energy dissipation has been investigated in Cleve et al. (2008) and it is concluded by analysing the breakdown coefficients that "except for the log-normal limit, this leaves no room for the log-stable modelling of the turbulent energy cascade." The present paper investigates the alternative of using a normal inverse Gaussian Lévy basis to model the energy dissipation and in particular addresses the one-point distributions and two-point statistics.

The use of normal inverse Gaussian distributions in turbulence modelling is not new. In Cleve et al. (2005), the parameters of the normal inverse Gaussian distribution cascade generator are estimated from scaling exponents and cumulants, which are moment estimates, notorious for their sensitivity to outliers. Indeed, estimation of the normal inverse Gaussian parameters (and those of other distributions) may not be feasible from sample moments. In this paper we will apply maximum likelihood methods instead, as these methods

		normal inverse Gaussian				stable					
data set	Re_λ	α	β	μ_ϵ	δ_ϵ	α	μ_ϵ	δ_ϵ	d.s.	$\Delta x_{\mathrm{eff}}/\eta$	rms_τ
1	85	2.23	−1.77	2.02	2.71	1.61	−1.80	1.30	3	3.60	5.1%
2	89	2.23	−1.77	2.09	2.85	1.63	−1.83	1.32	3	3.15	3.2%
3	124	2.23	−1.77	2.09	2.86	1.63	−1.83	1.32	3	2.94	2.9%
4	208	2.25	−1.75	2.36	3.35	1.67	−1.97	1.42	2	3.50	1.1%
5	209	2.23	−1.77	2.05	2.81	1.62	−1.81	1.31	3	2.91	12.8%
6	283	2.24	−1.76	2.22	3.08	1.65	−1.89	1.37	4	—	0.3%
7	352	2.25	−1.75	2.35	3.34	1.67	−1.95	1.41	2	4.50	0.4%
8	463	2.25	−1.75	2.31	3.26	1.66	−1.93	1.40	3	5.79	2.7%
9	703	2.24	−1.76	2.18	3.03	1.65	−1.88	1.36	3	—	2.0%
10	885	2.25	−1.75	2.23	3.14	1.66	−1.89	1.37	2	6.90	0.6%
11	929	2.25	−1.75	2.22	3.12	1.65	−1.89	1.37	2	7.34	2.9%
12	985	2.24	−1.76	2.21	3.08	1.65	−1.89	1.37	2	9.66	0.2%
13	1181	2.24	−1.76	2.10	2.90	1.63	−1.83	1.33	2	9.94	1.1%

TABLE B.1. Summary of the thirteen data sets. The Taylor micro-scale Reynolds numbers are from Chanal et al. (2000). The normal inverse Gaussian parameters (constrained to yield finite exponential moment of order 4 according to (B.11)) and the stable parameters are estimated from the distribution (B.10) of $\log \epsilon$ using maximum likelihood methods. The factor with which each data set was downsampled is denoted by "d.s.", and Δx_{eff} denotes the effective resolution after downsampling in units of the Kolmogorov length η. Finally, rms_τ denotes the root mean square of the relative error in the consistency check of the estimated scaling exponents (B.16).

suffer no such deficiencies.

The paper is organised as follows. Section B.2 provides some background on the data analysed in this paper. Section B.3 recalls the construction of continuous cascade processes in terms of integrals with respect to Lévy bases. Section B.4 applies the theory to the data and shows how the distribution of the surrogate energy dissipation determines the scaling and self-scaling exponents of the two-point correlators. Section B.5 concludes. The two appendices provide necessary background on the normal inverse Gaussian distribution and integration with respect to Lévy bases.

B.2 BACKGROUND ON THE DATA

We analyse thirteen data sets consisting of one-point time records of the velocity component in the mean stream direction in helium gas jet flow (Chanal et al., 2000). The time series can be assumed to be stationary. In Cleve et al. (2004), eleven of the thirteen data sets are used in an analysis of the intermittency exponent of the turbulent energy cascade. In particular, Cleve et al. (2004, table I) summarises useful information about the data sets. Data set nos. 6 and 9 are not considered in Cleve et al. (2004). For the present paper it suffices to note that each time series consists of sixteen million samples, the resolution scale (mean velocity times sampling time) is 1–5 times the Kolmogorov length, and the Taylor-microscale based Reynolds number Re_λ varies from 85 to 1181. Table B.1 lists Re_λ in addition to parameters that will be explained later. Data set no. 7 is representative for the general features of all the data sets and will throughout the paper be used as the example data set. All figures for the other data sets are available upon request.

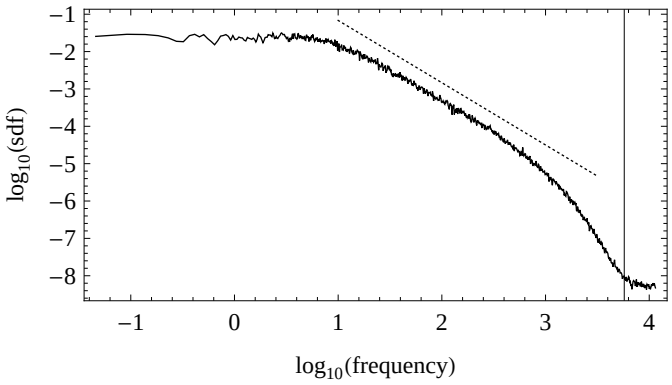

FIGURE B.1. The spectral density function for data set no. 7. The vertical line indicates the cut-off induced by the downsampling. The slope of the dashed line is −5/3.

The spectral density of the velocity component in the mean stream direction is estimated using Welsh's overlapping segment averages with a Hanning taper, a block length of 500 000 and an overlap of 50%, see e.g. Percival and Walden (1993) for details about the method. Figure B.1 shows the spectral density for data set no. 7. The inertial range is found at frequencies from approximately 10 Hz to 1000 Hz after which the transition to the dissipation range occurs. The slope in the inertial range is approximately −5/3, obeying Kolmogorov's 5/3-law. At the highest frequencies, the spectral density function changes behaviour and attains an almost constant value. Whether this is due to measurement noise will not be addressed here. We downsample the data by a factor specified in tab. B.1 to eliminate the spectral content at the highest frequencies. The vertical line in fig. B.1 indicates the cut-off induced by downsampling data set no. 7 by a factor of 2. A time step of 1 corresponds to the smallest time step of the downsampled data. Table B.1 shows the effective resolution Δx_{eff} (mean velocity times sampling time after downsamling) in units of the Kolmogorov length η.

Let u denote the velocity component in the mean stream direction, and let U denote the mean stream velocity. Since the flow can be assumed to be homogeneous and isotropic, we use the surrogate energy dissipation $\epsilon(x) = 15\nu(\partial u/\partial x)^2$ as a proxy for the energy dissipation. Here x denotes the position along the mean stream direction, and ν denotes the viscosity. We apply the Taylor frozen flow hypothesis to express the surrogate energy dissipation in terms of the measured time series. We do not invoke an "instantaneous Taylor correction" (Chanal et al., 2000) since it introduces spurious effects in correlators of the surrogate energy dissipation. Since any change of the surrogate energy dissipation by a multiplicative constant is inconsequential for the conclusions, we scale the surrogate energy dissipation to have unit mean. Finally, the derivative $\partial u/\partial t$ is calculated from the discrete samples using interpolation with third-order splines.

To assess the existence of moments, we consider, for a given time series $y = \{y_1, \ldots, y_{N_{\max}}\}$, the relative absolute sample moment $M_N^p(y)$ of order p and

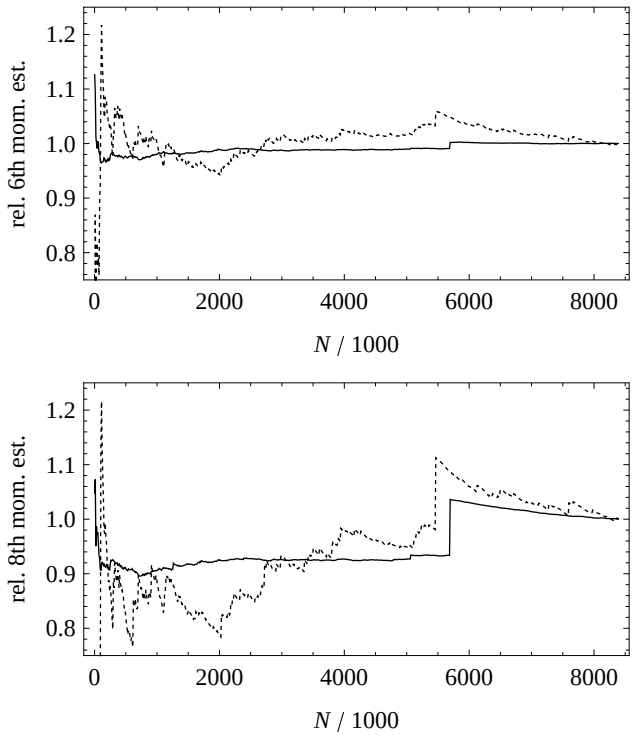

FIGURE B.2. Relative absolute sample moment of order 6 (top) and 8 (bottom) of $\log \epsilon$ (black curve) and $\partial u/\partial t$ (dashed) as a function of the sample size N for data set no. 7.

sample size N defined by

$$M_N^p(y) = \frac{1}{N}\sum_{i=1}^{N}|y_i|^p \Big/ \frac{1}{N_{\max}}\sum_{i=1}^{N_{\max}}|y_i|^p.$$

Figure B.2 shows $M_N^p(\partial u/\partial t)$ and $M_N^p(\log\epsilon)$ for $p = 6$, $p = 8$ and $N_{\max} = 8 \times 10^6$ for data set no. 7. The jumps near $N = 5.5 \times 10^6$ are confirmed to be due to outliers. We conclude that the 6th order moments of $\partial u/\partial t$ and $\log\epsilon$ can be estimated from the sample moments. We will not use moment estimates of order higher than 6.

B.3 A LÉVY BASED CONTINUOUS MULTIPLICATIVE CASCADE MODEL

In this section we present the model for the surrogate energy dissipation which we will later apply to the data. The model provides a link between the distribution and the two-point correlators of the surrogate energy dissipation.

In Schmiegel (2005) the surrogate energy dissipation ϵ is modelled as a $(1+1)$-dimensional stochastic process (one dimension in space and one in time) given as the exponential of an integral with respect to a Lévy basis Z on $\mathbb{R}^2$,

$$\epsilon(x,t) = \exp\Big(\int_{A(x,t)} Z(dx'\,dt')\Big), \tag{B.1}$$

where $A(x,t) \subseteq \mathbb{R}^2$ is called the *ambit set*. We will assume that the Lévy basis is homogeneous (see appendix B.B), and that the ambit sets are defined by

$A(x,t) = (x,t) + A$ for some bounded Borel set $A \subseteq \mathbb{R}^2$. Thus we ensure that ϵ is stationary in space and time. The model (B.1) is an example of a random multiplicative cascade process in continuous space and time. Since only one-point time series are available for our analysis, we will ignore the spatial dependency and consider the surrogate energy dissipation as a function of time alone and at a fixed position in space. However, it must be emphasised that the model is equally capable of modelling the spatial behaviour.

The distribution of $\log \epsilon$ is given by (B.22) or (B.23). Since the integrand in (B.1) is constant, we have that

$$K(s \ddagger \log \epsilon(t)) = K(s \ddagger Z')|A|, \tag{B.2}$$

where $K(s \ddagger X) = \log E[\exp(sX)]$ denotes the logarithm of the Laplace transform of the random variable X, Z' denotes the Lévy seed corresponding to the Lévy basis Z, and $|-|$ denotes the Lebesgue measure whenever applied to a set. We denote by $E[-]$ the expectation in the probabilistic sense. By (B.2), the distribution of the surrogate energy dissipation is, under the model (B.1), closely related to the distribution of the Lévy seed Z'.

B.3.1 TWO-POINT CORRELATORS

The two-point correlator $c_{p,q}$ of order (p,q) of the surrogate energy dissipation is defined as

$$c_{p,q}(t_1,t_2) = E[\epsilon(t_1)^p \epsilon(t_2)^q]/(E[\epsilon(t_1)^p]E[\epsilon(t_2)^q]).$$

The sum $p+q$ is the *total order* of the correlator $c_{p,q}$. It is shown in Schmiegel (2005) that

$$c_{p,q}(t_1,t_2) = \exp(K(p,q)|A(0,t_1) \cap A(0,t_2)|) \tag{B.3}$$

where

$$K(p,q) = K(p+q \ddagger Z') - K(p \ddagger Z') - K(q \ddagger Z'). \tag{B.4}$$

We observe that the exponent in (B.3) is expressed as a product where the first factor depends only on the Lévy basis and the order of the correlator, and the second factor depends only on the overlap of the ambit sets. This provides a way of modelling a wide range of correlators, since the shape of the ambit set, under suitable assumptions, can be determined from the correlator, see subsec. B.3.2 or Schmiegel (2005) for details.

Experiments (Cleve et al., 2004; Schmiegel et al., 2004) reveal that, at least for $p+q \leq 3$, the two-point correlators exhibit *scaling*,

$$c_{p,q}(\Delta t) := c_{p,q}(t, t+\Delta t) \propto \Delta t^{-\tau(p,q)}, \tag{B.5}$$

in a range of Δt comparable to the inertial range of the velocity structure functions. For $(p,q) = (1,1)$, the exponent $\tau(1,1)$ is known as the *intermittency exponent*. Furthermore, in Schmiegel (2005) it is shown that the two-point correlators also enjoy the property of *self-scaling*,

$$c_{p_2,q_2}(\Delta t) = c_{p_1,q_1}(\Delta t)^{\tau(p_1,q_1;p_2,q_2)},$$

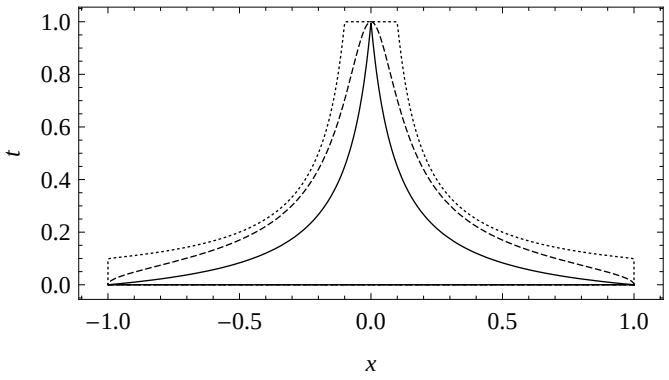

FIGURE B.3. The boundary of the ambit set (B.7) for the values $\theta = 1$ (solid), $\theta = 2$ (long dashes), and $\theta = 100$ (short dashes). The other parameters are $X = 1$, $T = 1$, and $L = 10$.

for an even wider range of Δt, much like the scaling range of extended self-similarity (Benzi et al., 1993) of the structure functions is wider than the scaling range of the pure structure functions. Here $\tau(p_1, q_1; p_2, q_2) = \tau(p_2, q_2)/\tau(p_1, q_1)$ is the self-scaling exponent.

By (B.3) we immediately obtain self-scaling of the correlators under the model (B.1),

$$c_{p_2,q_2}(\Delta t) = c_{p_1,q_1}(\Delta t)^{K(p_1,q_1;p_2,q_2)},$$

where

$$K(p_1, q_1; p_2, q_2) = K(p_2, q_2)/K(p_1, q_1)$$

is the self-scaling exponent. As noted in Schmiegel (2005), the self-scaling property is independent of the shape of the ambit set and thus scaling of the correlators is not necessary for self-scaling of the correlators. The Lévy seed Z' determines though (B.2) the distribution of the surrogate energy dissipation and through (B.4) the self-scaling exponents. Both, the distribution and the self-scaling exponents, can be estimated from data and hence compared with the model.

The correlators are moment estimates. Therefore they may not exist beyond a certain order. When they exist, they are sensitive to noise and outliers, particularly at high orders. By Hölder's inequality we have

$$E[\epsilon(t_1)^p \epsilon(t_2)^q] \leq E[\epsilon(t_1)^{p+q}]^{p/(p+q)} E[\epsilon(t_2)^{p+q}]^{q/(p+q)}.$$

It follows that the correlator $c_{p,q}$ exists provided the velocity derivative $\partial u/\partial t$ has finite moment of order $2(p+q)$. Under the model (B.1) it follows by (B.2) that $c_{p,q}$ exists if and only if the Lévy seed Z' has exponential moment of order $p+q$. In the following we will assume that $\partial u/\partial t$ has moments of order 8. This is equivalent to assuming that $\log \epsilon$ and Z' have finite exponential moments of order 4. This assumption is justified by the fact that the sample moments of order 8 of $\partial u/\partial t$ are corrupted by just a few extreme values out of more than eight million samples

B.3.2 AMBIT SETS AND SCALING OF CORRELATORS

While the self-scaling of the correlators is independent of the shape of the ambit set A, the scaling property (B.5) requires A to be specified appropriately according to (B.3). We define for $X > 0$, $T > 0$, $L > 1$, and $\theta > 0$ the function g by

$$g(t) = X\left(\frac{1-(t/T)^\theta}{1+(t/(T/L))^\theta}\right)^{1/\theta} \quad 0 \le t \le T. \tag{B.6}$$

In the limit $\theta = \infty$ we have that

$$g(t) = \begin{cases} X & 0 \le t \le T/L, \\ XT/(Lt) & T/L < t \le T. \end{cases}$$

The ambit set A is given as

$$A = \{(x,t) \mid 0 \le t \le T, |x| \le g(t)\}. \tag{B.7}$$

Figure B.3 shows examples of the ambit set for three values of the parameter θ. By (B.3),

$$c_{p,q}(\Delta t) = \exp\left(K(p,q)\int_{\Delta t}^{T} 2g(s)\,ds\right). \tag{B.8}$$

It follows that

$$\frac{d\log c_{p,q}(\Delta t)}{d\log \Delta t} \approx -K(p,q)\frac{2X}{L}T, \quad T/L \ll t \ll T. \tag{B.9}$$

Hence $K(p,q)(2X/L)(T/L)$ is the scaling exponent of $c_{p,q}$. In the limit $\theta = \infty$ we have perfect scaling,

$$\frac{d\log c_{p,q}(\Delta t)}{d\log \Delta t} = -K(p,q)\frac{2X}{L}T, \quad T/L < t < T.$$

The parameter θ is merely a tuning parameters to account for imperfect scaling of the correlators. In view of (B.3), where the overlap of the ambit sets determine the correlator, T and $2X$ may be interpreted as the decorrelation time and decorrelation length, respectively. Furthermore, T/L and $2X/L$ are time and length scales below which the scaling behaviour has terminated.

The model (B.1) is also able to reproduce empirical three-point correlators (Schmiegel et al., 2004), but these are not considered in the present paper.

B.3.3 THREE LÉVY BASES

We consider three distributions of the Lévy seed Z':

$$Z' \sim \begin{cases} \mathrm{N}(\mu,\delta) & \text{normal (N)}, \\ \mathrm{S}(\alpha,\beta,\mu,\delta) & \text{stable (S)}, \\ \mathrm{NIG}(\alpha,\beta,\mu,\delta) & \text{normal inv. Gaussian (NIG)}. \end{cases}$$

The normal Lévy seed yields a log-normal model for the surrogate energy dissipation, consistent with the Kolmogorov-Oboukhov theory (Oboukhov, 1962). The stable Lévy seed is included to enable comparison with Cleve et al.

(2008). The use of a normal inverse Gaussian Lévy seed can be motivated in several ways. The normal inverse Gaussian distribution is computationally tractable and allows a wide range of distributions (see fig. B.10). Furthermore, the representation (B.21) shows that the normal inverse Gaussian distributions form a natural generalisation of the normal distributions by allowing the variance of the normal distribution to be random. Since the variance is positive, and if there is a "typical variance", it is natural to model the variance using an unimodal distribution on the positive real line. A flexible distribution of this type is the inverse Gaussian law as shown in fig. B.11.

Other infinitely distributions could be considered as well. However, the three classes of distributions above exhaust a wide range of unimodal distributions with a specific tail behaviour: The normal distributions have "light tails", the stable distributions have "heavy tails", decaying algebraically, and the normal inverse Gaussian distributions have "semi-heavy tails", decaying exponentially, see (B.17).

The common symbols for the parameters $(\alpha, \beta, \mu, \delta)$ have been chosen due to the similarity of their interpretations. In all three cases, μ is a location parameter, δ is a scale parameter, α and β are shape parameters, and β determines the asymmetry of the distribution. The domain of the parameters is $\mu \in \mathbb{R}$ and $\delta > 0$ in all three cases; $0 < \alpha \leq 2$ and $-1 \leq \beta \leq 1$ in the stable case; and $|\beta| < \alpha$ in the normal inverse Gaussian case. The parametrisation of the stable distribution is chosen to follow Samorodnitsky and Taqqu (1994, eq. (1.1.6)), so that the log-characteristic function is given by

$$\log E[\exp(is\,\mathrm{S}(\alpha,\beta,\mu,\delta))] = \begin{cases} i\mu s - \delta^\alpha |s|^\alpha (1 - i\beta\,\mathrm{sign}(s)\tan(\pi\alpha/2)), & \alpha \neq 1, \\ i\mu s - \delta|s|(1 - i\beta\tfrac{2}{\pi}\,\mathrm{sign}(s)\log|s|), & \alpha = 1. \end{cases}$$

It follows from (B.22) or (B.23) that the distribution of $\log \epsilon$ in each of the three cases is

$$\log \epsilon \sim \begin{cases} \mathrm{N}(|A|\mu, |A|\delta) & Z' \sim \mathrm{N}, \\ \mathrm{S}(\alpha, \beta, |A|\mu, |A|^{1/\alpha}\delta) & Z' \sim \mathrm{S}, \\ \mathrm{NIG}(\alpha, \beta, |A|\mu, |A|\delta) & Z' \sim \mathrm{NIG}. \end{cases} \tag{B.10}$$

We see that the shape parameters of the distribution of $\log \epsilon$ are, in all three cases, identical to the shape parameters of the distribution of the Lévy seed Z', and that the location and scale parameters of $\log \epsilon$ are multiplied with a factor determined by the size of the ambit set, $|A| = 2\int_0^T g(s)\,ds$.

The normal distribution has exponential moments of all orders. Provided $\beta = -1$, the stable distribution has exponential moments of all non-negative orders. We will therefore assume that $\beta = -1$ in the stable case. The normal inverse Gaussian distribution has exponential moment of order s, if the shape parameters satisfy

$$-\alpha < \beta < \alpha - s. \tag{B.11}$$

In these cases the log-Laplace transform of the Lévy seed is given by

$$K(s \ddagger Z') = \begin{cases} \mu s + \frac{1}{2}\delta s^2 & Z' \sim \mathrm{N}, \\ \mu s - \left(\delta^\alpha / \cos(\pi\alpha/2)\right) s^\alpha & S' \sim \mathrm{S}, \\ \mu s + \delta\left((\alpha^2 - \beta^2)^{1/2} - (\alpha^2 - (\beta + s)^2)^{1/2}\right) & Z' \sim \mathrm{NIG}. \end{cases} \tag{B.12}$$

It follows that

$$K(p,q) = \kappa(p,q) \cdot \begin{cases} \frac{1}{2}\delta & Z' \sim \mathrm{N}, \\ -\left(\delta^\alpha / \cos(\pi\alpha/2)\right) & Z' \sim \mathrm{S}, \\ \delta & Z' \sim \mathrm{NIG}, \end{cases} \tag{B.13}$$

where

$$\kappa(p,q) = \begin{cases} pq & Z' \sim \mathrm{N}, \\ (p+q)^\alpha - p^\alpha - q^\alpha & Z' \sim \mathrm{S}, \\ (\alpha^2 - (\beta+p)^2)^{1/2} + (\alpha^2 - (\beta+q)^2)^{1/2} & \\ \quad - (\alpha^2 - \beta^2)^{1/2} - (\alpha^2 - (\beta+p+q)^2)^{1/2} & Z' \sim \mathrm{NIG}. \end{cases} \tag{B.14}$$

Note that κ depends only on the order (p,q) and the shape parameters. The self-scaling exponents are given by

$$K(p_1,q_1;p_2,q_2) = \kappa(p_2,q_2)/\kappa(p_1,q_1). \tag{B.15}$$

We conclude from (B.10), (B.14) and (B.15) that the self-scaling exponents are uniquely determined by the orders of the correlators and the shape of the marginal distribution of $\log\epsilon$.

B.4 DATA ANALYSIS

In this section we apply the model from section B.3 to the data. The marginal distribution of the surrogate energy dissipation is used to predict the scaling and self-scaling exponents of the two-point correlators.

B.4.1 DISTRIBUTION OF THE SURROGATE ENERGY DISSIPATION

Figure B.4 shows that the distribution of $\log\epsilon$ has a distinct, non-Gaussian, asymmetric shape. A few outliers lie in the range -50 to -35 and are not shown in the figure. Four parametric distributions are fitted to the data using maximum likelihood methods: normal, stable, normal inverse Gaussian, and normal inverse Gaussian constrained to have finite exponential moment of order 4 according to (B.11). Clearly, the normal inverse Gaussian distribution provides a very accurate fit. The left tail is overestimated by the stable distribution. The unconstrained normal inverse Gaussian distribution is able to accurately capture the left tail but slightly overestimates the right tail. The constrained normal inverse Gaussian distribution is able to capture the steep descent of the right tail while only slightly underestimating the left tail. In what follows, any reference to the normal inverse Gaussian distribution will imply the constrained version.

Table B.1 summarises the estimated parameters for each of the thirteen data

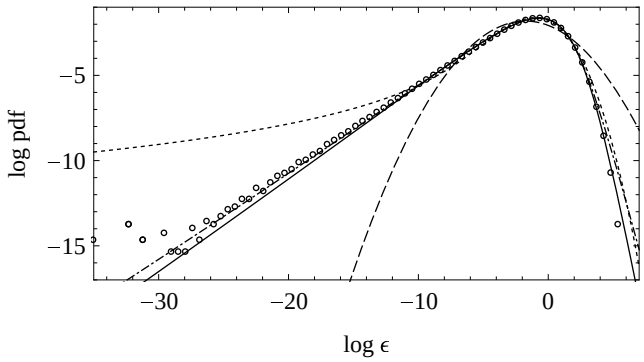

FIGURE B.4. Distribution of the logarithm of the surrogate energy dissipation represented by the logarithm of the probability density function for data set no. 7: data (circles), normal fit (long dashes), stable fit (short dashes), normal inverse Gaussian fit (dots and dashes), and normal inverse Gaussian fit constrained to possess finite exponential moments of order four (black curve).

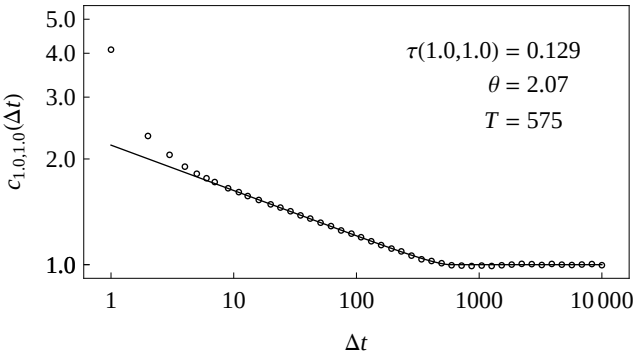

FIGURE B.5. The two-point correlator $c_{1,1}$ as a function of lag Δt for data set no. 7 in double logarithmic representation (circles). The solid curve shows the least squares fit of (B.8) in the double logarithmic representation. The estimated scaling exponent $\tau(1,1)$, decorrelation time T, and auxiliary parameter θ are shown in the figure.

sets. Note that for both, the normal inverse Gaussian distribution and the stable distribution, the estimated shape parameters do not depend on the Taylor micro-scale Reynolds number, while the location and scale parameters vary only slightly. This is a clear indication of universality of the distribution of the surrogate energy dissipation, at least within the thirteen data sets considered here.

B.4.2 SCALING AND SELF-SCALING OF CORRELATORS

Since the sample moments of the velocity derivative do not allow reliable estimation of correlators of order greater than 3, we consider the orders (p,q) for which p and q are positive half-integers with $p+q \leq 3$. This leads to 36 non-trivial combinations in the analysis of self-scaling of the correlators. The self-scaling exponents satisfy

$$\tau(p_1,q_1;p_3,q_3) = \tau(p_1,q_1;p_2,q_2)\tau(p_2,q_2;p_3,q_3),$$

and it is therefore sufficient to consider eight combinations.

Figure B.5 shows that the correlator $c_{1,1}$ for data set no. 7 exhibits scaling

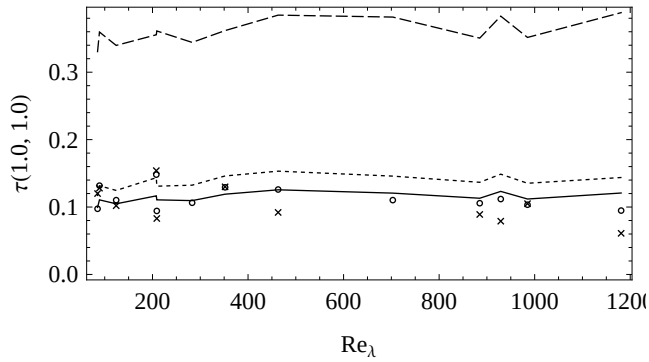

FIGURE B.6. The intermittency exponent $\tau(1,1)$ as a function of the Taylor micro-scale Reynolds number Re_λ: estimates from two-point correlator (circles), prediction under the normal model (long dashes), stable model (short dashes), and normal inverse Gaussian model (black curve). The crosses mark the estimated intermittency exponent found in (Cleve et al., 2004, tab. I, col. μ) for eleven of the thirteen data sets.

for $10 \leq \Delta t \leq 200$. The figure also shows that the correlator (B.8) determined by (B.6) provides a very good fit to the data for lags $\Delta t \geq 10$. The parameter θ determines the behaviour of the correlator for lags close to the decorrelation time T. At lags $\Delta t < 10$, the correlators are corrupted by surrogacy effects (Cleve et al., 2003). Lags $\Delta t < 10$ have therefore been excluded from the fit. Similar results hold for the other data sets and other orders of the correlators.

Since only temporal data are available, the parameter X of the ambit set (B.7) cannot be identified and can be chosen arbitrarily, say, $X = 1$. The parameter L, which determines the extend of the scaling range of the correlators, cannot be identified either, since surrogacy effects corrupt the correlator at small lags. We have chosen $L = 10^7$ as it yields no perceptible lower limit of the scaling behaviour.

The scaling exponents, under model (B.1), follow from (B.9), (B.10), and (B.13),

$$\tau(p,q) = \frac{2XT}{L|A|}\kappa(p,q) \cdot \begin{cases} \frac{1}{2}\delta_\epsilon & Z' \sim \mathrm{N}, \\ \dfrac{-\delta_\epsilon^\alpha}{\cos(\pi\alpha/2)} & Z' \sim \mathrm{S}, \\ \delta_\epsilon & Z' \sim \mathrm{NIG}. \end{cases}$$

The scale parameter δ of the Lévy seed Z' is determined by the size $|A|$ of the ambit set and the estimated scale parameter δ_ϵ of the distribution (B.10) of $\log \epsilon$. The size of the ambit set is in turn dependent on the parameter L which cannot be determined from the data and was therefore fixed somewhat arbitrarily at $L = 10^7$. Figure B.6 shows the scaling exponent $\tau(1,1)$ for the thirteen data sets. The normal inverse Gaussian model and the stable model agree reasonably well and both are markedly different from the normal model. The normal inverse Gaussian model displays the best agreement. By increasing L, either the stable model or the normal model can be made to display the best agreement instead, while the behaviour of the correlators for $\Delta t \geq 10$ will remain unchanged. The predicted intermittency exponents are almost independent of Re_λ. This is a direct consequence of the fact that the shape parameters of $\log \epsilon$ are independent of Re_λ, see tab. B.1. Similar results hold for the other orders of the correlators.

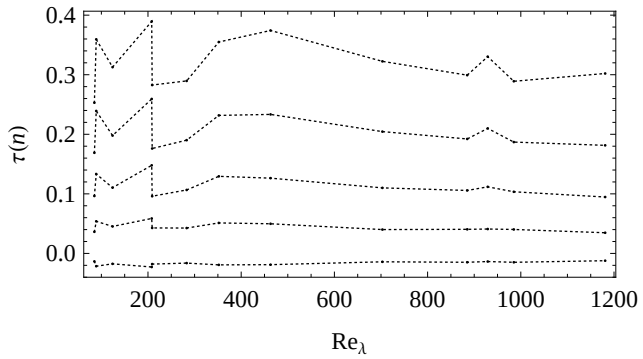

FIGURE B.7. The estimated $\tau(n)$ for $n = 0.5, 1.5, 2.0, 2.5, 3.0$ (from bottom to top) as a function of Re_λ.

The intermittency exponent $\tau(1,1)$ is, in fig. B.6, also compared to the intermittency exponent found in (Cleve et al., 2004, tab. I, col. μ) and agrees reasonably well with the findings therein. The differences are likely to be due to the different estimation procedures. Note that the predicted intermittency exponents are not based on moment estimates, but rather maximum likelihood methods.

As a final consistency check, we note that it follows from (B.4) and (B.9) that the scaling exponents satisfy the relation

$$\tau(p,q) = \tau(p+q) - \tau(p) - \tau(q). \tag{B.16}$$

By (B.12), we may choose $\tau(1) = 0$. The other unknowns $\tau(n)$ are found by solving the linear least squares system corresponding to (B.16), see fig. B.7. The root mean square rms_τ of the relative error $(\tau(p+q)-\tau(p)-\tau(q))/\tau(p,q)-1$ is reported in tab. B.1. Except for data set no. 5, rms_τ is around a few percent, confirming (B.16).

The self-scaling of the correlators is confirmed by fig. B.8. Under model (B.1), the self-scaling exponent $\tau(p_1,q_2;p_2,q_2)$ is given by the ratio $\kappa(p_2,q_2)/\kappa(p_1,q_1)$. It depends only on the shape parameters of the distribution of $\log\epsilon$ and on the order of the involved correlators. In particular, the self-scaling exponents are independent of the ambit set and the location and scale parameters of $\log\epsilon$. Therefore, the self-scaling exponents are predicted directly from the estimated shape parameters listed in tab. B.1, and they inherit the Re_λ-independence from $\log\epsilon$.

Figure B.9 shows the estimated self-scaling exponents as a function of Re_λ. For each displayed combination of orders, the variation of the self-scaling exponents is 10%–20%. The figure shows that the stable and normal inverse Gaussian models are superior to the normal model, except for the case $(1.0, 1.5; 0.5, 2.5)$ where all models fail to predict the observed self-scaling exponents by approximately 10%. The stable model appears in a few cases to be slightly better than the normal inverse Gaussian model, though both lie within the variation of the data. At low Reynolds numbers, the self-scaling exponents tend to deviate from the self-scaling exponents at higher Reynolds numbers. At low Reynolds numbers the inertial range is shorter. Whether this affects the estimation of the self-scaling exponents remains to be investigated.

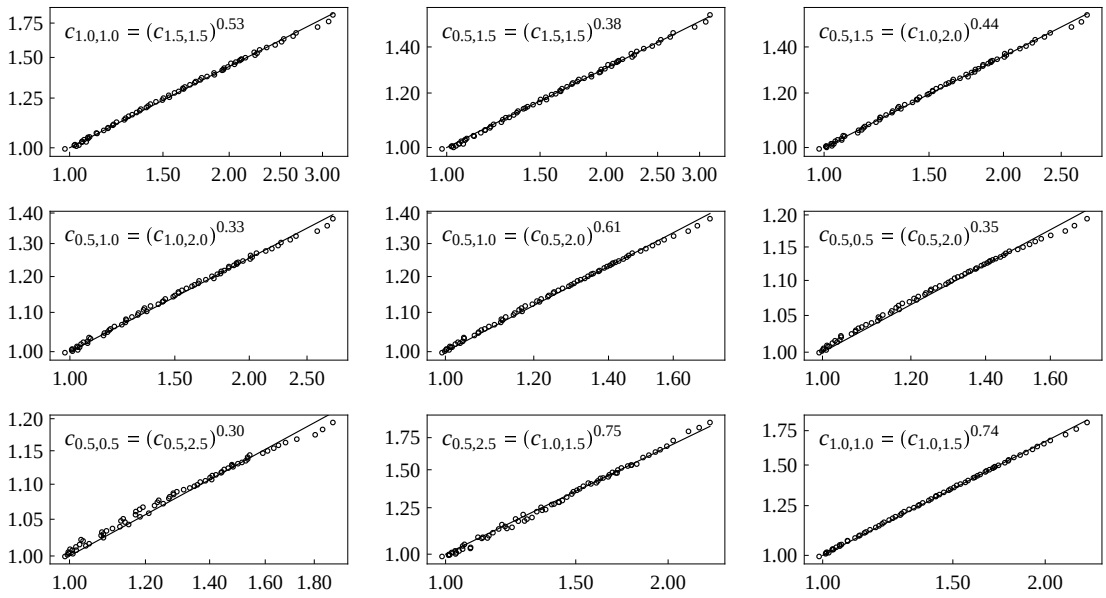

FIGURE B.8. The two-point correlator c_{p_2,q_2} (y-axis) as a function of the two-point correlator c_{p_1,q_1} (x-axis) for data set no. 7 in double logarithmic representation. The black line indicates the self-scaling behaviour $c_{p_2,q_2} = (c_{p_1,q_1})^{\tau(p_1,q_1;p_2,q_2)}$ as shown in each subfigure. Similar results hold for the other data sets.

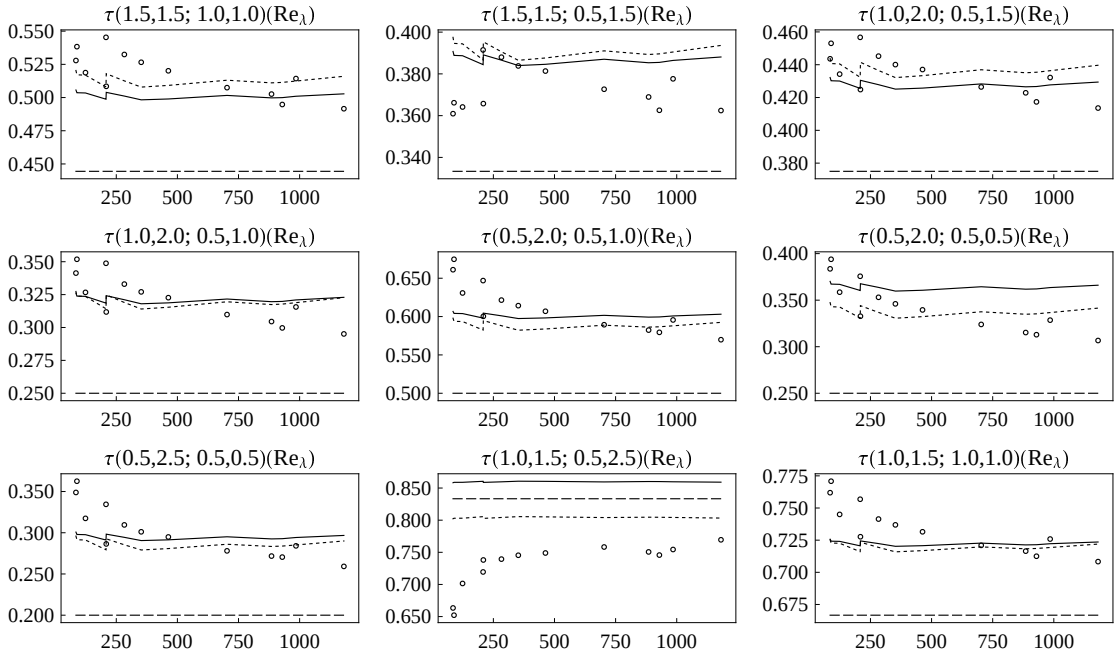

FIGURE B.9. The self-scaling exponents $\tau(p_1,q_1;p_2,q_2)$ (y-axis) as function of the Taylor micro-scale Reynolds number Re_λ (x-axis): data (circles), normal model (long dashes), stable model (short dashes), normal inverse Gaussian model (black curve).

Further observations may be drawn from fig. B.9. Firstly, the predicted self-scaling exponents are in all three cases almost independent of the Taylor micro-scale Reynolds number. This is a consequence of the estimated shape parameters of the distribution of $\log \epsilon$ displayed in tab. B.1. As noted previously, this hints at a universal character of the self-scaling exponents and the distribution of $\log \epsilon$. Secondly, the shape parameters are derived from one-point statistics, while the self-scaling exponents are derived from two-point statistics. The predictability of the latter from the former hints at a parsimonious description of the surrogate energy dissipation as the exponential of an integral with respect to a Lévy basis: Higher order statistics are reasonably well predicted from lower order statistics.

B.5 CONCLUSION AND OUTLOOK

Thirteen time series of one-point measurements of the velocity component in the mean stream direction in a helium jet are analysed from the point of view of the (surrogate) energy dissipation. The distribution of the logarithm of the surrogate energy dissipation is shown to be well approximated by normal inverse Gaussian distributions, a property possessed by neither the normal distribution nor the stable distribution. Furthermore, the shape of the distribution is apparently universal, i.e., it does not depend on the Reynolds number.

The two-point correlators of the surrogate energy dissipation show scaling and self-scaling. By modelling the surrogate energy dissipation as the exponential of an integral with respect to a Lévy basis, a connection is established between the shape of the distribution of the logarithm of the surrogate energy dissipation and the scaling and self-scaling exponents of the two-point correlators. Thus the model is parsimonious: the two-point correlators are all, to good accuracy, determined by the one-point distribution. The use of normal inverse Gaussian distributions is compared to the use of stable distributions. While the stable distributions are also capable of modelling the scaling and self-scaling exponents, they are not capable of accurately modelling the distribution of the surrogate energy dissipation. In particular, the stable model implies infinite variance of $\log \epsilon$, yet the data suggest that $\log \epsilon$ has finite moments at least up to order 6. The use of normal inverse Gaussian distributions allows accurate modelling of both the correlators and the distribution of the surrogate energy dissipation.

The surrogate energy dissipation exhibits stylised features beyond the scaling and self-scaling of the two-point correlators. In Cleve et al. (2008), breakdown coefficients and Kramers-Moyal coefficients are employed, in particular, to evaluate the use of stable distributions in the modelling. A similar analysis remains to be performed in the case of the normal inverse Gaussian distributions.

B.A THE NORMAL INVERSE GAUSSIAN DISTRIBUTION

The normal inverse Gaussian distributions form a four-parameter family of probability distributions on the real line. They are a special case of the generalised hyperbolic distributions introduced in Barndorff-Nielsen (1977) to describe the law of the logarithm of the size of sand particles (see also Barndorff-Nielsen and Halgreen (1977), Barndorff-Nielsen (1978), Barndorff-Nielsen and Blæsild (1981), Blæsild (1990), and Eberlein and Hammerstein (2004)). The generalised hyperbolic distributions are applied in many areas of science, see e.g. Prause (1999) and Barndorff-Nielsen et al. (2004) and the references therein.

The probability density function of a normal inverse Gaussian distribution is given by

$$\mathrm{pdf}_{\mathrm{NIG}(\alpha,\beta,\mu,\delta)}(x) = \frac{\alpha e^{\delta\gamma}}{\pi} e^{\beta(x-\mu)} \frac{K_1\Big(\delta\alpha q\Big(\frac{x-\mu}{\delta}\Big)\Big)}{q\Big(\frac{x-\mu}{\delta}\Big)}$$

where $\gamma = \alpha^2 - \beta^2$, $q(x) = \sqrt{1+x^2}$, and K_1 denotes the modified Bessel function of the second kind with index 1. The real parameter μ determines the location, and the positive parameter δ determines the scale. The parameters α and β are shape parameters and lie within the shape cone: $|\beta| < \alpha$.

From the asymptotic property $K_1(x) \propto x^{-1/2} e^{-x}$ as $x \to \infty$ it follows that the NIG distribution has semi-heavy tails, specifically

$$\mathrm{pdf}_{\mathrm{NIG}(\alpha,\beta,\mu,\delta)}(x) \propto |x|^{-3/2} \exp(-\alpha|x| + \beta x) \tag{B.17}$$

as $x \to \pm\infty$. This illuminates the role of α and β in determining the tails of the distribution.

The cumulant function $K(t;\alpha,\beta,\mu,\delta) = \log E \exp(tX)$ of a random variable X with distribution $\mathrm{NIG}(\alpha,\beta,\mu,\delta)$ is given by

$$K(t;\alpha,\beta,\mu,\delta) = \mu t + \delta\Big(\gamma - \sqrt{\alpha^2 - (\beta+t)^2}\Big), \tag{B.18}$$

and the radius of convergence for the cumulant function is $|\alpha - \beta|$.

By differentiating (B.18) we obtain the following expressions for the first four cumulants,

$$\begin{aligned} \kappa_1 &= \mu + \delta\frac{\rho}{(1-\rho^2)^{1/2}}, & \kappa_2 &= \frac{\delta}{\alpha}\frac{1}{(1-\rho^2)^{3/2}}, \\ \kappa_3 &= 3\frac{\delta}{\alpha^2}\frac{\rho}{(1-\rho^2)^{5/2}}, & \kappa_4 &= 3\frac{\delta}{\alpha^3}\frac{1+4\rho^2}{(1-\rho^2)^{7/2}}, \end{aligned} \tag{B.19}$$

where $\rho = \beta/\alpha$. Hence, the standardised third and fourth cumulants are

$$\frac{\kappa_3}{\kappa_2^{3/2}} = 3\frac{\rho}{(\delta\alpha(1-\rho^2)^{1/2})^{1/2}}, \quad \frac{\kappa_4}{\kappa_2^2} = 3\frac{1+4\rho^2}{\delta\alpha(1-\rho^2)^{1/2}}. \tag{B.20}$$

Equations (B.19) and (B.20) further illuminate the roles of the four parameters: μ and δ determine location and scale, respectively; β is related to the skewness, specifically the tail asymmetry (if $\beta = 0$, the distribution is symmetric); and α is related to the kurtosis.

It follows immediately from (B.18) that if $X_1, \ldots, X_n$ are independent nor-

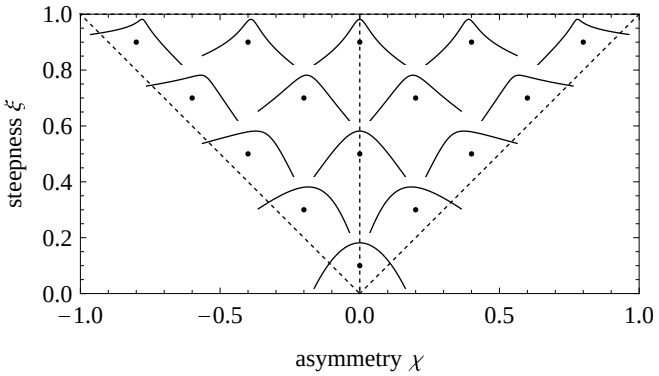

FIGURE B.10. The normal inverse Gaussian shape triangle. The black dots mark positions (χ, ξ) in the shape triangle, and the small graph nearby shows the logarithm of the probability density function with the corresponding asymmetry χ, steepness ξ, zero mean, and unit variance, plotted on the interval $[-3, 3]$.

mal inverse Gaussian variables with common parameters α and β, but with individual location and scale parameters μ_i and δ_i $(i = 1, \ldots, n)$, then the distribution of the sum $X_+ = X_1 + \cdots + X_n$ is $\mathrm{NIG}(\alpha, \beta, \mu_+, \delta_+)$ where $\mu_+ = \mu_1 + \cdots + \mu_n$ and $\delta_+ = \delta_1 + \cdots + \delta_n$. Therefore, the normal inverse Gaussian distributions are *infinitely divisible*, see also Barndorff-Nielsen and Halgreen (1977).

It is often desirable to describe the NIG distributions in terms of location-scale invariant parameters. By letting $\bar{\alpha} = \delta\alpha$ and $\bar{\beta} = \delta\beta$ we have that $\bar{\alpha}$ and $\bar{\beta}$ are invariant under change of location and scale. For the purpose of interpreting the shape parameters it is sometimes advantageous to express the shape in terms of the location-scale invariant *steepness* ξ and *asymmetry* χ, defined by

$$\xi = \frac{1}{\sqrt{1+\bar{\gamma}}}, \qquad \chi = \rho\xi = \frac{\rho}{\sqrt{1+\bar{\gamma}}},$$

where $\bar{\gamma} = \delta\gamma = \delta\sqrt{\alpha^2 + \beta^2}$, and $\rho = \beta/\alpha = \bar{\beta}/\bar{\alpha}$ is the *alternative asymmetry*. These parameters are within the *shape triangle*, defined by

$$\{(\chi, \xi) \mid 0 < \xi < 1, -\xi < \chi < \xi\}.$$

Figure B.10 shows the shape of the normal inverse Gaussian distributions for various values of the asymmetry χ and steepness ξ. A wide range of shapes is possible. (See Blæsild (1990) for details on the shape of the family of generalised hyperbolic distributions).

If the variance is held constant, the normal distribution is obtained in the limit of zero steepness. For details and examples of other limiting distributions, see Barndorff-Nielsen (1978) and Eberlein and Hammerstein (2004).

A useful property of the normal inverse Gaussian distribution is the representation in terms of a mean-variance mixture of a normal distribution with the mixing distribution being an inverse Gaussian distribution, hence the name. Specifically, if X is normal with mean $\mu + \beta\sigma^2$ and variance σ^2, and if σ^2 is endowed with an independent inverse Gaussian distribution with parameters γ and δ, then X follows a normal inverse Gaussian distribution with

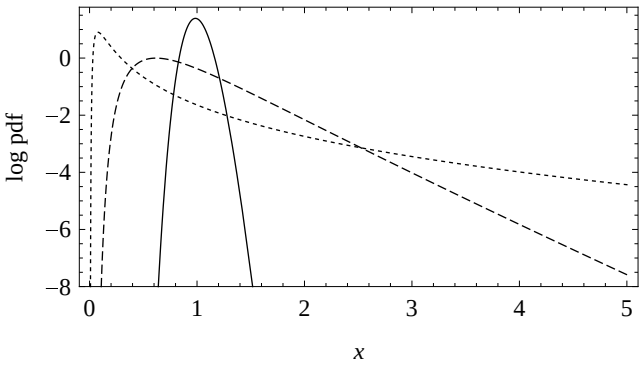

FIGURE B.11. The logarithm of the probability density function of the inverse Gaussian distribution with parameters chosen to yield normal inverse Gaussian distributions with zero mean, unit variance, zero asymmetry, and steepness $\xi = 0.1$ (black), $\xi = 0.5$ (long dashes), and $\xi = 0.9$ (short dashes), see fig. B.10.

parameters $(\alpha, \beta, \mu, \delta)$. In short we may write

$$X \sim \mu + \beta\sigma^2 + \sigma U \tag{B.21}$$

where U is a normal distribution with zero mean and unit variance. For reference, the probability density function of an inverse Gaussian distribution with parameters γ and δ is

$$\mathrm{pdf}_{\mathrm{IG}(\gamma,\delta)}(x) = \frac{\delta e^{\gamma\delta}}{\sqrt{2\pi}} x^{-3/2} \exp(-\tfrac{1}{2}(x\gamma^2 + x^{-1}\delta^2))$$

for $x > 0$. Figure B.11 shows the logarithm of the probability density functions of the inverse Gaussian distribution corresponding to the three symmetric normal inverse Gaussian distributions in fig. B.10. As the steepness increases, the probability that the random variance σ^2 in (B.21) will attain large values increases.

To estimate the normal inverse Gaussian parameters from data one may apply maximum likelihood methods. The maximum likelihood estimation is non-trivial since the likelihood function is very flat near the optimum. The computer program "hyp" (Blæsild and Sørensen, 1992) implements numerical maximisation of the likelihood function, but, in general, non-linear optimisation algorithms may also be applied. The approach of expectation-maximisation developed in Karlis (2002) may be used in conjunction with other optimisation algorithms.

B.B INTEGRATION WITH RESPECT TO LÉVY BASES

The stochastic processes to be considered in the present paper are expressed in terms of integrals of deterministic functions with respect to Lévy bases on $\mathbb{R}^2$. A Lévy basis Z on $\mathbb{R}^2$ is an *infinitely divisible, independently scattered random measure*, i.e., to each bounded Borel subset A of $\mathbb{R}^2$, an infinitely divisible random variable $Z(A)$ is associated, the random variables associated to disjoint subsets are independent, and the random variable associated to a disjoint union is almost surely equal to the sum of the random variables asso-

ciated to each subset, provided the union is a bounded Borel subset. For more details and mathematical rigour we refer to Rajput and Rosinski (1989).

The stochastic integral $\int f\,dZ$ of a deterministic function $f : \mathbb{R}^2 \to \mathbb{R}$ with respect to a Lévy basis Z is defined in three steps. Firstly, for an indicator function 1_A we define $\int 1_A\,dZ = Z(A)$. Secondly, by requiring that the integral is linear in the integrand, the integral is extended to simple functions, i.e., linear combinations of indicator functions. Finally, since a measurable function $f : \mathbb{R}^2 \to \mathbb{R}$ may be approximated by a sequence of simple functions, the integral $\int f\,dZ$ is defined to be the limit in probability of the sequence of integrals of the simple functions, provided this limit exists.

An important class of Lévy bases has the property that, informally, the distribution of the random variable associated to a subset does not depend on the location of the subset. In this case, we have the following fundamental representations of the Laplace transform and the characteristic function of the integral of a deterministic function f with respect to a Lévy basis Z. Let $K(s \ddagger X) = \log E[\exp(sX)]$ and $C(s \ddagger X) = \log E[\exp(isX)]$ denote the logarithm of the Laplace transform and the characteristic function of the random variable X, respectively. Then

$$K\Big(s \ddagger \int_A f(a)Z(da)\Big) = \int_A K(sf(a) \ddagger Z')\,da, \tag{B.22}$$

$$C\Big(s \ddagger \int_A f(a)Z(da)\Big) = \int_A C(sf(a) \ddagger Z')\,da, \tag{B.23}$$

where Z' is a random variable (called the *Lévy seed*) whose cumulant function is related to the Lévy basis Z by

$$K(s \ddagger Z(da)) = K(s \ddagger Z')\,da,$$
$$C(s \ddagger Z(da)) = C(s \ddagger Z')\,da,$$

see Barndorff-Nielsen and Schmiegel (2004) for more details. It follows that the distribution of the stochastic integral is determined by the function f and the log-characteristic function of the Lévy seed Z'.

ACKNOWLEDGEMENTS

The authors wish to thank B. Chabaud for granting permission to use the data. The authors furthermore acknowledge useful comments from Ole E. Barndorff-Nielsen and M. Greiner.

BIBLIOGRAPHY

O. E. Barndorff-Nielsen. Exponentially decreasing distributions for the logarithm of particle size. *Proc. R. Soc. Lond. A*, 353(1674):401–419, 1977.

O. E. Barndorff-Nielsen. Hyperbolic distributions and distributions on hyperbolae. *Scand. J. Statist.*, 5:151–157, 1978.

O. E. Barndorff-Nielsen and P. Blæsild. Hyperbolic distributions and ramifications: Contributions to theory and application. In C. Taillie, G. Patil, and

B. Baldessari, editors, *Statistical Distributions in Scientific Work*, volume 4, pages 19–44. Reidel, Dordrecht, 1981.

O. E. Barndorff-Nielsen and C. Halgreen. Infinite divisibility of the hyperbolic and generalized inverse Gaussian distributions. *Z. Wahrscheinlichkeitstheorie verw. Gebiete*, 38(4):309–311, 1977.

O. E. Barndorff-Nielsen and J. Schmiegel. Lévy-based spatial-temporal modelling, with applications to turbulence. *Russian Math. Surveys*, 59(1):65–90, 2004.

O. E. Barndorff-Nielsen, P. Blæsild, and J. Schmiegel. A parsimonious and universal description of turbulent velocity increments. *Eur. Phys. J. B*, 41: 345–363, 2004.

R. Benzi, G. Paladin, G. Parisi, and A. Vulpiani. On the multifractal nature of fully developed turbulence and chaotic systems. *J. Phys. A*, 17(18):3521, 1984.

R. Benzi, S. Ciliberto, C. Baudet, G. Chavarria, and R. Tripiccione. Extended self-similarity in the dissipation range of fully developed turbulence. *Europhys. Lett.*, 24(4):275–279, 1993.

P. Blæsild. The shape cone of the d-dimensional hyperbolic distribution. Technical report, Dep. of Theoretical Statistics, Inst. of Mathematics, Univ. of Aarhus, 1990.

P. Blæsild and M. K. Sørensen. Hyp: A Computer Program for Analyzing Data by Means of the Hybolic Distribution. Technical report, Dep. of Theoretical Statistics, Inst. of Mathematics, Univ. of Aarhus, 1992.

O. Chanal, B. Chabaud, B. Castaing, and B. Hébral. Intermittency in a turbulent low temperature gaseous helium jet. *Eur. Phys. J. B*, 17(2):309–317, 2000.

J. Cleve and M. Greiner. The Markovian metamorphosis of a simple turbulent cascade model. *Phys. Lett. A*, 273:104–108, 2000.

J. Cleve, M. Greiner, and K. R. Sreenivasan. On the effects of surrogacy of energy dissipation in determining the intermittency exponent in fully developed turbulence. *Europhys. Lett.*, 61(6):756, 2003.

J. Cleve, M. Greiner, B. R. Pearson, and K. R. Sreenivasan. Intermittency exponent of the turbulent energy cascade. *Phys. Rev. E*, 69(6):066316, 2004.

J. Cleve, T. Dziekan, J. Schmiegel, O. E. Barndorff-Nielsen, B. R. Pearson, K. R. Sreenivasan, and M. Greiner. Finite-size scaling of two-point statistics and the turbulent energy cascade generators. *Phys. Rev. E*, 71(2):026309, 2005.

J. Cleve, J. Schmiegel, and M. Greiner. Apparent scale correlations in a random multifractal process. *Eur. Phys. J. B*, 63(1):109–116, 2008.

E. Eberlein and E. A. v. Hammerstein. Generalized hyperbolic and inverse gaussian distributions: limiting cases and approximation of processes. In R. C. Dalang, M. Dozzi, and F. Russo, editors, *Seminar on Stochastic Analysis, Random Fields and Applications IV*, volume 58 of *Progress in Probability*, pages 221–264. Birkhäuser Verlag, 2004.

U. Frisch. *Turbulence*. Cambridge Univ. Press, 1995.

U. Frisch, P. L. Sulem, and M. Nelkin. A simple dynamical model of intermittent fully developed turbulence. *J. Fluid Mech.*, 87(04):719–736, 1978.

B. Jouault, P. Lipa, and M. Greiner. Multiplier phenomenology in random multiplicative cascade processes. *Phys. Rev. E*, 59:2451–2454, 1999.

B. Jouault, M. Greiner, and P. Lipa. Fix-point multiplier distributions in discrete turbulent cascade models. *Physica D*, 136:125–144, 2000.

D. Karlis. An EM type algorithm for maximum likelihood estimation of the normal-inverse Gaussian distribution. *Statist. Probab. Lett.*, 57(1):43–52, 2002.

A. N. Kolmogorov. A refinement of previous hypotheses concerning the local structure of turbulence in a viscous incompressible fluid at high Reynolds number. *J. Fluid Mech.*, 13(1):82–85, 1962.

B. B. Mandelbrot. Intermittent turbulence in self-similar cascades: divergence of high moments and dimension of the carrier. *J. Fluid Mech.*, 62(02):331–358, 1974.

C. Meneveau and K. R. Sreenivasan. The multifractal nature of turbulent energy dissipation. *J. Fluid Mech.*, 224:429–484, 1991.

A. M. Oboukhov. Some specific features of atmospheric tubulence. *J. Fluid Mech.*, 13(01):77–81, 1962.

D. B. Percival and A. T. Walden. *Spectral Analysis for Physical Applications: Multitaper and Conventional Univariate Techniques*. Cambridge University Press, 1993.

K. Prause. *The Generalized Hyperbolic Model: Estimation, Financial Derivatives and Risk Measures*. PhD thesis, Albert-Ludwigs University, 1999.

B. S. Rajput and J. Rosinski. Spectral representations of infinitely divisible processes. *Probab. Th. Rel. Fields*, 82(3):451–487, 1989.

G. Samorodnitsky and M. S. Taqqu. *Stable non-Gaussian random processes*. Chapman & Hall, 1994.

D. Schertzer and S. Lovejoy. Physical modeling and analysis of rain and clouds by anisotropic scaling multiplicative processes. *J. Geophys. Res*, 92(D8): 9693–9714, 1987.

J. Schmiegel. Self-scaling of turbulent energy dissipation correlators. *Phys. Lett. A*, 337:342–353, 2005.

J. Schmiegel, J. Cleve, H. C. Eggers, B. R. Pearson, and M. Greiner. Stochastic energy-cascade model for $(1 + 1)$-dimensional fully developed turbulence. *Phys. Lett. A*, 320(4):247–253, 2004.

K. R. Sreenivasan and R. Antonia. The phenomenology of small-scale turbulence. *Annu. Rev. Fluid Mech.*, 29:435–472, 1997.

PAPER C

WIND TURBINE POWER CURVES INCORPORATING TURBULENCE INTENSITY

E. Hedevang[1,2]

1 · Department of Mathematics, Aarhus University, Denmark
2 · Siemens Wind Power, Borupvej 16, 7330 Brande, Denmark

ABSTRACT

The performance of a wind turbine in terms of power production (the power curve) is important to the wind energy industry. The current IEC-61400-12-1 standard for power curve evaluation recognizes only the mean wind speed at hub height and the air density as relevant to the power production. However, numerous studies have shown that the power production depends on several variables, in particular turbulence intensity. This paper presents a model and a method that are computationally tractable and able to account for some of the influence of turbulence intensity on the power production. The model and method are parsimonious in the sense that only a single function (the zero-turbulence power curve) and a single auxiliary parameter (the equivalent turbulence factor) are needed to predict the mean power at any desired turbulence intensity. The method requires only ten minute statistics but can be applied to data of higher temporal resolution as well.

C.1 INTRODUCTION

The performance of a wind turbine in terms of power production under given wind conditions is a complex topic. Only the performance can be guaranteed, not the presence of certain wind conditions. The knowledge of the performance is important to both the design, verification, certification and subsequent monitoring of a wind turbine.

A wind turbine's production of power depends in particular on the atmospheric conditions. The current IEC 61400-12-1 standard recognizes that the mean power (ten minute mean) depends on the mean wind speed at hub height and the air density. The influence of the air density can be accounted for through a correction factor as defined in the standard. In numerous papers and reports it has been demonstrated that the mean power depends on other parameters in addition to mean hub height wind speed and air density, including wind speed profile (shear), inflow angle, wind direction profile (veer), turbulence intensity, turbulent kinetic energy, and the dynamic response of the wind turbine to the wind; see Christensen and Dragt (1986), Elliott and Cadogan (1990), Sheinman and Rosen (1992), Rosen and Sheinman (1994), Rosen and Sheinman (1996), Frandsen et al. (2000), Kaiser et al. (2003), Langreder et al. (2004), Pedersen (2004), van Radecke (2004), Eecen et al. (2006), Gottschall et al. (2006), Sumner and Masson (2006), Albers et al. (2007), Gottschall and Peinke (2007), Kaiser et al. (2007), Anahua et al. (2008), Gottschall and Peinke (2008), Tindal et al. (2008), Albers (2009), Wagner et al. (2011), Wagner et al. (2009), Wächter et al. (2011), Wharton and Lundquist (2012a), Wharton and Lundquist (2012b), Rauh and Peinke (2004), and references therein. The mean power as a function of the mean wind speed is called the *power curve*.

The contribution of this paper is a new method for power curve estimation that is able to account for some of the influence of turbulence intensity (i.e., the ratio of the standard deviation of the wind speed to the mean wind speed). The method is parsimonious in the sense that only a single function (the *zero-turbulence power curve*) and an auxiliary parameter (the *equivalent turbulence factor*) need to be estimated. The method requires only ten minute means and standard deviations of the wind speed and the turbine power but can benefit from data sampled at a higher rate. The method is orthogonal to the methods of shear correction presented in Wagner et al. (2009, 2011) in the sense that the latter method can be used as a preprocessing step to the method of this paper. The new method is similar in spirit to that of Albers (2009) and Albers et al. (2007) but the optimization problem is different and the conceptual differences between the upstream wind, the virtual wind, and the driving wind (Christensen and Dragt, 1986) (see below) are handled explicitly through a single auxiliary parameter. This parameter also serves to take into account some consequences of the dynamic response of the turbine described in Rosen and Sheinman (1996), Rosen and Sheinman (1994), Sheinman and Rosen (1992), and Rauh and Peinke (2004).

The paper is organized as follows. Section C.2 elaborates on the concepts of upstream, virtual, and driving wind and summarizes various attempts at

FIGURE C.1. An informal sketch of the concepts of upstream wind u, virtual wind v, and driving wind w. The upstream wind is not disturbed by the wind turbine. The virtual wind is the fictive wind field at the location of the wind turbine if the wind turbine was not there to disturb the wind field. The driving wind is the fictive wind field that is completely homogeneous across the rotor and causes the same power production as the virtual wind field.

eliminating the influence of turbulence on the estimation of the power curve. In sec. C.3 the measured data are presented. In sec. C.4 the modeling framework is introduced and analyzed. The implementation details are given in appendix C.A. In sec. C.5 the new method is applied to various situations and the results are discussed. Section C.6 indicates some further applications and directions for future work. Section C.7 concludes.

C.2 BACKGROUND

C.2.1 UPSTREAM, VIRTUAL, AND DRIVING WIND

Since the wind turbine disturbs the flow, any wind speed measured at the location of the turbine cannot be used as a reference wind in a power curve measurement. To acknowledge this, Christensen and Dragt (1986) introduces three useful wind fields: the upstream wind u, the virtual wind v, and the driving wind w. See fig. C.1 for an informal sketch. The *virtual wind* v is defined to be the fictive wind field at the location of the wind turbine as it would be if the wind turbine was not there to disturb the flow. The virtual wind therefore defines the wind energy resource at the location of the wind turbine.

Suitably far upstream of the wind turbine (assuming that it is not in the wake of another wind turbine) the influence of the wind turbine is negligible. The wind field here is called the *upstream wind* u. In the setting of this paper, only ten minute means and standard deviations of the upstream wind are measured by cup anemometers at hub height and at the lowest tip height. It will therefore be assumed that the mean and standard deviation of the virtual wind speed at a given height are equal to those of the upstream wind speed at the same height. The measurement of the upstream wind is itself subject to the atmospheric conditions, see e.g. Albers and Klug (2001) and Albers et al. (2000).

The virtual wind is not homogeneous over the rotor. It is therefore useful to introduce the *driving wind* w as the fictive wind field that is completely

homogeneous across the rotor and causes the same power production as the virtual wind. Since the driving wind is homogeneous, it is at each point in time determined by a single value which will also be called the driving wind. While the driving wind is often not mentioned explicitly, it is used implicitly whenever the wind turbine power is considered as a function of a single wind speed. In the IEC 61400-12-1 standard the mean driving wind is implicitly taken to be the hub height upstream mean wind speed.

One application of the three concepts is to account for the effect of vertical shear on the mean power. In Elliott and Cadogan (1990), the mean driving wind speed is represented as the spatial average of the mean virtual wind speed over the rotor disk. The mean virtual wind speed at a given height is in turn taken to be the mean upstream wind speed at the same height. Alternatively, in Wagner et al. (2011) the mean driving wind speed (termed *equivalent wind speed* in the reference) is based on the total kinetic energy flux through the rotor. Other representations are possible, see e.g. Wagner et al. (2009). In all cases it is demonstrated that the dispersion of the mean power at a given mean driving wind speed is less than the dispersion of the mean power at a given mean hub height upstream wind speed.

For any time-dependent quantity $x(t)$, the capital letter X denotes the time-wise average $\langle x \rangle = \frac{1}{T}\int_0^T x(s)\,ds$, where T denotes the length of the time interval, e.g. ten minutes. The standard deviation σ_x of $x(t)$ is defined by $\sigma_x^2 = \langle x^2 \rangle - \langle x \rangle^2$. Thus, U, V, W denote the mean upstream, virtual, and driving wind speeds; σ_u, σ_v, σ_w denote the corresponding standard deviations; and $I_u = \sigma_u/U$, $I_v = \sigma_v/V$, $I_w = \sigma_w/W$ denote the corresponding turbulence intensities. Similarly, p, P, σ_p denote the instantaneous power, the mean power, and the standard deviation of power. The upstream wind will henceforth refer to the measured wind speed at hub height at the meteorology mast, not the whole upstream wind field. The descriptions of the models below are cast in the language of driving wind, but in the cited references it is implicitly assumed that the driving wind is equal to the upstream wind, i.e., $W = U$, $\sigma_w = \sigma_u$, and $I_w = I_u$.

C.2.2 THE STATIC MODEL

The simplest model for the production of power as a function of the driving wind is the *static* model (Rosen and Sheinman, 1994). It assumes that the instantaneous power $p_s(t)$ at time t is a function of only the mean driving wind speed, i.e., $p_s(t) = f_s(W)$. Therefore, the mean power P_s is also a function of only the mean driving wind speed, $P_s = f_s(W)$. The function $f_s(W)$ is the *power curve* and can be estimated by the *method of binning* as described in the IEC 61400-12-1 standard. Hence the IEC 61400-12-1 standard essentially assumes a static model which cannot take into account the turbulent nature of the wind. In Sumner and Masson (2006) and Tindal et al. (2008), it is suggested that the turbulence intensity should be accounted for by stratifying the measured data by turbulence intensity. This increases the amount of data to be gathered, since for each turbulence intensity bin, enough data has to be gathered to satisfy the requirements of the IEC 61400-12-1 standard. In par-

ticular, the time required to complete a power curve measurement campaign can be expected to increase.

C.2.3 THE QUASI STATIC MODEL

A generalization of the static model is the *quasi static* model considered in Christensen and Dragt (1986), Rosen and Sheinman (1996), Rosen and Sheinman (1994), Sheinman and Rosen (1992), Albers (2009), and Albers et al. (2007). It assumes that the instantaneous power $p_{\mathrm{qs}}(t)$ at time t is a function of the instantaneous driving wind $w(t)$ alone,

$$p_{\mathrm{qs}}(t) = f_{\mathrm{qs}}(w(t)).$$

A second order Taylor expansion of f_{qs} around the mean driving wind speed W yields

$$p_{\mathrm{qs}}(t) \approx f_{\mathrm{qs}}(W) + f'_{\mathrm{qs}}(W)(w(t)-W) + \tfrac{1}{2} f''_{\mathrm{qs}}(W)(w(t)-W)^2. \tag{C.1}$$

The mean power is then

$$P_{\mathrm{qs}} = f_{\mathrm{qs}}(W) + \tfrac{1}{2} f''_{\mathrm{qs}}(W)\sigma_w^2 = f_{\mathrm{qs}}(W)(1 + 3I_w^2\delta(W)) \tag{C.2}$$

where $\delta(W) = 1 + WC'_P(W)/C_P(W) + \frac{1}{6}W^2C''_P(W)/C_P(W)$ as shown in Christensen and Dragt (1986), and C_P denotes the power coefficient. If the turbulence intensity I_w is zero, then $P_{\mathrm{qs}} = f_{\mathrm{qs}}(W)$, and so f_{qs} can be interpreted as the *zero-turbulence power curve*. Equation (C.2) can be used to qualitatively explain the observation that mean power tends to increase with increasing turbulence intensity at low wind speeds where the power curve is approximately convex ($f''_{\mathrm{qs}}(W)$ is positive), and that the mean power tends to decrease around rated power where the power curve is approximately concave ($f''_{\mathrm{qs}}(W)$ is negative). See e.g. Christensen and Dragt (1986), Albers (2009), and Albers et al. (2007).

Equation (C.2) has been used as an inspiration to incorporate turbulence intensity into the power curve estimation. Firstly, in Kaiser et al. (2007), Langreder et al. (2004), Kaiser et al. (2003), and van Radecke (2004), data sets consisting of W, σ_w, P are partitioned into bins by W. For each bin the regression coefficients P_{o} and ζ are estimated from $P = P_{\mathrm{o}} + \zeta\sigma_w^2$. Now P_{o} as a function of W is the zero-turbulence power curve, and ζ as a function of W determines the influence of turbulence intensity. Somewhat related, Frandsen et al. (2000) and Eecen et al. (2006) consider the mean power for each mean wind speed bin as a linear combination of several parameters π_i (including turbulence intensity, shear, flow inclination, wind direction), $P = P_{\mathrm{o}} + \sum_i \zeta_i\pi_i$, and estimate for each wind speed bin the coefficients P_{o} and $\pi_1, \pi_2, \ldots$ by regression. In both cases the method requires a sufficient amount of data in each mean wind speed bin.

Secondly, the relation $P = \frac{1}{2}\rho A W^3 C_P(W)$ defining the power coefficient, where ρ is the air density and A the rotor area, suggests the use of a corrected mean wind speed $W_{\mathrm{c}} = W(1 + 3I_w^2\delta(W))^{1/3}$, so the power curve is the mean power as a function of the corrected mean wind speed W_{c}. However, the correction is useless since knowledge of the function δ is equivalent to knowledge of the power curve itself. As noted in Christensen and Dragt (1986), the sim-

plifying assumption that $\delta \approx 1$ is unrealistically crude and should not be used to allow for the simpler correction $W_c = W(1 + 3I_w^2)^{1/3}$.

Finally, one of the two methods presented in Albers (2009) and Albers et al. (2007) considers the mean powers $P_{qs}(I_1)$ and $P_{qs}(I_2)$ at the two turbulence intensities I_1 and I_2 with the common mean wind speed W. From (C.2) it follows that $P_{qs}(I_2) = P_{qs}(I_1) + \frac{1}{2} f''_{qs}(W)(I_2^2 - I_1^2)$. So given f_{qs} it is possible to transform (*renormalize* in the words of the references) the mean power from one turbulence intensity to another. From this a recursive scheme is suggested to estimate f_{qs}. While it is not proved that the scheme converges to the desired result, it is noted in the references that convergence is obtained after just one iteration. Moreover, is it also demonstrated that the method only works well when the source and target turbulence intensities are not too far apart. In general, any correction for turbulence intensity based on (C.1) and (C.2) is likely to fail for high turbulence intensities, since high turbulence intensity implies large excursions of $w(t)$ away from the mean W and hence the second order Taylor approximation is unlikely to be valid, especially near the region of transition to rated power.

In Albers (2009) and Albers et al. (2007), the quasi static model is used to derive another method of incorporating the turbulence intensity into the power curve estimation. That method does not suffer from the same drawbacks as the approaches based on the second order Taylor expansion. By calculating the timewise average directly, one obtains

$$P_{qs} = \langle p_{qs}(t) \rangle = \frac{1}{T} \int_0^T f_{qs}(w(t))\, dt = \int_0^\infty f_{qs}(x)\phi_w(x)\, dx \tag{C.3}$$

where ϕ_w denotes the probability density function of the driving wind speeds $w(t)$ in the time interval under consideration. In the case where the driving wind speed is constant and equal to its mean, (C.3) reduces to $P_{qs} = f_{qs}(W)$ which reconfirms the interpretation of f_{qs} as the zero-turbulence power curve. When only ten minute means and standard deviations are available, ϕ_w cannot be known exactly and some model for the distribution of driving wind speeds must be employed. The *Normal Distribution Model* is obtained in the cited references by assuming that the driving wind speeds follow a normal distribution which is completely determined by its mean and standard deviation.

Given a zero-turbulence power curve, (C.3) provides an explicit expression for the mean power as a function of the wind speed statistics and therefore the power curve at any desirable turbulence intensity. To obtain a power curve at a given turbulence intensity, the cited references suggest a correction of the measured mean power based on (C.3) followed by the method of binning. In order to estimate the zero-turbulence power curve, these references suggest various possible methods, including a recursive scheme based on corrections of the measured mean power and one based on minimization of the total absolute errors,

$$\sum_{i=1}^{n} \left| \frac{1}{T} \int_0^\infty f(x)\phi_i(x)\, dx - P_{i,\text{meas}} \right|,$$

where $P_{i,\text{meas}}$ is the i'th measured mean power and ϕ_i is the probability den-

sity function of the corresponding i'th driving wind speed distribution. In Albers (2009) it is noted that this optimization problem is "complicated" but that it can be solved using a "Newton solver". However, it is not stated wherein the complexity lies nor how the Newton solver should be implemented. It will be shown in this paper, that by considering the total squared error instead of the total absolute error, the optimization problem can be solved efficiently using numerical linear algebra and an implementation is outlined in appendix C.A. Furthermore, it will also be shown that the turbulence intensity I_w of the driving wind should be smaller than the measured turbulence intensity I_u of the upstream wind.

C.2.4 THE CORRECTED, QUASI STATIC MODEL

The quasi static model is by construction incapable of taking the dynamic response of the wind turbine to the wind into account. Sheinman and Rosen (1992), Rosen and Sheinman (1994), and Rosen and Sheinman (1996) address this and introduce the important concept of *modified turbulence intensity*. It is shown that for wind speed fluctuations of low frequency, the quasi static model is realistic, but as the frequency increases, the dynamic response of the wind turbine becomes significant. Under this corrected model, the mean power P_c is $P_c = f_{qs}(W)(1 + 3I_{w,1}^2\delta(W))$ where f_{qs} is the zero-turbulence power curve and $I_{w,1}$ is a modification of the turbulence intensity I_w defined in terms of the spectral density function S_w of the wind and a function G_1 determining the dynamic response of the wind turbine at the mean wind speed W. Sheinman and Rosen (1992), Rosen and Sheinman (1994), and Rosen and Sheinman (1996) demonstrate that the corrected model is more capable of explaining the influence of turbulence in the power production than the quasi static model. Unfortunately, determination of the function G_1 requires detailed knowledge on the wind turbine which an independent third party cannot be expected to have when performing power curve estimation. Hence this method is not generally feasible for power curve estimation. Nevertheless, it is an important observation that the turbulence intensity should be modified to take into account the dynamic response of the wind turbine.

C.2.5 THE DYNAMIC MODEL

Another model for the dynamic response of the wind turbine is the stochastic differential equation (here the Langevin equation)

$$dp_{dyn}(t) = -\beta_1(t)\Big(p_{dyn}(t) - f_{dyn}(w(t))\Big)\,dt + \beta_2(t)\,dB(t), \tag{C.4}$$

as studied in Gottschall et al. (2006), Gottschall and Peinke (2007), Anahua et al. (2008), Gottschall and Peinke (2008) and Wächter et al. (2011). The first term is the *relaxation term* stating that the power $p_{dyn}(t)$ will tend towards $f_{dyn}(w(t))$. The factor $\beta_1(t)$ determines the speed of the change in that $1/\beta_1(t)$ can be interpreted as a response time. The second term is the *noise term* and models the random noise in the system, B is a standard Wiener process (Brownian motion), and the factor $\beta_2(t)$ determines the strength of the

noise. If the wind speed $w(t)$ is constant and equal to its mean W, and if there is no noise, i.e., $\beta_2 = 0$, then the power will tend exponentially fast to $f_{\text{dyn}}(W)$. Hence the function f_{dyn} can be interpreted as the zero-turbulence power curve. The cited references consider the estimation of the function f_{dyn} from simultaneous, high-frequency measurements of wind and power. This is not possible in the setting of this paper since only ten minute statistics are available.

C.3 MEASUREMENTS

The data set used in the analysis consists of ten minute statistics from an onshore wind turbine and accompanying meteorology mast. For reasons of confidentiality, the exact details of the wind turbine cannot be given here. The wind turbine is a horizontal axis, actively pitched, multi-megawatt wind turbine. The wind and power data have been scaled so that all wind speeds and powers are dimensionless and between 0 and 1. Therefore the scales on the figures are all dimensionless unless explicitly stated otherwise. This is of no consequence for the conclusions.

The onshore wind turbine is located in flat terrain. The meteorology mast is located 2.5 rotor diameters away from the wind turbine, thus complying with the IEC 61400-12-1 standard. Cup anemometers are mounted at hub height and at the lowest tip height. The data have been filtered to include only ten minute events where the following criteria are satisfied: The mean angle[1] between the wind direction and the line-of-sight between the wind turbine and the meteorology mast was less than 30°; the wind turbine operated without any errors; the wind turbine was connected to the grid; no power reduction was active. Furthermore, to reduce the influence of vertical shear of the wind profile as much as possible, data is retained only from periods where the shear is low and the turbulence intensity in general is high. Finally, the shear exponent α is estimated according to the power law

$$\frac{U_{\text{hub}}}{U_{\text{lowest tip}}} = \left(\frac{z_{\text{hub}}}{z_{\text{lowest tip}}}\right)^{\alpha}, \tag{C.5}$$

and only data with $0 \leq \alpha \leq 0.1$ is retained. Here U_{hub} and $U_{\text{lowest tip}}$ denote the mean upstream wind speeds at hub height z_{hub} and at the lowest tip height $z_{\text{lowest tip}}$, respectively. The filtered data set contains 2827 records.

The mean upstream wind speed U is corrected for air density according to the IEC 61400-12-1 standard, $U = U_{\text{meas}}(\rho_{\text{meas}}/\rho_0)^{1/3}$ where the measured air density ρ_{meas} is calculated from measured pressure and temperature at the meteorology mast, the hub height, and the terrain elevation above sea level; and where $\rho_0 = 1.225\,\text{kg/m}^3$ is the reference air density. To leave the turbulence intensity invariant under the correction for air density, the standard deviation of upstream wind speeds is corrected in a similar manner: $\sigma_u = \sigma_{u,\text{meas}}(\rho_{\text{meas}}/\rho_0)^{1/3}$. This is in agreement with Albers (2009).

1 · Here the mean angle is the arithmetic average of K sampled directions d_k during ten minutes, $\sum_k d_k/K$, not the directional average defined by the average wind direction, $(\sum_k \cos d_k/K, \sum_k \sin d_k/K)$, as would be more appropriate. However, the wind directions relevant to the analysis are not close to 0°, so the error of using the arithmetic average is not large.

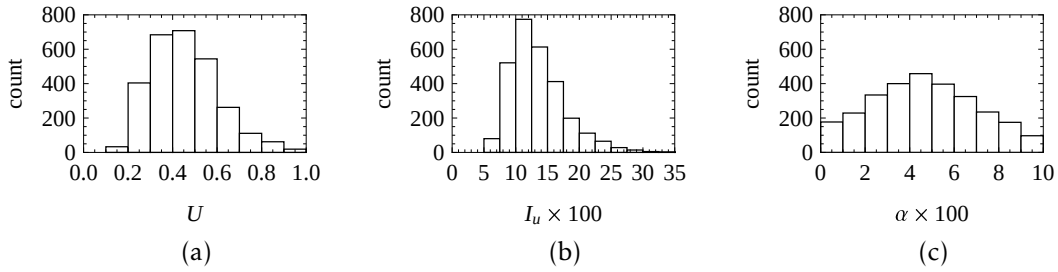

FIGURE C.2. Distributions of (a) mean upstream wind speed U, (b) upstream turbulence intensity I_u, and (c) shear exponent α.

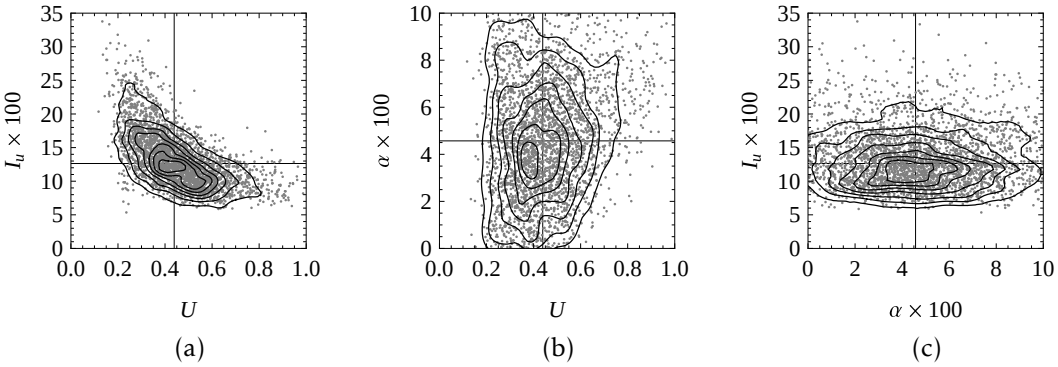

FIGURE C.3. Level curves (solid) of the joint probability density functions of (a) mean upstream wind speed U and upstream turbulence intensity I_u; (b) mean upstream wind speed U and shear exponent α; and (c) shear exponent α and upstream turbulence intensity I_u. The gray dots denote the individual data points. The thin, black lines mark the medians of the marginal distributions.

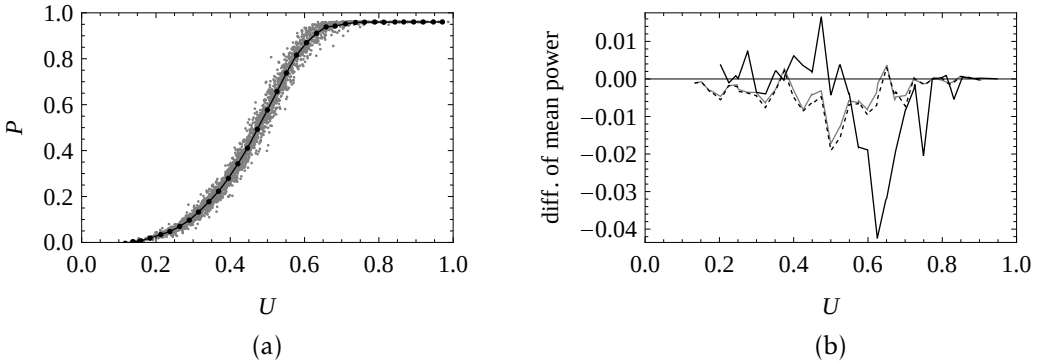

FIGURE C.4. (a) Mean power P as a function of mean upstream wind speeds U. Gray dots denote the 2827 data points of the filtered data set. The black curve denotes the IEC 61400-12-1 power curve. (b) Solid and dashed curves denote the differences $P_{I_2} - P_{I_1}$ and $P_{\alpha_2} - P_{\alpha_1}$, respectively. The gray curve denotes the difference $P_{\alpha_2} - P_{\alpha_1}$ in the case where the mean upstream wind speed U has been shear-corrected according to Wagner et al. (2011).

Figure C.2 shows histograms of mean upstream wind speed U, upstream turbulence intensity I_u, and shear exponent α for the filtered data set. Rated power is attained near $U = 0.65$, and the data set covers the whole relevant wind speed range. The turbulence intensity is in general high with a median equal to 0.126. The shear exponent is low by construction and approximately evenly distributed around the median at 0.046. Figure C.3 shows the simultaneous distribution of combinations of the three ten-minute statistics from fig. C.2. In the filtered data set, the correlation coefficient between the mean anemometer wind speed U and the shear exponent α is low (0.17), and likewise the correlation coefficient between the turbulence intensity I_u and the shear exponent α is also low (0.024). Figure C.4 (a) shows the IEC power curve for the filtered data set. To demonstrate the influence of turbulence intensity and of shear on the mean power, four subsets of the filtered data set are formed: I_1 and I_2 where the turbulence intensity less than and greater than the median turbulence intensity (0.126), respectively; and α_1 and α_2 where the shear exponent less than and greater than the median shear exponent (0.046), respectively. For each data set the corresponding IEC power curve (denoted by P_{I_1}, P_{I_2}, P_{α_1}, and P_{α_2}, respectively) is calculated and the differences $P_{I_2} - P_{I_1}$ and $P_{\alpha_2} - P_{\alpha_1}$ are plotted in fig. C.4 (b). Evidently, the mean power depends on both turbulence intensity and shear exponent, in particular in the regions around $U \approx 0.65$ and $U \approx 0.50$. However, the turbulence intensity has the dominant effect in the region around $U \approx 0.65$.

While the shear exponent in the filtered data set is low by construction, one may consider the correction of mean wind speed as proposed in Wagner et al. (2011) in the case of a vertical wind profile following the power law (C.5). The gray curve in fig. C.4 (b) shows the difference $P_{\alpha_2} - P_{\alpha_1}$ after the shear correction has been performed. It is observed that the shear correction provides only a slight decrease in the difference between the two power curves. A likely explanation for the small reduction is that the shear correction is based on only two measurements (at hub height and lowest tip height) over the lower half of the rotor disk, wherefore the vertical wind profile is poorly resolved. In the rest of this paper, no correction for shear is performed. It must be emphasized, however, that the methods presented in this paper can be applied to shear corrected data as well.

C.4 MODEL AND METHOD

In this section, a method is derived to estimate the zero-turbulence power curve from ten minute statistics of wind and power. In subsec. C.4.1, the method is derived given distributions of the driving wind and ten minute statistics of power. In order to bridge the gap between the measured upstream wind and the driving wind used in the quasi static model, a simple model is in subsec. C.4.2 employed to indicate how the statistics of the driving wind can be represented in terms of the upstream wind. Since the quasi static model does not include the wind turbine's dynamic response, another simple model is employed in subsec. C.4.3 to indicate how to compensate for this on the level of ten minute statistics. Finally, subsec. C.4.4 connects the results of the

three preceeding subsections and describes the new method. The concept of modified turbulence intensity (see subsec. C.2.4) is implicit in the modeling of the driving wind in terms of the upstream wind.

C.4.1 THE QUASI STATIC MODEL REVISITED

Recall that under the quasi static model, the instantaneous power $p(t)$ at time t is given by $p(t) = f(w(t))$ where $w(t)$ denotes the instantaneous driving wind speed at time t and f denotes the zero-turbulence power curve. The mean power during some time interval of length T is now

$$P = \langle p \rangle = \frac{1}{T}\int_0^T p(t)\,dt = \frac{1}{T}\int_0^T f(w(t))\,dt = \int_0^\infty \phi(x) f(x)\,dx$$

where ϕ denotes the probability density function of the driving wind speeds during the time interval under consideration. Given a data set $\{(\phi_i, P_i, \sigma_{p,i}) \mid i = 1,\ldots,N\}$ of distributions of driving wind speeds and corresponding means and standard deviations of power, the problem to solve is

$$\text{find} \quad f \quad \text{such that} \quad \int_0^\infty f(x)\phi_i(x)\,dx = P_i \quad \text{for all} \quad i = 1,\ldots,N. \tag{C.6}$$

This problem is *ill-posed*: a solution may not exist, if a solution exists it may not be unique, and small changes to the input data may cause large changes in the solution. The last part is especially important since the $P_1,\ldots,P_N$ are measurements to which some error will always be connected, since the distribution of the fictive driving wind speeds must be modeled in terms of other measurements, and since the quasi static model is a very simplified model of the wind turbine. Therefore, some kind of robustness to errors and misspecifications must be introduced. Informally, the problem (C.6) has the structure of a Fredholm equation of the first kind, though the variable i is discrete instead of continuous as in e.g. the formulation in Tikhonov (1963b). Tikhonov regularization (Tikhonov, 1963a,b) will be employed to solve (C.6). Consider the *smoothing functional*

$$S(f,\theta) = \mathrm{MSE}_P(f) + \theta R(f) \tag{C.7}$$

where

$$\mathrm{MSE}_P(f) = \frac{1}{N}\sum_{i=1}^{N}\left(\int_0^\infty f(x)\phi_i(x)\,dx - P_i\right)^2$$

is the *mean squared error functional*;

$$R(f) = \sum_{j=1}^{J}\int_0^\infty K_j(x)\left(\frac{d^j f}{dx^j}(x)\right)^2 dx$$

is the *regularizing functional* with non-negative weight functions K_j; and $\theta \geq 0$ is the *regularization weight*, a parameter which determines the importance of the regularizing functional in (C.7). The regularized problem to solve is

$$\text{minimize} \quad S(f,\theta) \quad \text{with respect to} \quad f. \tag{C.8}$$

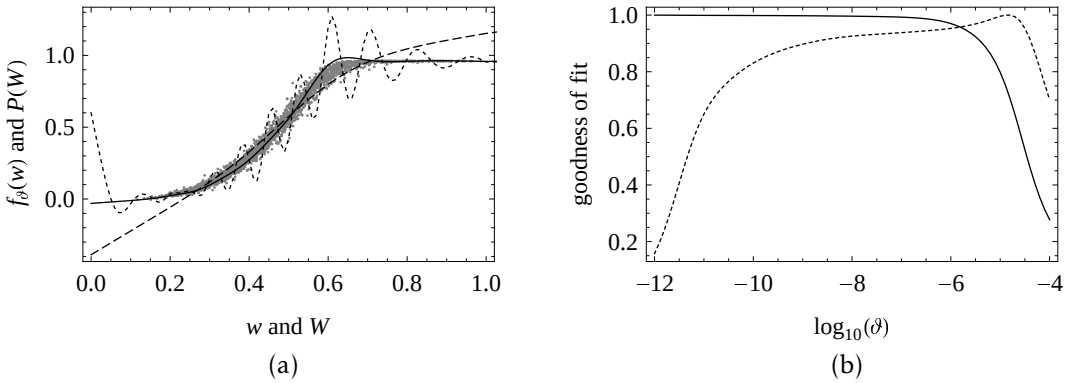

FIGURE C.5. (a) The black curves show the solution f_θ to (C.8) as a function of the instantaneous driving wind speed w for $\theta = 10^{-12}$ (short dashes), $\theta = 10^{-8}$ (solid), and $\theta = 10^{-4}$ (long dashes). The gray dots show the measured mean power P as a function of the mean driving wind speed W. (b) The proxies for the goodness of fits, $\mathrm{GOF}_P(f_\theta)$ (solid) and $\mathrm{GOF}_{\sigma_P}(f_\theta)$ (dashed), as a function of $\log_{10}(\theta)$.

If $\theta = 0$, the ill-posed problem (C.6) is obtained. If the regularization is not employed, solutions to (C.6) or (C.8) will exhibit the same irregular, undesirable behaviour as illustrated in e.g. Phillips (1962). The specification of the regularizing functional determines the character of the solution f to (C.8) by penalizing undesirable behaviour of f. Therefore the regularizing functional should be specified according to the problem under consideration. In the context of power curves, and assuming that the zero-turbulence power curve will resemble the conventional power curve, it is not reasonable to penalize large values of f, since the value of f at high wind speeds is expected to be much greater than the value of f at low wind speeds. Likewise, large values of the first derivative f' should not be penalized either, since the first derivative is expected to be large below rated power compared to at rated power. The following regularizing functional will be employed through the rest of the present paper,

$$R(f) = \int_0^\infty \big(f''(x)\big)^2 \, dx. \tag{C.9}$$

It penalizes large values of the second derivative f'', i.e., essentially the curvature of the zero-turbulence power curve. In other words, it favours solutions that locally are approximately linear. One may argue that the regularizing functional should not penalize zero-turbulence power curves with non-zero curvature near the cut-in wind speed and near the wind speed where rated power is attained. The regularizing functional in (C.9) was chosen for its simplicity. The study of more sophisticated regularizing functionals is left for future work. It is shown in appendix C.A how (C.8) for fixed θ may be solved efficiently by the methods of numerical linear algebra.

The above discussion does not specify how to choose the regularization weight θ appropriately. Consider the data set from sec. C.3 and assume for now that the driving wind speeds are normally distributed with means and standard deviations equal to those of the upstream wind speeds. Let f_θ denote the solution to (C.8) for a given value of θ. Figure C.5 (a) shows how the solution f_θ depends on θ (it has appeared to be natural to consider the regular-

izing weight θ on a logarithmic scale). At $\theta = 10^{-12}$, the solution shows large oscillations. At $\theta = 10^{-4}$, the solution does not deviate much from a straight line. In between, at $\theta = 10^{-8}$, the solution is both regular and, informally, shaped like a conventional power curve. The unregularized solution f_0 is not shown as it attains values that are several orders of magnitude greater than the rated power. A measure of the *goodness of fit of mean power* of a solution f_θ is the ratio

$$\mathrm{GOF}_P(f_\theta) = \frac{\min\{\mathrm{MSE}_P(f_{\theta^*}) \mid 0 \le \theta^*\}}{\mathrm{MSE}_P(f_\theta)}.$$

A goodness of fit close to 1 implies that the mean squared error of the mean power is close to the optimum which is attained for the unregularized solution. Likewise, a measure of the *goodness of fit of the standard deviation of power* of a solution f_θ is the ratio

$$\mathrm{GOF}_{\sigma_p}(f_\theta) = \frac{\min\{\mathrm{MSE}_{\sigma_p}(f_{\theta^*}) \mid 0 \le \theta^*\}}{\mathrm{MSE}_{\sigma_p}(f_\theta)},$$

where

$$\mathrm{MSE}_{\sigma_p}(f) = \frac{1}{N}\sum_{i=1}^{N}\left(\sqrt{\int_0^\infty f(x)^2\phi_i(x)\,dx - \left(\int_0^\infty f(x)\phi_i(x)\,dx\right)^2} - \sigma_{p,i}\right)^2$$

is the mean squared error of standard deviation of power. As proxies for the goodness of fits, the range $0 \le \theta^*$ is in this subsection replaced by $10^{-12} \le \theta^* \le 10^{-4}$. The case $\theta^* = 0$ is not included due to the ill-posedness of (C.8) in the non-regularized case. The use of proxies does not pose a problem to the applicability of the method.

Figure C.5 (b) shows how (the proxies for) $\mathrm{GOF}_P(f_\theta)$ and $\mathrm{GOF}_{\sigma_p}(f_\theta)$ depend on θ. As θ increases, $\mathrm{GOF}_P(f_\theta)$ decreases first very slowly and then around $\theta = 10^{-6}$ starts to decrease very quickly. Therefore, a near optimal goodness of fit of the mean power is attainable in a wide range of values of θ. At $\theta = 10^{-8}$ the goodness of fit of the mean power is 0.996. The goodness of fit of the standard deviation of power is low for the smallest and largest values of θ while somewhat constant for intermediate values of θ around 10^{-8}. The behaviour of $\mathrm{GOF}_{\sigma_p}(f_\theta)$ can be explained. At small values of θ, the solution f_θ possesses large oscillations, i.e., $f_\theta(w)$ will cover a wide range of values even for small variations in w. Therefore, the standard deviation of power will in general tend to be overestimated when θ is too small. Similar arguments can be applied when θ is too large. In both cases, the mean squared error of the standard deviation of power will be large, and hence the goodness of fit will be low. This motivates the use of $\mathrm{GOF}_{\sigma_p}(f_\theta)$ to help determine an appropriate value of θ.

Finally, it should be noted that the use of a mean squared error functional makes the optimization problem sensitive to outliers compared to the use of a mean absolute error functional. However, this problem can easily be avoided through an iterative approach like in robust regression. Outliers have not been found to pose a problem in the analysis in this paper.

C.4.2 THE UPSTREAM, VIRTUAL, AND DRIVING WIND REVISITED

While the fictive driving wind is a convenient concept, it must be represented in terms of the upstream wind, since only the upstream wind can be measured. The present subsection elaborates on a very simple model of the driving wind in order to indicate how the driving wind on the level of statistical quantities can be represented in terms of the upstream wind. It must be emphasized that this simple model is not intended to provide an exact specification of this representation.

Recall that the virtual wind field is the fictive wind field at the location of the wind turbine if the wind turbine was not there to disturb the wind. Assume that only the longitudinal velocity component is relevant and let u and v denote the longitudinal component of the upstream and virtual wind fields, respectively. Assume that the statistics (means, correlations, etc.) of the virtual wind field are the same as those of the upstream wind field. Assume that the upstream wind field is stationary and isotropic, and assume that its correlation structure is that of von Kármán[2]. The transversal correlation function is then given by

$$\rho_{\text{trans}}(r) = \rho\left(\frac{r}{L}\gamma\right) \quad \text{where} \quad \rho(x) = \frac{2^{2/3}x^{1/3}}{\Gamma(1/3)}\left(K_{1/3}(x) - \frac{x}{2}K_{2/3}(x)\right),$$

where $\gamma = \sqrt{\pi}\,\Gamma(5/6)/\Gamma(1/3) \approx 0.747$, K_ν is the modified Bessel function of the second kind with index ν, and where L denotes the (longitudinal) integral length[3]. The driving wind speed w is the common wind speed of a wind field that is completely homogeneous across the rotor disk and that yields the same power production as the virtual wind field. Inspired by Elliott and Cadogan (1990), the following rotor disk average of the virtual wind is used as a model for the driving wind speed,

$$w = \frac{1}{\pi R^2}\int_{\text{rotor}} v(\vec{r})\,d\vec{r}, \tag{C.10}$$

where R denotes the rotor radius. A less idealized model would be to consider the average kinetic energy flux like in Wagner et al. (2011). While the conclusion is essentially the same, the calculations are more involved, so only the model in (C.10) will be considered here. It can now be shown that the mean driving wind speed W is equal to the mean upstream wind speed U, and that the standard deviation σ_w of the driving wind is given by

$$\sigma_w = k'\sigma_u \quad \text{where} \quad k' = \sqrt{\frac{16}{\pi}\int_0^1 \kappa(s)\rho\left(\frac{R}{L}2\gamma s\right)ds} \tag{C.11}$$

and where $\kappa(s) = s\arccos(s) - s^2\sqrt{1-s^2}$. The factor k' in (C.11) depends under the simple model only on the ratio R/L of the rotor radius R and the integral length L.

Figure C.6 (a) shows the factor k' as a function of the ratio R/L. When the

2 · The von Kármán correlation structure corresponds to a spectral density of the longitudinal velocity component given by $S(\omega) = 2L\sigma_u^2(1+70.7\cdot L^2\omega^2)^{-5/6}$.

3 · The longitudinal integral length is defined as $L = \int_0^\infty \rho_{\text{long}}(r)\,dr$ where ρ_{long} is the longitudinal autocorrelation function.

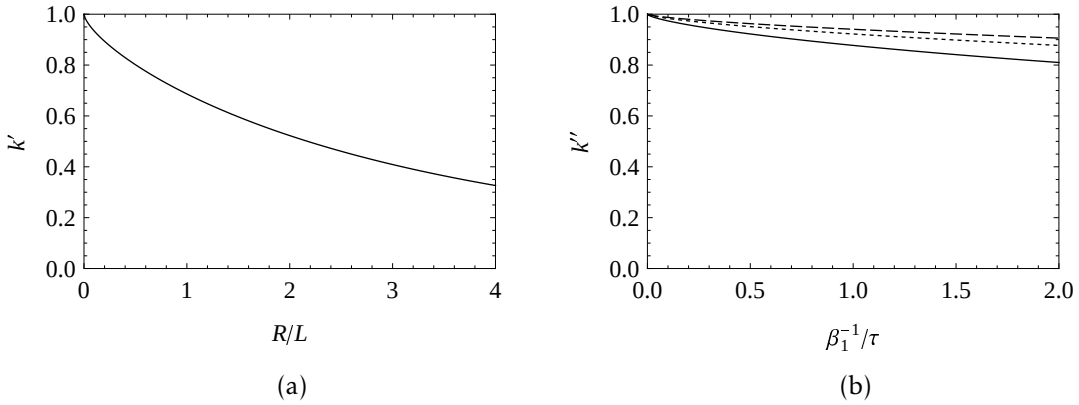

FIGURE C.6. (a) The factor k' in (C.11) as a function of the ratio R/L of the rotor radius R to the integral length L. (b) The factor k'' in (C.15) as a function of the ratio β_1^{-1}/τ of the characteristic response time β_1^{-1} to the integral time τ for mean driving wind speeds $W = 5\,\mathrm{m/s}$ (solid), $W = 10\,\mathrm{m/s}$ (short dashes), and $W = 15\,\mathrm{m/s}$ (long dashes).

size of the rotor is comparable to the integral length, which is the case for modern wind turbines, the factor k' is significantly smaller than 1. This implies that a one-point measurement of the standard deviation of the upstream wind speed must be appropriately scaled down to represent the standard deviation of the driving wind speed. Scaling by the exact factor k' in (C.11) is of course only true under the highly idealized model considered in this subsection. Nevertheless, the model does indicate the necessity of transforming the measured upstream wind speed, if the standard deviation (or the turbulence intensity) of the wind is to be incorporated into the power curve estimation.

C.4.3 THE DYNAMIC MODEL REVISITED

While the quasi static model provides a way of estimating the zero-turbulence power curve, it has the undesirable property that it ignores the dynamic behavior of the wind turbine. Consider therefore the following dynamic model for the power $p(t)$ defined in terms of a stochastic differential equation (the Langevin equation),

$$dp_{\mathrm{dyn}}(t) = -\beta_1(p_{\mathrm{dyn}}(t) - f(w(t)))\,dt + \beta_2\,dB(t). \tag{C.12}$$

Here $1/\beta_1$ (the characteristic response time) and β_2 (the noise strength) are constants, f (the zero-turbulence power curve) is a deterministic function, w is the driving wind, and B is a standard Brownian motion independent of the driving wind. In the limit $\beta_1 \to \infty$, the quasi static model is obtained. The model in (C.12) is an idealized version of the model in (C.4) in the sense that the coefficients β_1 and β_2 are here assumed to be constant. Equation (C.12) with initial condition $p_{\mathrm{dyn}}(0) = p_0$ has the solution

$$p_{\mathrm{dyn}}(t) = p_0 e^{-\beta_1 t} + \int_0^t \beta_1 e^{-\beta_1(t-s)} f(w(s))\,ds + \frac{\beta_2}{\beta_1}\int_0^t \beta_1 e^{-\beta_1(t-s)}\,dB(s).$$

The influence of the initial value p_0 decreases exponentially fast, so when $t \gg 1/\beta_1$, then $p_0 e^{-\beta_1 t} \approx 0$. By similar reasoning, extending the lower integration limit to $-\infty$ constitutes a negligible change. Hence the solution can be

approximated by

$$p_{\mathrm{dyn}}(t) = \int_{-\infty}^{t} \beta_1 e^{-\beta_1(t-s)} f(w(s))\,ds + \frac{\beta_2}{\beta_1} \int_{-\infty}^{t} \beta_1 e^{-\beta_1(t-s)}\,dB(s). \qquad \text{(C.13)}$$

If the driving wind is stationary, it follows immediately from (C.13) that the mean power (in the sense of the probabilistic expectation) is

$$E[p_{\mathrm{dyn}}(t)] = \int_{-\infty}^{t} \beta_1 e^{-\beta_1(t-s)} E[f(w(s))]\,ds = E[f(w(t))].$$

From the law of large numbers it follows that the mean power (in the sense of the time-wise average) is

$$\begin{aligned} P_{\mathrm{dyn}} &= \frac{1}{T}\int_0^T p_{\mathrm{dyn}}(s)\,ds \approx E[p_{\mathrm{dyn}}(t)] = E[f(w(t))] \\ &\approx \frac{1}{T}\int_0^T f(w(s))\,ds = \int_0^\infty \phi(x) f(x)\,dx = P_{\mathrm{qs}}, \end{aligned}$$

where ϕ again denotes the probability density function of the driving wind speeds. Therefore, it has under mild assumptions been shown that the quasi static model on the level of mean values is equivalent to the slightly more sophisticated dynamic model in (C.12).

To compare the dynamic model with the quasi static model in terms of the standard deviation of power, let $w_{\mathrm{dyn}}(t)$ and $w_{\mathrm{qs}}(t)$ denote two stationary driving wind speed time series with common mean W. Suppose that $w_{\mathrm{dyn}}(t)$ drives the dynamic model and that $w_{\mathrm{qs}}(t)$ drives the quasi static model. The variance of power under the dynamic model is

$$\begin{aligned} \mathrm{var}(p_{\mathrm{dyn}}(t)) &= \int_0^\infty \beta_1 e^{-\beta_1 s} \mathrm{cov}\Big(f(w_{\mathrm{dyn}}(s)), f(w_{\mathrm{dyn}}(0))\Big)\,ds + \frac{\beta_2^2}{2\beta_2} \\ &\approx \int_0^\infty \beta_1 e^{-\beta_1 s} \mathrm{cov}\Big(f(w_{\mathrm{dyn}}(s)), f(w_{\mathrm{dyn}}(0))\Big)\,ds, \end{aligned} \qquad \text{(C.14)}$$

since $\beta_2^2/(2\beta_1) \approx 0$ as shown in appendix C.B. By a first order approximation, $f(w) \approx f(W) + f'(W)(w - W)$, one obtains

$$\frac{\sigma_{p_{\mathrm{dyn}}}}{\sigma_{p_{\mathrm{qs}}}} \approx k'' \frac{\sigma_{w_{\mathrm{dyn}}}}{\sigma_{w_{\mathrm{qs}}}} \quad \text{where} \quad k'' = \sqrt{\int_0^\infty \beta_1 e^{-\beta_1 s} \rho_{w_{\mathrm{dyn}}}(s)\,ds} \le 1. \qquad \text{(C.15)}$$

Hence, in order for the quasi static model to match the standard deviation of power of the dynamic model, the standard deviations of the respective driving wind speeds should satisfy

$$\sigma_{w_{\mathrm{qs}}} \approx k'' \sigma_{w_{\mathrm{dyn}}}.$$

Suppose for the sake of the example that $w_{\mathrm{dyn}}(t)$ has the von Kármán correlation structure[4]. Then fig. C.6 (b) shows the factor k'' as a function of the ratio β_1^{-1}/τ of the characteristic response time β_1^{-1} to the integral time τ, where τ is related to L through $L = \tau W$. It is seen from fig. C.6 (b) that, under the many assumptions of the simple dynamic model, the standard deviation of driving

4 · This assumption only serves to simplify the computations behind fig. C.6 (b). The correlation structure of the fictive driving wind will in general not be like the correlation structure of the upstream wind. It can, for example, be shown that the famous 2/3-law of Kolmogorov must be replaced by a 6/3-law under the simple model in (C.10).

wind speed should be scaled down slightly in order to compensate for the fact that the quasi static model by construction does not take the dynamic response of the wind turbine into account.

C.4.4 THE NEW METHOD

In subsec. C.4.1 it was shown how the zero-turbulence power curve f may be estimated given distributions of the driving wind and ten minute statistics of the power. Given that only ten minute statistics of the upstream wind are available, the driving wind speeds must be assumed to lie within some class of parametric distributions. Like in the "Normal Distribution Model" from Albers (2009) and Albers et al. (2007) it will here be assumed that the driving wind speeds are normally distributed. This is a strong assumption which unfortunately is impossible to verify or falsify from the quite coarse ten minute statistics. The distribution of the driving wind speeds are therefore determined completely from their means and standard deviations.

Let $\{(U_i, \sigma_{u,i}, P_i, \sigma_{p,i}) \mid i = 1, \dots, N\}$ denote the measured data set. Since the wind shear in the data set is low by construction, it will be assumed that the mean driving wind speed W_i is equal to the mean upstream wind speed U_i measured at hub height at the meteorology mast. Deviations from the assumption $W_i = U_i$ will later be used to explain some of the variation observed in the fit residuals. If information about the wind profile is available, the equvalent wind (Wagner et al., 2009, 2011) may be used to provide a better representation of the mean driving wind speed.

In subsecs. C.4.2 and C.4.3 it was indicated that the standard deviation σ_u of the upstream wind speed should be scaled down by some factor k' to account for the size of the rotor and then further by some factor k'' to compensate for the fact that the quasi static model is incapable of modeling the dynamic response of the wind turbine. The models employed to derive these factors are highly idealized and should therefore not be used directly to specify the downscale factors. Instead, it will just be assumed that

$$\sigma_w = k\sigma_u$$

for some unknown factor k, the *equivalent turbulence factor*, which is to be determined from the data. In this paper, k is assumed to be constant. The use of the equivalent turbulence factor is consistent with the concept of modified turbulence intensity from Sheinman and Rosen (1992), Rosen and Sheinman (1994) and Rosen and Sheinman (1996).

With the assumptions above, the problem (C.8) replaced by

$$\text{minimize} \quad S(f, \theta, k) \quad \text{with respect to} \quad f, \tag{C.16}$$

where $S(f, \theta, k) = \mathrm{MSE}_P(f, k) + \theta R(f)$ is the new smoothing functional,

$$\begin{aligned} \mathrm{MSE}_P(f, k) &= \frac{1}{N} \sum_{i=1}^{N} \left(\int_0^\infty f(x) \phi(x; W_i, \sigma_{w,i})\, dx - P_i \right)^2 \\ &= \frac{1}{N} \sum_{i=1}^{N} \left(\int_0^\infty f(x) \phi(x; U_i, k\sigma_{u,i})\, dx - P_i \right)^2, \end{aligned}$$

is the new mean squared error functional, and $\phi(x; W, \sigma_w)$ denotes the probability density function of a normal distribution with mean W and standard deviation σ_w. Let $f_{\theta,k}$ denote the solution to (c.16) for given values of θ and k. A measure of the goodness of fit of the mean power is the ratio

$$\mathrm{GOF}_P(f_{\theta,k}) = \frac{\min\{\mathrm{MSE}_P(f_{\theta^*,k^*}, k^*) \mid 0 \le k^* \le 1, 0 \le \theta^*\}}{\mathrm{MSE}_P(f_{\theta,k}, k)}$$

Likewise, a measure of the goodness of fit of the standard deviation of power is the ratio

$$\mathrm{GOF}_{\sigma_p}(f_{\theta,k}) = \frac{\min\{\mathrm{MSE}_{\sigma_p}(f_{\theta^*,k^*}, k^*) \mid 0 \le k^* \le 1, 0 \le \theta^*\}}{\mathrm{MSE}_{\sigma_p}(f_{\theta,k}, k)},$$

where

$$\mathrm{MSE}_{\sigma_p}(f,k) = \frac{1}{N}\sum_{i=1}^{N}\left(\left(\int_0^\infty f(x)^2\psi_i(x)\,dx - \left(\int_0^\infty f(x)\psi_i(x)\,dx\right)^2\right)^{1/2} - \sigma_{p,i}\right)^2,$$

is the mean squared error of the standard deviation of power. Here $\psi_i(x) = \phi(x; U_i, k\sigma_{u,i})$ for brevity. Due to the ill-posedness of (c.16) when $\theta = 0$, the goodness of fits will be replaced by proxies defined similarly but where the ranges of the parameters k^* and θ^* are $0.5 \le k^* \le 1$ and $10^{-11} \le \theta^* \le 10^{-5}$. This is in analogy with subsec. c.4.1.

Figure c.7 shows the level curves for (the proxies for) the goodness of fits $\mathrm{GOF}_P(f_{\theta,k})$ and $\mathrm{GOF}_{\sigma_p}(f_{\theta,k})$ in the (θ,k)-plane. The level curves of the goodness of fit of the mean power shows that when $k \approx 0.77$, the solutions $f_{\theta,k}$ can attain the highest goodness of fit of the mean power. Furthermore, as k approaches 0.77 it is possible to increase the regularizing weight θ while maintaining the same goodness of fit. In other words, $k \approx 0.77$ allows for the smoothest zero-turbulence power curves without compromizing the goodness of fit of the mean power. The value $k \approx 0.77$ should be compared with fig. c.6 (a). It corresponds loosely to a ratio $R/L \approx 1$ of the rotor radius to the integral length. This is in agreement with the size of the rotor of the turbine under consideration and the integral length of the turbulence at the location of the wind turbine.

The goodness of fit of the standard deviation of power is maximized when $(\theta,k) \approx (10^{-9.5}, 0.77)$. As the shape of the level curves show, this maximum is located on a ridge parallel to the θ-axis and perpendicular to the k-axis. The behaviour of the goodness of fit of the standard deviation of power can be explained qualitatively. If k is large, then the width of the distribution of the driving winds w will be large as well. Consequently, a wide range of powers $f(w)$ will be covered, and the quasi static model will predict a large standard deviation of power. Likewise, if k is small, then the standard deviation of power will be small as well. Therefore, if k is not near a reasonable value, the goodness of fit of the standard deviation of power will be small. The explanation for the behaviour as a function of θ is like in subsec. c.4.1. This suggests that the optimal value of (θ,k) may be determined from data as the point which maximizes $\mathrm{GOF}_{\sigma_p}(f_{\theta,k})$.

When the zero-turbulence power curve f and the equivalent turbulence factor k have been estimated, the problem of incorporating the turbulence

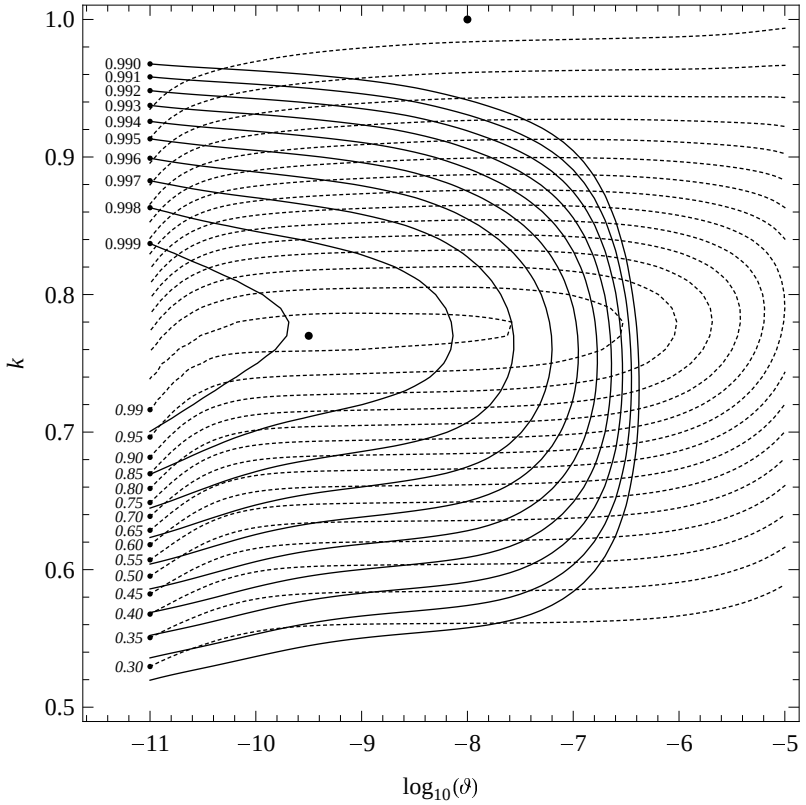

FIGURE C.7. Level curves of the proxies for the goodness of fit of the mean power (solid curves) and of the standard deviation of power (dashed curves). For each level curve, the number to the left of the small black dot at the end of the curve denotes the value of the goodness of fit along the curve. Roman numbers correspond to the mean power and italic numbers correspond to the standard deviation of power. The black dot at $(-9.5, 0.77)$ marks the position where the goodness of fit of the standard deviation of power is maximized. The black dot at $(-8.0, 1)$ corresponds to the zero-turbulence power curve found in subsec. C.4.1.

intensity into the estimation of power curves has been solved. Under the quasi static model, the mean power $P(W, I_u)$ at mean driving wind speed W and upstream turbulence intensity I_u is now given by

$$P(W, I_u) = \int_0^\infty f(x)\phi(x; W, kWI_u)\,dx, \tag{C.17}$$

where $\phi(x, W, \sigma_w)$ denotes the probability density function of a normal distribution with mean W and standard deviation σ_w. Thus, $P(W, I_u)$ as a function of W is the conventional power curve at turbulence intensity I_u.

C.5 RESULTS AND DISCUSSION

The new method is applied to different situations and the results are discussed. In subsec. C.5.1, the method is applied to estimate the zero-turbulence power curve when the equivalent turbulence factor k is chosen according to subsec. C.4.4 and when $k = 1$. The corresponding derived conventional power curves are compared with data and it is demonstrated that choosing k according to the method from subsec. C.4.4 is superior to letting $k = 1$. In subsec. C.5.2 it is shown how the new method can be applied to predict the per-

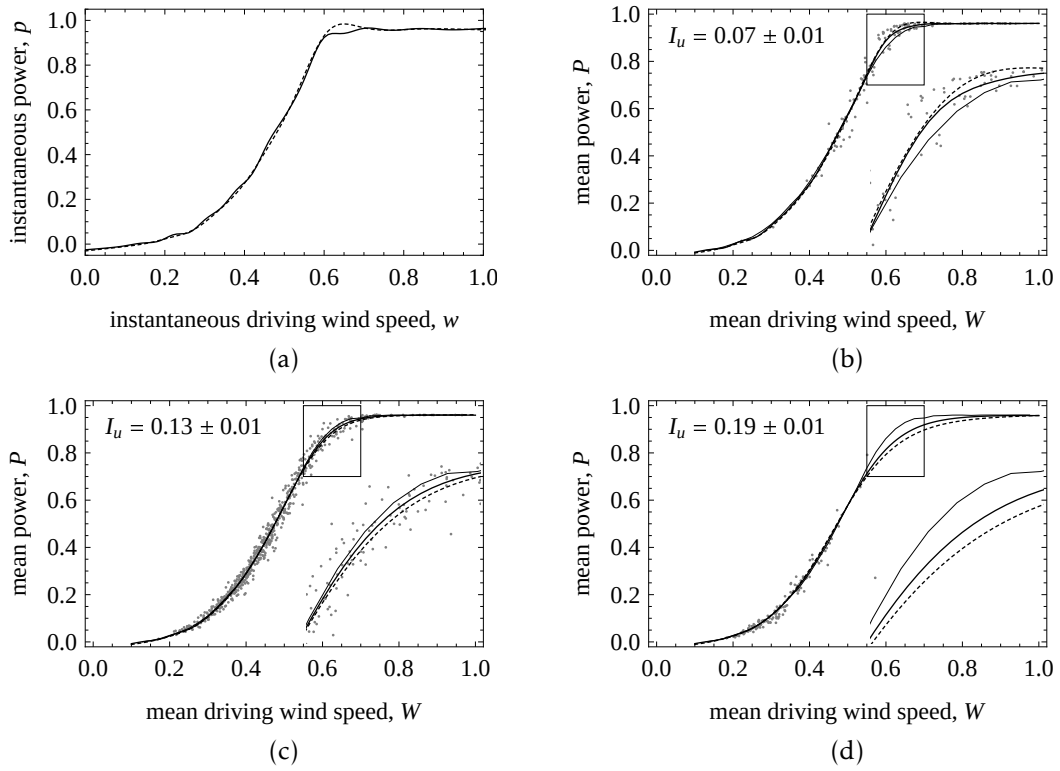

FIGURE C.8. (a) The estimated zero-turbulence power curves corresponding to f_k (solid) and f_1 (dashed). (b)–(d) Three examples of conventional power curves derived from f_k and f_1 at turbulence intensities $I_u = 0.07$ (b), $I_u = 0.13$ (c), and $I_u = 0.19$ (d). The solid and dashed curves denote the conventional power curves derived from f_k and f_1, respectively, and the thin curve denotes the IEC 61400-12-1 power curve calculated from the whole main data set. The gray dots denote a subset of the main data set with turbulence intensities as indicated in each subfigure. A magnified version of the part in the rectangle is shown in the lower right corner.

formance of a wind turbine under unmeasured turbulence intensities. In subsec. C.5.3 it is shown how the new method can be applied to estimate the power curves when a wide range of wind speeds are not measured. Finally, in subsec. C.5.4 it is demonstrated how the new method is capable of estimating power curves from very few data points.

C.5.1 THE ESTIMATED ZERO-TURBULENCE POWER CURVES AND DERIVED CONVENTIONAL POWER CURVES

First, a zero-turbulence power curve f_1 is estimated according to the method described in C.4.1 assuming $k = 1$ and choosing $\theta = 10^{-8.0}$ guided by GOF_P and GOF_{σ_p}, see fig. C.5 (b). Second, a zero-turbulence power curve f_k is estimated according to the method described in subsec. C.4.4 where $(\theta, k) = (10^{-9.5}, 0.77)$ is chosen to maximize GOF_{σ_p}, see fig. C.7. Figure C.8 shows that f_k and f_1 are similar, though f_k displays some small oscillations whereas f_1 has a small "bump" near $w = 0.6$. The small oscillations in f_k disappear if θ is chosen to be as high as for f_1. However, such a choice is not necessary since the conventional power curve derived according to (C.17) is insensitive to small oscillations in the zero-turbulence power curve. Moreover, manually choosing the value of θ introduces an undesirable subjectiveness and weakens the

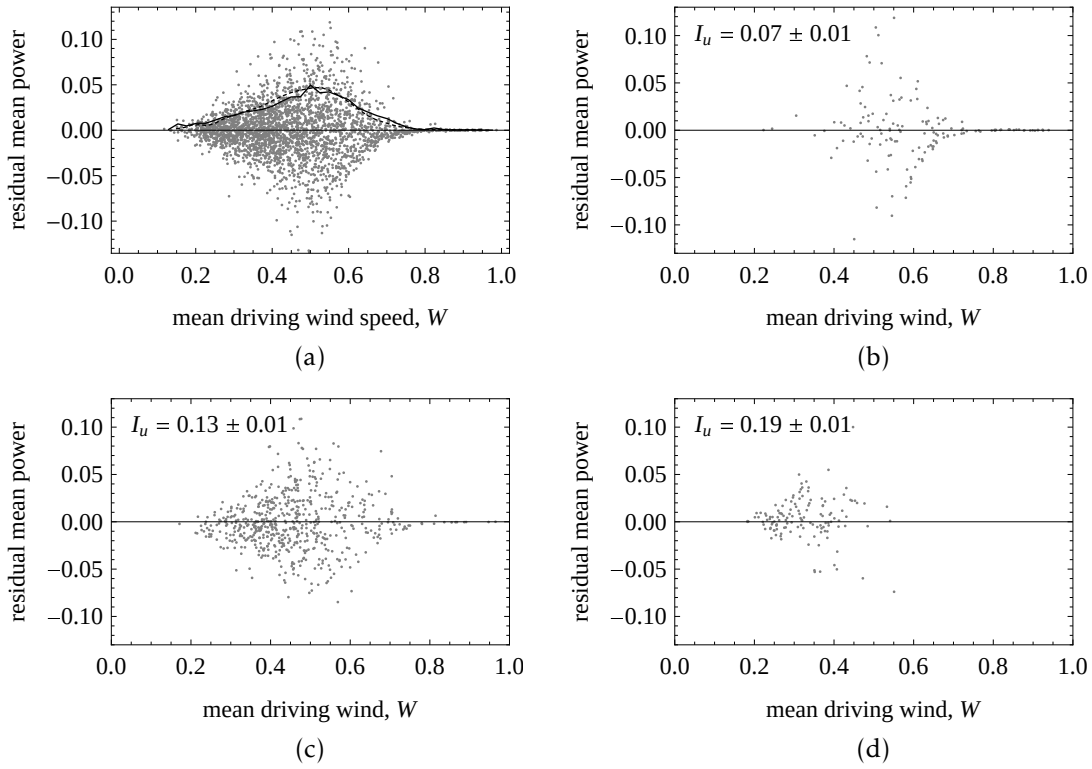

FIGURE C.9. The residual mean power corresponding to f_k as a function of the mean driving wind speed. The residual mean power corresponding to f_1 is similar and not shown here. (a) All turbulence intensities. The solid curve shows the binwise standard deviation of the residual mean power. The dashed curve show the predicted binwise standard deviation of the residual mean power according to (C.18). (b)–(d) Turbulence intensities in the ranges 0.07 ± 0.01 (b), 0.13 ± 0.01 (c), and 0.19 ± 0.01 (d).

data-driven nature of the new method.

Figures C.8 (b), (c), and (d) show that the conventional power curves at turbulence intensities 0.07 ± 0.01, 0.13 ± 0.01, and 0.19 ± 0.01 derived from the estimated zero-turbulence power curves f_k and f_1 in most cases lie well within the point cloud consising of the data points with the specified turbulence intensities. However, a closer look at fig. C.8 (b) shows that around $W = 0.65$ the conventional power curve derived from f_1 appears to slightly overestimate the mean power whereas the conventional power curve derived from f_k does not. Figure C.8 (c) shows that both derived conventional power curves agree well with data for the dominant turbulence intensities of the data set. Finally, fig. C.8 (d) shows that both derived conventional power curves appear to slightly overestimate the mean power around $W = 0.3$. Therefore, a careful analysis of the residual mean power,

$$P(U_i, I_{u,i}) - P_i = \int_0^\infty f(x)\phi(x; U_i, k\sigma_{u,i})\,dx - P_i,$$

is warranted. Figure C.9 (a) shows that the residuals corresponding to f_k are approximately evenly distributed around zero. The residuals corresponding to f_1 are similar and not shown here. This is not surprising, since the zero-turbulence power curve is found essentially by minimizing the sum of the squared residuals. Figures C.9 (b), (c), and (d) reveal that the residuals also

	f_k				f_1			
$I_u \downarrow$ $W \rightarrow$	0.2 ± 0.1	0.4 ± 0.1	0.6 ± 0.1	0.8 ± 0.1	0.2 ± 0.1	0.4 ± 0.1	0.6 ± 0.1	0.8 ± 0.1
0.07 ± 0.01		$+0.64$	-0.37 •	$+0.00$ •		$+0.06$ •	$+0.48$	$+0.06$
0.09 ± 0.01	-0.23 •	-0.45 •	-0.02 •	-0.02 •	-0.72	-0.93	$+0.21$	$+0.07$
0.11 ± 0.01	$+0.13$ •	-0.22 •	-0.08 •	-0.10	-0.19	-0.34	-0.32	-0.06 •
0.13 ± 0.01	-0.40 •	-0.35 •	-0.05 •	-0.11 •	-0.55	-0.47	-0.41	-0.29
0.15 ± 0.01	$+0.01$ •	$+0.21$ •	$+0.67$		-0.12	$+0.33$	-0.38 •	
0.17 ± 0.01	$+0.07$	$+0.27$ •	-0.22 •		$+0.04$ •	$+0.46$	-1.50	
0.19 ± 0.01	$+0.16$	$+0.54$ •			$+0.14$ •	$+0.98$		
0.21 ± 0.01	$+0.13$ •	$+0.68$ •			$+0.22$	$+1.24$		
0.23 ± 0.01	$+0.31$	-1.01 •			$+0.23$ •	-0.08		
0.25 ± 0.01	$+0.16$ •				$+0.19$			

TABLE C.1. The median (times 100) of the residual mean power for each combination of mean wind driving speed intervals and turbulence intensity intervals. The left group corresponds to f_k and the right group corresponds to f_1. A black dot flags that the magnitude of the median residual is less than the magnitude of the corresponding median residual in the other case. The empty entries correspond to combinations containing less than 10 data points.

appear to be approximately evenly distributed around zero when binned by turbulence intensity.

To investigate whether bias occurs at certain combinations of mean wind speeds and turbulence intensities, the residuals are divided into groups with $W = 0.2 \pm 0.1, \ldots, 8.0 \pm 0.1$ and $I_u = 0.07 \pm 0.01, \ldots, 0.25 \pm 0.01$. The median of the residual mean power is then calculated for each combination and the results are shown in tab. C.1. The median is preferred over the mean since the median is less sensitive to outliers. In the majority of the combinations, the magnitudes of the medians corresponding to f_k are smaller than the magnitudes of the medians corresponding to f_1. This is further evidence in favor of the use of the equivalent turbulence factor to represent the driving wind in terms of the upstream wind. However, the sign of the medians reveal for both f_k and f_1 a small negative bias at low turbulence intensities ($I_u \leq 0.14$) and a small positive bias at high turbulence intensities ($I_u \geq 0.14$). For f_k the bias is typically around ± 0.002 whereas it for f_1 typically is around ± 0.003. Since the bias is so low across all turbulence intensities, it has been demonstrated that the new method is capable of accounting for the influence of turbulence intensity on the mean power production.

The variation in the residuals can be explained by the quasi static model. It has been assumed that $W = U$ and that $\sigma_w = k\sigma_u$ in order to represent the driving wind in terms of the measured upstream wind. The assumption $W = U$ is of course only an approximation, so in reality $W = U + \xi$ where ξ is some random variable with zero mean and standard deviation σ_ξ. Under the quasi static model, the real mean power is

$$\int_0^\infty f(x)\phi(x; U + \xi, \sigma_w)\, dx \approx \int_0^\infty f(x + \xi)\phi(x; U, \sigma_w)\, dx.$$

With the assumption $W = U$ the mean power is $\int_0^\infty f(x)\phi(x; U, \sigma_w)\, dx$. Hence

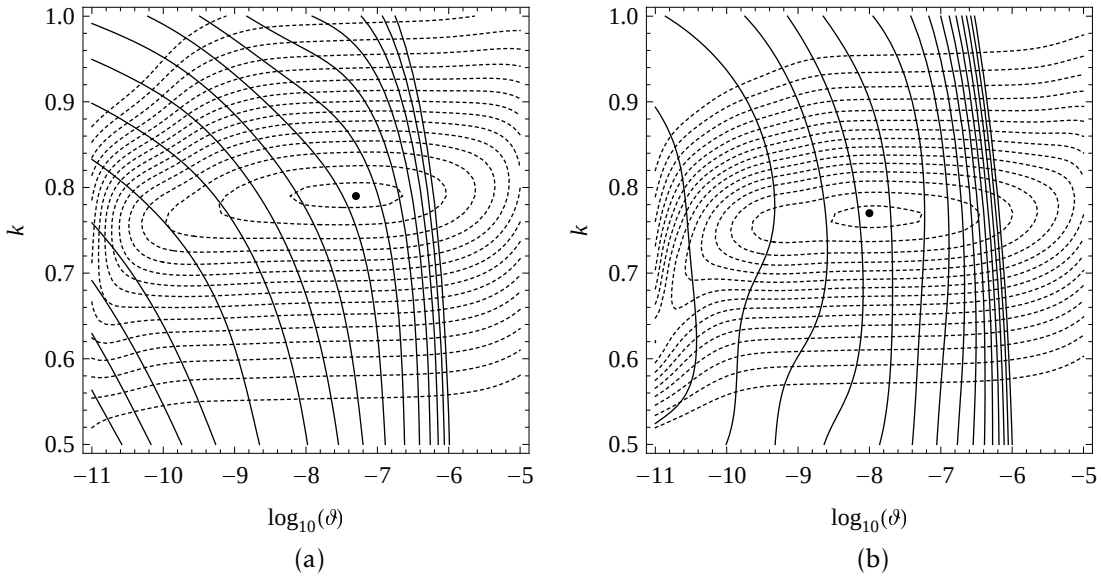

FIGURE C.10. Level curves of $\mathrm{GOF}_P(f_{\theta,k})$ (solid) and $\mathrm{GOF}_{\sigma_p}(f_{\theta,k})$ (dashed) for subset 1 (a) and subset 2 (b). The black dots mark the positions of the maximal goodness of fit of the standard deviation of power, $(\log_{10}(\theta), k) = (-7.3, 0.79)$ for subset 1, and $(\log_{10}(\theta), k) = (-8.1, 0.71)$ for subset 2. For the dashed level curves, the levels are the same as in fig. C.7. For the solid level curves, the levels are (from left to right) 0.999, 0.998, ..., 0.985.

the residual mean power r is approximately

$$r = \int_0^\infty (f(x) - f(x+\xi))\phi(x; U, \sigma_w)\,dx \approx \int_0^\infty f'(x)(x-\xi)\phi(x; U, \sigma_w)\,dx.$$

A simple calculation shows that the standard deviation σ_r of the residual mean power is then

$$\sigma_r \approx \sigma_\xi \left| \int_0^\infty f'(x)\phi(x; U, \sigma_w)\,dx \right|.$$

It is reasonable to suppose that σ_ξ, to first order, is proportional to σ_u, since the error in the assumption $W = U$ should increase with increasing wind speed fluctuations. Assume therefore that $\sigma_\xi = q\sigma_u$ for some constant q. Let $\sigma_u(U)$ denote the binwise mean of the measured σ_u as a function of U. The mean turbulence intensity of the whole data set is approximately 0.13. Therefore the following approximate expression for σ_r as a function of U is obtained,

$$\sigma_r(U) \approx q\sigma_u(U) \left| \int_0^\infty f'(x)\phi(x; U, 0.77 \cdot U \cdot 0.13)\,dx \right|. \tag{C.18}$$

For $q = 0.25$, fig. C.9 shows fine agreement between the observed binwise standard deviation of the residual mean power and the prediction (C.18). This shows, qualitatively and under mild assumptions, that the variation in the residual mean power can be explained by the quasi static model.

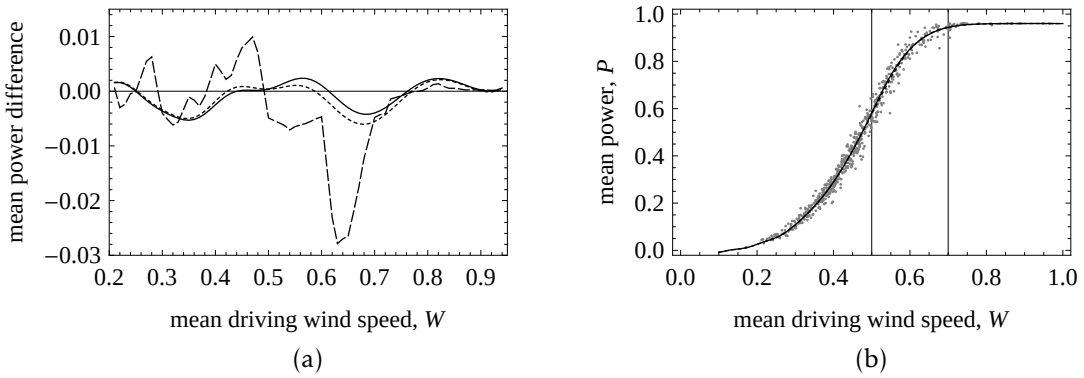

FIGURE C.11. (a) The differences $P_{21} - P_{11}$ (solid), $P_{22} - P_{12}$ (short dashes), and $P_2^{\mathrm{IEC}} - P_1^{\mathrm{IEC}}$ (long dashes) as a function of the mean driving wind speed W. (b) The conventional power curve at turbulence intensity 0.13 derived from the zero-turbulence power curve estimated from data excluding data points with $0.5 \le W \le 0.7$ (solid), and from the zero-turbulence power curve estimated from the whole data set (dashed). The two power curves are almost indistinguishable. The gray dots denote data points with $I_u = 0.13 \pm 0.01$.

C.5.2 FILLING IN THE BLANKS: PREDICTION OF PERFORMANCE UNDER UNMEASURED TURBULENCE INTENSITIES

To demonstrate how the new method may be used to predict the wind turbine performance under unmeasured turbulence intensities, two subsets of the main data set are formed based on turbulence intensity:

$$\begin{aligned} &\text{subset 1:} \quad 0.099 \le I_u \le 0.126, \quad \text{median } I_1 = 0.113, \\ &\text{subset 2:} \quad 0.126 \le I_u \le 0.166, \quad \text{median } I_2 = 0.143. \end{aligned}$$

For the two subsets, zero-turbulence power curves f_1 and f_2 are estimated according to the new method. Figure C.10 shows the level curves of the two goodness of fits, GOF_P and GOF_{σ_P}. The optimal choices of the equivalent turbulence factor are $k_1 = 0.79$ and $k_2 = 0.77$, respectively. Denote by I_j the median turbulence intensity for subset j, and by P_{ij} the conventional power curve at turbulence intensity I_j derived from the zero-turbulence power curve f_i,

$$P_{ij}(W) = \int_0^\infty f_i(x)\phi(x; W, k_i W I_j)\, dx.$$

For the sake of comparison, let P_i^{IEC} denote the IEC 61400-12-1 power curve calculated from subset i. Figure C.11 shows the differences $P_{21} - P_{11}$, $P_{22} - P_{12}$, and $P_2^{\mathrm{IEC}} - P_1^{\mathrm{IEC}}$. Ideally, $P_{2j} - P_{1j}$ should be equal to zero. The difference $P_2^{\mathrm{IEC}} - P_1^{\mathrm{IEC}}$ is not expected to be zero, but serves as a benchmark of the new method: The new method is an improvement if the difference $P_{2j} - P_{1j}$ is smaller in magnitude than the difference $P_2^{\mathrm{IEC}} - P_1^{\mathrm{IEC}}$. At low wind speeds ($0.2 \le W \le 0.4$), the magnitude of the difference $P_{2j} - P_{1j}$ is approximately the same as that of $P_2^{\mathrm{IEC}} - P_1^{\mathrm{IEC}}$; at medium wind speeds ($0.4 \le W \le 0.7$), the magnitude is considerably smaller; at high wind speeds ($0.7 \le W$), the magnitude is slightly larger. Since the rated power is easily known with great accuracy and since it does not appear to depend much on the turbulence intensity, the difference $P_2^{\mathrm{IEC}} - P_1^{\mathrm{IEC}}$ will consequently be very small. However, the new method can easily be extended to allow the rated power to be specified in advance, if this

is desired; see appendix C.A.

The power curves may also be compared through the expected annual energy production (AEP). In this paper the AEP is defined as the integral of the power curve with respect to a distribution of mean wind speeds, multiplied by the number of hours per year.[5] Let ψ denote the probability density function of a Weibull distribution with shape parameter 2 and the same mean as the mean of the mean upstream wind speeds of the main data set. Let $\mathrm{AEP}_{ij} = 8760 \int_0^\infty P_{ij}(W)\psi(W)\,dW$ and $\mathrm{AEP}_i^{\mathrm{IEC}} = 8760 \int_0^\infty P_i^{\mathrm{IEC}}(W)\psi(W)\,dW$ denote the AEP corresponding to each of the power curves considered above. Then

$$\begin{aligned} \mathrm{AEP}_{21} - \mathrm{AEP}_{11} &= -7.9, \\ \mathrm{AEP}_{22} - \mathrm{AEP}_{12} &= -9.9, \\ \mathrm{AEP}_2^{\mathrm{IEC}} - \mathrm{AEP}_1^{\mathrm{IEC}} &= -19.3. \end{aligned}$$

This shows that if the purpose is to predict the AEP under unmeasured turbulence intensities, then the error under the new method is half of the error under the IEC 61400-12-1 method.

C.5.3 BRIDGING THE GAP: WHEN SOME WIND SPEEDS ARE NOT OBSERVED

In the quasi static model, each data point contributes with information about the performance of the wind turbine over a range of wind speeds as determined by the distribution of the driving wind speeds. Therefore, when the turbulence intensity is around 0.13, the data points with mean upstream wind speed equal to 0.5 or 0.7 will provide information about the power curve at wind speeds near 0.6. To illustrate this, a subset of the main data set is formed by discarding data points with mean upstream wind speed in the interval 0.5–0.7. From this subset a zero-turbulence power curve is estimated and the corresponding conventional power curve at turbulence intensity 0.13 is derived. Figure C.11 shows that this conventional power curve is almost identical to the conventional power curve derived from the zero-turbulence power curve estimated from the main data set where no data points are discarded. This shows that the new method allows estimation of power curves even when a large range of mean wind speeds is not represented in the data set.

C.5.4 CONNECTING THE DOTS: A POWER CURVE FROM FEW DATA POINTS

The argument that data points under the quasi static model contribute with extra information about the wind turbine performance through the distribution of driving wind speeds also motivates the use of the new method to attempt to estimate power curves from few data points. As an example, a subset of 144 random data point are formed from the main data set. The number 144 was chosen since 144×10 minutes is 24 hours. Figure C.12 (a) shows the conventional power curve at turbulence intensity 0.13 derived from this subset using the new method and the IEC 61400-12-1 power curve calculated from

5 · This is not the definition used in the IEC 61400-12-1 standard, where the AEP is equal to the integral of a piecewise constant function with respect to a Weibull distribution with shape parameter 2, multiplied by the number of hours per year. See (IEC 61400-12-1 standard, sec. 8.3).

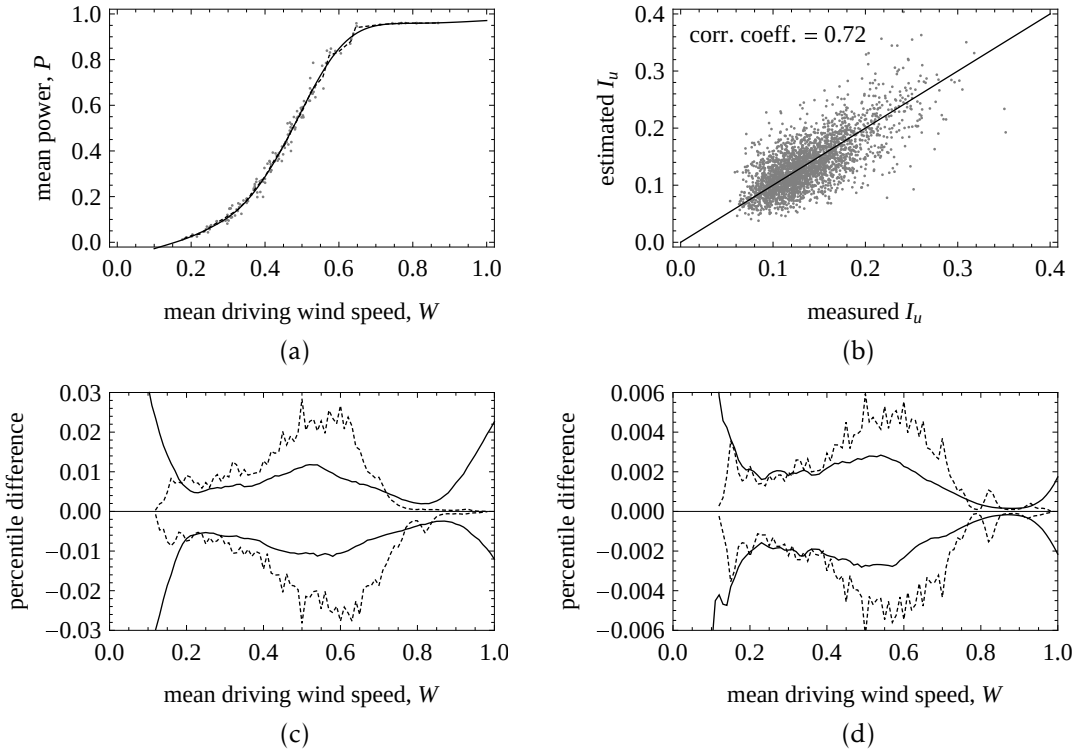

FIGURE C.12. (a) Gray dots represent a subset consisting of 144 random samples from the main data set. The solid curve represents the conventional power curve at turbulence intensity 0.13 derived from the zero-turbulence power curve estimated from the 144 chosen data points. The dashed curve represents the IEC 61400-12-1 power curve estimated from the same 144 data point. The conventional power curve derived using the whole data set is not shown as it is almost indistinguishable from the solid curve. (b) The upstream turbulence intensity estimated from the power data versus the measured upstream turbulence intensity. (c) Percentile differences $q_{5\%}(W)-q_{50\%}(W)$ (lower curves) and $q_{95\%}(W)-q_{50\%}(W)$ (upper curves) for the power curves derived using the new method (solid) and for the IEC 61400-12-1 power curves (dashed). The size of each of the 1000 samples is 144. (d) The same as (c), but the size of the samples is 2827.

the same subset. Since the latter is defined through binwise averages, it appears jagged due to the small number of data points. The conventional power curve derived from the small subset turns out to be almost indistinguishable from the conventional power curve derived from the whole main data set (not shown here), except at the two extremes $W \approx 0.2$ and $W \approx 0.9$.

Since the 144 data point were chosen at random, it should be investigated whether it is a coincidence that the derived conventional power curve agrees with the conventional power curve derived from the main data set. To do this, 1000 subsets are formed, each consisting of 144 data points drawn at random (with replacement) from the main data set. For each subset, the new method is applied to calculate a conventional power curve at turbulence intensity 0.13. In addition, an IEC 61400-12-1 power curve is calculated from each of those 1000 subsets. The randomly chosen subsets give for each mean driving wind speed W rise to a set $\{P_1(W),\ldots,P_{1000}(W)\}$ of corresponding mean powers where P_i for the i'th subset denotes either the power curve derived using the new method or the IEC 61400-12-1 power curve. A simple measure of the dispersion of the mean powers at the mean driving wind speed W is given by the

percentile differences

$$q_{5\%}(W) - q_{50\%}(W) \quad \text{and} \quad q_{95\%}(W) - q_{50\%}(W),$$

where $q_{x\%}(W)$ is short-hand for the x%-percentile of $\{P_1(W), \ldots, P_{1000}(W)\}$. A large percentile difference implies that the power curve at W is sensitive to the choice of data points from which it was calculated, and vice versa. Figure C.12 (c) shows that the new method produces power curves with smaller percentile differences than the IEC 61400-12-1 method when $0.2 \leq W \leq 0.7$. At the smallest and highest wind speeds, the percentile differences of the new method is larger than those of the IEC 61400-12-1 method. This can be explained by the nature of the random sampling. Given the distribution of the mean wind speeds as shown in fig. C.2 (a), some of the random subsets will contain no data points at low or high wind speeds. Therefore, there will be little guidance in the optimization problem (C.16) to determine the zero-turbulence power curve at low or high wind speeds. Consequently, the derived conventional power curve can attain almost arbitrary values for mean wind speeds sufficiently far outside of the interval defined by the extrema of the measured mean wind speeds. If the size of the 1000 samples is increased from 144 to 2827 (the number of data points in the main data set), then the percentile differences decrease by a factor of 5 as shown in fig. C.12 (d). Moreover, the percentile differences of the new method in the region $0.7 \leq W \leq 0.93$ decrease to not exceed those of the IEC 61400-12-1 method. In summary, this suggests that the new method may be used to estimate power curves from few data points.

C.6 FURTHER APPLICATIONS AND FUTURE WORK

The wind turbine can be used as an anemometer, albeit a rather large one. Since the mean and standard deviation of power are expressed as functions of the mean and standard deviation of wind speed, one obtains a mapping $(W, \sigma_w) \mapsto (P, \sigma_p)$ which for a large range of mean powers can be inverted. Thus, for measured P and σ_p the corresponding W and σ_w can be calculated. In turn, $I_u = (\sigma_w/W)/k$ yields an estimate for the upstream turbulence intensity. Figure C.12 (b) shows that I_u can be estimated from the measured power statistics with a correlation coefficient of 0.72. The estimation of turbulence intensity could find use in wake analyses as part of a wake detection scheme. The nacelle anemometer only measures the wind near the center of the rotor and its measurements are of course affected by the rotor and the nacelle. The rotor on the other hand has a large spatial extension and can detect the wake even in partial wake situations.

The wind speeds have been assumed to be normally distributed. This was done out of necessity since only measured means and standard deviations were available. As high-frequency measurements become more common, the wind speed distributions may be measured and replace the assumption of normality. Furthermore, it remains to be investigated how the new method works with shear-corrected wind speed data. The method for shear-correction proposed in Wagner et al. (2011) may be used as a preprocessing step for the

method of this paper.

The power coefficient curve can be calculated from the power curve once the latter has been estimated. Alternatively, one may formulate the quasi static model in terms of the power coefficient, $P_{\mathrm{qs}} = \int_0^\infty \frac{1}{2}\rho A x^3 c_{\mathrm{qs}}(x)\phi_w(x)\,dx$, and hence derive a method that estimates the power coefficient curve c_{qs} directly from measured power data.

Any given IEC power curve that is assumed to be valid at a certain turbulence intensity can be used as input to the new method. From the obtained zero-turbulence power curve, new power curves can be generated at any desired turbulence intensity.

The new method should be tested on other data sets, including data sets obtained from simulations of the interaction of the wind turbine with synthetic wind fields, and it should be compared with all the methods mentioned in sec. C.2. However, this is a major undertaking which is postponed to future work.

C.7 CONCLUSION

The quasi static model and the more general, yet simple, dynamic model for a wind turbine's production of power as a function of wind speed are used to derive a method to estimate the zero-turbulence power. The zero-turbulence power curve is in turn used to calculate the conventional power curve at any desired level of turbulence intensity. The model is shown to be able to account for some of the influence of turbulence intensity on the mean power production as well as the variation found in the data. The new method may be used to predict the performance of a wind turbine, in particular the annual energy production, at unmeasured turbulence intensities. Furthermore, the new method is insensitive to large gaps in the measured wind speeds and may be used to estimate the power curve from few data points. The estimation is essentially non-parametric and assumes no particular shape of the zero-turbulence power curve. Moreover, the method is shown to be numerically tractable and easy to implement. Several applications and possible directions of future work are indicated. The concepts of upstream, virtual, and driving wind speeds have proved to be useful, and in particular the concept of modified turbulence intensity has proved to be necessary to account for the smoothing effects of the spatial extension of the rotor and the response of the wind turbine. The modification of turbulence intensity is determined by a single auxiliary parameter, the equivalent turbulence factor, that itself is estimated from data as part of the estimation of the zero-turbulence power curve.

C.A IMPLEMENTATION OF THE NEW METHOD

In the general case, where the driving wind speeds are not assumed to be normally distributed, the problem is to minimize the smoothing functional $S(f,\theta)$ with respect to f when θ is given and then determine the optimal θ

according to some criterion. Recall that $S(f,\theta) = \mathrm{MSE}_P(f) + \theta R(f)$ where

$$\mathrm{MSE}_P(f) = \frac{1}{N}\sum_{i=1}^{N}\left(\int_0^\infty f(x)\phi_i(x)\,dx - P_i\right)^2, \quad \text{and} \quad R(f) = \int_0^\infty (f''(x))^2\,dx.$$

Here $P_1,\dots,P_N$ denote the measured mean powers, and $\phi_1,\dots,\phi_N$ denote the corresponding probability density functions of the driving wind speed. The problem is first discretized. Let $0 \le x_0 < \cdots < x_n$ denote a mesh and suppose that the function f is piecewise linear,

$$f(x) = \sum_{j=1}^{n} \mathbf{1}_{(x_{j-1},x_j]}(x)\left(y_{j-1} + \frac{y_j - y_{j-1}}{x_j - x_{j-1}}(x - x_{j-1})\right), \tag{C.19}$$

where $\mathbf{1}_{(a,b]}(x)$ is equal to 1 if $a < x \le b$ and 0 otherwise, and where $y_0,\dots,y_n$ are coefficients to be determined. It is easy to show that the first moment of the power under the quasi static model is given by

$$\begin{aligned}&\int_0^\infty f(x)\phi_i(x)\,dx \\ &\quad= \frac{x_1\Phi^0_{i,1} - \Phi^1_{i,1}}{x_1 - x_0}y_0 + \sum_{j=1}^{n-1}\left(\frac{x_{j+1}\Phi^0_{i,j+1} - \Phi^1_{i,j+1}}{x_{j+1} - x_j} - \frac{x_j\Phi^0_{i,j} - \Phi^1_{i,j}}{x_j - x_{j-1}}\right)y_j \\ &\qquad- \frac{x_n\Phi^0_{i,n} - \Phi^1_{i,n}}{x_n - x_{n-1}}y_n = \sum_{j=0}^{n} c_{i,j}y_j\end{aligned}$$

where $\Phi^s_{i,j} = \int_{x_{j-1}}^{x_j} x^s\phi_i(x)\,dx$ denotes the truncated moment of order s of ϕ_i. Note that the mean power is a linear combination of the coefficients $y_0,\dots,y_n$. The second moment of the power under the quasi static model is given by

$$\begin{aligned}&\int_0^\infty f(x)^2\phi_i(x)\,dx \\ &\quad= \sum_{j=1}^{n}\frac{1}{(x_j - x_{j-1})^2}\Big((x_jy_{j-1} - x_{j-1}y_j)^2\Phi^0_{i,j} + 2(x_jy_{j-1} - x_{j-1}y_j)(y_j - y_{j-1})\Phi^1_{i,j} \\ &\qquad\qquad + (y_j - y_{j-1})^2\Phi^2_{i,j}\Big).\end{aligned}$$

Let $y = (y_0,\dots,y_n)^T$ denote the column vector of coefficients to be determined, let C denote the $N \times (n+1)$-matrix whose (i,j)'th entry is $c_{i,j}$, and let $P = (P_1,\dots,P_N)^T$ denote the column vector of meaured mean powers. Then the mean squared error functional is given by

$$\mathrm{MSE}_P(f) = \frac{1}{N}\Big(y^TC^TCy - 2P^TCy + P^TP\Big).$$

The function f in (C.19) is not twice differentiable, so $R(f) = \int_0^\infty (f''(x))^2\,dx$ is meaningless. However, it is easy to see that a reasonable replacement defined in terms of second order difference quotients is given by

$$R(f) = \sum_{j=1}^{n-1}\frac{\left(\dfrac{y_{j+1} - y_j}{x_{j+1} - x_j} - \dfrac{y_j - y_{j-1}}{x_j - x_{j-1}}\right)^2}{\frac{1}{2}(x_{j+1} - x_{j-1})} = \sum_{j=1}^{n-1}\begin{pmatrix}y_{j-1} & y_j & y_{j+1}\end{pmatrix}D_j\begin{pmatrix}y_{j-1}\\ y_j\\ y_{j+1}\end{pmatrix}$$

where

$$D_j = \begin{pmatrix} \frac{2}{(x_j - x_{j-1})^2(x_{j+1} - x_{j-1})} & \frac{-2}{(x_j - x_{j-1})^2(x_{j+1} - x_j)} & \frac{2}{(x_j - x_{j-1})(x_{j+1} - x_{j-1})(x_{j+1} - x_j)} \\ \frac{-2}{(x_j - x_{j-1})^2(x_{j+1} - x_j)} & \frac{2(x_{j+1} - x_{j11})}{(x_j - x_{j-1})^2(x_{j+1} - x_j)^2} & \frac{-2}{(x_j - x_{j-1})(x_{j+1} - x_j)^2} \\ \frac{2}{(x_j - x_{j-1})(x_{j+1} - x_{j-1})(x_{j+1} - x_j)} & \frac{-2}{(x_j - x_{j-1})(x_{j+1} - x_j)^2} & \frac{2}{(x_{j+1} - x_j)^2(x_{j+1} - x_{j-1})} \end{pmatrix}.$$

Let $\tilde{D}_j$ denote the block diagonal matrix of size $(n+1)\times(n+1)$ where the first block is the zero matrix of size $(j-1)\times(j-1)$, the second block is D_j, and the third block is the zero matrix of size $(n-1-j)\times(n-1-j)$. Let $D = \sum_{j=1}^{n-1} \tilde{D}_j$. Then $R(f) = y^T D y$, and it follows that

$$S(f,\theta) = y^T\left(\frac{1}{N}C^T C + \theta D\right)y - \frac{2}{N}P^T C y + \frac{1}{N}P^T P.$$

For a given θ, the vector y which minimizes $S(f,\theta)$ is the solution to the following linear system,

$$\left(\frac{1}{N}C^T C + \theta D\right)y = \frac{1}{N}P^T C. \tag{C.20}$$

Equation (C.20) is easily and efficiently solved using numerical linear algebra.

Next, the problem is specialized to the case where the driving wind speeds are assumed to follow a normal distribution, i.e., ϕ_i is the probability density function of a normal distribution with mean W_i and standard deviation $\sigma_{w,i}$. The statistics of the driving wind are assumed to be related to the statistics of the upstream wind through $W_i = U_i$ and $\sigma_{w,i} = k\sigma_{u,i}$ where k denotes the equivalent turbulence factor. In this case the truncated moments $\Phi^0_{i,j}, \Phi^1_{i,j}, \Phi^2_{i,j}$ are given by

$$\begin{aligned}
\Phi^0_{i,j} &= \frac{1}{2}\Big(\operatorname{erf}(z_{i,j}) - \operatorname{erf}(z_{i,j-1})\Big), \\
\Phi^1_{i,j} &= \frac{1}{2}U_i\Big(\operatorname{erf}(z_{i,j}) - \operatorname{erf}(z_{i,j-1})\Big) - \frac{k\sigma_{u,i}}{\sqrt{2\pi}}\Big(\exp(-z^2_{i,j}) - \exp(-z^2_{i,j-1})\Big), \\
\Phi^2_{i,j} &= \frac{1}{2}\Big(U_i^2 + k^2\sigma^2_{u,i}\Big)\Big(\operatorname{erf}(z_{i,j}) - \operatorname{erf}(z_{i,j-1})\Big) \\
&\quad - \frac{k\sigma_{u,i}}{\sqrt{2\pi}}\Big((U_i + x_j)\exp(-z^2_{i,j}) - (U_i + x_{j-1})\exp(-z^2_{i,j-1})\Big)
\end{aligned}$$

where $z_{i,j} = (x_j - U_i)/(\sqrt{2}k\sigma_{u,i})$. The discretized version of the smoothing functional $S(f,\theta,k)$ from (C.16) is therefore

$$S(f,\theta,k) = y^T\left(\frac{1}{N}C(k)^T C(k) + \theta D\right)y - \frac{2}{N}P^T C(k) y + \frac{1}{N}P^T P,$$

where the matrix $C(k)$ depends on the parameter k through the truncated moments $\Phi^0_{i,j}$ and $\Phi^1_{i,j}$.

If the coefficient vector y is supposed to satisfy $y = A\tilde{y} + b$ for a given matrix A and vector b, then it is easy to show that the linear equation to solve is

$$\left(\frac{1}{N}A^T C(k)^T C(k) A + \theta D\right)\tilde{y} = \frac{1}{N}(P - C(k)b)^T C(k) A$$

with respect to $\tilde{y}$. In particular, this allows a user to impose a predetermined rated power on the estimation of the zero-turbulence power curve.

Figure C.13 outlines the algorithm used to estimate the zero-turbulence

Let $U_i, \sigma_{u,i}, P_i, \sigma_{p,i}$ for $i = 1, \ldots, N$ be the mean and std. dev. of upstream wind speed and power.
Let $0 \leq x_0 < \cdots < x_n$ be a mesh.
Let K be a set of k-values and let Θ be a set of θ-values.
for all $k \in K$ **do**
  Calculate the truncated moments $\Phi_{i,j}^s$ for $i = 1, \ldots, N$, $j = 1, \ldots, n$, and $s = 0, 1, 2$.
  Form the matrices $C(k)$ and D.
  for all $\theta \in \Theta$ **do**
    Let $y_{\theta,k}$ be the solution to $(\frac{1}{N} C(k)^T C(k) + \theta D) y = \frac{1}{N} P^T C(k)$ with respect to y.
    Let $\mathrm{MSE}_P(f_{\theta,k})$ be the corresponding mean squared error of mean power.
    Let $\mathrm{MSE}_{\sigma_p}(f_{\theta,k})$ be the corresponding mean squared error of std. dev. of power.
  end for
end for
Calculate the proxies for the goodness of fits, $\mathrm{GOF}_P(f_{\theta,k})$ and $\mathrm{GOF}_{\sigma_p}(f_{\theta,k})$.
Let θ^* and k^* be chosen to maximize $\mathrm{GOF}_{\sigma_p}(f_{\theta,k})$.
The zero-turb. power curve is now given by the mesh $x_0 < \cdots < x_n$ and the coeff. vector y_{θ^*,k^*}.
The equivalent turbulence factor is k^*.

FIGURE C.13. Pseudo code for an algorithm to estimate the zero-turbulence power curve and the equivalent turbulence factor from ten-minute means and standard deviations of upstream wind speed and power.

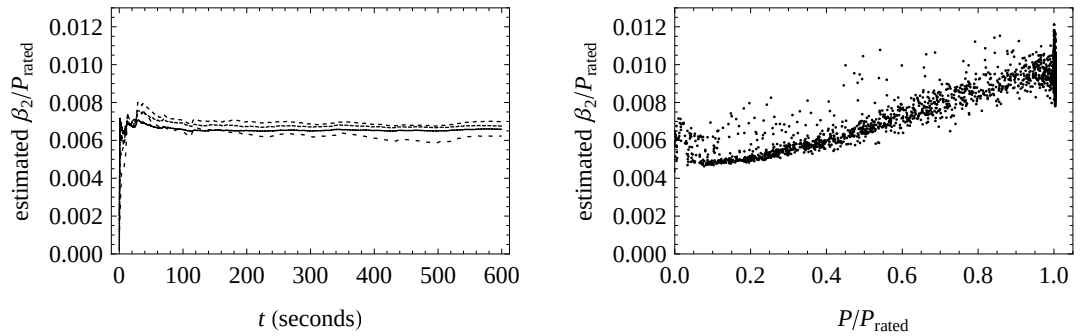

FIGURE C.14. (a) The estimator of β_2 defined through the realized quadratic variation of power for the values $\delta = 0.04\,\mathrm{s}, 0.08\,\mathrm{s}, 0.16\,\mathrm{s}, 0.32\,\mathrm{s}$ (from solid to loosely dashed). (b) The estimated noise strength β_2 as a function of normalized mean power P/P_{rated}.

power curve and equivalent turbulence factor according to the method described in subsec. C.4.4. The mesh was $0.00 < 0.01 < \cdots < 0.99 < 1.00 < 2.00$, the set of k-values was $K = \{0.50, 0.51, \ldots, 1.00\}$, and the set of θ-values was $\Theta = \{10^r \mid r = -11.0, -10.9, \ldots, -5.0\}$. The author's straight-forward implementation in Mathematica took two minutes to execute.

C.B QUADRATIC VARIATION OF POWER

A high-frequency data set is used in this appendix. It originates from another wind turbine than the main data set employed in the remainder of this paper. The high-frequency data set was not found to be suitable for a first exposition of the new method as the shear is not low and furthermore as the wind profile is not adequately resolved to allow for correction for the shear. The purpose of the high-frequency data set is only to demonstrate the validity of

the approximation in (C.14).

Consider the dynamic model $dp(t) = -\beta_1(p(t) - f(w(t)))\,dt + \beta_2\,dB_t$. To evaluate the variance of power under the model, the noise strength parameter β_2 must be known, i.e., estimated from data. To that end, the concept of *quadratic variation* from stochastic calculus can be applied, see e.g. Iacus (2008). The quadratic variation process $\mathrm{QV}(t)$ of the power p is, under the dynamic model, given by $\mathrm{QV}(t) = \beta_2^2 t$. The quadratic variation itself can be estimated from the *realized quadratic variation* calculated from high-frequency data at a given lag δ, $\mathrm{RQV}(t,\delta) = \sum_{i=1}^{\lfloor t/\delta \rfloor}(p(i\delta) - p((i-1)\delta)^2$, since $\mathrm{RQV}(t,\delta) \to \mathrm{QV}(t)$ as $\delta \to 0$. Hence, if δ can be chosen small enough, $\sqrt{\mathrm{RQV}(t,\delta)/t}$ is an estimate of β_2. Figure C.14 (a) shows a typical example of $\sqrt{\mathrm{RQV}(t,\delta)/t}$ as a function of time t for a ten minute long time series sampled at 25 Hz. After a few minutes a stable level is attained and the estimate of β_2 (normalized by the rated power) has been found. To ensure convergence has been reached in terms of δ, the realized quadratic variation is calculated for four values of the lag variable: $\delta = 0.04\,\mathrm{s}, 0.08\,\mathrm{s}, 0.16\,\mathrm{s}, 0.32\,\mathrm{s}$. The lag $\delta = 0.04\,\mathrm{s}$ is the smallest possible allowed by the 25 Hz sampling rate of the high-frequency data set. From the figure it is reasonable to conclude that convergence has been reached. For each ten minute long time series of the high-frequency data set, β_2 is then calculated and plotted in fig. C.14 (b) as a function of the mean power of the time series (normalized by rated power). There is a clear, well-behaved functional dependency of β_2 on the mean power, and it is seen that $0.005 \leq \beta_2/P_{\mathrm{rated}} \leq 0.010$ holds almost always. Therefore, $\beta_2^2 \ll \beta_1$ when the characteristic response time $1/\beta_1$ is of the order 1 s.

ACKNOWLEDGEMENTS

The author wishes to express his thanks to his colleagues Uffe V. Poulsen from Aarhus University and Ioannis Antoniou from Siemens Wind Power for fruitful discussions and helpful comments. This paper benefitted from discussions with Julie K. Lundquist and Andrew Clifton during a visit to the University of Colorado at Boulder. Likewise, the author thanks the anonymous reviewers for their critique which has improved this paper in numerous ways.

BIBLIOGRAPHY

Wind turbines – Part 12-1: Power performance measurements of electricity producing wind turbines (IEC 61400-12-1). International Electrotechnical Commission, 2005.

A. Albers. Turbulence normalisation of wind turbine power curve measurements. Technical report, Deutsche WindGuard Consulting GmbH, 2009.

A. Albers and H. Klug. Open field cup anemometry. *DEWI Magazine*, 19:276, 2001.

A. Albers, H. Klug, and D. Westermann. Outdoor comparison of cup anemometers. In *DEWEK*, pages 107–111, Wilhelmshaven, 2000.

A. Albers, T. Jakobi, R. Rohden, and J. Stoltenjohannes. Influence of meteorological variables on measured wind turbine power curves. In *Proceedings of EWEC*, Milan, 2007.

E. Anahua, S. Barth, and J. Peinke. Markovian power curves for wind turbines. *Wind Energy*, 11(3):219–232, 2008.

C. J. Christensen and J. B. Dragt. Accuracy of power curve measurements (M-2632). Technical report, Risø National Laboratory, 1986.

P. Eecen, F. Mouzakis, and A. Cuerva. Accuwind. Technical report, Energy Research Centre of the Netherlands, 2006.

D. Elliott and J. Cadogan. Effects of wind shear and turbulence on wind turbine power curves. In *European Community Wind Energy Conference and Exhibition*, Madrid, 1990.

S. Frandsen, I. Antoniou, J. Hansen, L. Kristensen, H. Madsen, B. Chaviaropoulos, D. Douvikas, J. Dahlberg, A. Derrick, and P. Dunbabin. Redefinition power curve for more accurate performance assessment of wind farms. *Wind Energy*, 3(2):81–111, 2000.

J. Gottschall and J. Peinke. Stochastic modelling of a wind turbine's power output with special respect to turbulent dynamics. *J. Phys. Conf. Ser.*, 75: 012045, 2007.

J. Gottschall and J. Peinke. How to improve the estimation of power curves for wind turbines. *Environ. Res. Lett.*, 3:015005, 2008.

J. Gottschall, E. Anahua, S. Barth, and J. Peinke. Stochastic modelling of wind speed power production correlations. *Proc. Appl. Math. Mech.*, 6:665–666, 2006.

S. M. Iacus. *Simulation and Inference for Stochastic Differential Equations*. Springer, 2008.

K. Kaiser, H. Hohlen, and W. Langreder. Turbulence correction for power curves. In *EWEC*, Madrid, 2003.

K. Kaiser, W. Langreder, H. Hohlen, and J. Højstrup. Turbulence correction for power curves. In J. Peinke, P. Schaumann, and S. Barth, editors, *Wind Energy, Proceedings of the Euromech Colloquium*, pages 159–162. Springer, 2007.

W. Langreder, K. Kaiser, H. Hohlen, and J. Højstrup. Turbulence correction for power curves. In *EWEC*, London, 2004.

T. F. Pedersen. On wind turbine power performance measurements at inclined airflow. *Wind Energy*, 7(3):163–176, 2004.

D. L. Phillips. A technique for the numerical solution of certain integral equations of the first kind. *J. ACM*, 9:84–97, 1962.

A. Rauh and J. Peinke. A phenomenological model for the dynamic response of wind turbines to turbulent wind. *J. Wind Eng. Ind. Aerod.*, 92(2):159–183, 2004.

A. Rosen and Y. Sheinman. The average output power of a wind turbine in a turbulent wind. *J. Wind Eng. Ind. Aerod.*, 51(3):287–302, 1994.

A. Rosen and Y. Sheinman. The power fluctuations of a wind turbine. *J. Wind Eng. Ind. Aerod.*, 59(1):51–68, 1996.

Y. Sheinman and A. Rosen. A dynamic model of the influence of turbulence on the power output of a wind turbine. *J. Wind Eng. Ind. Aerod.*, 39:329–341, 1992.

J. Sumner and C. Masson. Influence of atmospheric stability on wind turbine power performance curves. *J. Sol. Energ. Eng.*, 128(4):531–538, 2006.

A. N. Tikhonov. Solution of incorrectly formulated problems and the regularization method. *Soviet Math. Dokl.*, 5:1035–1038, 1963a.

A. N. Tikhonov. Regularization of incorrectly posed problems. *Soviet Math. Dokl.*, 4:1624–1627, 1963b.

A. Tindal, C. Johnson, M. LeBlanc, K. Harman, E. Rareshide, and A. Graves. Site-specific adjustments to wind turbine power curves. In *AWEA WINDPOWER*, Houston, 2008.

H. van Radecke. Turbulence correction of power curves. In *DEWEK*, Wilhelmshaven, 2004.

M. Wächter, P. Milan, T. Mücke, and J. Peinke. Power performance of wind energy converters characterized as stochastic process: applications of the Langevin power curve. *Wind Energy*, 14(6):711–717, 2011.

R. Wagner, I. Antoniou, S. M. Pedersen, M. S. Courtney, and H. E. Jørgensen. The influence of the wind speed profile on wind turbine performance measurements. *Wind Energy*, 12(4):348–362, 2009.

R. Wagner, M. Courtney, J. Gottschall, and P. Lindelöw-Marsden. Accounting for the speed shear in wind turbine power performance measurement. *Wind Energy*, 14:993–1004, 2011.

S. Wharton and J. K. Lundquist. Assessing atmospheric stability and its impacts on rotor-disk wind characteristics at an onshore wind farm. *Wind Energy*, 15:525–546, 2012a.

S. Wharton and J. K. Lundquist. Atmospheric stability affects wind turbine power collection. *Environ. Res. Lett.*, 7:014005, 2012b.

PAPER D

HIGH-FREQUENCY PARAMETRIZATION OF ENGINEERING WIND-FARM WAKE MODELS

U. V. Poulsen[1,2], J. Scholz[2], E. Hedevang[2,3], J. Cleve[3], and M. Greiner[1,2]

1 · Department of Engineering, Aarhus University, Denmark
2 · Department of Mathematics, Aarhus University, Denmark
3 · Siemens Wind Power, Borupvej 16, 7330 Brande, Denmark

ABSTRACT

High-frequency wind farm data is used to discuss the parametrization of engineering wind-farm wake models when applied to the average production patterns in individual periods of duration between 15 seconds and 10 minutes. As the averaging time is increased, the models can be made to fit the data better, but even with 10 minutes averaging a significant error remains indicating a residual limitation of these models. The fitted wake parameters turn out to be independent from the time resolution and are significantly smaller than those values obtained from standard sector-averaged model fits. A previously reported speculation on a possible dependence of the wake parameters on the turbine spacing is not confirmed and traced back to a specific modeling of the multiple wake interactions. The inclusion of crosswind upwind heterogeneity leads to a good improvement of the model fits. The additional inclusion of streamwise non-stationarity, where the wake models are formulated in a co-moving Lagrangian reference frame, only leads to a rather small increase in mean fit quality; however, for some rare non-stationary events the improvements are quite significant.

D.1 INTRODUCTION

As wind farms are increasing in numbers, they are also becoming larger and more complex. Their design and operation require a sound understanding of the complex intra-farm wind flows, with various levels of sophistication depending on the concrete objectives. For example, layout optimization and resource analysis (Barthelmie and Jensen, 2010; Barthelmie et al., 2003, 2006, 2009, 2010; Gar, 2011; Mortensen et al., 2009; Vermeer et al., 2003) frequently use simple engineering wake models (Frandsen et al., 2006; Jensen, 1983). These models are intended to describe the mean wake-flow behaviour inside a wind farm in a highly averaged manner with predictions of the annual energy production as the important output. For other objectives, like the reduction of turbine loads, models beyond the mean description are required (Ainslie, 1988; Knudsen et al., 2011; Larsen et al., 2011). Recent progress in computational fluid dynamics (Calaf et al., 2010; Troldborg et al., 2010, 2011; Wußow et al., 2007) as well as in Lidar (Bingol et al., 2010; Trujillo et al., 2011) and wind-tunnel experiments (Cal et al., 2010; España et al., 2011; Sanderse et al., 2011) reveal that the intra-farm wind flows are very dynamic. They are dominated by wake meandering, wake interaction and the entrainment of kinetic energy from the atmospheric layer above the wind-farm boundary layer. The challenge with respect to the load objective is to formulate intra-farm wind flow models which on the one hand take these dynamical effects into account, but on the other hand are still simple and tractable enough to be used efficiently in an optimization calculation.

Due to their simplicity the standard engineering wind-farm wake models have also been employed for the design of control optimizations that maximize wind-farm power by making upwind turbines behave altruistically to let more wind pass to the downwind turbines (Bjarnason and Sveinsson, 2010; Machielse et al., 2007; Spudić et al., 2010). However, first results from experiments in wind-tunnels and on wind-farm test sites do not appear to fully match the expectations obtained from such a model-based optimization. Since the optimization can only be as good as the quality of the underlying models, there is now a strong need to learn about the limitations of current engineering wake models when applied to dynamic wind-farm production patterns. To analyse these limitations and to explore improvements to the models is the main motivation for the work presented in this paper.

We analyze high-frequency intra-farm power generation data from the offshore wind farm Nysted and compare it to several variations of engineering wake models, which differ in the description of single wakes as well as multiple wake interactions. Contrary to Cleve et al. (2009), where a smooth-event filter has rejected about two-third of the events, this time all events are treated, including those with crosswind upwind heterogeneity as well as streamwise non-stationarity. Also, the respective event time windows are now not restricted to only 10 min, but range down to 15 sec. All details about the data, the wind-farm wake models and the fitting procedure are presented in Sect. D.2. Sect. D.3 discusses the fit results obtained with the wake models constrained to a constant upwind profile. The quality of the model fits

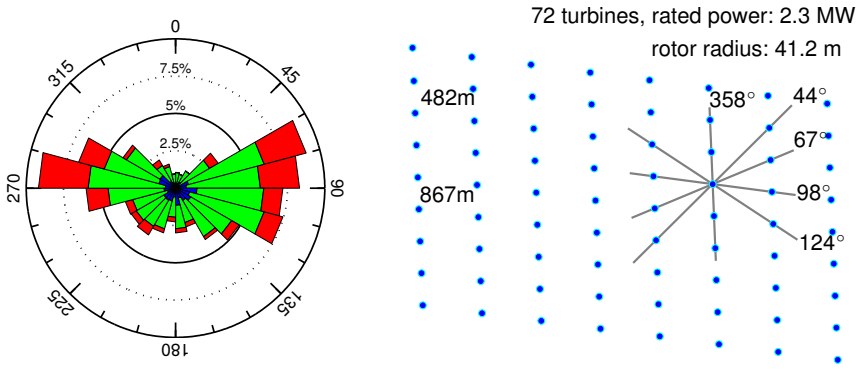

FIGURE D.1. Left: The wind rose derived from the used data. The three blocks for each 15° sector indicate on a linear scale the percentage of the data, for which the frontline turbine generation is below 150 kW (blue), between 150 and 2150 kW (green), and above 2150 kW (red). Right: The Nysted wind farm layout.

increases with decreasing event time resolution and saturate at a time resolution around 10 min, indicating a residual limitation of these models. The fitted wake parameters turn out to be independent from the time resolution and significantly smaller than those values obtained from standard sector-averaged model fits. A previously reported speculation (Cleve et al., 2009) on a possible dependence of the wake parameters on the turbine spacing is not confirmed and traced back to a specific modeling of the multiple wake interactions. Sect. D.3.3 introduces crosswind upwind heterogeneity into the wake models, which leads to a good improvement of the model fits. Streamwise non-stationarity, where the wake models are formulated in a co-moving Lagrangian reference frame, is discussed in Sect. D.3.4. It leads to a rather small increase in mean fit quality. However, for some rare non-stationary events the improvements are quite significant. Sect. D.4 gives a summary and a short outlook.

D.2 DATA, WAKE MODELS, AND FITTING OBJECTIVE

D.2.1 THE DATA

The used data set consists of three months (March–May 2009) of high-frequency recordings from the 72 Siemens-Bonus 2.3 MW turbines comprising the Nysted off-shore wind farm. The temporal resolution of the recordings, including turbine power and yaw, is 1 second. Data from nearby meteorology masts is not used. Figure D.1 illustrates the wind rose derived from the used data. Compared to the typical wind rose (Barthelmie and Jensen, 2010), easterly winds are clearly over-represented. This, however, is of little consequence for our investigations here.

The 3 month time span of the data is divided into disjoint 10 minutes periods. Only data where the frontline turbines produce more than 150 kW and less than 2150 kW are considered. As can be seen from the wind rose in Fig. D.1, this filter excludes about 20% of the data because of low wind and another 20% because of high wind. The filter is applied because we want

to be able to translate power to wind speed via the inverse power curve of the Nysted turbines, which can only be done comfortably between cut-in and rated power. The power and C_T curves of the Nysted turbines are shown in Fig. 1 of Barthelmie and Jensen (2010). From the filtered 10 minutes periods the first 15, 30, 60, 120, 300, and 600 seconds averaged data points are selected. These form the ensemble of events to be fitted to the models. We have not identified any periodes of down-regulation in this ensemble, but we cannot completely exclude that some exist. Note that we do not need to exclude periodes where some of the turbines are out of operation since we analyze each event separately and can simply leave out the non-active turbines from our modelling of farm as they do not produce (appreciable) wakes. This is one advantage of our single-event method compared with sector-averaged approaches.

D.2.2 WAKE MODELS

A number of engineering wake models have been proposed in the literature. We will be concerned with the Jensen model (Jensen, 1983; Katic et al., 1987) and what we will refer to as the Frandsen model (Frandsen et al., 2006; Rathmann et al., 2006). As a function of the downwind distance x from a given turbine, both models use a wake radius $R(x)$ and a wake velocity $u(x)$. Outside the wake the wind is undisturbed and has speed v_0. Inside the wake the wind speed is $u(x)$.

The Jensen model uses the linear parametrisation

$$R_{\text{Jensen}}(x) = R + kx$$

for the wake radius and the expression

$$u_{\text{Jensen}}(x) = v_0\left[1 - \left(1 - \sqrt{1 - C_T(v_0)}\right)\left(\frac{R}{R_{\text{Jensen}}(x)}\right)^2 \frac{A_{\text{overlap}}}{A_{\text{rotor}}}\right] \tag{D.3}$$

for the down-wind speed. R is the rotor radius, and C_T is the thrust coefficient. For the latter we employ the parametrization given in Barthelmie and Jensen (2010). The adjustable wake parameter k determines how fast the wake expands and hence how fast the wind speed recovers to v_0. The last factor on the right-hand-side of (D.3) represents the fraction of the downwind rotor disc that falls inside the wake.

The Frandsen model uses the wake parametrization

$$R_{\text{Frandsen}}(x) = R\sqrt{\max\left\{\beta, \frac{\alpha x}{2R}\right\}}$$

with the adjustable expansion parameter α and the minimal expansion $\beta = \frac{1}{2}\left(1 + \sqrt{1 - C_T}\right)/\sqrt{1 - C_T}$, and a wake velocity

$$u_{\text{Frandsen}}(x) = \frac{v_0}{2}\left[1 + \sqrt{1 - 2C_T(v_0)\left[\frac{R}{R_{\text{Frandsen}}(x)}\right]^2 \frac{A_{\text{overlap}}}{A_{\text{rotor}}}}\right].$$

When a turbine faces more than one wake from two or more upwind turbines, one has to decide on a combination of the multiple influences. We adopt

two different approaches: the Katic procedure (Katic et al., 1987) and the semi-linear procedure (Frandsen et al., 2006). The Katic procedure calculates the effective velocity u_{Katic} at the turbine with the empirical rule that velocity deficits should be added in square:

$$\frac{v_0 - u_{\text{Katic}}}{v_0} = \sqrt{\sum_j \left(\frac{v_0 - u_j}{v_0}\right)^2} \tag{D.7}$$

with u_j being the velocity calculated based on the influence from upwind turbine j alone. We use this approach in combination with both the Jensen and the Frandsen model. The semi-linear procedure is used only in combination with the Frandsen model. It adds the thrusts of the upwind turbines:

$$u_{\text{semi-linear}} = \frac{v_0}{2}\left[1 + \sqrt{1 - 2\sum_j C_{T,j}\left[\frac{R}{R_{\text{Frandsen}}(x_j)}\right]^2 \frac{A_{\text{overlap},j}}{A_{\text{rotor}}}}\right]. \tag{D.9}$$

Note that in the expressions (D.7) and (D.9) the thrust coefficients of the upwind turbines j are determined with their respective effective velocities.

D.2.3 PARAMETRIZATION OF THE FREE WIND

Apart from the farm layout and the C_T curve of the turbines, the input variables into both the Jensen and the Frandsen model are the free wind speed v_0, the wind direction θ, and the wake parameter k or α. We choose to extract the free wind speed directly from the data in the following way: First an approximate wind direction is determined by a simple average of the yaw readings of all turbines with a whole-farm correction described in Cleve et al. (2009). This determines which turbines on the farm perimeter that are not experiencing wakes from other turbines. Because of the farm geometry there are always (barring turbine outages) at least 8 such turbines: 8 when the wind is near the South-North direction, 9 from when the wind is near the West-East symmetry axis, and 16 for the directions inbetween that are more aligned with the farm diagonals. We base our estimate of the free wind on the maximally 9 most upwind of these free wind turbines, both in order to work with approximately the same number of turbines for all wind directions and to extract the free wind near the "front end" of the farm. This approach is similar to one used in Barthelmie and Jensen (2010). Once this choice of free wind turbines has been made, we use the inverse power curve to estimate the wind speed experienced by these turbines. We then either assume the free wind speed to be *homogeneous* or allow it to be *heterogenous* in the crosswind direction. In the homogeneous case, the single v_0 is simply taken as the average of the free wind estimates. In the heterogenous case, we still want a smooth, few-parameter description and we choose a second order polynomial, i.e. we express the free upwind as

$$v_0^{\text{hetero}}(y) = a_2 y^2 + a_1 y + a_0$$

where y is the crosswind position and a_0, a_1 and a_2 are estimated from the most upwind turbines selected as described above. In this way we obtain a

free wind profile which is then used in the wake models: We replace in the expressions (D.3), (D.5)–(D.9) used to calculate the velocity u_{Katic} or $u_{\text{semi-linear}}$ at a given downwind turbine, the homogeneous upwind velocity v_o by the heterogeneous upwind velocity $v_o^{\text{hetero}}(y)$ evaluated at the crosswind position of the most upwind turbine producing a wake at the considered downwind turbine.[1] Other than this, all other calculational details remain the same as in the homogeneous case.

D.2.4 TEMPORAL REFERENCE FRAME

Usually when working with wind farm data averaged over e.g. 10 minutes, one uses a fixed, Eulerian temporal reference frame in the sense that a single event consists of data from the *same* 10 minutes for all turbines. However, for a typical wind speed of 10 m/s along the main West-East symmetry axis, the wind takes about 1.5 min to propagate from one turbine row to the next one. To propagate through the whole wind farm it then takes seven times as much, which is about 10 min. By this time the first-in-row turbines might already experience a different wind condition than the last-in-row turbines. Based on this consideration, it is natural to try to capture as much of the propagation effects as possible with a simple change from the fixed to a Lagrangian, co-moving temporal frame of reference. In the latter, the downstream turbines are polled with a delay corresponding to the expected propagation time. In this way an event will change from being a snapshot to being the generation pattern as a certain air-parcel is followed down through the wind farm.

A simple definition of a co-moving frame of reference uses time delays according to a streamwise uniform propagation velocity, which is taken as the heterogeneous free wind speed divided by some correction factor η. The most upwind turbine has a zero time delay. Another turbine, say j with downwind distance x_j, then has a delay time

$$\tau_j = \frac{\eta x_j}{v_{oj}}\,.$$

Note, that we will use the heterogeneous upwind velocities v_{oj} as described in Sec. D.3.3. We will treat the correction factor η as an adjustable parameter.

D.2.5 FIT OBJECTIVE

We finally find the best wind direction and expansion parameter for describing each single event by considering the farm model a function of these with free wind extracted as above. The fitting procedure minimizes the expression

$$\varepsilon = \frac{\sum_i \left|P_i - P_i^{\text{fit}}\right|}{\sum_i P_i}\,,$$

1 · For wind directions along farm diagonals, extrapolation is needed for the turbines with the most extreme crosswind positions. We truncate the polynomial fit at the value at the nearest data point in order to avoid trends in the data to have an exaggerated influence at extreme crosswind positions.

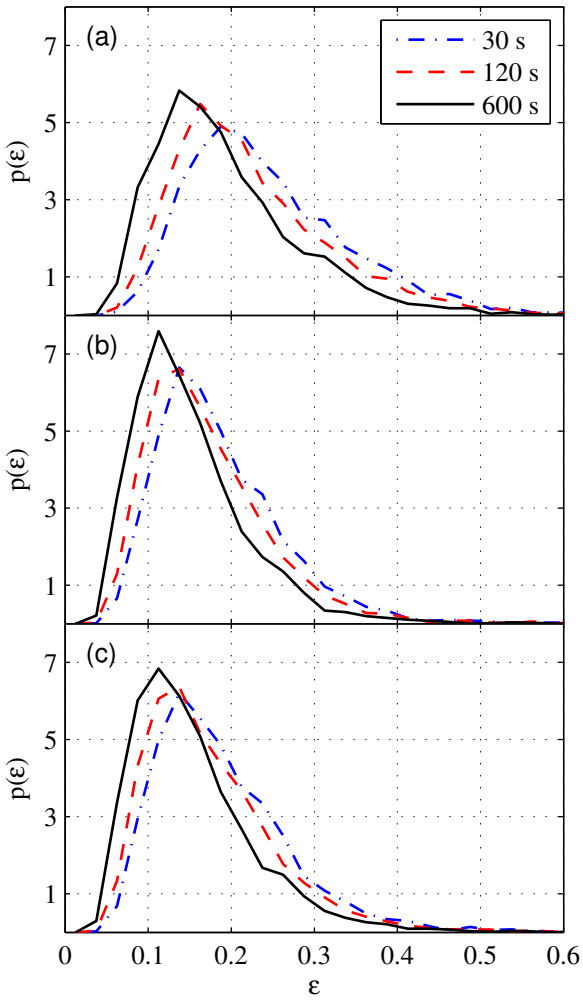

FIGURE D.2. Fit-error probability density function for (a) the Jensen model with Katic wake interaction, (b) the Frandsen model with Katic wake interaction, and (c) the Frandsen model with the semi-linear wake interaction. All results assume homogeneous free wind and use an Eulerian fixed temporal reference frame. Note that the area under the curve is normalized to unity.

which is the normalized sum of absolute differences between actual turbine power production and model prediction. A steepest descent method is used to find the minimum.

D.3 RESULTS

D.3.1 QUALITY OF FITS

The quality of the three wake models is determined by fits to the data. The distributions of the fit-error (D.12) are shown in Fig. D.2 for three different time averages. The shown results are for the homogeneous free wind and using a fixed temporal reference frame, but there is little qualitative change by going to the heterogeneous or co-moving cases. The distributions are peaked around $\varepsilon \approx 10$-20%, with significant tails in the 30-50% range. The results are quite similar for all three models, with the Jensen model slightly poorer than

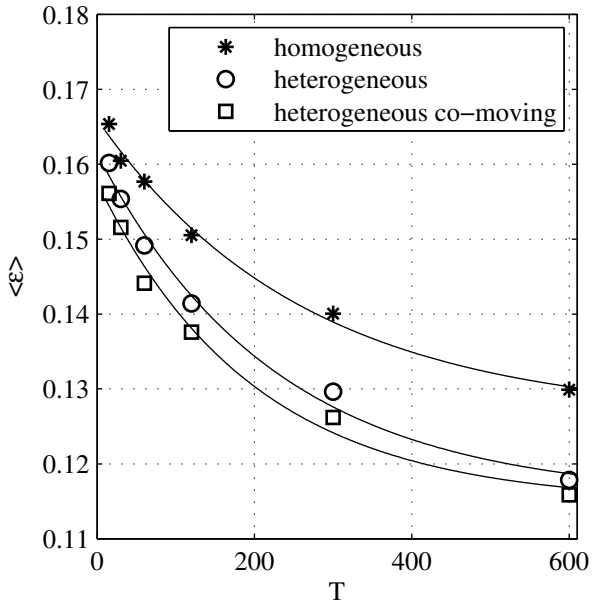

FIGURE D.3. Mean fit error of the Frandsen model with Katic wake interaction as a function of the event averaging time T for the data. The curve with the ⋆ symbols assumes a homogeneous upwind velocity, which is taken the same for all most upwind turbines. The curve with the ○ symbols assumes heterogeneous upwind velocities, which differ for different most upwind turbines; more details are described in Sec. D.3.3. The curve with the □ symbols considers heterogeneous upwind velocities in a co-moving reference frame with $\eta = 0.8$; see Sec. D.3.4 for more details. The lines are fits of the form $a+b\exp(-T/T_0)$ with parameters $(a, b, T_0) = (0.126, 0.040, 260\text{s})$ (homogeneous), $(0.116, 0.046, 240\text{s})$ (heterogeneous) and $(0.115, 0.043, 200\text{s})$ (heterogeneous co-moving), respectively.

the two versions of the Frandsen model. The fits tend to get poorer with decreasing event averaging times. However, there is no dramatic change in the shape of the error distributions when going from 600 via 120 to 30 seconds averages. The peak and the tail at large ε are slightly moved to higher values.

The decrease in fit quality for short averaging times is to be expected. The wakes can no longer assumed to be stationary. Turbulence, but also meandering (Larsen et al., 2008) and vertical transport of momentum and kinetic energy across the wind-farm boundary layer (Cal et al., 2010; Calaf et al., 2010) lead to increased fluctuations on the short time scales. Fig. D.3 illustrates the mean fit error in the Frandsen model with Katic wake interaction as a function of the event averaging time for the data. The error increases smoothly with shorter durations and is nicely described by an exponential of the form $a + b\exp(-T/T_0)$. For homogeneous free wind and a fixed reference frame we get an asymptotic offset $a = 0.126$ and a charateristic time $T_0 = 260$ s. This finding suggests that even for $T \gg T_0$ the fit quality of the engineering wake models can not become better than the offset a. The offset can be interpreted as a fundamental limitation of the engineering wake models ability to describe the wind-farm power-generation patterns, even when short-term fluctutations are averaged out. In fact, the standard event averaging time of 10 min is well taken, as it averages out almost all short-term fluctuations and produces fit qualities very close to the asymptotic offset. For shorter event

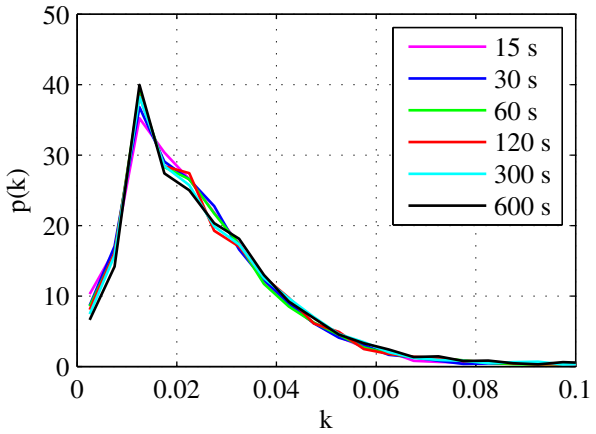

FIGURE D.4. Probability density function for the fitted wake parameter k for the Jensen model with Katic wake interaction with various event averaging times. The free wind is assumed homogeneous and a fixed temporal reference frame has been used.

averaging times the impact of the short-term fluctuations becomes visible. However when compared to the 10 min event averaging time, even a very short event averaging time $T = 15$ s leads to only a 30% increase of the fitting errors.

D.3.2 MODEL PARAMETER DISTRIBUTIONS

The distribution of the fitted wake parameters k and α are plotted in Figs. D.4 and D.5. In both cases the homogeneous free wind asumptions has been applied and a fixed temporal reference frame used. The first thing to note is that the distributions are quite broad. They are also independent of the event averaging time. At first this appears to be a little bit surprising for the very short event averaging times, but apparently the meandering of narrow wakes is still not resolved. This could well be due to spatial averaging effects as we impose a single wind direction for the whole farm. For the Jensen model the mean wake parameter $k = 0.025$ turns out to be significantly smaller than the standard value $k = 0.04$. This result is similar to the result found in Cleve et al. (2009). The same holds true for the Frandsen model, where the Katic and semi-linear wake interaction lead to a mean $\alpha = 0.16$ and 0.21, respectively. Both values are strikingly different to the literature values $\alpha \approx 0.5$–0.7 (Bjarnason and Sveinsson, 2010; Rathmann et al., 2006). The main reason for these differences is simple. It is the standard procedure to first average over events belonging to a common wind-direction sector, and then to fit the sector-averaged event to the wake model. As the sector-averaged event includes contributions from many different close-by wind directions, the resulting wake appears to be broadly smeared out. The single-event procedure, which we are adopting, is sharp in wind direction. Consequently, the fitted wakes turn out to be more narrow.

In the left column of Fig. D.6 the dependence of the fitted wake parameters on the estimated upwind speed is illustrated. For the Jensen model we observe a weak decrease of k with v_0. For the two versions of the Frandsen model, α

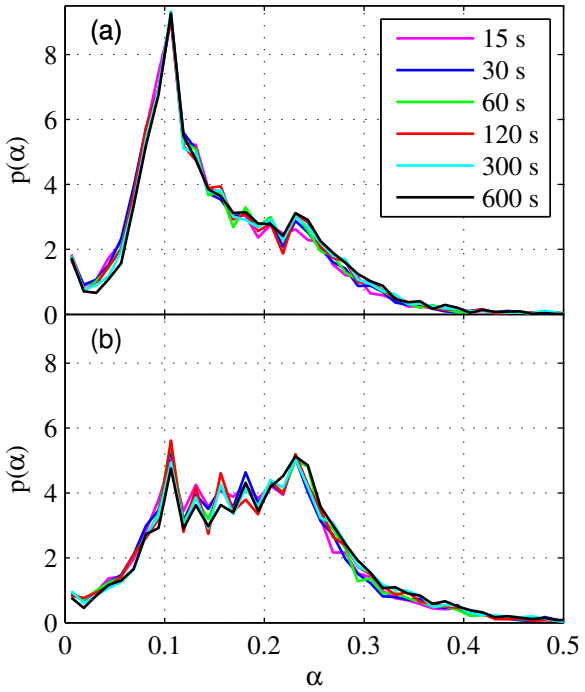

FIGURE D.5. Probability density function for the wake parameter α for the Frandsen model with (a) Katic and (b) semi-linear wake interaction with various event averaging times. The free wind is assumed homogeneous and a fixed temporal reference frame has been used.

appears to be quite constant. Without showing we state that all three model variants produce slightly better fits to events with a large upwind velocity than to events with a low upwind velocity.

The dependence of the fitted wake parameters on the fitted wind direction is plotted in the right column of Fig. D.6. The results for the two event averaging times 15 and 600 seconds show little difference. The wake parameter k of the Jensen model turns out to be larger along the symmetry axis of the wind farm. The main symmetry axes of the Nysted wind farm are at $\Theta = 98°$ (278°) and 178° (358°), which represent the East-West and the South-North directions. Other symmetry directions are 44° (224°), 67° (247°), 124° (304°) and 140° (320°). This result confirms the findings shown in Fig.9 of Cleve et al. (2009), where a different Nysted data set with only 10 min resolution has been used. Also the results obtained with the two versions of the Frandsen model confirm this dependence, although it is not so pronounced for the version with the semi-linear wake interaction. It is also interesting to note that for the Jensen model the wake parameter k turns out to be significantly larger for North-South wind directions than for the other directions. In Cleve et al. (2009) the speculation has been put forward, that this might indicate an additional dependence of the wake parameter on the turbine spacing of the Nysted wind farm, which is about 5.9 rotor diameters in North-South direction and 10.5 rotor diameters in West-East direction. However, for the Frandsen model we do not see this effect so clearly. The wake parameter α along the North-South wind directions is only slightly larger than for the other symme-

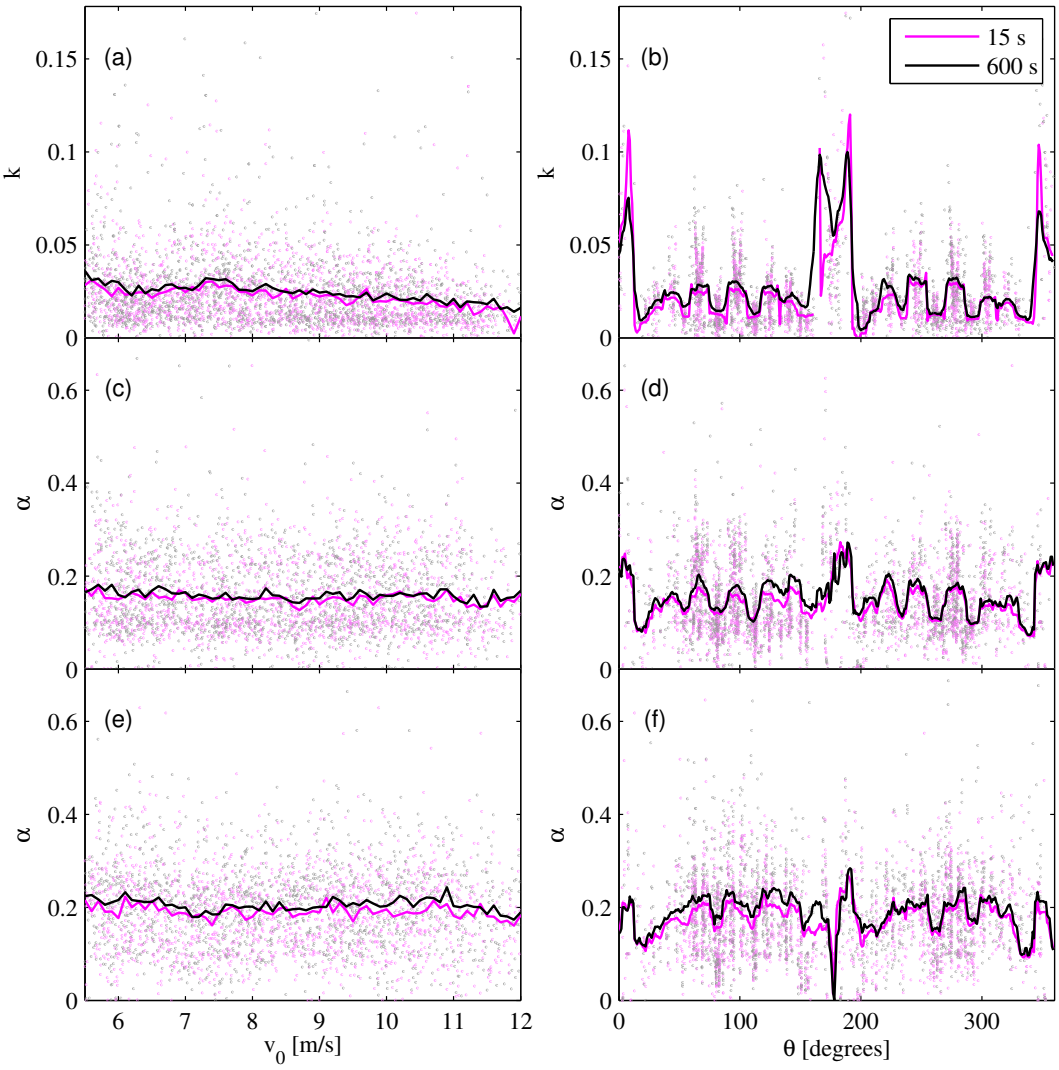

FIGURE D.6. Wake parameters of the Jensen model (top row) and the Frandsen model with Katic wake interaction (middle row) and semi-linear interaction (bottom row) as a function of the estimated up-wind speed (left column) and the fitted wind direction (right column). The dots represent all events with respect to 15 s (magenta) and 600 s (grey) averaging times. The lines are running averages based on a 0.1 m/s and 10° window width, respectively. The free wind is assumed homogeneous and a fixed temporal reference frame has been used.

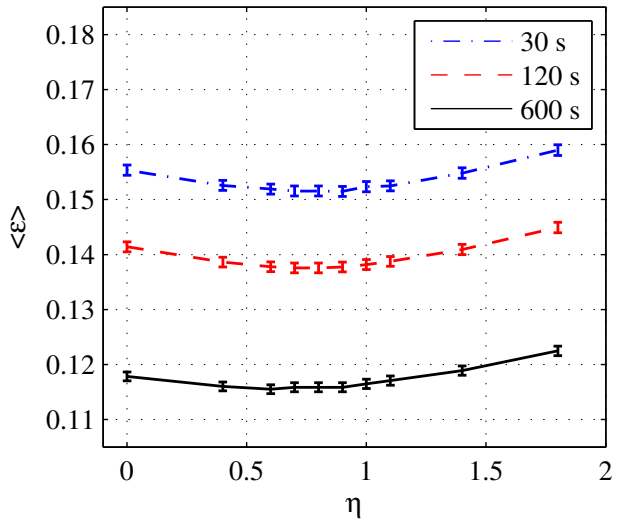

FIGURE D.7. Mean fit error for the Frandsen model with Katic wake interaction and heterogeneous upwind velocities as a function of the correction factor η defining the co-moving frame of reference. The event averaging times are 30 s (blue), 120 s (green) and 600 s (black). The error bars represent the standard deviation around the mean fit error.

try axes. This indicates that the dependence on the turbine spacing might not be as strong as has been speculated, but rather that the parametrization (D.4) of the wake radius used in the Frandsen model might be more realistic than the Jensen-model parametrization (D.1). When translated into the latter, the former parametrization produces a larger wake parameter k for small turbine spacings and a smaller k for large turbine spacings. For example, for $C_T = 0.8$ and a Frandsen wake parameter of $\alpha = 0.2$, the Jensen k needs to be 0.046 to match the Frandsen radius at $x = 5.9R$, but only 0.026 to match at $10.5R$.

D.3.3 HETEROGENEOUS FREE WIND

As mentioned above, when introducing free wind heterogeneity, the resulting fit error distributions qualitatively look very similar to the ones obtained in Fig. D.2 assuming a homogeneous free upwind. However, there is a small, but noticeable shift towards lower errors, which leads to reduced mean fit errors; consult Fig. D.3. The relative decrease in mean error is approximately 3% for the short event averaging time $T = 15$ s and approximately 9% for the longer $T = 600$ s. Inbetween these two time scales the mean fit error behaves again like the expression $a + b\exp(-T/T_0)$, thus supporting its tentative interpretation put forward in the previous section. Also all other conclusions drawn in the previous section based on the homogeneous upwind assumption fully carry over to the heterogeneous generalization.

D.3.4 CO-MOVING TEMPORAL FRAME OF REFERENCE

We now consider the Lagrangian, co-moving temporal frame of reference introduced in Sec. D.2.4. Fig. D.7 illustrates the mean fit error for one of the wake

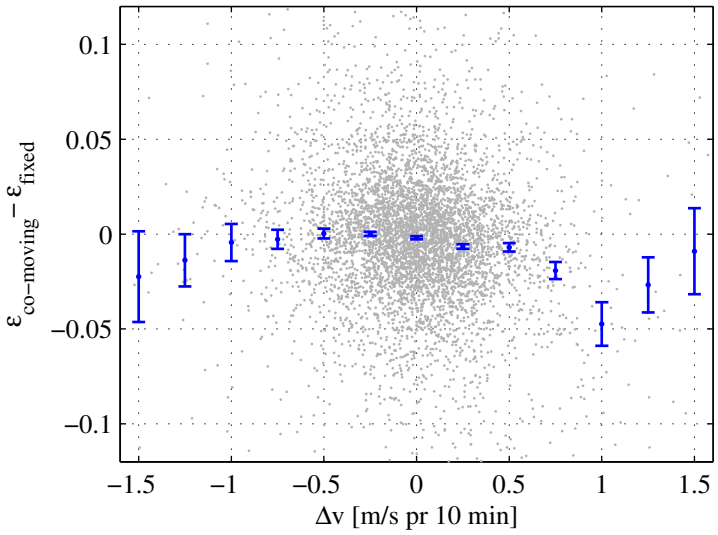

FIGURE D.8. Change in fit error (Frandsen model with Katic wake interaction and 30 s averaging time) when going from the fixed $\eta = 0$ to the co-moving $\eta = 0.8$ reference frame plotted versus change in wind speed. The grey dots are a scatter plot of all events while the blue symbols indicate binned averages (bins 0.25 m/s wide). The statistical uncertainty on this average is estimated by the standard deviation divided by the square root of the number of events in each bin and included as errorbars. Wind speed change is quantified by the difference in 10 min averaged wind speed from one event to the next.

models in the co-moving frame of reference. More or less independent of the event averaging time, it reaches a minimum at a delay correction factor [cf. Eq. (D.11)] of about $\eta = 0.8$. This is somewhat surprising. Naively we would have expected the minimum to be at a value larger than one. An optimal value smaller than one indicates that the propagation velocity is larger than the estimated free upwind speed. In principle this can happen via processes like the entrainment of faster velocities from the atmospheric layer above the wind-farm boundary layer (Calaf et al., 2010). However, it should be emphasized that the average fit error is by no means a direct indicator of the correct co-moving frame of reference.

Compared to the mean fit error obtained in the fixed frame of reference at $\eta = 0$, the minimum mean fit error at $\eta = 0.8$ is only slightly smaller. See also again Fig. D.3, which clearly demonstrates that the introduction of upwind heterogeneity has a much bigger impact on the reduction of the fit errors than the additional introduction of a co-moving reference frame. One reason for the very small average benefit of switching to a co-moving reference frame is the fact that the majority of all events contained in the employed data set have rather stationary wind conditions. This effect is illustrated in Fig. D.8 where we plot the change in fit error versus change in wind speed. The latter is quantified by the change in average wind speed from one 10 min period to the next – a measure that captures overall changes in the weather conditions rather than short-time fluctuations. The first thing to notice is the large spread in fit error changes: The change of frame is almost equally likely to give a worse or better fit, and the typical magnitude of 0.04–0.07 is much larger than the change in average fit error of 0.004 (difference between squares and circles

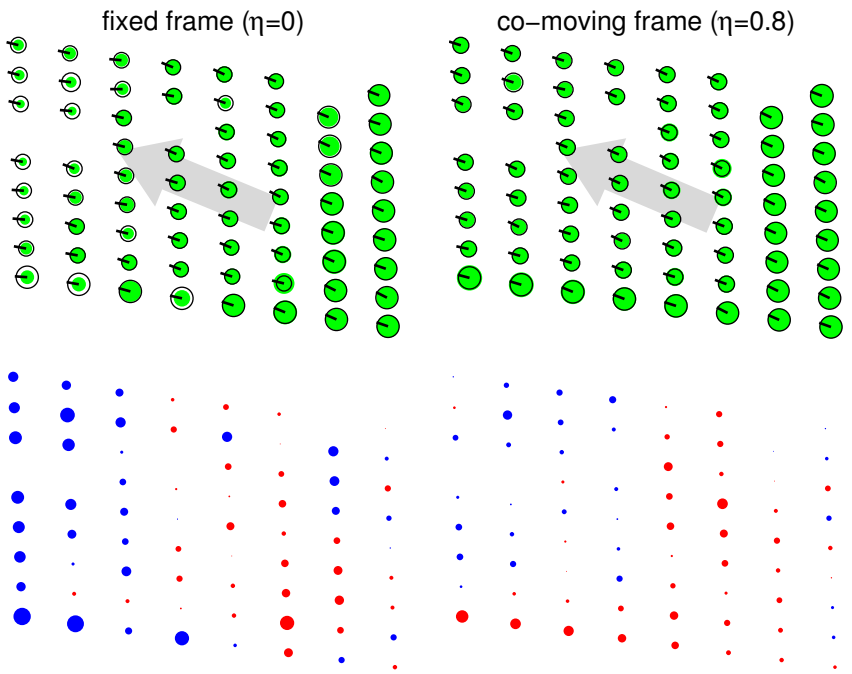

FIGURE D.9. Production pattern caused by an event with increasing wind speed from East-Southeast (gray arrow), as seen in the fixed (left) and the co-moving (right, with $\eta = 0.8$) reference frame. The averaging time is $T = 30$ sec. The filled green circles in the upper row illustrate the power production of the turbines, while the unfilled black circles indicate the best fit of the Frandsen model with Katic wake interaction. The small wind vanes indicate the yaw of each active turbine. The lower row shows the differences between production and fit; red (blue) circles indicate that the actual production is above (below) the best model fit. The free wind speed is about 8 m/s resulting in a maximal time-delay of about 760 sec when selecting data for the Lagrange frame, cf. Eq. (D.11).

in Fig. D.3 or between $\eta = 0$ and $\eta = 0.8$ for the blue symbols in Fig. D.7). This is because a new frame constitutes a new sampling of the short-term random fluctuations in production at each turbine. The second thing to notice is that when we bin the data according to wind change, the fit error is indeed reduced significantly more for the relatively rare, large wind speed changes than for the much more common, steady wind conditions. There also seems to be an asymmetry in the reductions so that *increasing* winds make the co-moving frame more benificial than corresponding *decreasing* winds. The asymmetry could have meteorological origins where the two signs of wind speed change are accompanied by different other effects e.g. changes in wind direction, but our normalization of the fit error to the total production [cf. Eq. (D.12)] may also contribute.

Let us finally show in more detail a specific event where the wind speed change can clearly be identified and there is a significant improvement when going from fixed to co-moving reference frame. Fig. D.9 illustrates an event where an increased wind speed has arrived in the South-East corner of the wind farm. At the same time the wind is changing to a more Easterly direction. In the fixed Eulerian reference frame, the model clearly has difficulties to fit the production pattern in a satisfactory manner and the power production of the downwind turbines is generally overestimated. This is both because the

downwind turbines still experience the low wind speed and because the turbines on the Southern perimeter are predicted to experience free wind while they are in fact still wake affected. The fit error turns out to be $\varepsilon_{\text{fixed}} = 0.24$. In the co-moving reference frame, on the other hand, the power productions of the downwind turbines are evaluated with a time delay which means that their production is much more consistent with the conditions at the upwind turbines, i.e. the free wind speed is higher and the turbines on the Southern perimeter are not wake affected. The resulting production pattern is much better fitted, resulting in $\varepsilon_{\text{co-moving}} = 0.097$, a major part of which stems from an underestimation of the production in the South-Western corner of the farm that seems to stem from a wind gust.

D.4 CONCLUSION

Existing engineering wake models have first been tested with high-frequency wind farm data, and then various model generalizations have been introduced. As expected the fit quality of the models decreases with increasing time resolution. However, this increase is only about 35% when going from a 10 min down to a 15 sec time resolution. The saturation of the fit error at a time resolution of around 10 min appears to indicate a residual limitation of the engineering wake models. The fitted wake parameters turn out to be independent from the time resolution and are significantly smaller than those values obtained from standard sector-averaged model fits. A previously reported speculation (Cleve et al., 2009) on a possible dependence of the wake parameters on the turbine spacing is not confirmed. It appears to be an artifact of the Jensen wake model (Jensen, 1983) and is only weakly observed with the Frandsen wake model (Frandsen et al., 2006), which describes the wakes and their interaction in a different way. An important generalization of the engineering wake models is the inclusion of heterogeneous crosswind wind speed profiles. A large fraction of the short-term wind-farm patterns appear to reveal this upwind heterogeneity. Its inclusion leads to a significant improvement of the model fits. A smaller fraction of the short-term wind-farm patterns are also influenced by non-stationary wind conditions, where wind fronts pass through and lead to a time-delayed temporal ramp-up or down of the wind turbine powers. A respective model generalization, which introduces a co-moving reference frame, leads to only a small further improvement of the average fit quality. However, for some non-stationary events the improvements can turn out to be quite significant.

The presented results obtained from the introduced generalizations of engineering wake models are important findings in view of the control optimization of wind farms, in particular for wind-farm power optimization as well as for ultra-short wind-farm power forecasting. Since a model-based optimization and control of wind farms can only be as good as the underlying models, there is need for further model generalizations. Dynamic effects like wake meandering and the entrainment of fresh kinetic energy from the atmospheric layer above the wind-farm boundary layer also have to be taken into account and formulated in such a way that the resulting models are still

simple, but tractable enough to be used efficiently in an optimization calculation. We consider the single-event methodology presented here as a tool in the development of such dynamics generalizations. Perhaps such generalizations could even indicate ways to achieve the *a priori* quite different goal of better predictions of the annual energy production by revealing general relations between wake model parameters and wind condition characteristics or by enabling a better uncertainty assessment.

ACKNOWLEDGEMENT

The authors acknowledge DONG Energy A/S and Siemens Wind Power for providing the data used in this study.

BIBLIOGRAPHY

J. F. Ainslie. Calculating the flowfield in the wake of wind turbines. *J. Wind Eng. Ind. Aerod.*, 27:213—224, 1988.

R. J. Barthelmie and L. E. Jensen. Evaluation of wind farm efficiency and wind turbine wakes at the nysted offshore wind farm. *Wind Energy*, 13(6):573–586, 2010.

R. J. Barthelmie, L. Folkerts, F. T. Ormel, P. Sanderhoff, P. J. Eecen, O. Stobbe, and N. M. Nielsen. Offshore wind turbine wakes measured by SODAR. *J. Atmos. Ocean. Technol.*, 20(4):466–477, 2003.

R. J. Barthelmie, G. C. Larsen, S. T. Frandsen, L. Folkerts, K. Rados, S. C. Pryor, B. Lange, and G. Schepers. Comparison of wake model simulations with offshore wind turbine wake profiles measured by sodar. *J. Atmos. Ocean. Technol.*, 23(7):888–901, 2006.

R. J. Barthelmie, K. Hansen, S. T. Frandsen, O. Rathmann, J. G. Schepers, W. Schlez, J. Phillips, K. Rados, A. Zervos, E. S. Politis, and P. K. Chaviaropoulos. Modelling and measuring flow and wind turbine wakes in large wind farms offshore. *Wind Energy*, 12(5):431–444, 2009.

R. J. Barthelmie, S. C. Pryor, S. T. Frandsen, K. S. Hansen, J. G. Schepers, K. Rados, W. Schlez, A. Neubert, L. E. Jensen, and S. Neckelmann. Quantifying the impact of wind turbine wakes on power output at offshore wind farms. *J. Atmos. Ocean. Technol.*, 27(8):1302–1317, 2010.

F. Bingol, J. Mann, and G. C. Larsen. Light detection and ranging measurements of wake dynamics part i: One-dimensional scanning. *Wind Energy*, 13(1):51–61, 2010.

B. Bjarnason and Ö. Sveinsson. Wind farm controller – optimization of power production. Master's Thesis, DTU Electrical Engineering, Lyngby, 2010.

R. B. Cal, J. Lebron, L. Castillo, H. S. Kang, and C. Meneveau. Experimental study of the horizontally averaged flow structure in a model wind-turbine array boundary layer. *J. Renew. Sustain. Energy*, 2d(1):013106, 2010.

M. Calaf, C. Meneveau, and J. Meyers. Large eddy simulation study of fully developed wind-turbine array boundary layers. *Phys. Fluids*, 22(1):015110, 2010.

J. Cleve, M. Greiner, P. Enevoldsen, B. Birkemose, and L. Jensen. Model-based analysis of wake-flow data in the Nysted offshore wind farm. *Wind Energy*, 12:125–135, 2009.

G. España, S. Aubrun, S. Loyer, and P. Devinant. Spatial study of the wake meandering using modelled wind turbines in a wind tunnel. *Wind Energy*, 14(7):923–937, 2011.

S. Frandsen, R. Barthelmie, S. Pryor, O. Rathmann, S. Larsen, J. Højstrup, and M. Thøgersen. Analytical modelling of wind speed deficit in large offshore wind farms. *Wind Energy*, 9:39–53, 2006.

WindFarmer Theory Manual. Garrad Hassan, Bristol, England, 4.2 edition, 2011.

N. O. Jensen. A note on wind turbine interaction (m-2411). Technical report, Risø National Laboratory, Roskilde, Denmark, 1983.

I. Katic, J. Højstrup, and N. Jensen. A simple model for cluster efficiency. In W. Palz and E. Sesto, editors, *European Wind Energy Association Conference and Exhibition, Rome, 1986*, volume 1, pages 407–410, Rome, 1987. A. Raguzzi.

T. Knudsen, T. Bak, and M. Soltani. Prediction models for wind speed at turbine locations in a wind farm. *Wind Energy*, 14(7):877–894, 2011.

G. C. Larsen, H. A. Madsen, K. Thomsen, and T. J. Larsen. Wake meandering: A pragmatic approach. *Wind Energy*, 11:377–395, 2008.

G. C. Larsen, T. Buhl, H. A. Madsen, N. Troldborg, T. J. Larsen, S. Ott, J. Mann, M. Nielsen, H. Markou, P.-E. Réthoré, P. Fuglsang, J. N. Sørensen, K. S. Hansen, R. Mikkelsen, V. Okulov, W. Z. Shen, M. Heath, J. King, G. McCann, W. Schlez, I. Carlén, H. Ganander, E. Migoya, A. Crespo, A. Jiménez, J. Prieto, A. Stidworthy, D. Carruthers, J. Hunt, S. Gray, D. Veldkamp, A. S. Mouritzen, L. Jensen, T. Krogh, , B. Schmidt, K. Argyriadis, and P. Frohböse. *TOPFARM – next generation design tool for optimisation of wind farm topology and operation*, 2011.

L. A. H. Machielse, S. Barth, E. T. G. Bot, H. B. Hendriks, and G. J. Schepers. ECN-E-07-105: Evaluation of "heat and flux" farm control – final report. Technical report, ECN, Petten, 2007.

N. Mortensen, D. Heathfield, O. Rathmann, and M. Nielsen. *Wind Atlas Analysis and Application Program: WAsP 10 Help Facility.* Risø National Laboratory for Sustainable Energy, Technical University of Denmark, Roskilde, Denmark, 2009.

O. Rathmann, R. Barthelmie, and S. Frandsen. Turbine wake model for wind resource software. In *European Wind Energy Conference and Exhibition*, Athens, 2006.

B. Sanderse, S. P. van der Pijl, and B. Koren. Review of computational fluid dynamics for wind turbine wake aerodynamics. *Wind Energy*, 14:799–819, 2011.

V. Spudić, M. Baotić, and M. J. N. Perić. Hierarchical wind farm control for power/load optimization. In *Proceedings of Torque 2010*, Heraklion, Greece, 2010.

N. Troldborg, J. N. Sørensen, and R. Mikkelsen. Numerical simulations of wake characteristics of a wind turbine in uniform inflow. *Wind Energy*, 13 (1):86–99, 2010.

N. Troldborg, G. C. Larsen, H. A. Madsen, K. S. Hansen, J. N. Sørensen, and R. Mikkelsen. Numerical simulations of wake interaction between two wind turbines at various inflow conditions. *Wind Energy*, 14(7):859–876, 2011.

J.-J. Trujillo, F. Bingol, G. C. Larsen, J. Mann, and M. Kuehn. Light detection and ranging measurements of wake dynamics. part II: two-dimensional scanning. *Wind Energy*, 14(1):61–75, 2011.

L. J. Vermeer, J. N. Sørensen, and A. Crespo. Wind turbine wake aerodynamics. *Progr. Aero. Sci.*, 39(6–7):467–510, 2003.

S. Wußow, L. Sitzki, and T. Hahm. 3d-simulation of the turbulent wake behind a wind turbine. *J. Phys. Conf. Ser.*, 75(1):012033, 2007.